



Lehrstuhl für Elektrische Energiespeichertechnik
Fakultät für Elektrotechnik und Informationstechnik
Technische Universität München

Techno-economic evaluation of stationary battery energy storage systems with special consideration of aging

Dipl.-Ing. (Univ.) Maik Naumann

Vollständiger Abdruck der von der Fakultät für Elektrotechnik und Informationstechnik der
Technischen Universität München zur Erlangung des akademischen Grades eines

Doktor-Ingenieur (Dr.-Ing.)

genehmigten Dissertation.

Vorsitzender: Prof. Dr.-Ing. Georg Sigl
Prüfer der Dissertation: 1. Prof. Dr.-Ing. Andreas Jossen
2. Prof. Dr.-Ing. Ulrich Wagner

Die Dissertation wurde am 28.03.2018 bei der Technischen Universität München eingereicht und durch
die Fakultät für Elektrotechnik und Informationstechnik am 03.07.2018 angenommen.

Kurzfassung

Mit dem steigenden Anteil erneuerbarer Energien in den Stromnetzen weltweit und vor allem in Deutschland entstehen neue Herausforderungen der elektrischen Energieversorgung aufgrund der fluktuierenden Stromerzeugung der erneuerbaren Energiequellen. Stationäre Batteriespeichersysteme (BESS) sind gut geeignet um das Stromnetz zu unterstützen und die Integration erneuerbarer Energiequellen zu erleichtern. Vor allem BESS auf Basis von Lithium-Ionen-Batterien etablierten sich in den letzten Jahren auf dem deutschen Markt, da sich einerseits die technischen Eigenschaften stetig verbessert haben und gleichzeitig die Anschaffungskosten der Systeme gesunken sind. Jedoch steht die technische und wirtschaftliche Eignung dieser Energiespeichertechnologie für die verschiedenen stationären Anwendungsbereiche noch zur Diskussion.

Diese Arbeit präsentiert eine detaillierte technisch-ökonomische Bewertung von zwei stationären BESS Anwendungen PV-Heimenergiespeichersystem (PV-HESS) und Primärregelleistung (PCR)-Bereitstellung unter besonderer Berücksichtigung der Alterung der untersuchten $\text{LiFePO}_4/\text{Graphit}$ (LFP/C) Batteriezelle. Dazu wird die Software-Plattform SimSES entwickelt und zusammen mit Methoden zur Bewertung der technischen und wirtschaftlichen Ergebnisse der Simulation von stationären BESS vorgestellt. Um das Alterungsverhalten der LFP/C-Zellen zu verstehen, werden umfassende kalendarische und zyklische Alterungsstudien mit einer Dauer von fast 900 Tagen durchgeführt und ausgewertet. Die gewählten Testpunkte in den Alterungsstudien spiegeln alle möglichen Einflussgrößen hinsichtlich des Betriebs von BESS wider. Auf Basis dieser experimentellen Zellstudien werden semiempirische Alterungsmodelle entwickelt, die eine Abschätzung des Kapazitätsverlusts und des Widerstandsanstiegs der Zellen hinsichtlich der kalendarischen und zyklischen Alterung in Simulationen mit dynamischen Lastprofilen ermöglichen. Diese Alterungsmodelle werden mit dynamischen Lastprofilen validiert, die fast 900 Tage gleichzeitig mit den weiteren statischen Testpunkten der Alterungsstudien getestet werden. Für beide Profile folgt die simulierte Alterung sehr gut den gemessenen Werten des Kapazitätsverlustes und des Widerstandsanstiegs mit absoluten Modellfehlern kleiner 1 % für den Kapazitätsverlust und kleiner 2 % für den Widerstandsanstieg über die gesamte Messung. Diese Alterungsmodelle werden in das Software-Framework SimSES integriert und ermöglichen so eine präzise Simulation der Batteriealterung während des Betriebs von BESS. Auf dieser Grundlage wird eine techno-ökonomische Bewertung und ein Vergleich der beiden ausgewählten stationären Anwendungen PV-HESS und PCR-Bereitstellung mit geeigneten technischen und wirtschaftlichen Bewertungsparametern durchgeführt. Die Auswertung der Basisszenarien zeigt, dass BESS basierend auf der untersuchten LFP/C Zelle für einen Betrieb über 20 Jahre geeignet ist, wobei die Kapazitätsverluste und Widerstandszunahmen circa 20 bis 25 % betragen. Allerdings ist die BESS-Leistungsfähigkeit und die Batteriealterung stark von der jeweiligen Dimensionierung des Energiespeichers und seines Umrichters abhängig. Darüber hinaus ergibt die Bewertung von verschiedenen Preisszenarien, dass BESS bereits heute wirtschaftlich in den beiden ausgewählten stationären Anwendungen PV-HESS und PCR-Bereitstellung eingesetzt und betrieben werden können.

Abstract

With the increasing share of renewable energy sources in power grids all over the world and especially in Germany, new challenges in electric supply networks emerge due to the fluctuating power generation of the renewable energy sources. Stationary battery energy storage systems (BESS) are well suited to support the power grid and to facilitate the integration of renewable energy sources. Especially BESS based on lithium-ion batteries became established on the German market in the recent years due to the steady improvement of the technical properties together with the decreasing costs of these systems. However, the technical and economic suitability of this energy storage technology is still under discussion for the various stationary applications.

This work presents a detailed techno-economic evaluation of two stationary BESS applications PV-home energy storage system (PV-HESS) and primary control reserve (PCR)-supply with special consideration of the aging of the investigated $\text{LiFePO}_4/\text{graphite}$ (LFP/C) cell. Therefore, the software framework SimSES is developed and presented together with methods to assess the technical and economic results of the simulation of stationary BESS. In order to understand the aging of the LFP/C cells, comprehensive calendar and cycle aging studies with a duration of almost 900 days are performed and evaluated. The chosen test points in the aging studies reflect all possible influence parameters with regard to the operation of BESS. Based on this experimental cell studies, semi-empirical aging models are developed which allow for the estimation of the cells' capacity loss and resistance increase due to calendar and cycle aging in simulations with dynamic load profiles. These aging models are validated with dynamic load profiles, tested over almost 900 days simultaneously to the further static test points. For both profiles, the simulated aging trends followed very close the measured values of the capacity loss and resistance increase with absolute model errors less than 1% for the capacity loss and less than 2% for the resistance increase over the whole course of the measurement. These aging models are integrated into the software framework SimSES enabling a precise simulation of battery degradation during the BESS operation. On that basis, a techno-economic assessment and comparison of the two chosen stationary applications PV-HESS and PCR-supply are performed with appropriate technical and economic evaluation parameters. The evaluation of the baseline scenarios shows, that BESS based on the investigated LFP/C cell are suited to be operated over 20 years with capacity losses and resistance increases of about 20 to 25%. Though, the BESS performance and the resulting battery degradation strongly depends on the respective sizing of the energy storage and its inverter. Furthermore, the assessment of different price scenarios reveals, that already today BESS can be implemented and operated profitably in the two chosen stationary applications PV-HESS and PCR-supply.

Vorwort und Danksagung

Die vorliegende Dissertation entstand im Rahmen meiner Tätigkeit als wissenschaftlicher Mitarbeiter am Lehrstuhl für Elektrische Energiespeichertechnik unter der Betreuung von Prof. Dr.-Ing. Andreas Jossen an der Technischen Universität München. Finanziert wurde sie aus einem Forschungsvorhaben des Bundesministeriums für Wirtschaft und Energie sowie mit Mitteln der Technischen Universität München.

Vor allem möchte ich Prof. Dr.-Ing. Andreas Jossen herzlich danken, der mir die Chance zur Promotion gegeben hat und meine Arbeit stets mit großem Interesse begleitet und betreut hat. Weiterhin danke ich Dr. rer. nat. Holger Hesse, der als Teamleiter und weiterer fachlicher Ansprechpartner in zahlreichen anregenden Diskussionen mit neuen Impulsen den Fortschritt meiner Arbeit stets förderte.

Während meiner Promotion ist das Forschungsthema der stationären Energiespeichersysteme und folglich das Team SES am Lehrstuhl erst entstanden und gewachsen. Für die überaus fruchtbare Zusammenarbeit und den sehr guten Zusammenhalt bedanke ich mich bei allen Teammitgliedern. Vor allem gilt mein Dank Nam Truong, mit dem in sehr vertrauensvoller und produktiver Kooperation die Entwicklung und Veröffentlichung des Software-Frameworks SimSES gelang. Weiterhin gilt mein Dank allen Studenten und Kollegen am Lehrstuhl, die an meinen Arbeiten und meiner Forschung mitgewirkt haben.

Abschließend möchte ich meiner Familie und vor allem meiner Frau Adriana Fernández, der ich diese Arbeit widme, für die Geduld und fortwährende Unterstützung danken.

List of Publications

Conference Contributions

M. Naumann, C.N. Truong, R.Ch. Karl, A. Jossen. Betriebsabhängige Kostenberechnung von Energiespeichern. In: Technische Universität Graz (Publisher): EnInnov2014 - 13. Symposium Energieinnovation. Innehalten und Ausblick: Effektivität und Effizienz für die Energiewende. Graz, Österreich, 12.-14.02.2014.

M. Naumann, A. Jossen. Charakterisierung von Lastprofilen verschiedener Batterieanwendungen zur qualitativen Beschreibung der Alterung. In: DESIGN&ELEKTRONIK. Entwicklerforum Batterien & Ladekonzepte. München, 19.02.2014.

M. Naumann, R.Ch. Karl, C.N. Truong, H.C. Hesse, A. Jossen. Lithium-ion battery cost analysis in PV-household application. In: IRES. International Renewable Energy Storage Conference. Düsseldorf, 09.-11.03.2015: The European Association for Renewable Energy.

M. Naumann, H.C. Hesse. PV-Heimspeicher: Wirtschaftlicher Speicherbetrieb und Alterungseinfluss | Netz- und Systemdienlicher Einsatz. In: VDE ETG Fachtagung - Batteriespeicher und Power-to-Heat - Konkurrenz oder Koexistenz? Berlin, 22.-23.10.2015.

M. Naumann, C.N. Truong, M. Schimpe, M. Müller, A. Jossen, H.C. Hesse. SimSES: Software for techno-economic Simulation of Stationary Energy Storage Systems. In: Batterieforum Deutschland. Batterieforum Deutschland 2017. Berlin, 25.-27.01.2017.

M. Naumann, V. Kumtepli, H.C. Hesse, A. Tripathi, A. Jossen. Design and control of battery energy storage systems in island grids. In: Singapore Battery Meeting 2017. Singapore, 23.-24.03.2017.

M. Naumann, J. Stückrad, M. Schimpe, K.Ch. Karl, A. Jossen, H.C. Hesse. Battery lifetime prediction for different technologies based on stress characterization and aging experiments. In: Kraftwerk Batterie 2017. Aachen, 29.-30.03.2017.

M. Naumann, C.N. Truong, M. Schimpe, D. Kucevic, A. Jossen, H.C. Hesse. SimSES: Software for techno-economic Simulation of Stationary Energy Storage Systems. In: ETG Congress 2017 - Die Energiewende. Bonn, 28.-29.11.2017.

Peer-Reviewed Scientific Reports

VDE - Energietechnische Gesellschaft. Batteriespeicher in der Nieder- und Mittelspannungsebene. Anwendungen und Wirtschaftlichkeit sowie Auswirkungen auf die elektrischen Netze. In cooperation with M. Naumann, M. Müller, A. Jossen, H.C. Hesse. Published by VDE - ETG. Frankfurt a.M., 2015.

Energie-Forschungszentrum Niedersachsen, H.-P. Beck, H. Bart, B. Bayer, J. Klee Barillas, M. Danzer, M. Dennenmoser, M. Naumann. Potentiale elektrochemischer Speicher in elektrischen Netzen in Konkurrenz zu anderen Technologien und Systemlösungen (ESPEN): Abschlussbericht. Göttingen. 2016. ISBN: 9783736994232. DOI: 10.2314/GBV:869930222.

Software Publications

M. Naumann, C.N. Truong. SimSES - Software for techno-economic simulation of stationary energy storage systems. 2017. DOI: 10.14459/2017MP1401541. URL: <https://mediatum.ub.tum.de/1401541>.

Peer-Reviewed Journal Contributions (Co-Author)

C.N. Truong, M. Naumann, R. Karl, M. Müller, A. Jossen, H.C. Hesse (2016). Economics of Residential Photovoltaic Battery Systems in Germany. The Case of Teslas Powerwall. In: *Batteries 2* (2), P. 14-30. DOI: 10.3390/batteries2020014.

A. Zeh, M. Müller, M. Naumann, H.C. Hesse, A. Jossen, R. Witzmann (2016). Fundamentals of Using Battery Energy Storage Systems to Provide Primary Control Reserves in Germany. In: *Batteries 2* (3), P. 29. DOI: 10.3390/batteries2030029.

H.C. Hesse, R. Martins, P. Musilek, M. Naumann, C.N. Truong, A. Jossen (2017). Economic Optimization of Component Sizing for Residential Battery Storage Systems. In: *Energies 10* (7), P. 835. DOI: 10.3390/en10070835.

K. Rumpf, M. Naumann, A. Jossen (2017): Experimental investigation of parametric cell-to-cell variation and correlation based on 1100 commercial lithium-ion cells. In: *Journal of Energy Storage 14*, P. 224-243. DOI: 10.1016/j.est.2017.09.010.

C.N. Truong, M. Schimpe, M. Naumann, A. Jossen, H.C. Hesse (2017). Impact of sub-components on the overall performance of stationary battery systems: Insights on the prototype Energy Neighbor. In: *International ETG Congress 2017, Bonn, Germany*, pp. 1-6. URL: <http://ieeexplore.ieee.org/document/8278767/>

M. Schimpe, M. Kuepach, M. Naumann, H.C. Hesse, K. Smith, A. Jossen (2018): Comprehensive Modeling of Temperature-Dependent Degradation Mechanisms in Lithium Iron Phosphate Batteries. In: *Journal of The Electrochemical Society 2018* (165, 2), P. 181-193. DOI: 10.1149/2.1181714jes.

M. Schimpe, M. Naumann, N. Truong, H.C. Hesse, S. Santhanagopalan, A. Saxon, A. Jossen (2018): Energy efficiency evaluation of a stationary lithium-ion battery container storage system via electro-thermal modeling and detailed component analysis. In: *Applied Energy 210*, P. 211-229. DOI: 10.1016/j.apenergy.2017.10.129.

Journal Contributions (Lead Author)

M. Naumann, C.N. Truong, R.Ch. Karl, A. Jossen. Betriebsabhängige Kostenberechnung von Energiespeichern. In: Technische Universität Graz (Publisher): EnInnov2014 - 13. Symposium Energieinnovation. Innehalten und Ausblick: Effektivität und Effizienz für die Energiewende. Graz, Österreich, 12.-14.02.2014.

Peer-Reviewed Journal Contributions (Lead Author) *

(1) M. Naumann, R.Ch. Karl, C.N. Truong, A. Jossen, H.C. Hesse (2015). Lithium-ion Battery Cost Analysis in PV-household Application. In: Energy Procedia 73, P. 37-47. DOI: 10.1016/j.egypro.2015.07.555.

(2) M. Naumann, C.N. Truong, M. Schimpe, D. Kucevic, A. Jossen and H.C. Hesse. SimSES: Software for techno-economic Simulation of Stationary Energy Storage Systems. In: International ETG Congress 2017, Bonn, Germany, 2017, pp. 1-6. URL: <http://ieeexplore.ieee.org/document/8278770/>.

(3) M. Naumann, M. Schimpe, P. Keil, H.C. Hesse, A. Jossen. Analysis and modeling of calendar aging of a commercial LiFePO₄/graphite cell. In: Journal of Energy Storage (16). P. 153-169. DOI: 10.1016/j.est.2018.01.019.

* Self-produced sections of peer-reviewed lead author journal contributions are partially contained in this thesis without further reference in the running text; in particular, this involves Chapter 3^{(1),(2)}, 4⁽³⁾, 5⁽³⁾

List of Contents

| | |
|--|-------------|
| Kurzfassung | I |
| Abstract | II |
| Vorwort und Danksagung | III |
| List of Publications | IV |
| List of Abbreviations | IX |
| List of Formula Symbols | XIII |
| 1 Introduction | 1 |
| 1.1 Motivation and research questions | 1 |
| 1.2 Objectives | 3 |
| 1.3 Structure | 3 |
| 2 Fundamentals | 7 |
| 2.1 Stationary battery energy storage systems | 7 |
| 2.1.1 System design | 7 |
| 2.1.2 Techno-economic modeling | 8 |
| 2.2 PV home energy storage systems | 10 |
| 2.2.1 Technical and economic overview | 10 |
| 2.2.2 State-of-the-art | 11 |
| 2.3 Battery storage systems for primary control reserve supply | 12 |
| 2.3.1 Control power reserve and spot market | 12 |
| 2.3.2 Technical framework for primary control reserve supply | 15 |
| 2.3.3 State-of-the-art | 16 |
| 2.4 Aging of LiFePO ₄ /graphite cells | 17 |
| 2.4.1 Calendar aging | 18 |
| 2.4.2 Cycle aging | 20 |
| 3 Development of a model framework for the assessment of battery energy storage systems | 23 |
| 3.1 Simulation software SimSES | 23 |
| 3.1.1 Basic software structure | 24 |
| 3.1.2 Fields of application | 24 |
| 3.1.3 Control algorithms | 25 |
| 3.1.4 System model | 26 |
| 3.1.5 Battery degradation model | 27 |
| 3.1.6 Technical evaluation | 28 |
| 3.1.7 Economic evaluation | 28 |

| | | |
|----------|---|-----------|
| 3.2 | Assessment methods | 29 |
| 3.2.1 | Technical evaluation parameters | 29 |
| 3.2.2 | Economic evaluation parameters | 31 |
| 3.3 | Computational performance evaluation | 34 |
| 3.3.1 | Calculation time | 35 |
| 3.3.2 | Aging results | 37 |
| 4 | Experimental studies on LiFePO₄-graphite cells | 41 |
| 4.1 | Investigated cell | 41 |
| 4.1.1 | Influence of the anode overhang | 42 |
| 4.1.2 | Cell-to-cell parameter variation | 43 |
| 4.1.3 | Cell selection procedure | 44 |
| 4.2 | Measurement equipment | 46 |
| 4.3 | Measurement procedures | 46 |
| 4.4 | Testing procedure | 48 |
| 4.5 | Concept of the aging studies | 49 |
| 4.5.1 | Basic assumptions | 49 |
| 4.5.2 | Limitations and principal concept | 50 |
| 4.5.3 | Static calendar aging | 50 |
| 4.5.4 | Dynamic calendar aging | 51 |
| 4.5.5 | Static cycle aging | 52 |
| 4.5.6 | Dynamic cycle aging | 55 |
| 4.6 | Aging results | 57 |
| 4.6.1 | Static calendar aging | 57 |
| 4.6.2 | Static cycle aging | 63 |
| 5 | Aging model development of the investigated LiFePO₄-graphite cell | 71 |
| 5.1 | Calendar aging model | 71 |
| 5.1.1 | Model limitations | 71 |
| 5.1.2 | Development | 71 |
| 5.1.3 | Validation | 77 |
| 5.2 | Cycle aging model | 79 |
| 5.2.1 | Model limitations | 79 |
| 5.2.2 | Development | 79 |
| 5.2.3 | Validation | 84 |
| 5.3 | Combined aging model | 86 |
| 5.3.1 | Development | 86 |
| 5.3.2 | Validation | 87 |
| 6 | Techno-economic evaluation of battery energy storage system applications | 89 |
| 6.1 | General simulation configuration | 89 |
| 6.1.1 | Technical parameters | 89 |
| 6.1.2 | Economic parameters | 90 |
| 6.2 | PV-Home energy storage system | 90 |
| 6.2.1 | Input data | 91 |
| 6.2.2 | System configuration | 94 |

| | | |
|----------|---|------------|
| 6.2.3 | Performance | 98 |
| 6.3 | Primary control reserve supply | 104 |
| 6.3.1 | Input data | 104 |
| 6.3.2 | System configuration | 107 |
| 6.3.3 | Performance | 108 |
| 6.4 | Comparison of the battery energy storage system applications | 113 |
| 6.4.1 | Analysis of the key characteristics | 113 |
| 6.4.2 | Economic sensitivity analysis | 115 |
| 7 | Conclusion | 117 |
| 7.1 | Aging and modeling of LiFePO ₄ /graphite cells | 117 |
| 7.2 | Techno-economic simulation results of the investigated applications | 119 |
| 8 | Outlook | 121 |
| | List of References | 123 |
| | List of Figures | 133 |
| | List of Tables | 135 |

List of Abbreviations

| | | |
|-----------|-----------|---|
| AC | | alternating current |
| BESS | | battery energy storage system |
| BMS | | battery management system |
| BOL | | begin of life |
| CC | | constant-current |
| CDA | | capacity difference analysis |
| CM | | capacity measurement |
| CPU | | central processing unit |
| CTS | | cell test system |
| CU | | check-up |
| CV | | constant-voltage |
| DC | | direct current |
| DOC | | depth-of-cycle |
| DP | | depreciation period |
| DVA | | differential voltage analysis |
| ECM | | equivalent circuit model |
| EIS | | electrochemical impedance spectroscopy |
| EMS | | energy management system |
| ENTSO-E | | European Network of Transmission System Operators for Electricity |
| EOL | | end of life |
| EOT | | end of test |
| EPEX SPOT | . . . | European Power Exchange |
| EV | | electric vehicle |
| FEC | | full equivalent cycle |
| FPD | | frequencies per decade |

- IDM intraday continuous market
- IRR internal rate of return
- LAM loss of active material
- LCOES levelized cost of energy stored
- LEOES levelized earnings of energy stored
- LFP lithium iron phosphate
- LLI loss of lithium inventory
- LPOES levelized profit of energy stored
- LTO lithium titanate
- MATLAB matrix laboratory, simulation framework of *MathWorks*
- MPF measures per frequency
- NMC lithium nickel magnesium cobalt
- NPV net present value
- OCV open circuit voltage
- PbA lead-acid
- PCR primary control reserve
- PER power-to-energy ratio
- PI profitability index
- PPEI profit per energy installed
- PV photovoltaic
- PV-HESS PV-home energy storage system
- ROI return on investment
- SEI solid electrolyte interphase
- SES stationary energy storage systems
- SimSES software for techno-economic simulation of stationary energy storage systems
- SOC state-of-charge
- SOH state-of-health
- TMS thermal management system
- TP test point

TSO transmission system operators

UCTE Union for the Coordination of Transmission of Electricity

V-RFB vanadium redox-flow

List of Formula Symbols

| | | |
|-------------------|------------------------------------|----------------------------------|
| A | surface area | m^2 |
| α | heat transfer coefficient | $\text{W m}^{-2} \text{K}^{-1}$ |
| C | cost/revenue | Euro |
| c_p | specific heat capacity | $\text{J kg}^{-1} \text{K}^{-1}$ |
| δ | self-sufficiency rate/autarky rate | % |
| \vec{DF} | discount factor | |
| DOC | depth-of-cycle | % |
| E | energy | W s |
| f | function | |
| $f_{power\ line}$ | power line frequency | Hz |
| FEC | full equivalent cycles | |
| I | current | A |
| i | interest rate/inflation rate | % |
| m | mass | kg |
| η | efficiency | % |
| P | power | W |
| \dot{Q} | heat flow | W |
| Q_{loss} | capacity loss | % |
| R_i | inner resistance | Ω |
| R_{inc} | resistance increase | % |
| R | economic return | Euro |
| σ | self-consumption rate | % |
| SOC | state-of-charge | % |
| $T_{sim.}$ | simulation period | s |
| τ | utilization ratio | % |

List of Formula Symbols

| | | |
|-----------|------------------------------|--|
| T | temperature | K |
| t | time | s |
| U | voltage | V |
| c | variable cost | Euro kWh ⁻¹ Euro kW ⁻¹ |
| \vec{Y} | years of depreciation period | |

1 Introduction

1.1 Motivation and research questions

With the increasing share of renewable energy sources in power grids all over the world and especially in Germany, the demand for flexibility options in power grids increased in the last years [1], because new challenges in power grids emerged due to the fluctuating power generation of the renewable energy sources. Beside the different existing flexibility options, battery energy storage systems are well suited to support the power grid by supplying, for example, primary control reserve [2]. Furthermore, BESS are also technically suited for many of the different stationary applications [3]. Especially BESS based on lithium-ion batteries have been established on the market in the recent years due to their steadily improving technical applicability for stationary applications together with the decreasing costs of these systems [4]. However, the technical and economic suitability of these technologies is still under discussion for the various stationary fields of application [3; 5].

With decreasing lithium-ion battery prices and the growth of the renewable energy share in the last years, stationary applications for lithium-ion batteries have evolved rapidly along with the existing and also emerging portable applications and electric vehicles (EVs). In portable and EV applications the batteries' energy density is one of the most important technical parameters for the choice of technology and system design. In contrast, for stationary applications, the economic outcome of a BESS is primarily assessed when designing these systems.

In addition to the investment price of the battery system, the achievable lifetime is a crucial parameter for the profitability of BESS due to the long required system lifetime of up to 20 years [6]. As current mass-produced LiFePO_4 /graphite (lithium iron phosphate (LFP)/C) battery cells show cycle stability up to 10 000 full equivalent cycles (FECs) until the capacity underruns 80 % of the original capacity [7; 8], the cycle lifetime is commonly not a limiting factor in stationary applications: Within an operation of 20 years, only about 6000 FECs are expected for photovoltaic (PV) home energy storage systems (PV-HESS) [6] and no more than about 8000 FECs for the supply of primary control reserve (PCR-supply) dependent on sizing [2; 3; 9]. The total aging result is a combination of calendar and cycle aging when the superposition model of lithium-ion battery aging [10; 11] is applied. Consequently, the overall contribution of calendar aging can be expected to be dominant for battery cells with high cycle life. However, due to the various operational requirements of the different stationary applications for BESS, both, the calendar and the cycle lifetime have to be estimated precisely when assessing the influence of battery lifetime on the profitability in stationary battery applications.

In this context, **Figure 1.1** gives an overview regarding the different issues of stationary energy storage systems by showing the various applications, the diverse available storage technologies and the possible design scopes of the energy storage systems. Here, the following research questions emerge:

1. What are the technical requirements and economic conditions of the different stationary energy storage applications?

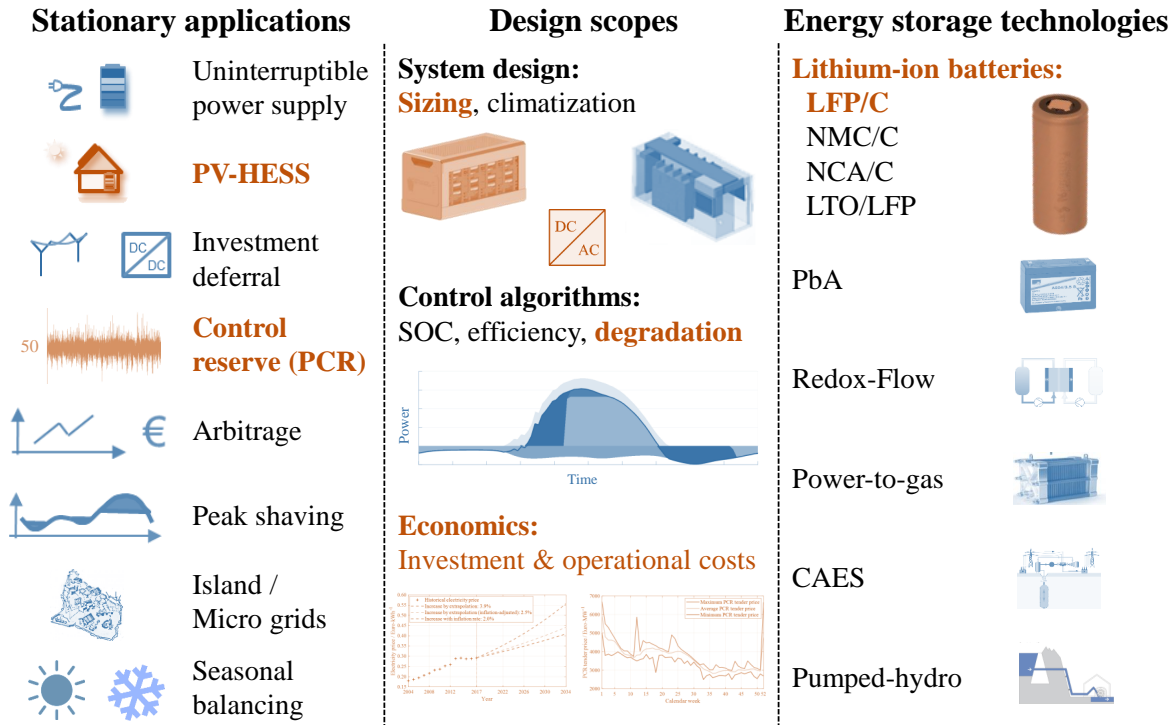


Figure 1.1: Overview regarding stationary energy storage applications, possible design scopes and a selection of energy storage technologies. The orange marked parts are in the main focus of this work.

2. Are BESS based on lithium-ion batteries technically and economically suited for the particular stationary applications?
3. How to determine the best economic system design and control algorithms of BESS for a given stationary application?

To answer these questions, the various stationary energy storage applications have to be analyzed by considering a wide variety of technical and economic influence parameters. Furthermore, there are numerous technical design scopes in the energy storage system design that can be optimized, such as the choice of energy storage technology or the physical sizing of the individual components. In order to be able to investigate these and further research questions concerning BESS, holistic models are required which are able to simulate BESS accurately considering all important technical and economic parameters. Due to this large scope of the research questions, this work focuses on particular issues which are marked in **Figure 1.1** and are motivated in the following:

Stationary application:

The two emerging BESS applications PV-HESS and PCR-supply are chosen, because for both a technical and economic maturity can be assumed since thousands of PV-HESS systems have been installed in Germany [12] (61.300 until end of April 2017) and various BESS-projects have been realized (30 MW until March 2016) or are planned (100 to 150 MW) [4; 13; 14] in the last years in Germany. Although BESS are utilized in the PV-HESS and PCR-supply applications in other countries worldwide, this work focuses exemplarily on the case in Germany, because the BESS configuration and operation strongly depends on the regulatory framework, which is not investigated in this work.

Energy storage technology:

Among the many different lithium-ion battery technologies, this work evaluates only BESS based on LFP/C batteries due to its anticipated high technical suitability for stationary applications [5]. Furthermore, within the project work of *EEBatt*, a BESS container based on LFP/C cells have been developed and analyzed, which allowed extensive evaluations on the applied cell which are presented later [15].

Evaluation scope:

Due to the fact, that the economics of BESS in stationary applications are of special interest, this work assesses the economics of the two BESS applications PV-HESS and PCR-supply by evaluating the investment and operational costs together with the revenue of the particular applications. The sizing of the battery storage and the inverter is another focus issue in this work because the dimensions of the BESS components influence strongly the investment costs. Furthermore, the sizing has a big impact on the resulting battery operation and consequently the battery degradation. Assuming long depreciation periods of 10 years and even longer in stationary BESS applications, the steady battery aging can lead to a significant decrease of the battery's capacity and performance. Thus, the battery degradation deteriorates the BESS economics due to less available energy capacity and higher efficiency losses. Hence, the battery degradation has to be considered precisely in stationary BESS applications and is consequently one of the main topics in this work.

1.2 Objectives

In consequence of the above-mentioned research questions together with the chosen particular topics of high interest, this work has the main goal to perform a techno-economic evaluation of the two stationary applications PV-HESS and PCR-supply with special consideration of battery aging. Thereby the main topics of this work are the BESS component sizing, the battery degradation, and the economics by evaluating LFP/C batteries as well suited exemplary energy storage technology. Thus, the following objectives and tasks have been set for this work:

1. Examination of the aging mechanisms and effects of the investigated LFP/C cell.
2. Development of an aging model LFP/C cell based on the experimental studies.
3. Development of a software framework permitting a detailed techno-economic evaluation of stationary BESS applications.
4. Integration of the LFP/C aging model in the software framework allowing for the precise simulation of battery degradation during the BESS operation.
5. Techno-economic assessment and comparison of the two chosen stationary applications PV-HESS and PCR-supply with appropriate technical and economic evaluation parameters.

1.3 Structure

Figure 1.2 gives an overview regarding the structure of this work. After this introduction, **Chapter 2** presents the fundamentals of the stationary BESS and the two evaluated BESS applications PV-HESS and PCR-supply. Additionally, the state-of-the-art about LFP/C cell aging is given.

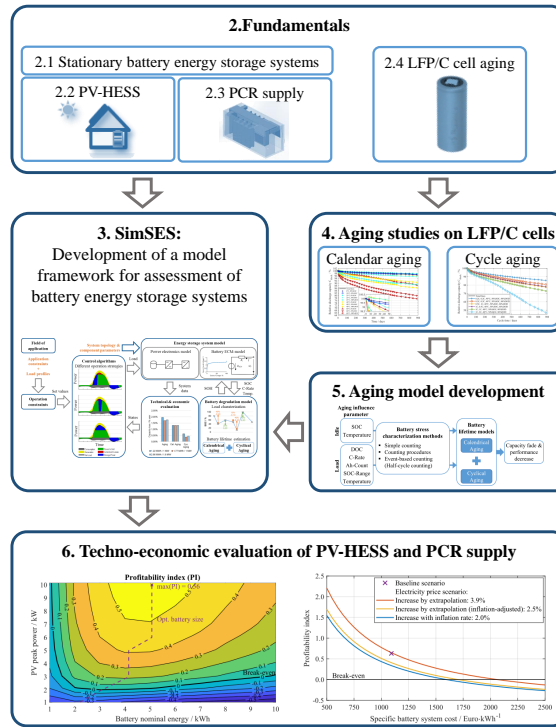


Figure 1.2: Structure of this thesis 'Techno-economic evaluation of stationary battery energy storage systems with special consideration of aging' with assigned numbers of chapters.

The following **Chapter 3** deals with the development of a model framework for the assessment of stationary BESS by introducing the software for techno-economic simulation of stationary energy storage systems (SimSES) together with the technical and economic assessment methods. This chapter closes with a performance evaluation of SimSES to determine the parameters for the correct utilization of the aging model in the subsequent BESS simulations.

Due to the fact, that the evaluation of BESS is performed with special consideration of aging, the two following chapters cover the battery aging of the investigated LFP/C cell with experimental studies and the aging model development. First, **Chapter 4** shows the experimental studies by introducing the investigated cell and presenting the description of the measurement equipment and procedures. Then, the concepts and the experimental setup of the aging studies are described. This chapter concludes with the presentation of the aging results of the aging studies.

In the following **Chapter 5**, the aging model of the investigated LFP/C cell is developed and validated.

Subsequently, **Chapter 6** presents a techno-economic evaluation of the two stationary BESS applications PV-HESS and PCR-supply including the aging model of the investigated LFP/C cell. After introducing the general technical and economic parameters, the configuration of the simulation together with the results of both applications are shown and finally compared with each other.

This work's conclusion is given in **Chapter 7** by first summarizing the results of the battery aging studies and the aging model development. Afterward, the results of the techno-economic evaluation of the PV-BESS and PCR-supply application are outlined.

Finally, in **Chapter 8** an outlook is given regarding the battery aging studies and aging model development together with the proposition of the next steps in the development of BESS models for further techno-economic evaluations.

2 Fundamentals

This chapter presents the fundamentals of the design and modeling of stationary BESS and the two evaluated BESS applications PV-HESS and PCR-supply. Afterward, the state-of-the-art about the investigated LFP/C cell aging is given.

2.1 Stationary battery energy storage systems

2.1.1 System design

Figure 2.1 shows in the upper part a schematic of a BESS and its main components together with the system coupling to the alternating current (AC) power grid and further technical units.

In general, a BESS comprises a battery rack or pack (battery), a thermal management system, a battery management systems and an energy management system. The battery consists of single battery cells, which can be connected in series or parallel within battery modules. A couple of battery modules can be coupled in series or parallel to a battery pack or rack, representing generally the highest direct current (DC) voltage level in a BESS. The battery pack or a couple of racks can be connected individually to dedicated power electronics or in series or parallel to one unit of power electronics. The battery management system (BMS) monitors the single cell states such as voltages, currents and temperatures and enables together with the energy management system (EMS) the operation of the

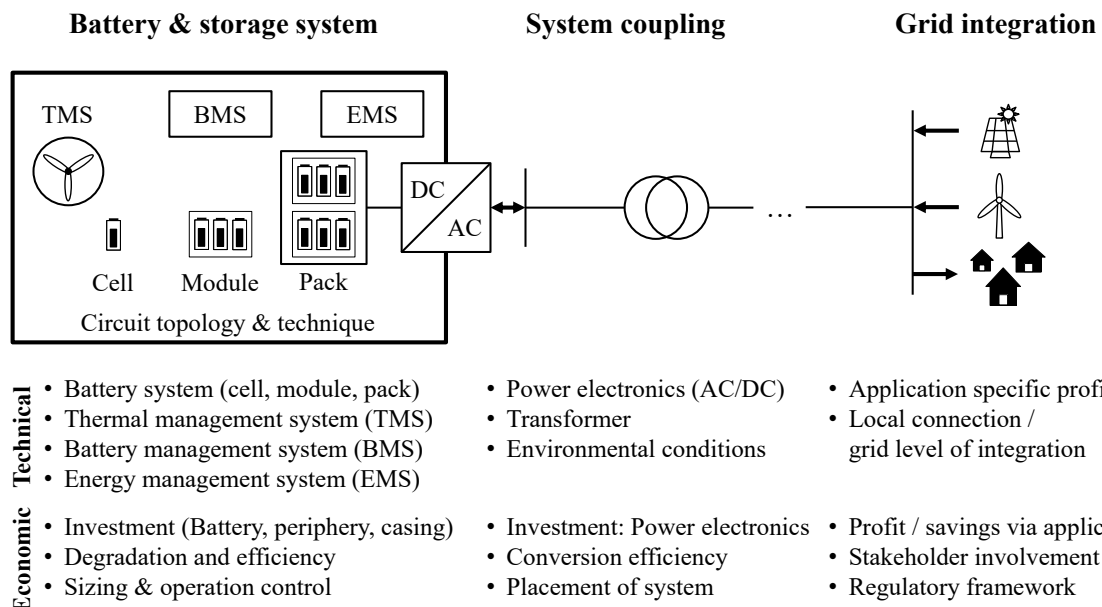


Figure 2.1: Schematic of BESS and its main components together with the system coupling to the power grid or further technical units (Derivative of Figure from [16]).

BESS. The thermal management system (TMS) can consist of different climatization components such as fans or liquid cooling systems and is applied to control the temperature of the battery pack and the power electronics inside the storage system if necessary. The battery is coupled with further systems like the power grid, energy generation or consumption units through power electronics, which can be realized in different topologies of DC/AC inverters together with transformers. Dependent on the stationary application, BESS are coupled directly to the power grid (PCR-supply) or are operated inside a household with a residual load profile resulting from PV electricity generation and household electricity consumption (PV-HESS). Furthermore, BESS can be connected to different grid levels in dependency of the installed rated power of the BESS and the appropriate power electronics.

In the lower part of **Figure 2.1**, the particular economic issues of BESS and its system coupling towards the grid are given. The main part of the BESS costs results from the investment costs for the battery, the peripheral components like the EMS and the TMS, the storage casing and the power electronics. Additional operational cost can result from the efficiency losses and the battery degradation leading to less usable capacity and worse efficiency. The BESS investment costs and the operational costs are strongly influenced by the sizing of all components, which can have an inverse influence on the operational costs for example due to less cycle aging when a larger battery is utilized less than a smaller battery. The EMS allows controlling the BESS operation and its costs by trying to operate the inverter at the power within the best efficiency range for example. In the context of the different stationary BESS applications, different forms of profits or savings can be obtained. However, the regulatory framework of each stationary applications comprises of different and individual settings and limits of the BESS operation and its economics, which are explained for the evaluated applications PV-HESS in **Section 2.2** and PCR-supply in **Section 2.3**.

BESS can be realized with different battery technologies with individual strengths and weaknesses. **Figure 2.2** compares the five typically lithium-ion battery types lithium nickel magnesium cobalt (NMC)/C, LFP/C, LFP/lithium titanate (LTO), lead-acid (PbA) and vanadium redox-flow (V-RFB) with respect to the investment costs, the lifetime, efficiency/self-discharge and the scalability. In the past, PbA batteries have mainly been used in stationary applications due to the low investment costs. This main advantage of PbA lost importance with the decreasing prices of lithium-ion batteries, which generally have higher efficiencies and longer calendar as well as cycle lifetimes. However, the different lithium-ion battery types have their individual advantages and disadvantages with respect to the prices and the technical capabilities. LFP/C batteries represent in this comparison a good trade-off between battery price and the lifetime, which both are of special interest in stationary applications. V-RFB as one of the various redox-flow battery types might have a long calendar and cycle lifetime at low investment prices. However, the system efficiency is lower than the values of lithium-ion batteries. In contrast to lithium-ion batteries, Redox-flow batteries permit an almost independent scaling of power and energy. Thus, redox-flow batteries are principally suited for stationary applications, but most of the stationary BESS systems are realized with lithium-ion batteries due to their high technical maturity and steadily decreasing costs.

2.1.2 Techno-economic modeling

Battke et al. presented the comparison of life-cycle costs for various different stationary energy storage technologies with a literature review, expert interviews, and Monte Carlo based simulations [18]. A more detailed analysis of the matter of levelized cost of energy stored (LCOES) in the PV-HESS

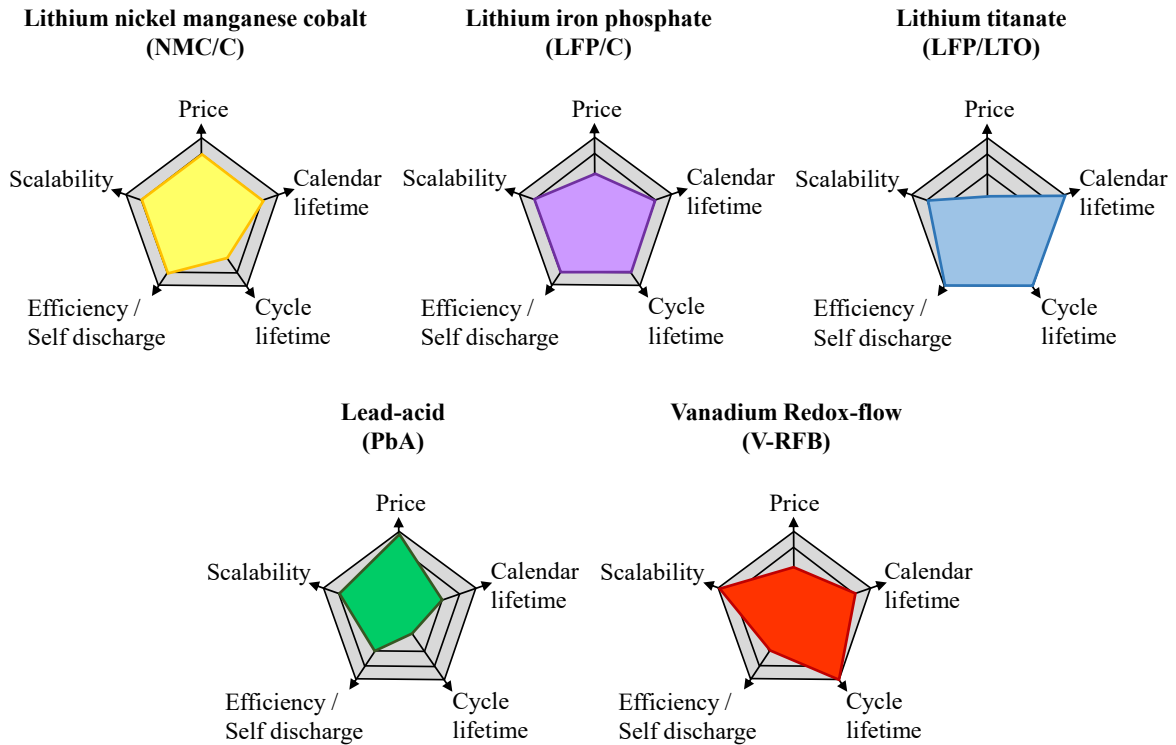


Figure 2.2: Comparison of different battery technologies with respect to the price, lifetime, efficiency / self-discharge and scalability (Derivative of Figure from [17]).

application has been given by Pawel et al. [19]. The study analyzes the dependence of LCOES for energy storage systems due to economic parameter variation to assess the potential of PV-storage combinations for the replacement of diesel electricity generation, e.g. for off-grid solutions. You et al. showed an aging-dependent cost analysis model, which was used to investigate the economic viability of a sodium-sulfur battery for the Danish electricity market [20]. In the last mentioned publication, the authors use and describe the so-called 'rain-flow cycle counting algorithm' for conducting a battery cycle-aging analysis. The degradation analysis for the lithium-ion batteries used in SimSES is based on a similar approach.

Currently, there is only a small number of software projects, which mainly focus on batteries and are able to analyze various BESS applications. A few examples are worth mentioning and do not represent an exhaustive list of all relevant tools for BESS. *PerModAC* from the *University of Applied Sciences* Berlin and *BLAST* from the *National Renewable Energy Laboratory* (NREL) in Denver are two major examples of BESS simulation tools, both showing individual strengths and shortcomings. The major characteristic features of these software tools in comparison to SimSES are summarized and compared in **Table 2.1**:

PerModAC [21] is an open source tool and has been developed to analyze AC coupled PV-HESS. The focus of this tool is to analyze the energy performance of the entire energy storage system including periphery and PV generation. The degradation of the energy storage system is completely neglected.

BLAST [22] has been developed to analyze three different fields of application: electric vehicles, stationary applications, and behind-the-meter applications. The focus of this tool is the economic evaluation of these three different applications. *BLAST* combines various battery models (degradation

Table 2.1: Comparison of software tools for the simulation of energy storage systems.

| | SimSES | PerModAC | BLAST |
|-----------------------|--|-------------------------|--|
| Application | Various e.g. PV-HESS, PCR | AC coupled - PV-HESS | Vehicles, Stationary applications Behind the meter |
| Focus | Techno-economic | Energy performance | Economic value |
| Software availability | Open source | Open source | Freeware (lite version) |
| Input data | Profiles, technical and and economic parameters | Profiles | Profiles, rate structure |
| Battery degradation | Empirical model, user input | - (not modeled) | Empirical model |

and thermal) with user input data (e.g. driving data) and historic climate data. The *BLAST* tool is available in a freeware version with reduced capabilities only and the source code is not available for further development.

In addition, there are several other software projects, which focus less on energy storage systems. One of them, *SAM* (System Advisor Model) [23] managed by the NREL in Denver, analyzes the performance and predicates the investment and operation costs for grid-connected power projects. *FreeGreenius* [24] is another tool focusing on performance calculations hosted by the *Institute of Solar Research of the German Aerospace Center* (DLR). *HOMER Energy LLC* [25], developed by the eponymous company, focuses on modeling and optimizing micro grids including power generation, load management, and energy storage systems. For all the presented tools, the capabilities of battery storage model integration are fairly limited. Battery cell aging, the topology of the energy storage system and detailed system efficiency modeling is not within their main scope. The approach of SimSES is to link these detailed energy storage system simulation capabilities to a series of application scenarios within one tool-chain.

2.2 PV home energy storage systems

2.2.1 Technical and economic overview

The PV-HESS application consists of a solar-plus-battery system i.e. a residential customer having a PV-system installed with the aim of reducing his electricity bill by equipping the system with a battery storage [26; 27]. The building comprises of a consumer (possibly several), a solar panel on the rooftop to generate electricity, and a BESS to buffer the amount of electricity that is exchanged between the building and the electricity grid. The calculations presented here reflect the economic and regulatory framework of the renewable energy sources act (EEG) in Germany of the year 2015 [28]. The aim of the BESS utilization is to increase the share of self-consumed electricity and to avoid grid-supplied electricity as the consumption of self-generated electricity is preferred over remuneration for selling electricity and subsequent withdrawal of grid-power at other times. For this system to be economically favorable, the reduction of the electricity bill must exceed the investment cost of the battery system. Other motives for investing in a BESS might be to increase self-dependency and/or power quality and to enhance the reliability of the electricity supply. However, given the high supply quality and reliability in Germany and excluding non-monetary aspects, here the last mentioned aspects of autarky increase and reliability enhancement are not taken into account. The evaluated benefit of this application is only the revenues obtained by electricity cost reduction, as installing a BESS unit can reduce the

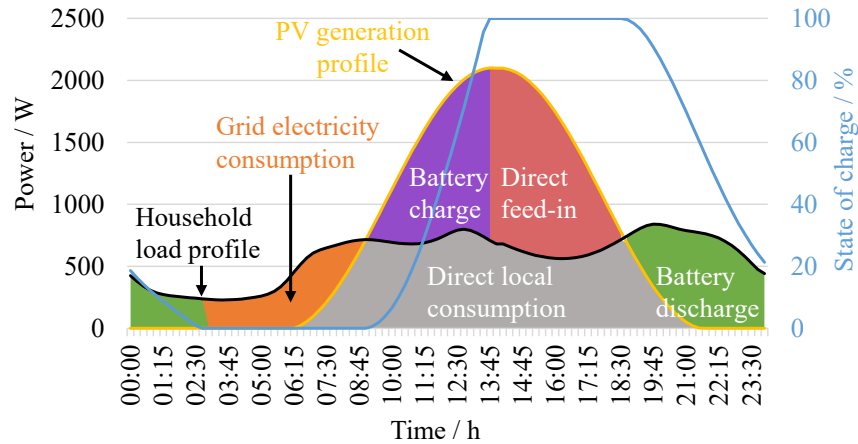


Figure 2.3: Schematic of power and SOC course of a PV-HESS during one day (Derivative of Figure from [29]).

electricity consumption from the power grid.

Figure 2.3 shows an exemplary ideal course of the different power profiles in the PV-HESS application together with the battery state-of-charge (SOC) over one day. The battery is charged when the PV generation exceeds the consumption of the household and discharged when no PV generated power is available for direct consumption. However, depending on the battery size, the battery might be fully charged until the afternoon and the PV generation surplus is fed into the power grid. When the battery is empty in the early morning, the household electricity consumption is supplied by the power grid.

2.2.2 State-of-the-art

Waffenschmidt [30] and Weniger et al. [31] investigated the optimal sizing of residential PV battery systems and concluded that the combination of a residential PV-system with a battery is able to increase the economic profit in comparison to the case without a battery. The sensitivity of technical and economic parameters for PV-HESS has been investigated in previous work for the implementation in Germany [6; 32]. For this purpose, the modeling framework SimSES was developed in matrix laboratory, simulation framework of *MathWorks* (MATLAB) to simulate stationary BESS and is presented in **Chapter 3**. Further techno-economic analysis of the PV-HESS application together with the determination of the optimal parameters was presented by Hesse et al. in [5].

However, most investigations revealed that considering battery prices of the year 2015 and moderate development of the electricity prices, the economic break-even of BESS in the PV-HESS application in Germany has not been reached yet in the year 2015. It can be concluded, that the profitability of BESS in the PV-HESS application strongly depends on different technical and economic parameters, including:

1. Battery aging: Due to the fact, that PV-systems are operated with a depreciation period of 20 years due to the regulatory framework of the EEG in Germany [28], the impact of battery aging has to be considered due to limited lifetime and steadily decreasing of the performance of the batteries.

2. BESS component sizing: The sizing of the BESS energetic capacity and inverter has an impact on the economic result due to the relatively high investment costs and the sizing-dependent opportunities to decrease the electricity bill [6]. Furthermore, the component sizing is sensitive to the individual household electricity consumption and the size of the PV-system [32].
3. BESS operation: Zeh et al. [33] showed, that different BESS operation strategies lead to different economic results due to PV curtailment losses and the varying utilization of the BESS.
4. Investment costs: A previous work showed the strong dependancy of the BESS investment costs on the economic results [6]. Based on the steadily falling price of lithium-ion batteries in the recent years, the economic evaluation is very sensitive to the individual investment cost assumptions for BESS.
5. Electricity price: Due to the fact, that the development of the electricity price is not predictable, the assumptions on the development of the electricity price within the long depreciation period of 20 years has also a big impact on the overall economic result [6].

All these technical and economic parameters influence parameters can be addressed with the BESS model in SimSES. However, in **Section 6.2** only the most sensitive technical and economic parameters are varied and evaluated.

2.3 Battery storage systems for primary control reserve supply

The stabilization of power grid frequency is supported by the PCR in various countries worldwide. In the Union for the Coordination of Transmission of Electricity (UCTE) and hence in Germany BESS can participate in a particular market and offer the provision of PCR power. In the following, first, the fundamentals about the control power reserve and the electricity spot markets are given in order to understand the framework for the configuration and operation of a BESS in this context, which is presented afterward. Finally, a short literature review shows related work about the BESS application for the supply of PCR.

2.3.1 Control power reserve and spot market

Germany and its transmission system operators (TSO) are part of the European Network of Transmission System Operators for Electricity (ENTSO-E) having the tasks to provide a secure electricity transmission network, to provide a platform for energy markets and to enable a sustainable development in the electricity sector and in particular of renewable energy [34]. Under the organization of the ENTSO-E, there are different electricity power grid areas covering different regions in Europe. Germany and its neighboring countries are part of the UCTE sharing the same electricity network codes and especially the nominal power line frequency of 50 Hz. The widely extended power grid helps to stabilize the electric energy supply since local failures can be supported by a large amount of the electricity generation units and electricity surpluses can be distributed better. Nevertheless, the integrated electricity network must be controlled actively against disturbances to be able to compensate errors and deviations adequately. For that purpose, control reserve power is required.

2.3.1.1 Control reserve for stabilizing grid frequency

The TSOs are responsible for maintaining a stable power grid at all times. This includes the adaptation of generation and demand of electrical energy since electric power generation and consumption have to be balanced at all time. Both, power plants and large consumers have to comply and follow a predetermined timetable [35; 36]. Nevertheless, due to unforeseen fluctuations, deviations of these timetables occur and consequently, there might be too less or too much electric energy in the power grid available. These electric energy deficits or surpluses are intercepted in the first instance by the so-called instantaneous reserve, which is mainly provided by the mechanical inertia of the rotating masses of the large turbines and generators of the conventional thermal power plants. Due to the immediate feedback through the grid frequency, the rotating masses are either decelerated or gain additional speed, which directly affects the network frequency. In order to control these grid frequency fluctuations exceeding the abilities of the instantaneous reserve, the TSOs have to hold ready control reserve power. Therefore, three coordinated control reserve power types are carried out in a time-shifted manner to keep the grid frequency at its nominal setpoint of 50 Hz and to balance the deficits and surpluses in defined control zones. The necessary reserve for this control power is apportioned among the ENTSO-E members with respect to the proportional amount of the installed electricity generation power of the total generation power amount. In Germany, the control reserve power market is coordinated by the four major TSOs *50Hertz*, *Amprion*, *TENNET* and *TRANSNET BW* and is organized via a common internet platform *www.regelleistung.net* [36].

2.3.1.2 Control reserve market

It is the inherent task of the TSOs to ensure the balance of the electricity generation and consumption in their respective control areas at all times. In Germany, the TSOs apply three different types of control reserve. These three control reserve types vary with respect to the conditions for activation and their activation speed [36]. All three types are presented here in a short overview, however, the BESS application to supply PCR is described more in detail in **Section 2.3.2**:

Primary control reserve (PCR):

- Provided according to the solidarity principle by all TSOs synchronously connected within the ENTSO-E area.
- Automatic and complete activation of primary control reserve within 30 s.
- Period per incident to be covered: $0 < t < 15$ min.

Secondary control reserve (SCR):

- Energy balance of the control area and frequency control.
- Immediate automatic activation by the concerned TSO.
- Complete activation within five minutes (at most).

Tertiary control reserve (TCR, minute reserve):

- The activation is based on merit-order-list (automatic activation) since 2012.

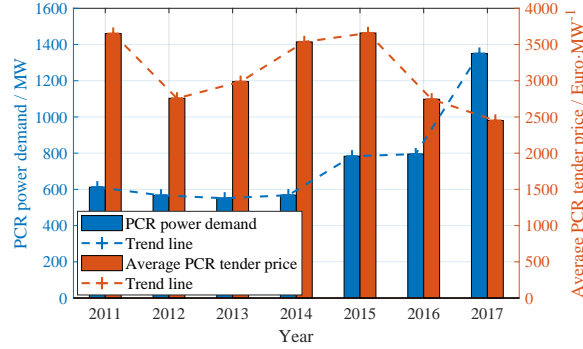


Figure 2.4: Historical PCR power demand and average tender prices between 2011 and 2017 (Data from [36]).

- Complete activation within fifteen minutes.
- Period per incident to be covered $t > 15$ min up to several hours in case of several incidents.

Although BESS are principally suited to provide control reserve power for all three control reserve types, the PCR-supply offers the highest remuneration and the technical requirements fit the best with the typical properties of a BESS and is analyzed in the following.

The tender offer for PCR-power is realized in weekly intervals and providers have the opportunity to submit offers with the minimum bid size of 1 MW. The allocation takes place according to the merit order principle in a pay-as-bid tendering process: The cheapest offers are accepted until the tendered amount of PCR power is covered. However, the remuneration per offered MW is paid as offered in the individual bid. The energy amount, which is needed to supply the PCR demand given by the course of the grid frequency profile, is not remunerated separately. The offered PCR power must be available throughout of the entire time interval of one week. In case of non-performance of the required PCR power, high penalties are applied and in recurrent cases the exclusion from the market is possible.

Figure 2.4 shows the historical trend of the PCR power demand and the weekly average tender prices between 2011 and 2017 in the power grid area of Germany, Austria, Netherlands, and Switzerland sharing the same PCR power market. Even though the market volume and prices decreased until 2012/2013, afterward the PCR power demand and also the prices started to increase until 2015. The PCR power demand in this market increased from the year 2016 to 2017, because in August 2016 a Belgian TSO joined the market and in January 2017 a French TSO joined the cooperation resulting in the largest PCR market of Europe with a total current PCR power demand of over 1350 MW. As a possible consequence of this market volume increase with more competing market participants, the average PCR prices decreased from 3659 Euro in 2015 to 2451 Euro in 2017.

2.3.1.3 Trading at the electricity spot market

When operating a BESS in the control reserve power market, it is necessary to charge or discharge the BESS at certain points in time due to the limited energy storage capacity. Among further possibilities, trading transactions of electric energy at the European Power Exchange (EPEX SPOT) allows dynamic charge and discharge operation by buying or selling electric energy from the power grid [37]. The EPEX SPOT covers the electricity markets of Germany, France, the United Kingdom, the Netherlands, Belgium, Austria, Switzerland, and Luxembourg and offers a marketplace where the participants can

exchange electric energy by bidding for buying and selling electric energy. The EPEX SPOT market is split into the day-ahead auction market, intraday auction trading and intraday continuous trading. For the day-ahead market hourly contracts consisting of a volume and a price are negotiated the day before. In addition, in the intraday auction at 15:00 the day before, contracts for individual hours of the following day can be traded. The term 'intraday' is easily misleading since the intraday auction is basically also a day-ahead auction in smaller time intervals. Only in the intraday continuous trading market/intraday continuous market (IDM), transactions are possible for the current day: Up to 30 min before the negotiated energy delivery, electric energy can be traded in 15 min blocks. For the operation of BESS to supply PCR power, the transactions at the intraday continuous market of the EPEX SPOT allows to compensate efficiency losses and to balance the SOC to prove the required PCR power at all times.

2.3.2 Technical framework for primary control reserve supply

At first glance, BESS are ideally suited for the provision of PCR power: Fast control times enable the exact delivery of the required power services. The continuous fluctuation around the setpoint frequency of 50 Hz also leads to a relatively high temporal utilization of the BESS. Furthermore, due to the fact that the PCR power has to be provided in charge and discharge direction, the BESS SOC could thus be kept at an optimal state.

2.3.2.1 Prequalification of BESS to supply primary control reserve

In order to participate in the PCR power market, a BESS and also all further technical units have to demonstrate their ability to provide PCR by the *prequalification procedure* [36]. This prequalification is prescribed by the TSO to ensure that the technical unit is able to provide the offered PCR power properly.

Additional guidelines for BESS providing PCR power have been established in 2015 [38]: A BESS participating at the PCR market has to ensure that at all times of operation the full offered control power in positive and negative direction can be provided for 30 min as long as the power line frequency $f_{power\ line}$ is in *normal progression*. The normal progression is defined in case the frequency deviation Δf from the setpoint frequency of 50 Hz is continuously less than 50 mHz or none of the following criteria is met:

1. $\Delta f_{power\ line} > \pm 50$ mHz for more than 15 min
2. $\Delta f_{power\ line} > \pm 100$ mHz for more than 5 min
3. $\Delta f_{power\ line} > \pm 200$ mHz at all times

In case that at least one criterion is met, the BESS is allowed to leave the operational SOC range to supply PCR power. Due to the 30 min criterion, the BESS has to be operated in a limited SOC range depending on the power-to-energy ratio (PER), which defines the ratio of the nominal AC power to the nominal energy capacity of the BESS. For example, to offer 1 MW PCR power the BESS is required to have at least a nominal energy capacity of 2 MWh and the SOC has to be kept between 25 to 75 % to comply with the rules [38]. However, due to the unavoidable efficiency losses, the BESS PER has to be less than 0.5 to be able to comply with the prequalification rules at all times [38].

2.3.2.2 Operation of BESS to supply primary control reserve

The required PCR power $P^{\text{PCR}}(f_{\text{power line}})$ in relation to the offered power P_{max} has to follow linearly the frequency deviation Δf from the setpoint frequency 50 Hz leading to the P - $f_{\text{power line}}$ characteristic:

$$P^{\text{PCR}}(f_{\text{power line}}) = \frac{-(f_{\text{power line}} - 50 \text{ Hz})}{0.2 \text{ Hz}} \cdot P_{\text{max}} \quad (2.1)$$

However, this P - $f_{\text{power line}}$ characteristic is only valid in the frequency range between 49.8 to 50.2 Hz and outside this range, the respective PCR power is limited to the offered PCR power P_{max} . For example, if a frequency of 50.2 Hz is measured, the full negative tendered PCR power has to be provided by charging the BESS. In the case of a measured frequency of 49.8 Hz, the full positive tendered PCR power has to be provided by discharging the BESS.

The BESS can be operated with certain degrees of freedom which are defined in the 'Key points and degrees of freedom in the provision of primary control power' [39] and are explained in the following. By utilizing these degrees of freedom, the possible inertia of the PCR provision can be compensated. Additionally, the degrees of freedom allow the possibility to regulate the BESS SOC in a certain range or if necessary to control a defined SOC setpoint.

1. **Overfulfillment:** The required PCR power can be delivered with an increase up to 20 % at any time.
2. **Dead band:** The required PCR power given by the P - $f_{\text{power line}}$ characteristic can also be provided within the range of ± 10 mHz around the setpoint frequency of 50 Hz.
3. **30 s slope:** The required PCR power given by the P - $f_{\text{power line}}$ characteristic must be provided within 30 s or earlier. Therefore, the slope of the provided PCR power can be adjusted within the time interval of 30 s allowing to control the charging or discharging speed.

2.3.3 State-of-the-art

In the context of the rising number of BESS projects being subject to the supply of PCR [13], the configuration and operation of stationary BESS in the power grid is becoming increasingly of interest in studies and investigations. Koller et al. [40] showed beside two further stationary BESS applications the configuration and measurement results of a grid-connected BESS with a peak power of 1 MW. The VDE study 'Battery storage in the low and medium voltage level' [3] investigated the PCR-supply with a BESS: By analyzing the power grid frequency profile in detail, the theoretical requirements for the PCR-supply by a BESS are derived. Furthermore, the PCR market trends are discussed by evaluating the historical development of the PCR power requirements and the resulting tender prices. They state that the overall required PCR power will decrease in near future, due to the technical advantages of providing PCR power with BESS in comparison to market participants like conventional thermal power plants. Further operating strategies for the PCR operation and the implementation of the possible degrees of freedom are described by Hollinger et al. [41]. The provision of PCR through distributed BESS in combination with self-consumption of PV power was investigated by the same author [42]. Zeh et al. [2] analyzed the BESS operation in PCR application and estimates the battery aging effects. However, the battery degradation was not considered during the simulation of the BESS operation providing PCR power. Fler et al. [43] showed a techno-economic analysis of the BESS operation

path dependence of the aging rate when applying dynamic load profiles. However, there is plenty of literature on the calendar and cycle aging and corresponding lifetime models for various lithium-ion batteries and especially for LFP/C cells, which serve as the basis for this work and are presented in the following section.

2.4.1 Calendar aging

The review paper of Barré et al. [48] on battery aging mechanisms emphasizes that the growth of the solid electrolyte interphase (SEI) on the graphite anode is by far the most prominent aging mechanism that occurs when lithium-ion battery cells are stored in an experimental setup. The SEI growth leads to an irreversible loss of lithium inventory (LLI) (i.e. loss of cyclable lithium) as well as an increase of cell's impedances and is accelerated with increased temperatures and higher SOC. Additional capacity fade could occur due to the loss of active material (LAM) on the cathode and anode. Li et al. [49] showed for a commercial LFP/C cell an growth of the SEI (LLI) (see **Figure 2.6a**) and additionally blocking mechanisms of graphene layers of the anode (LAM) during the storage at high temperatures of about 60 °C (see **Figure 2.6b**). This effect also occurred in a cycle aging study for the same LFP/C cell, however, this LAM of the anode occurs mainly at high storage temperatures (60 °C) and is almost negligible at moderate temperatures. Hence, the LLI by SEI growth dominates for different cell types when exposed only to calendar aging as shown by Keil et al. [50]. Thereby, calendar aging results in capacity fade and resistance increase of the cell, reducing the maximum available power and energetic efficiency.

Alongside, there are effects that could lead to an increase of the available capacity when performing capacity measurements with several cycles: Gyenes et al. [51] originated this capacity increase for a LiNiMnCoO₂/C cell with the fact that lithium atoms are stored in the anode overhang areas, which is the portion of the anode that extends past the cathode electrode of commercial lithium-ion cells. The lithium atoms stored in the anode overhang areas can be recovered by performing several full cycles. Furthermore, Gyenes et al. showed that this capacity recovery effect depends strongly on the preceding storage SOC. Lewerenz et al. [52; 53] and Wilhelm et al. [54] investigated the same effect for LFP/C cells and stated additionally, that the recoverable capacity depends on the size of the overhang area. Wilhelm et al. quantified the anode overhang area with about 10 % in a commercial 18650 cell and measured a maximal capacity difference of 3.6 % between cells stored at a low and high storage SOC by

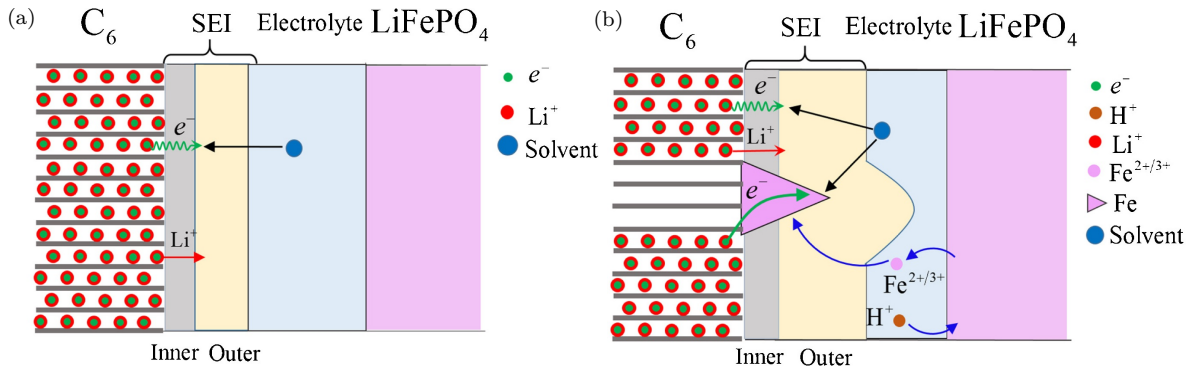


Figure 2.6: Schematic of the calendar aging mechanism at low (a) and at elevated temperatures (b) (Figures from [49]).

this effect. An important conclusion is the fact, that the possible capacity recovery due to the anode overhang areas has to be considered when assessing the state of health of battery cells. The influence of the anode overhang areas is estimated for the investigated cell of this work in **Section 4.1.1**.

The following **Table 2.2** shows a selection of different calendar aging studies. The studies are classified into the different existing aging model types that have been applied to simulate the aging behavior: Empirical, Semi-empirical and Physico-chemical. Some publications show experimental aging data without presenting models for lifetime predictions (see the first row). As LFP/C cell calendar aging is in the focus of this work, the literature was additionally classified into LFP/C and other cell types. All mentioned calendar aging studies investigate the influence of both, temperature and SOC, by applying several storage conditions with different temperatures and SOC of the stored cells. Most of the presented aging models are able to validate the measured capacity fade under constant storage conditions with acceptable prediction errors. Only a few of the studies also demonstrate models predicting the resistance increase [10; 59; 64], and only Prada et al. [75] evaluates the investigated resistance increase with an aging model for LFP/C cells.

The majority of the calendar aging studies show non-linear trends of the capacity fade for different storage temperatures and SOC. In contrast, in the aging study of Lewerenz et al. [52; 77] the capacity fade follows a linear trend at moderate storage temperatures, but at 60 °C a non-linear trend is shown for different storage SOC. Hence, they state that the capacity aging trends are path-invariant for temperatures lower than 45 °C and path-depending for temperatures higher than 50 °C. Furthermore, it could be concluded that the widely observed square root dependance over time of the capacity fade is possibly connected with the reversible capacity effect of the anode overhang areas as explained above. Then, the measured capacity fade would be accelerated by a reversible lithium flow into the anode overhang areas dependent on the storage SOC at the begin of a calendar aging study and slow down when the overhang areas are filled up. Even so, it remains unclear how to consider this effect correctly when developing calendar aging models, since the capacity trapped in the anode overhang areas can be recovered only by storing the cells at a low SOC for several days or performing several full cycles before every capacity measurement (CM), leading to an additional cycle aging effect. Furthermore, due to the different positions and distances to the cathode counterpart, the time constants of this lithium flow/capacity recovery are diverse for the different positions of the anode overhang areas, which implies the application of comprehensive physico-chemical models.

In fact, aging models should also be used for the simulation of dynamically changing cell storage conditions when estimating, for instance, the battery lifetime of a stationary application. Therefore, it is necessary to understand and correctly apply the path dependance of calendar aging when aging models are used in simulations with dynamic profiles of temperature and SOC. However, only the following studies on LFP/C calendar aging validate the respective aging models with dynamic storage conditions by alternating the temperature but only at a constant SOC [52; 61; 66; 67; 75]. Only

Table 2.2: Overview of lithium-ion battery calendar aging literature classified into different aging models and cell types.

| Aging model type | LFP/C | Other cell types |
|-------------------------|---------------------|-------------------------|
| None (tests only) | [49; 50; 52; 55–57] | [50; 55; 58–60] |
| Empirical | [47; 61–63] | [64; 65] |
| Semi-empirical | [66; 67] | [10; 67–71] |
| Physico-chemical | [72–75] | [76] |

Sarasketa-Zabala et al. [61] present a validation with alternating temperatures at different SOC with a relatively long experiment period of about 650 days. In contrast, in this work, additional model precision is obtained by:

1. Investigating multiple cells per storage condition in order to reduce thereby possible deviations in the aging behavior due to cell-to-cell parameter variations.
2. Examining different combinations of dynamically changing storage conditions.
3. Applying an aging model that uses the same set of parameters for every storage condition.

Although the aging model of Sarasketa-Zabala et al. shows prediction errors $< 1\%$, the model cannot be adapted to estimate the aging of further LFP/C cells due to the missing parameter fitting procedure and lack of customizable physico-chemical parameters.

There are further aging studies on path dependence of lithium-ion battery aging [64; 78–80]. However, only Su et al. [65] investigate the pure calendar aging under static and alternating (non-static) storage conditions of both, temperature and SOC, for a LiNiMnCoO₂/C cell. Additionally, they develop an empirical aging model based on the static aging study and validate it with the measurement data from the non-static aging study. The additional dynamic calendar aging study is designed similarly, which is presented later. However, by using 2 cells for each changing storage condition with switched order over time, the here performed dynamic calendar study is able to reveal the path dependence of calendar aging systematically for different storage conditions of temperature and SOC.

In conclusion, various authors have investigated the specific aging effects relevant to LFP/C calendar aging. In the later presented calendar aging study (see **Chapter 4**) these aspects are combined and an aging model is developed which is based on a long-lasting experiment with numerous storage conditions for both, temperature and SOC. Furthermore, this aging model is validated systemically with dynamically changing storage conditions. However, this calendar aging model applies only to one single cell. Considering a BESS consisting of many serial and parallel connected cells, the possible cell-to-cell parameter variation [81] and inhomogeneous temperature or SOC distribution [82] could lead to deviating operation conditions and hence to a deviating aging of the single cells [83]. Then, in a BESS simulation, the influence of the deviating capacity decrease and resistance increase due to calendar and cycle aging of each cell has to be considered. In case that all cells in a battery system would have the very same cell parameter values and operation conditions, the BESS capacity degradation and resistance increase can be estimated with the calendar aging of one single cell.

2.4.2 Cycle aging

Apart from calendar aging, cycle aging occurs when a battery cell is charged or discharged. Similar to calendar aging, cycle aging leads to LLI, LAM and the increase of the impedance [48]. Li et al. [84] showed for a commercial LFP/C cell an accelerated growth of the SEI (LLI) (see **Figure 2.7a**) during cyclization and additionally a blocking mechanism of graphene layers of the anode (LAM) during cyclization at high temperatures of 60 °C (see **Figure 2.7a**). They demonstrate that this LAM mechanism of the anode is mainly caused by Fe that dissolves from the cathode and is deposited on the graphite surface during the cyclization. In contrast to calendar aging, the surface area of the anode is changing during the cyclization: The lithiation and delithiation in the active material of the electrodes lead to a volume expansion and possible fracturing of the electrodes. Hence, different SEI surfaces with individual areas and growth speed emerge, which are illustrated in **Figure 2.7b** with A^{fr} (fresh

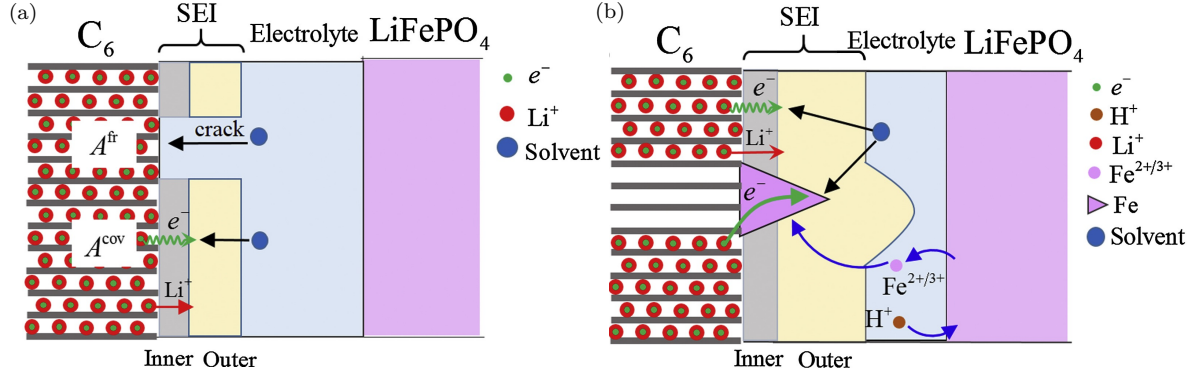


Figure 2.7: Schematic of the cycle aging mechanism at low (a) and at elevated temperatures (b) (Figures from [86]).

areas) and with A^{cov} (covered areas) [84]. Additionally to the SEI growth and the wear of active mass, lithium plating can occur at low temperatures or high currents leading to accelerated aging effects [85]. When investigating the aging effects of cells under operation, always the superposition of calendar and cycle aging (total aging) is measured because calendar aging occurs all the time. Hence, to obtain the pure cycle aging effects, the theoretical calendar aging effects have to be subtracted from the total aging. Then, the pure cycle aging is a function of the charge and discharge throughput in Ah or related to the nominal capacity in FEC. The possible influence factors on cycle aging are the cell's temperature, C-rate, depth-of-cycle (DOC) and the cycles' SOC-range. **Table 2.3** shows a selection of different cycle aging studies. The studies are classified into the different existing aging model types that have been applied to simulate the aging behavior: Empirical, Semi-empirical and Physico-chemical. Some publications show experimental aging data without presenting models for lifetime predictions (see the first row). As LFP/C cell aging is in the focus of this work, the literature was additionally classified into LFP/C and other cell types. Most of the cycle aging studies investigate the influence of temperature and C-rate. Half of the studies investigate the influence of DOC and cycles' SOC-range. However, only Lepiorz [47] (LFP/C cells) and de Hoog et al. [89] (NMC/C cells) considerate all four influence factors on cycle aging in their experiments. Lepiorz tested various conditions of SOC and DOC [47] but the presented aging model considers only the temperature and C-rate. Furthermore, this aging model was not validated with dynamic profiles with varying influence factors. Only some of the presented studies tested their aging models with dynamic profiles [10; 75; 87; 89; 90].

In conclusion, various authors have investigated the specific aging effects relevant to LFP/C cycle aging. In this work, these aspects are combined and a cycle aging model is developed based on a long-lasting experiment with numerous cycle aging conditions for temperature, C-rate, DOC and cycles SOC-range. Furthermore, this aging model is validated systemically with dynamic load profiles with changing operating conditions.

Table 2.3: Overview of lithium-ion battery cycle aging literature classified into different aging models and cell types.

| Aging model type | LFP/C | Other cell types |
|-------------------|--------------|------------------|
| None (tests only) | | [52; 58; 64; 85] |
| Empirical | [47; 62; 87] | |
| Semi-empirical | [67; 88] | [10; 71; 89] |
| Physico-chemical | [72–76] | |

3 Development of a model framework for the assessment of battery energy storage systems

3.1 Simulation software SimSES

Due to the new challenges in power grids and decreasing costs of BESS, the technical and economic suitability of these technologies is presently under discussion for the various stationary fields of application. However, there are numerous technical degrees of freedom in the storage system design that can be optimized, such as the choice of energy storage technology or the nominal sizing of the individual components. In order to be able to investigate these and other technical questions concerning stationary energy storage systems (SES), the software tool SimSES was developed.

SimSES is a software tool to simulate SES, with the current main focus on lithium-ion batteries, allowing detailed techno-economic evaluations for different applications and scenarios. Within the framework of SimSES BESS' submodels are coupled, allowing the independent and modular development of different component-models. Yet the combination of these submodels is a major benefit of SimSES, as the superior sophistication of each submodel is exploited for increased accuracy. The BESS model reflects the system's effect on the AC side. An efficiency model of the inverter/rectifier computes the according power at the battery terminals. The input power at the battery terminal is then used for the battery model to compute the resulting current and voltage values. This is required for the models to compute the effect on the battery itself. The nonlinearity and the present aging behavior of the battery require consideration of these effects. The battery is modeled as equivalent circuit model (ECM) model and is coupled with a thermal and degradation model. This complex model is required due to the high interdependencies: The utilization and environmental condition of the battery determine its thermal behavior. These factors together with the thermal behavior impact the battery's aging. Then, the BESS performance for the application is again determined by the reduced battery capabilities. The permanent interaction between the battery and the application is represented in SimSES. This method is by far more elaborate and accurate than analysis with static profiles. SimSES permits a variety of options to address and investigate the technical degrees of freedom of BESS by assessing technical, as well as economic performance indicators.

SimSES was developed by the members and students of the team SES at the institute EES. Most of the code elaboration was performed by Maik Naumann and Nam Truong and used for various publications [5; 6; 32]. The author of this work mainly contributed to the development of the general simulation framework, the modeling of the different fields of application, the energy storage system model, the battery stress characterization, the battery degradation model, and the technical and economic evaluation methods.

This software tool and its source code were published together with exemplary load profiles for example simulations under the BSD 3-clause License [91]. A comprehensive documentation of all scripts and functions is included in the source code. Hence, in this work, no additional documentation of the code

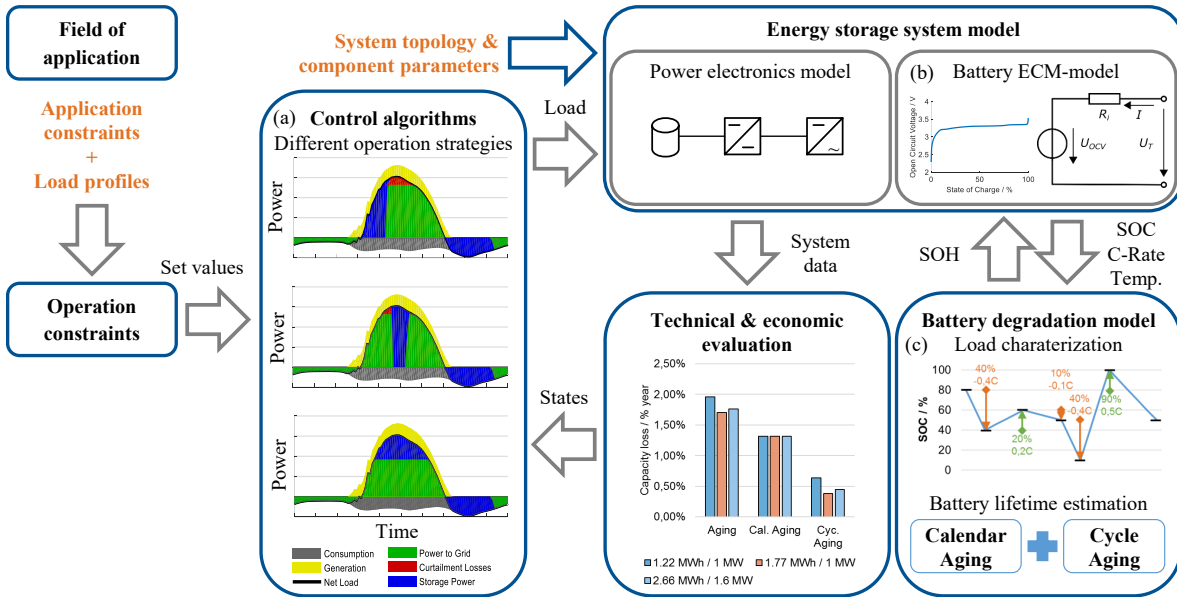


Figure 3.1: SimSES structure and functional blocks.

and the functions is given, however, the basics about SimSES are presented in the following.

3.1.1 Basic software structure

SimSES is programmed using *MathWorks MATLAB*[®] software. In order to provide a framework that enables the evaluation of different stationary BESS applications and the switching of different sub-models, flexibility, interchangeability, and modularity were key features demanded for the software design. By using object-oriented programming the software creates an encapsulated model of an energy storage system with the relevant technical parameters and functions. The modular framework allows a straightforward integration of future storage models developed by others. Furthermore, this concept permits to call multiple instances to evaluate parameter sweeps or to simulate multiple storage objects that interact. To enable compatibility to *MathWorks Simulink*[®], a programming environment widely used in engineering research, SimSES uses MATLAB's *System object*[™] structure. Thereby SimSES can be developed and executed both, as pure MATLAB code or alternatively be included in a Simulink environment, for instance, a power grid model interacting with the model of a SES. The main components of the software framework and their interdependencies are shown in **Figure 3.1** and are explained in the following.

3.1.2 Fields of application

SES can serve various tasks for power supply systems. These include behind the meter installation of storage for residential and industrial customers aiming for electricity bill reduction [92; 93], local grid support for distributed system operators (DSO), related tasks like voltage stabilization [94], and the provision of ancillary services like supra-regional frequency control [95]. Furthermore, all combinations thereof may be tackled with SES, a task that is highly relevant in micro grids and island grids for electricity supply stabilization [96]. To handle these function requirements, the energy storage system must meet application-specific tasks, which are derived from the EMS and its control algorithms (see

Section 3.1.3). Resulting power request profiles are used as a setpoint input for the SES, which in turn will lead to an output of the energy storage unit. For subsequent technical and economic evaluations, this storage behavior may be used as fundamental input parameter.

To date, several fields of application have been analyzed using an implementation of the SimSES framework:

PV-Home energy storage system (PV-HESS): For residential customers with a rooftop PV-system, battery storage can be used to time-shift local surplus PV-electricity generation and thus reduce electricity purchase at a given retail-tariff [26]. The sensitivity of technical and economic parameters for PV-HESS has been investigated using SimSES [6; 32].

Primary control reserve supply (PCR-supply): Grid frequency stabilization is supported by the provision of control reserve in various regions worldwide. BESS may participate in auctioning and provision of PCR power, provided that the storage system is kept at the mid-level state of charge for all times [93]. Using SimSES, a recent work analyzes BESS operation in PCR application and simulates the aging effects [2]. This allowed a reliable estimation of the required BESS size and the expected economic benefit.

Island grid support: In order to reduce the dependency on diesel generators and maintain stable grid operation, the integration of a battery storage system is a common strategy in various island grids. To date, it remains a challenging task to optimize sizing, location, and control of the storage systems. Current work tackles island grid control for a model region (Semakau Island, Singapore) and relies on state estimation for the BESS system via SimSES. SimSES is used in an iterative fashion to calculate new power flow setpoint values for the EMS [97].

Other applications: Several other applications are currently investigated using the SimSES framework. This includes peak-shaving for industrial customers by BESS in order to reduce peak-power related cost and grid-relief in the context of buffer storage system installation within electric vehicle fast-charging stations.

3.1.3 Control algorithms

Control algorithms determine the output power of BESS and consequently their usefulness. Different approaches for the control of BESS exist in the literature, that can be roughly categorized into two classes: Rule-based (expert-designed) and numerical optimization-based algorithms. The specific application determines the goal and the potential input values for the control algorithm. The assessment of control algorithms is often conducted under individual scenarios. The presented performances are therefore neither comparable nor informative. Different control algorithms use different input values and may optimize over a certain time horizon. Optimization requires iterative simulation runs over that time horizon.

The implementation of control algorithms in SimSES is straightforward because of the generic structure, that grants the control algorithm access to all properties of the storage object, i.e. BESS states and time-series of profile data. This includes historical, current and predicted values. The BESS states and the current time-step can be reset to any, previous simulation time-step. This enables development of optimization-based algorithms that require multiple simulation runs over a certain time horizon. The opportunity of straightforwardly implementing different types of control algorithms allows their assessment under equal conditions and assumptions. Consequently, objective comparison

of the different algorithms' performance is possible.

Three different example control algorithms for increasing a household's self-consumption are shown in **Figure 3.1a**. While the conditions remain the same, the effect of the three algorithms can be compared. The profile shown on the top, for example, indicates that the specific control algorithm experiences curtailment losses. The middle plot shows another control algorithm that reduces the curtailment losses, while the bottom plot depicts a control algorithm that completely prevents curtailment losses. Other effects, such as aging caused by different charging and discharging regimes can be the target of the control algorithms as well.

3.1.4 System model

Generally, a BESS consists of a battery, power electronics, and peripheral components such as a TMS, a BMS, and an EMS (see **Section 2.1.1**). To enable simulations of long time-horizons up to 20 years, only simplified models of the BESS components are applied in SimSES. Thus, simulation step-sizes of 1 minute and above are used and the electrical component models are coupled by the power flow instead of voltage and current values. The possible transient behavior of electrical and thermal components, the influence of the control system, and BMS state estimation errors are neglected. The BESS is controlled, based on the power request for the grid AC side of the power electronics. The power request is compared against power limitations of the power electronics and battery. Power output is limited to the nominal power of the inverter. The battery model calculates maximum power based on the operating voltage range of the cell, the SOC, and the state-of-health (SOH). Finally, the system response to the power request is determined.

3.1.4.1 Battery

The battery is implemented as a single-cell ECM based on full cell characterization. To scale up the battery's parameters from a single-cell towards a battery module and complete system, scaling factors are applied. These scaling factors can also be used to model the influence of battery cell parameter variation. The batteries' terminal voltage U_T is calculated from the open circuit voltage (OCV) U_{OCV} and the overvoltage ΔU across the series resistance R_i . The U_{OCV} is implemented as a function over the SOC. Exemplary values for the OCV and the model structure are shown in **Figure 3.1b**. The overvoltage ΔU is the difference between the cell terminal voltage U_T and the OCV (3.1). Resistance values are implemented as a function of SOC, cell temperature, and current direction I . Positive currents lead to charging the battery and negative currents lead to discharging the battery.

$$\Delta U = U_T - U_{OCV} = I \cdot R_i(\text{sgn}(I), SOC, T) \quad (3.1)$$

The losses caused by the overvoltage are assumed to fully dissipate into heat \dot{Q}_{Cell} :

$$\dot{Q}_{\text{Cell}} = I \cdot \Delta U \quad (3.2)$$

The influence of the reversible heat production of the battery cell is neglected due to the fact, that the reversible heat production is relatively small in comparison with the cell's Joule's losses in a long-term view.

For thermal modeling, the single cell is implemented as 0D lumped thermal capacity. The heat balance

of the cell with the ambient temperature T_{Ambient} through convective heat transfer depends on the heat transfer coefficient α , cell surface area A , mass m , and specific heat capacity c_p (3.3).

$$m \cdot c_p \frac{dT_{\text{Cell}}}{dt} = \dot{Q}^{\text{Cell}} - A \cdot \alpha \cdot (T - T_{\text{Ambient}}) \quad (3.3)$$

Self-discharge of the cell is implemented as a constant rate. The aging of battery cell's capacity and performance is considered in an aging model, described in **Section 3.1.5**.

3.1.4.2 Power electronics

The inverter/rectifier efficiency is modeled with a power dependent efficiency curve which relies on the inverter's output power $P_{\text{out}}^{\text{Inverter}}$ (3.4):

$$\eta^{\text{Inverter}} = f\left(p = \frac{P_{\text{out}}^{\text{Inverter}}}{P_{\text{rated}}^{\text{Inverter}}}\right) = \frac{p}{p + p_0 + k \cdot p^2} \quad (3.4)$$

Exemplary values used for a high-efficiency inverter are for the all load-dependent losses factor $k = 0.0345$ and for the constant load-independent parameter $p_0 = 0.0072$, according to Notton et al. [98]. Other inverter efficiency values or functions can be implemented in SimSES as well.

3.1.5 Battery degradation model

Despite the steadily increasing lifetime of newly available lithium-ion batteries, the degradation of capacity and performance of these batteries is still a major influencing parameter for the design and performance of BESS. Therefore a battery degradation model is integrated into SimSES (see **Figure 3.1c**), which estimates the battery's capacity fade and performance decrease. **Figure 3.2** shows the model's structure and the particular elements described in this section.

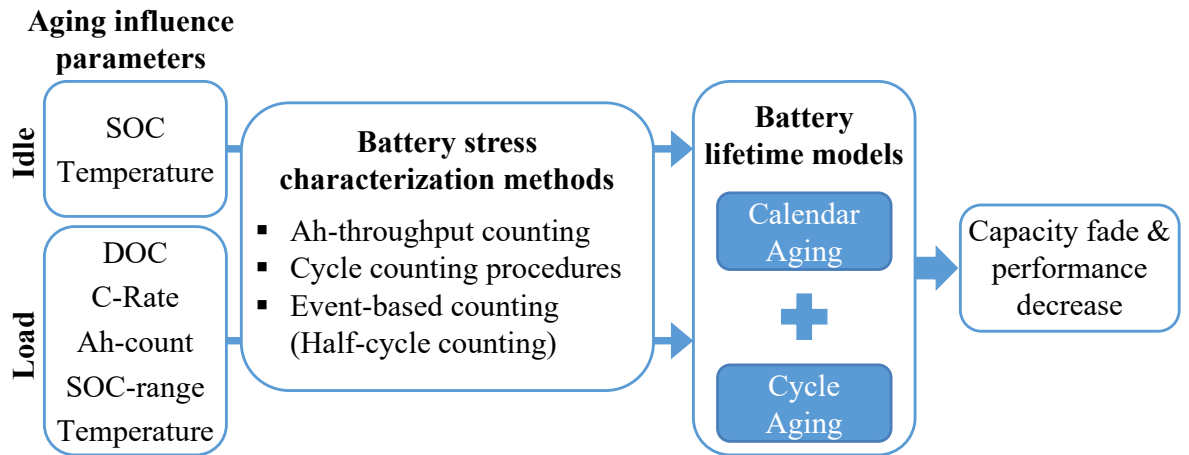


Figure 3.2: SimSES battery degradation model.

3.1.5.1 Battery stress characterization

Diverse methods for the battery stress detection and characterization are implemented. However, each method shows different properties on the output accuracy and the required computational effort when

being applied. The half-cycle counting (event-based counting procedure) is implemented to characterize the battery stress, i.e. battery's power, SOC, and temperature profile, after every load alternation as input for the battery lifetime models.

3.1.5.2 Aging influence parameters

The model considers the influence parameters on battery degradation, separated into *Idle* and *Load* stress. The batteries' SOC and temperature in idle periods are the input to estimate the calendar aging. During load periods, i.e. battery cyclization, the particular properties of a cycle are inputs to estimate the degradation by cycle aging: DOC, relative power (C-rate), cycle SOC-range, temperature and the cycle throughput (Ah-count).

3.1.5.3 Battery lifetime estimation

Battery lifetime models of various battery technologies with different degree of detail are implemented: On the one hand, information about the expected calendar and cycle lifetime from battery datasheets or warranty information are used in simple models. Literature battery lifetime models may be included with the given formulas and parameters. On the other hand, battery lifetime models developed with in-house battery aging experiments are integrated: These models cover a comprehensive list of aging influence parameters in idle or load periods of the battery operation to estimate the battery degradation with high precision. With the superposition of calendar and cycle aging effects of the respective idle and load periods, the total degradation is calculated step-wise: The batterie's SOH is reduced gradually i.e. the currently available power and usable energy within the battery system model decreases.

3.1.6 Technical evaluation

The object-oriented structure of the tool keeps a record of the system states for all simulated time-steps. This allows straightforward analysis of the simulation data. The whole range of values can be investigated, such as the influence of the BESS on the grid exchange power on the one end. The aging on the battery-cell level can be evaluated on the other end of the scale. Furthermore, the simulation gradually calculates the SOH decrease by calendar and cycle aging effects. Further technical parameters, such as the efficiency losses or the influence of adjusted control algorithms, can be analyzed with SimSES as well.

3.1.7 Economic evaluation

The economic evaluation in SimSES can be classified into two parts:

1. During the simulation of the energy storage operation, the economic impact of, for instance, the battery degradation can be taken into account to improve the profitability of storage operation with control algorithms.
2. After the simulation of the energy storage operation, economic performance indicators such as the LCOES or the profitability index (PI) are calculated by discounting with interest and inflation rate the gross cash flow, which consists of the most relevant costs and revenues during the simulation period (see **Section 3.2.2.2**). With these generic performance indicators, SimSES allows for comparing the

profitability of different fields of applications and scenarios by using the same the simulation framework. Furthermore, by comparing the economic results the best-suited storage technology can be selected and the sizing of energy storage and power electronics can be optimized by alternating the technical input parameters.

3.2 Assessment methods

In order to evaluate or to compare different BESS applications with SimSES, various assessment methods can be applied. Here, only a selection of evaluation parameters is presented which are later utilized and analyzed in **Chapter 6**. First, the technical evaluation parameters are described and followed by the economic evaluation parameters.

3.2.1 Technical evaluation parameters

3.2.1.1 General parameters

The average roundtrip efficiency η^{BESS} of the BESS is defined by the ratio of the total energy discharged $E_{\text{discharged}}^{\text{BESS}}$ to the total energy charged $E_{\text{charged}}^{\text{BESS}}$ during the complete simulation period.

$$\eta^{\text{BESS}} = \frac{E_{\text{discharged}}^{\text{BESS}}}{E_{\text{charged}}^{\text{BESS}}} = 1 - \frac{E_{\text{loss}}^{\text{BESS}}}{E_{\text{charged}}^{\text{BESS}}} \quad (3.5)$$

This equation is only valid for the case that the energy stored in the BESS would be the same at the beginning and at the end of the simulation. In order to consider the energy stored at the beginning and at the end of the simulation, the respective energies have to be subtracted respectively. The energetic losses $E_{\text{loss}}^{\text{BESS}}$ result from subtracting the total energy discharged $E_{\text{discharged}}^{\text{BESS}}$ from the total energy charged $E_{\text{charged}}^{\text{BESS}}$ and can be deployed in the equation of average roundtrip efficiency.

To compare different load profiles utilization ratios are defined [82]. The temporal utilization rate τ_{time} is the ratio of the time in which the BESS is operated $t_{\text{operation}}$ (battery power $P^{\text{Battery}} \neq 0$) to the evaluated simulation duration $t_{\text{Simulation}}$:

$$\tau_{\text{time}} = \frac{t_{\text{operation}}^{\text{BESS}}}{t_{\text{simulation}}^{\text{BESS}}} \quad (3.6)$$

The energy-based utilization rate τ_{energy} is the ratio of the energy-throughput of the BESS during operation $E_{\text{throughput operation}}^{\text{BESS}}$ to the theoretically possible maximum energy throughput during the simulation duration $E_{\text{throughput theoretical max}}^{\text{BESS}}$ when operating the system at the maximum BESS power

limited by the inverter:

$$\tau_{\text{energy}} = \frac{E_{\text{throughput operation}}^{\text{BESS}}}{E_{\text{throughput theoretical max.}}^{\text{BESS}}} = \frac{\int_{T_{\text{sim.}}} |P^{\text{Battery}}(t)| dt}{\int_{T_{\text{sim.}}} |P_{\text{max.}}^{\text{Battery}}| dt} \quad (3.7)$$

The determination of the FEC of the BESS operation depends on the selected battery model. When choosing a battery ECM, the count of the FEC is the ratio of the cumulative capacity throughput $Q_{\text{cum.}}^{\text{Battery}}$ related to the twice of nominal battery capacity $Q_{\text{nom.}}^{\text{Battery}}$ in order to count the FEC:

$$FEC_Q = \frac{Q_{\text{cum.}}^{\text{Battery}}}{2 \cdot Q_{\text{nom.}}^{\text{Battery}}} = \frac{Q_{\text{cum., charge}}^{\text{Battery}} + Q_{\text{cum., discharge}}^{\text{Battery}}}{2 \cdot Q_{\text{nom.}}^{\text{Battery}}} = \frac{1}{2 \cdot Q_{\text{nom.}}^{\text{Battery}}} \int_{T_{\text{sim.}}} |I^{\text{Battery}}(t)| dt \quad (3.8)$$

The cumulative capacity throughput $Q_{\text{cum.}}^{\text{Battery}}$ can be calculated by integrating the absolute battery current over the simulation time $T_{\text{sim.}}$. When choosing a battery power flow model the FEC represent the energetic capacity throughput with the ratio of the cumulative energetic throughput $E_{\text{nom.}}^{\text{Battery}}$ related to the twice of nominal battery energetic capacity $E_{\text{nom.}}^{\text{Battery}}$:

$$\begin{aligned} FEC_E &= \frac{E_{\text{cum.}}^{\text{Battery}}}{2 \cdot E_{\text{nom.}}^{\text{Battery}}} = \frac{1}{2 \cdot E_{\text{nom.}}^{\text{Battery}}} \int_{T_{\text{sim.}}} |P^{\text{Battery}}(t)| \cdot \eta^{\text{Battery}}(P^{\text{Battery}}(t)) dt \\ &= \frac{1}{2} \int_{T_{\text{sim.}}} \left| \frac{\partial SOC(t)}{\partial t} \right| \cdot SOH(t) dt \end{aligned} \quad (3.9)$$

The cumulative energetic capacity throughput $E_{\text{cum.}}^{\text{Battery}}$ can be calculated by integrating the absolute battery power $P^{\text{Battery}}(t)$ multiplied by the battery power dependent efficiency $\eta^{\text{Battery}}(P^{\text{Battery}}(t))$ over time. Another possibility to obtain the FEC is the integration of the SOC(t) multiplied by the current SOH(t) over time and divided by the factor 2 to represent the full cycles. Both, the SOC and the SOH are related to the energetic capacity of the battery.

3.2.1.2 PV-HESS application parameters

For the PV-HESS application, the self-consumption rate and self-sufficiency rate (autarky rate) serve to quantify the benefit of applying a BESS in a household with a PV-system. The self-consumption rate σ is the ratio of the self-consumed energy $E_{\text{self-consumption}}$ to the total generated energy $E_{\text{generated}}^{\text{PV}}$ by the PV-system.

$$\sigma = \frac{E_{\text{self-consumption}}}{E_{\text{generated}}^{\text{PV}}} = \frac{E_{\text{consumed directly}}^{\text{PV}} + E_{\text{stored in BESS}}^{\text{PV}}}{E_{\text{generated}}^{\text{PV}}} = 1 - \frac{E_{\text{fed into grid}}^{\text{PV}}}{E_{\text{generated}}^{\text{PV}}} \quad (3.10)$$

The self-consumed energy $E_{\text{self-consumption}}$ is thereby the sum of the PV energy which is directly con-

sumed $E_{\text{consumed directly}}^{\text{PV}}$ together with the PV energy which is stored in BESS $E_{\text{stored in BESS}}^{\text{PV}}$. Another possibility to obtain self-consumption rate is to calculate the self-consumed energy $E_{\text{self-consumption}}$ by subtracting the PV energy which is fed into the power grid $E_{\text{fed into grid}}^{\text{PV}}$ from the total PV energy generated $E_{\text{generated}}^{\text{PV}}$.

The self-sufficiency rate (autarky rate) δ is defined as the ratio of the self-dependent energy $E_{\text{self-dependent}}$ to the total energy consumed $E_{\text{consumption}}$.

$$\delta = \frac{E_{\text{self-dependent}}}{E_{\text{consumption}}} = \frac{E_{\text{consumed directly}}^{\text{PV}} + E_{\text{discharged}}^{\text{BESS}}}{E_{\text{consumption}}} = 1 - \frac{E_{\text{purchased}}}{E_{\text{consumption}}} \quad (3.11)$$

The self-dependent energy $E_{\text{self-consumption}}$ is the sum of the PV energy generation which is directly consumed $E_{\text{consumed directly}}^{\text{PV}}$ together with the energy which is discharged from the BESS to supply the household consumption $E_{\text{discharge}}^{\text{BESS}}$. Another possibility to obtain self-consumption rate is to calculate the self-dependent energy $E_{\text{self-dependent}}$ by subtracting the purchased energy from the grid $E_{\text{purchased}}$ from the total energy consumed $E_{\text{consumption}}$.

3.2.2 Economic evaluation parameters

3.2.2.1 Profit and loss account

In the economic evaluation of the BESS operation with SimSES, all costs and revenues are considered with the net present value (NPV) method by applying the respective discount factor vector \overrightarrow{DF} for every year of the depreciation period. Therefore, the real interest rate i_{real} is the base of the exponentiation to the power of the single entries of the vector $\overrightarrow{Y_{\text{DP}}}$ representing the years of the depreciation period with the values 1 until y_{end} for the last year of the depreciation period.

$$\overrightarrow{DF} = (1 + i_{\text{real}})^{\overrightarrow{Y_{\text{DP}}}} = (1 + i_{\text{real}})^{(1 \dots y_{\text{end}})} = \begin{pmatrix} (1 + i_{\text{real}})^1 \\ (1 + i_{\text{real}})^2 \\ \vdots \\ (1 + i_{\text{real}})^{y_{\text{end}}} \end{pmatrix} \quad (3.12)$$

The real interest rate i_{real} is defined by the ratio of the interest rate i_{interest} to the $i_{\text{inflation}}$ with the following equation:

$$i_{\text{real}} = \frac{(1 + i_{\text{interest}})}{(1 + i_{\text{inflation}})} - 1 \quad (3.13)$$

The total return $R_{\text{total}}^{\text{NPV}}$ is the sum of all costs and revenues defined by the addition of the sum of the all investment cost $C_{\text{Invest,total}}^{\text{NPV}}$, the BESS system costs $C_{\text{System}}^{\text{NPV}}$ and the sum of all cash flows $C_{\text{cash flow,total}}^{\text{NPV}}$:

$$R_{\text{total}}^{\text{NPV}} = C_{\text{cash flow,total}}^{\text{NPV}} - C_{\text{Invest,total}}^{\text{NPV}} - C_{\text{System}}^{\text{NPV}} \quad (3.14)$$

The total investment cost $C_{\text{Invest,total}}^{\text{NPV}}$ represent the BESS investment cost $C_{\text{Invest}}^{\text{NPV}}$ subtracted by the BESS investment subsidy $C_{\text{Subsidy}}^{\text{NPV}}$ in the PV-HESS application. In order to consider the fact that costs are defined negatively here, the resulting sum is inverted.

$$C_{\text{Invest,total}}^{\text{NPV}} = C_{\text{Invest}}^{\text{NPV}} - C_{\text{Subsidy}}^{\text{NPV}} = C_{\text{Invest}}^{\text{NPV}} \cdot (1 - r_{\text{Subsidy}}) \quad (3.15)$$

The $C_{\text{Subsidy}}^{\text{NPV}}$ are obtained by multiplying the BESS investment subsidy rate r_{Subsidy} with the BESS investment cost $C_{\text{Invest}}^{\text{NPV}}$.

The BESS investment cost $C_{\text{Invest}}^{\text{NPV}}$ is the sum of the investment costs of the battery $C_{\text{Invest}}^{\text{Battery}}$ and the inverter $C_{\text{Invest}}^{\text{Inverter}}$ together with the installation costs $C_{\text{Installation}}^{\text{BESS}}$:

$$C_{\text{Invest}}^{\text{NPV}} = C_{\text{Invest}}^{\text{Battery}} + C_{\text{Invest}}^{\text{Inverter}} + C_{\text{Installation}}^{\text{BESS}} \quad (3.16)$$

The BESS investment costs $C_{\text{Invest}}^{\text{NPV}}$ are realized at the beginning of the first year of the depreciation period. Hence, they represent already the NPV and no adaption with the discount factor \overrightarrow{DF} is necessary. The investment costs of the Battery $C_{\text{Invest}}^{\text{Battery}}$ is composed of a fix battery cost $C_{\text{fix}}^{\text{Battery}}$ and a variable cost $c_{\text{var}}^{\text{Battery}}$ which is multiplied by the battery nominal energy $E_{\text{nom}}^{\text{Battery}}$:

$$C_{\text{Invest}}^{\text{Battery}} = C_{\text{fix}}^{\text{Battery}} + c_{\text{var}}^{\text{Battery}} \cdot E_{\text{nom}}^{\text{Battery}} \quad (3.17)$$

The fixed battery costs $C_{\text{fix}}^{\text{Battery}}$ represent the price of the BESS peripheries and housing. The variable battery costs $c_{\text{var}}^{\text{Battery}}$ stand for the energy-specific price of the battery. The inverter investment costs $C_{\text{Invest}}^{\text{Inverter}}$ are structured similarly by the sum of fix inverter costs $C_{\text{fix}}^{\text{Inverter}}$ and variable costs $c_{\text{var}}^{\text{Inverter}}$ which are multiplied by the nominal power of the inverter $P_{\text{nom}}^{\text{Inverter}}$:

$$C_{\text{Invest}}^{\text{Inverter}} = C_{\text{fix}}^{\text{Inverter}} + c_{\text{var}}^{\text{Inverter}} \cdot P_{\text{nom}}^{\text{Inverter}} \quad (3.18)$$

The yearly BESS system costs $\overrightarrow{C}_{\text{System,y}}^{\text{BESS}}$ represent the sum of the yearly BESS maintenance costs $\overrightarrow{C}_{\text{Maintenance,y}}^{\text{BESS}}$ and the possible battery replacement costs $\overrightarrow{C}_{\text{Replacement,y}}^{\text{Battery}}$ for every year y of the depreciation period. The NPV of the BESS system costs $C_{\text{System}}^{\text{NPV}}$ is obtained by the scalar multiplication of the transposed vector of $\overrightarrow{C}_{\text{System,y}}^{\text{BESS}}$ with the discount factor \overrightarrow{DF} :

$$C_{\text{System}}^{\text{NPV}} = (\overrightarrow{C}_{\text{System,y}}^{\text{BESS}})^T \overrightarrow{DF} = (\overrightarrow{C}_{\text{Maintenance,y}}^{\text{BESS}} + \overrightarrow{C}_{\text{Replacement,y}}^{\text{Battery}})^T \overrightarrow{DF} \quad (3.19)$$

The vector of the yearly maintenance costs $\overrightarrow{C}_{\text{Maintenance,y}}$ is obtained by multiplying the BESS investment costs $C_{\text{Invest}}^{\text{NPV}}$ with a fixed maintenance cost rate $r_{\text{Maintenance}}$ and applying a scalar multiplication

with the vector $\overrightarrow{Y_{DP}}$, reflecting all years (1 until y_{end}) of the depreciation period.

$$\overrightarrow{C_{Maintenance,y}^{BESS}} = C_{Invest}^{NPV} \cdot r_{Maintenance} \cdot \overrightarrow{Y_{DP}} \quad (3.20)$$

In case that the battery end of life (EOL) criteria is reached before the end of the depreciation period, a replacement of the battery is necessary. Then, the costs of one battery replacement $C_{Replacement}^{Battery}(y)$ is considered with the investment cost of the battery from the start of the depreciation $C_{Invest}^{Battery}$. In order to consider the correct NPV of every replacement, the vector $\overrightarrow{Y_{Replacement}^{Battery}}$ is applied reflecting every year of the depreciation period with a positive entry in the years in which a replacement was performed.

$$\overrightarrow{C_{Replacement,y}^{Battery}} = C_{Invest}^{Battery} \cdot \overrightarrow{Y_{Replacement}^{Battery}} \quad (3.21)$$

The yearly total cash flow vector $\overrightarrow{C_{cash\ flow,total,y}}$ results by subtracting the particular yearly BESS costs $\overrightarrow{C_{Costs,y}^{BESS}}$ from the yearly revenues $\overrightarrow{C_{Revenues,y}^{BESS}}$, both reflecting all years of the depreciation period. The NPV of the total cash flow $C_{cash\ flow,total}^{NPV}$ is obtained by the scalar multiplication of the transposed vector of the $\overrightarrow{C_{cash\ flow,total,y}}$ with the discount factor \overrightarrow{DF} :

$$C_{cash\ flow,total}^{NPV} = (\overrightarrow{C_{cash\ flow,total,y}})^T \overrightarrow{DF} = (\overrightarrow{C_{Revenues,y}^{BESS}} - \overrightarrow{C_{Costs,y}^{BESS}})^T \overrightarrow{DF} \quad (3.22)$$

3.2.2.2 Economic evaluation parameters

Beside the pure economic output parameters for the BESS profit and loss account as presented before, different parameters are introduced in the following which allows for the comparison of the economic results between different applications and energy storage technologies.

The LCOES represent the ratio of the total BESS investment costs $C_{Invest,total}^{NPV}$ to the total energy discharged $E_{discharge,total}^{BESS}$ out of the BESS over the depreciation period:

$$LCOES = \frac{C_{Invest,total}^{NPV}}{E_{discharge,total}^{BESS}} \quad (3.23)$$

The total cash flow $C_{cash\ flow,total}^{NPV}$ related to the total energy discharged $E_{discharge,total}^{BESS}$ is expressed with the levelized earnings of energy stored (LEOES):

$$LEOES = \frac{C_{cash\ flow,total}^{NPV}}{E_{discharge,total}^{BESS}} \quad (3.24)$$

The total economic result R_{total}^{NPV} related to the total energy discharged $E_{discharge,total}^{BESS}$ is represented by

the levelized profit of energy stored (LPOES):

$$LPOES = \frac{R_{total}^{NPV}}{E_{discharge,total}^{BESS}} = LEOES - LCOES \quad (3.25)$$

If no further system costs are assumed, the LPOES can be obtained by subtracting LCOES from the LEOES as well.

In contrast to the LPOES, the profit per energy installed (PPEI) are calculated by relating the total economic result R_{total}^{NPV} to the installed nominal battery energy $E_{nom.}^{Battery}$:

$$PPEI = \frac{R_{total}^{NPV}}{E_{nom.}^{Battery}} \quad (3.26)$$

By dividing this quotient by the number of the years of the evaluated depreciation period, the yearly average of the PPEI is obtained.

The internal rate of return (IRR) allows a direct comparison with interest rates of different investments and is calculated with an interpolation method implemented with MATLAB's internal function 'irr'. This function considers the initial investment $C_{Invest,total}$ (the possible subsidy already included) and calculates the average rate of return over the whole depreciation period with the yearly total cash flow results $\vec{C}_{cash\ flow,total,y}$ together with the BESS system costs $\vec{C}_{System,y}^{BESS}$ without considering the discount factor \vec{DF} :

$$IRR = f_{IRR}(C_{Invest,total}, [\vec{C}_{cash\ flow,total,y} + \vec{C}_{System,y}^{BESS}]) \quad (3.27)$$

However, the IRR expresses an average rate of return during the depreciation period but does not reflect the limited BESS lifetime represented by the depreciation period. In contrast, the PI is able to represent the total economic result after the complete depreciation period and can be used to compare the investment result of a BESS with further investment object. The PI is defined by the ratio of the total economic result R_{total}^{NPV} to the BESS investment costs C_{Invest}^{NPV} without considering the BESS subsidy for example in the PV-HESS application [99]:

$$PI = \frac{R_{total}^{NPV}}{C_{Invest}^{NPV}} \quad (3.28)$$

3.3 Computational performance evaluation

Beside the technical accuracy of the BESS models, the computation time is limiting the simulations with the SimSES framework. In order to perform simulations with satisfactory accuracy within adequate computation time, the influence factors regarding the calculation time of the simulations have to be assessed. Thereby, the key influence factor of SimSES computation time is the general sample time

together with the simulation length/steps, since all sub-models are called in this frequency. However, the calling frequency of the battery stress detection and the subsequent calculation of the battery aging can be adjusted separately with the step size of the aging calculations. The step size of the aging calculations represent the frequency how often the stress detection and the subsequent aging calculations are performed in relation to the general sample time. Furthermore, the execution time of the stress detection and battery aging methods can account for more than a half of the total computation time of one SimSES simulation. Hence, in the following, the influence of the sample time and the calling frequency of the stress detection and aging models are evaluated. Besides the computation time, the mutation of the capacity loss is assessed additionally because all mentioned influence factors can influence the result of the aging model significantly.

In addition, two different calling methods of the aging models can be chosen in SimSES: The 'single value aging model calling method' calls the aging model in each step with the current values of the stress detection. The 'average value aging model calling method' calls the aging model with the average values of the stress detection. For example, in case that the step size of the aging calculations is set to 10, the aging model is called every 10 steps with the average values of the last 10 steps. In contrast, applying the single value aging calling method, the aging model is called in every of the 10 steps leading to more precision of the aging calculation. However, the computational effort is higher, because the aging model is called more frequently.

For this performance evaluation of SimSES, the PV-HESS baseline scenario is used with the same parameter set and the same input profiles as described in **Section 6.2.1**. Thereby, the battery aging model of the investigated LFP/C cell is applied (see **Chapter 5**). However, all simulations are performed with a simulation length of 1 year for a household consumption of 4400 kWh per year and with the following sizing of the technical components: PV peak power = 4.4 kW, inverter rated power = 4.4 kW, battery nominal energy = 4.4 kWh.

3.3.1 Calculation time

Although the input profiles of the baseline scenario are available in a sample time of 1 s, the minimum simulation sample time is set to 60 s: The input profiles show only few dynamics below the sample time of 60 s and the computational effort would be unnecessarily too high using smaller sample times. Hence, the input profiles are down-sampled to the respective simulation sample time.

Figure 3.3 shows the influence of the sample time on the calculation time in relation to the baseline case with a sample time of 60 s. Performing the simulation of the baseline case with a *Dell Precision T7610* system based on a *Intel Xeon* central processing unit (CPU) 'E5-2650 v2' with 2.60 GHz, the computational time of every step results on average 8.095 ms. Thereby, **Figure 3.3** reveals that the calculation time decreases disproportionately high when increasing the sample time until 600 s.

When increasing the sample time, the battery stress characterization and aging model are called consequently with lower frequencies. However, the step size of the battery stress characterization and the calling methods of the aging models can be adjusted separately in SimSES as explained in **Section 3.1.5.1**.

Figure 3.4 compares the influence of the general sample time and the influence of the step size of the aging calculations on the total calculation time. In **Figure 3.4a** the results are shown for simulations with a sample time of 60 s and in **Figure 3.4b** with a sample time of 300 s. For both sample times,

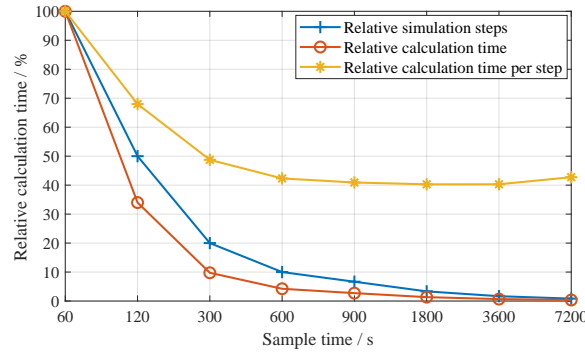


Figure 3.3: Influence of the sample time between 60 to 7200 s on the calculation time: Calculation time in relation to the simulation with a sample time of 60 s (red curve). Number of the relative simulation steps for each sample time in relation to the sample time of 60 s (blue curve). Resulting calculation time per step (yellow curve).

the calculation times decrease when increasing the step sizes for both, the single and the average aging model calling method, however, the decrease of the calculation time gets weaker with higher step sizes. The decrease of the calculation time is stronger for the average values method, because the aging models are called less often than with the single value methods with step sizes > 1 . The average values method shows even better results in comparison to the single values method when simulating with a sample time of 300 s as shown in **Figure 3.4b**. For comparison, the yellow curve in both figures represents the calculation time for the case that the general sample time is increased and the single or the average value method is called with the same general sample time. Though, only some of the simulation results can be drawn because the data points match only some of the frequencies of calling the aging models: In **Figure 3.4a** the sizes 1, 2, 5 and 10 represent the samples times of 60 s, 120 s, 300 s and 600 s and in **Figure 3.4b** the sizes 1, 2, 3, 6 and 12 represent the samples times of 300 s, 600 s, 900 s and 3600 s as shown in **Figure 3.3**. By increasing the general sample time/step size, the calculation time decreases stronger than for the case that only the step size of calling the aging models is increased, because all further models and calculations are called with a lower frequency.

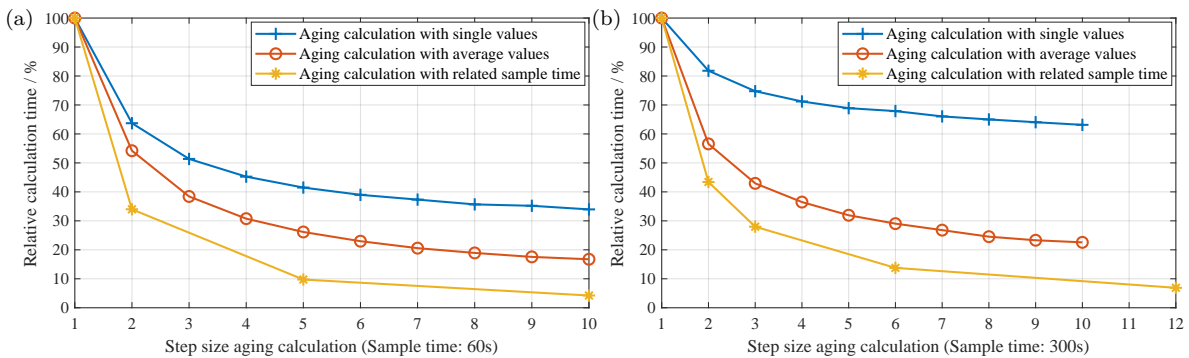


Figure 3.4: Influence of sample time and step size of aging calculation with single and average values on calculation time. Figure 3.4a: 60 s sample time. Figure 3.4b: 300 s sample time.

3.3.2 Aging results

The mutation of the sample time, the step size of the aging calculations, and the calling methods of the aging models lead to deviations of the aging model results, which are evaluated in the following. Thereby, the deviation of the results of the calendar and cycle aging are separately shown together with the combination of both, the total aging. By increasing the sample time, the relative calendar aging increases only with relative high sample times of > 1800 s, however, the cycle aging increases almost linearly up to 30% until a sample time of 3600 s and remains constant afterward as shown in **Figure 3.5**.

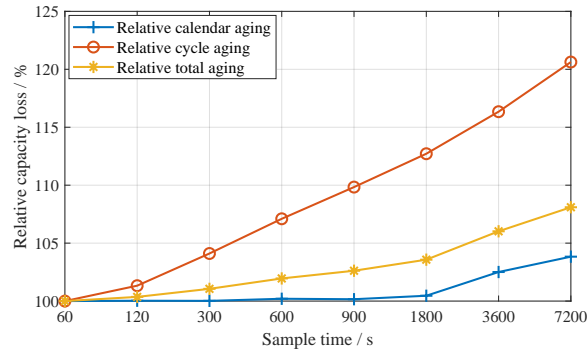


Figure 3.5: Influence of the sample time between 60 to 7200 s on the capacity loss: Deviation of the capacity loss due to calendar aging (blue curve), cycle aging (red curve) and the total aging (yellow curve) in relation to the simulation with a sample time of 60 s.

The reason for this increase of cycle aging is the fact, that the battery power and SOC profiles get smoother with bigger sample times. Then, less small cycles but longer and deeper cycles occur leading to a greater influence of cycle aging with the applied aging model. However, the total aging, which is the sum of the absolute values of calendar and cycle aging, increases only up to 10%, because the absolute calendar aging is stronger than the cycle aging. **Figure 3.6** compares the impact on the aging estimation between the sole increase of the sample time and increase of the step size of calling the aging models. Again, only some of the simulation results can be drawn because the data points match only some of the frequencies of calling the aging models: In **Figure 3.6a** the sizes 1, 2, 5 and 10 represent the samples times of 60 s, 120 s, 300 s and 600 s and in **Figure 3.6b** the sizes 1, 2, 3, 6 and 12 represent the samples times of 300 s, 600 s, 900 s and 3600 s as shown in **Figure 3.3**. It is shown,

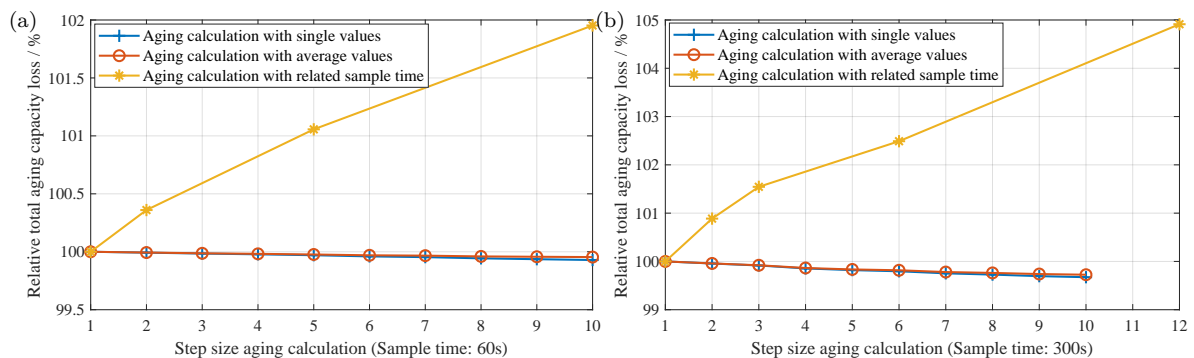


Figure 3.6: Influence of sample time and step size of aging calculation with single and average values on calculation time. Figure 3.6a: 60 s sample time. Figure 3.6b: 300 s sample time.

that the impact on the aging estimation due to the increase of the sample time is stronger than the increase of the step size of calling the aging models.

In **Figure 3.7** and in **Figure 3.8** the influence of the step size on the capacity loss is shown for the single and average value method for calling the aging models more in detail. In both figures, the left figures show the results with a general sample time of 60s and the right figures the results with a general sample time of 300s. In all figures, the calendar aging is almost not influenced by the step size or the general sample time. In contrast, the cycle aging values increase slightly over the step size for the sample time of 60s and decrease marginally over the step size for the sample time of 300s. However, the total aging changes for both calling methods of the aging models for both sample times less than 0.5%.

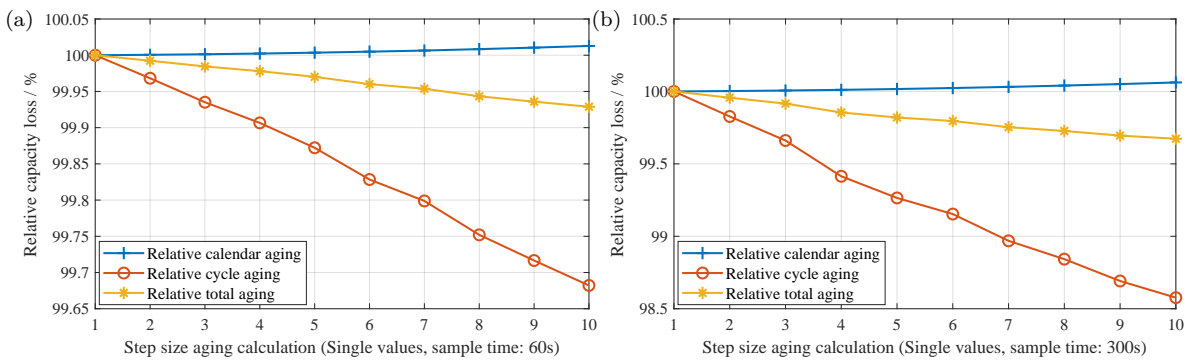


Figure 3.7: Influence of aging calculation step size with single values on the deviation of the capacity loss with different sample times. Figure 3.7a: 60 s sample time. Figure 3.7b: 300 s sample time.

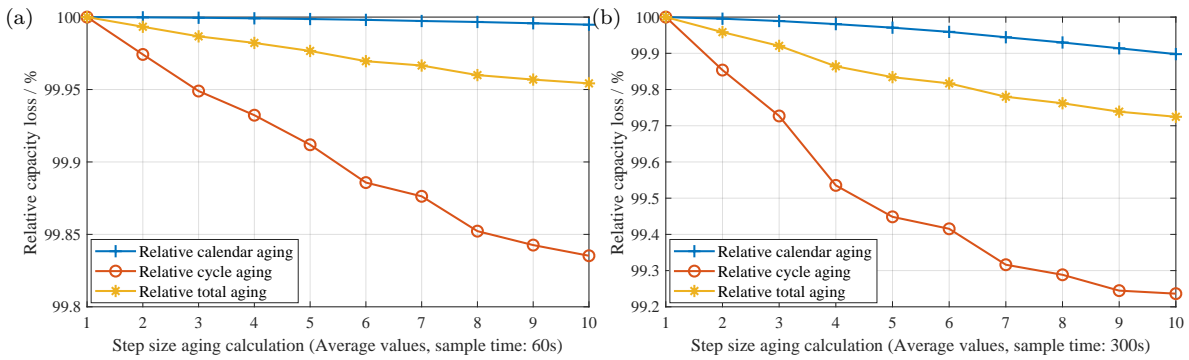


Figure 3.8: Influence of aging calculation step size with average values on the capacity loss with different sample times. Figure 3.8a: 60 s sample time. Figure 3.8b: 300 s sample time.

Conclusion

The evaluations showed, that the calculation time can be reduced significantly and with little additional errors of the estimated battery capacity degradation by increasing the sample time and applying the average values method for calling the aging models. However, the calculation time decreases only by slight portions with sample times > 300s but the error on the estimation of the capacity loss continues increasing linearly. When considering the general sample time of 300s the calculation time can be reduced additionally by about 70% when using the average value calling method for the aging

models with a step size of 10 with very weak impact on the resulting error of the estimated capacity loss. In comparison to the baseline case with a sample time of 60 s, the computational time of every step on average would decrease from about 8.095 ms to 0.418 ms (decrease by about 95 %) (simulations performed with a *Dell Precision T7610* system based on a *Intel Xeon CPU 'E5-2650 v2'* with 2.60 GHz). Hence, for the simulation of the PV-HESS application with the baseline scenario, a general sample time of 300 s with the average value calling method for the aging models with a step size of 10 is chosen.

Further results of the performance evaluation are, that the logging of different operational numbers over the whole simulation does not influence the calculation time significantly. In consequence, the duration and the resulting number of simulation steps do not influence the calculation time per step while the simulation data does not exceed the available working memory for the MATLAB execution.

4 Experimental studies on LiFePO₄-graphite cells

In order to optimize the design and operation of BESS, detailed battery aging models are required. Although there are aging models available from literature (see **Section 2.4**) for LFP/C cells, a dedicated aging study is carried out. The goal of the aging study is to develop an aging model which is able to estimate the development of the relevant parameters such as the capacity, internal resistance, and performance when simulating the operation of different stationary BESS applications. The aging model should take into account all aging effects due to calendar and cycle aging. Even though the aging model is going to be parametrized for one specific cell, the model structure could be adapted to further LFP/C cells.

First, the investigated cell is presented. Thereafter, the used measurement equipment and the single measurement procedures are shown. Then, the testing procedures applied in both aging studies are described and followed by the description of methods for the aging data analysis. A detailed characterization of the investigated cell is presented, including a statistical analysis of 1100 cells and the explanation of selection procedure of the cells needed for the following aging studies. At the end of this chapter, first, the design of the experiments of both the calendar aging study and the cycle aging study is explained and followed by the presentation of the aging results.

4.1 Investigated cell

In this aging study, the commercially available 3 Ah 26650 LFP/C cell from *Sony/Murata* named *US26650FTC1* is investigated. **Table 4.1** shows the most important cell parameter values from the manufacturer's datasheet. In the cell's datasheet, the rated capacity is defined with 2.85 Ah. However, in a preceding characterization of over 1100 cells out of two batches the mean discharge capacity resulted in 3.019 Ah [81]. In this preceding investigation, the capacity measurements were performed

Table 4.1: Datasheet values of the investigated LiFePO₄/graphite cell Sony US26650FTC1.

| Parameter | Value | Notes |
|-----------------------------------|-----------------|---|
| Nominal capacity | 2.850 Ah | Datasheet capacity |
| | 3.000 Ah | Measured cell capacity in this study |
| Nominal voltage | 3.2 V | |
| Max. charge voltage | 3.65 V | Datasheet definition |
| | 3.6 V | Voltage applied in this study |
| Min. discharge voltage | 2.00 V | |
| Ohmic impedance (1 kHz), AC | 18 mΩ | |
| Max. continuous charge current | 2.85 A | Datasheet definition |
| | 3.00 A | Current applied in this study |
| Max. continuous discharge current | 20 A | |
| Temperature range charge | 0 °C to 45 °C | Datasheet: Max. surface temperature 60 °C |
| Temperature range discharge | -20 °C to 60 °C | Datasheet: Max. surface temperature 80 °C |
| Mass | 84.5 g | |

with a full charge with a constant current of 3.0 A followed by constant-voltage (CV)-phase (CV with 3.6 V until $I_{\text{ch,CV}} < C/30 = 100 \text{ mA}$) and followed by a full discharge with a constant current of 3.0 A followed by a CV-phase (CV with 2.0 V until $I_{\text{disch,CV}} < C/20 = 150 \text{ mA}$). Consequently, 3.0 A is used and thereby 1 C is defined as the maximum continuous charge current in the measurements of this aging study. Other aging studies applied C-rates lower than 1 C in the CM [50], however, 1 C is used in order to minimize the duration of the check-up (CU). Furthermore, by discharging with a lower current with exemplary 0.2 C only about 1.4 % of the nominal capacity can be extracted additionally in the constant-current (CC)-phase. By combining a 1 C CC discharge with a CV-phase (CV with 2.0 V until $I_{\text{disch,CV}} < C/20 = 150 \text{ mA}$), the effect of the absolute current on the extractable capacity is remarkably reduced.

4.1.1 Influence of the anode overhang

Before the initial CM, all cells were stored at 50 % SOC at about 8 °C to minimize the inevitable calendar aging. Hence, it is assumed that all cells should have almost the same usable capacity at the beginning of the aging study without increased or decreased capacity differences due to the possible effect of the anode overhang areas. In order to assess the possible influence of the anode overhang area, one sample cell was opened at begin of life (BOL) and measured: The total coated area of the jelly roll's anode is $150.2 \times 5.7 \text{ cm}^2$ top side (inner side of the jelly roll) and $142.1 \times 5.7 \text{ cm}^2$ bottom side (outer side of the jelly roll). The overhang areas are separately shown in **Table 4.2** for the different positions on the anode and represent in sum 88.46 cm^2 . Hence, the anode overhang areas correspond together to 6.2 % of the total coated area of the anode.

Wilhelm et al. [54] measured about 10 % anode overhang for a different cell and observed a maximal decrease of the capacity difference of 3.6 % of the nominal capacity between cells stored for months at a low and high SOC by recovering the capacity of the anode overhang areas. By transferring these results to the here investigated cell, about 2.2 % of the nominal capacity would be the maximal recoverable capacity between cells stored a low and high SOC. However, only by storing the cells at a low SOC for several days or performing several full cycles before every CM (leading to an additional cycle aging effect) could recover most of the capacity of the anode overhang areas. Though, this is in conflict with the concept of a calendar aging study where the cyclization should be kept to a minimum.

In this aging study, the capacity measurements are performed with two consecutive full cycles in order

Table 4.2: Anode overhang areas: Position and areas. (Top side: Inner side of the jelly roll. Bottom side: Outer side of the jelly roll.)

| Anode position | Area: Width × height |
|--|---------------------------------|
| Total coated area top side | $150.2 \times 5.7 \text{ cm}^2$ |
| Total coated area bottom side | $142.1 \times 5.7 \text{ cm}^2$ |
| Anode overhang areas | |
| Start (outside jelly roll) top side | $1.3 \times 5.7 \text{ cm}^2$ |
| Start (outside jelly roll) bottom side | $1.9 \times 5.7 \text{ cm}^2$ |
| Middle top side (tabs) | $2.0 \times 5.7 \text{ cm}^2$ |
| Middle bottom side (tabs) | $2.0 \times 5.7 \text{ cm}^2$ |
| End (inside jelly roll) top side | $4.6 \times 5.7 \text{ cm}^2$ |
| End (inside jelly roll) bottom side | $1.2 \times 5.7 \text{ cm}^2$ |
| Edges top side | $143.6 \times 0.1 \text{ cm}^2$ |
| Edges bottom side | $143.6 \times 0.1 \text{ cm}^2$ |

to minimize the cycle aging and the influence of the preceding storage SOC due to the possible recovery effect of the anode overhang area. Hereby, for all test points (TP) the second cycle capacity does not exceed 0.4% of the first cycle capacity during the CM of the whole aging study. Only for the test points with a storage SOC of 0%, the second full cycle shows less capacity than the first cycle during the CM of the whole aging study. Furthermore, after the initial CM, only 2 out of the 17 TPs with different storage temperatures and SOC of this calendar aging study showed a slight capacity increase during the first CM. By using the average capacity of two consecutive full cycles during the CM the trend of the capacity recovery effect is considered at least in the results of this calendar aging study. In order to evaluate the influence of the anode overhang area more in detail during the whole aging study, Lewerenz et al. [100] suggest the capacity difference analysis (CDA) to compare the extractable capacities with different C-rates.

However, in this aging study, the periodic CU is performed with only one C-rate and applied a lower C-rate only in four measurements distributed over the whole aging study, which are evaluated with the differential voltage analysis (DVA) in **Section 4.6.1.2**. In conclusion, the anode overhang areas influence the measurable capacity dependent on the preceding storage condition in addition to the capacity loss due to calendar aging. However, this capacity effect of the anode overhang areas is considered as a theoretical capacity influence factor, since the impact of this effect was hard to determine accurately during this calendar aging study. In addition, the absolute influence is estimated to be quite small in comparison to the influence of the temperature and SOC on the resulting calendar aging.

4.1.2 Cell-to-cell parameter variation

Due to the fact, that 1100 units (Batch 1: 600 units. Batch 2: 500 units) of the investigated cell were available, a statistical analysis was derived analyzing the cell-to-cell variation and correlations of selected parameters [81]. The results of the statistical analysis are then used to select the cells for the aging studies, with the selection procedure described in the following subsection. However, in the following aging study only the cells' discharge capacity $C_{\text{DCH,CCCV}}$ and the resistance $R_{\text{DC},10\text{s}}$ are of interest and are illustrated here. The following **Table 4.3** shows the measured cell-to-cell parameter variation of all 1100 units and separated into the two batches (B1, B2) by giving the mean value μ_x , the standard deviation σ_x and the relation σ_x/μ_x for the cells' discharge capacity $C_{\text{DCH,CCCV}}$ and the resistance $R_{\text{DC},10\text{s}}$. Further parameters are shown in [81]. In addition, **Figure 4.1** shows the histograms of both parameters for batch 1 and 2.

Table 4.3: Measured cell-to-cell parameter variation of 1100 units out of two batches of the investigated cell.

| Parameter x | Batch | μ_x | σ_x | σ_x/μ_x |
|----------------------------|-------|-------------------|------------|------------------|
| $C_{\text{DCH,CCCV}}$ | B1 | 3.020 Ah | 0.007 Ah | 0.232 % |
| | B2 | 3.018 Ah | 0.010 Ah | 0.332 % |
| | B1+B2 | 3.019 Ah | 0.009 Ah | 0.284 % |
| $R_{\text{DC},10\text{s}}$ | B1 | 28.485 m Ω | 0.407 Ah | 1.430 % |
| | B2 | 28.744 m Ω | 0.353 Ah | 1.227 % |
| | B1+B2 | 28.603 m Ω | 0.404 Ah | 1.414 % |

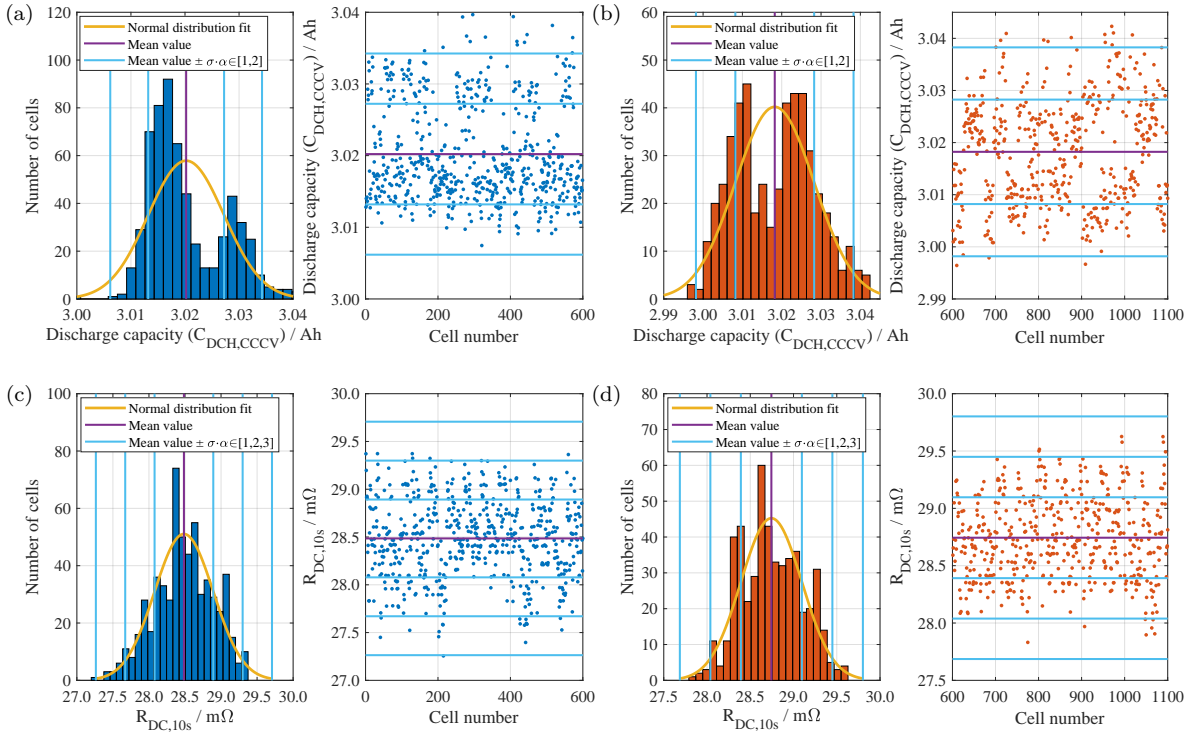


Figure 4.1: Variation of the cell parameters of the 1100 investigated cells. The individual plots on the left side show the parameter histograms by indicating the mean value and the values for the $\pm\sigma \cdot \alpha \in [1, 2]$ as well as the curve representing an assumed normal distribution. The individual plots on the right side show the same parameter over the respective cell number again with the markings for the mean value and the further σ factors.

Figure 4.1a shows the discharge capacity $C_{DCH,CCCV}$ of the cells 1-600 (batch 1) and Figure 4.1b of the cells 601-1100 (batch 2). Figure 4.1c shows the $R_{DC,10s}$ of the cells 1-600 and Figure 4.1d of the cells 601-1100.

4.1.3 Cell selection procedure

Over 125 cells are required for the various TPs of the aging test studies, which are later presented in **Section 4.5**. In order to be able to compare the aging effects of the individual cells and TPs with three cells each, the parameters of the test cells should be relatively homogeneous. It could be expected that the parameters of the cells deviate from each over the duration of the aging studies. Therefore, the parameter variation should be minimized by using a homogeneous selection of the test cells.

Due to the fact, that 1100 cells from two batches with 600 and 500 cells are available within the framework of the EEBatt project [15], the prerequisite can be met to make a certain selection from a larger group. The following criteria are feasible:

- As homogeneous as possible cell properties.
- As homogeneous as possible cell history.
- As homogeneous as possible parameters that influence aging: discharge capacity, internal resistance, efficiency, dynamic parameters.

A further important prerequisite in addition to the same cell type is the guarantee of the same measuring conditions (temperature, the temporal sequence of the measurements, etc.), test plans and

evaluation scripts in the characterization of the cells. In order to select from the 1100 available cells a total of 125 cells, a selection procedure was applied to obtain cells with preferably similar parameters to enhance the comparability between the cells: Before the required 125 individual cells are selected from the total number of 1100 cells, the selection should be limited to one batch. The individual batches do not differ in the cell type, but in the production date and thus in the history. In order to ensure better homogeneity according to the above selection criteria, a batch has to be selected. The following criteria can be used:

- The number of cells from the same batch.
- The relative deviation from the average of the individual parameters.

With the assumption of normally distributed cell parameters, it is more likely to select an equal number of homogeneous cells for larger batches. However, with a larger number of cells to be measured, there is at the same time a certain probability that there are deviations from measurement conditions and thus a falsification of the scattering is likely. According to the first criterion of the largest possible number of cells in a batch, only the batch 1 of 600 cells would be selected as final. For the selection, the individual relative deviations from the respective mean value (standard deviation/mean value) of the parameters measured in the CU were then considered as the decisive criterion. In this case, the batch of 600 cells exhibited a lower relative variation than the cells from the batch of 500 for over 39 of 68 parameters and also on average over all parameters. For example, the variation of the two batches in the discharge capacity and resistance is shown in **Figure 4.1**, with the less variation in the batch of 600 cells in blue on the left. Thus, the selection of the cells for the batch of 600 was chosen for further cell selection.

For the purpose to select as homogeneous cells as possible from a batch, the cells, which are as close as possible to the mean value, would be selected. However, many of the 68 parameters represent very diverse properties of the cells and are partly independent of each other. Hence, the selection can not only be performed via one parameter. Thus, a selection method is applied here, which has the goal of selecting cells with homogeneous properties by evaluating various of the parameters measured in the CU. The methods should select the cells from the batch of 600 cells, which are as close as possible to the mean value over all parameters to be selected. It is assumed here, that the measured values of a parameter are normally distributed if the characteristics of the cells are identical and thus the variation reflects ideally only the measurement noise. Consequently, the measured values outside the $1 \cdot \sigma$ range of the distribution would probably not be measurement noise [101; 102], but measurement errors or differences in the characteristics of the cell. These cells must then be assessed less preferentially for the selection.

As already described, over 68 parameters of each cell were determined with the weight, and the electrical measurement in the time (measurements with the cell test system (CTS)) and frequency (electrochemical impedance spectroscopy (EIS) measurements) domain. These 68 parameters are distributed as follows: weight 1, CTS 51, EIS 16. In the following, it is explained which parameters were used for the final selection procedure of the 68 parameters. Some of these 68 parameters are partly redundant, such as the capacities of the individual test steps, certain resistances, and temperature variables. Further parameters are varied through the measuring conditions. For example, despite the use of a climatization chamber, it was not possible to measure all cells exactly at an ambient temperature of 25 °C. Furthermore, there were certain influences due to the variation of the contact resistance of the terminal boards, in which the cells were clamped and contacted. In the case of the temperature values,

erroneous measured values appeared and some cells lost contact with the temperature sensor during the measurement. Moreover, certain parameters showed significantly greater variation than others due to possible different measurement conditions or measurement errors. Other parameters revealed a strong correlation with each other because they are directly dependent on each other. Certain parameters are similar to each other because they were used only to control test plan parameters, e.g. specific times or the charge throughput. Finally, a selection of a total of 28 parameters with the following allocation was made: The cell weight, 24 CTS parameters, and 3 EIS parameters. The 24 CTS parameters comprise of the average cell capacities and energy contents of the single CC and CV-phases, the voltages at the end of the relaxation phases, different resistance values, and temperature values measured at different points in time of the CM. The 3 EIS parameters comprise of the inner cell resistance R_i , the frequency $f(R_i)$ where R_i is measured and the cell impedance $Z_{AC,1000Hz}$ measured at 1000 Hz.

The following selection procedure was applied to the final selection of the required 125 cells from the batch of 600 cells. Due to the fact that the various cell parameters do not correlate perfectly with each other [81], more than one parameter was necessary to consider in the selection procedure. Thus, an algorithm was applied which is able to select a defined count of cells by step-by-step choosing only those cells whose parameters are the closest to the mean values μ of every single parameter of the whole cell batch. Starting from the mean value μ of the 28 variables to be considered, the tolerated range in the positive and negative directions is incremented by the factor α (selection multiplier) for σ of the standard distribution around the mean value $\mu + \sigma \cdot \alpha$. A cell is selected, when the cell parameter values are close the mean value over all parameters to be considered in the tolerated range. This range is incremented step by step over all parameters until the minimum number of 125 cells has been reached for selection. For the batch of 600 cells, a selection multiplier $\alpha = 1.3156$ was determined to select exactly 125 cells. When assuming a normal distribution of all parameters, these cells would lie in an interval of 81.17% on average.

With this selection procedure, 125 cells were selected for the static and dynamic aging studies. The selected cells' standard deviation σ of the discharge capacity C_{disch} decreased from $\sigma = 0.007$ Ah with a mean value of $\mu = 3.020$ Ah (batch of 600 cells) to $\sigma = 0.005$ Ah ($\mu = 3.018$ Ah). The standard deviation of the resistance $R_{DC,10s}$ decreased from $\sigma = 0.407$ m Ω ($\mu = 28.485$ m Ω) (batch of 600 cells) to $\sigma = 0.337$ m Ω ($\mu = 28.499$ m Ω).

4.2 Measurement equipment

All relevant measurements and the aging test of this study were performed with two *BaSyTec* CTS, each with 32 channels, and an *Espec* LU-123 climate chamber with $T = 25$ °C for the CM and $T = 40$ °C for the cycle aging study. An additional *BaSyTec* XCTS was used for currents bigger than 5 A in the cycle aging study. The surface temperature of each cell was monitored using NTC thermistors. To perform EIS measurements a *BioLogic* VMP3 potentiostat with 16 channels and a climate chamber at $T = 25$ °C was used.

4.3 Measurement procedures

Two different measurement procedures were applied: Standard CU and extended CU. The standard CU consists of a CM and is followed by an EIS measurement. The extended CU is principally the

same as the standard CU, but between the CM and EIS, a low rate charge and discharge measurement is performed. Both procedures involve the following CM test plan at 25 °C:

1. Initial discharge: CCCV protocol to 2.0 V using a CC $I_{\text{disch,CC}} = 1 \text{ C} = 3 \text{ A}$ followed by a CV until $I_{\text{disch,CV}} < C/20 = 150 \text{ mA}$. 25 min relaxation pause.
2. Two consecutive full cycles:
 Full charge: CCCV protocol to 3.6 V using a CC $I_{\text{ch,CC}} = 1 \text{ C} = 3 \text{ A}$ followed by a CV until $I_{\text{ch,CV}} < C/30 = 100 \text{ mA}$. 25 min relaxation pause.
 Full discharge: CCCV protocol to 2.0 V using a CC $I_{\text{disch,CC}} = 1 \text{ C} = 3 \text{ A}$ followed by a CV until $I_{\text{disch,CV}} < C/20 = 150 \text{ mA}$. 25 min relaxation pause.
3. SOC adjust: Charging with $I_{\text{ch,CC}} = 1 \text{ C} = 3 \text{ A}$ until reaching 50% SOC by Ah-counting related to the mean value of the actual capacity measured in the two full discharge steps. 25 min relaxation pause.
4. Pulses: 1/3 C discharge pulse for 10 s, 10 min relaxation, 1/3 C charge pulse. 10 min relaxation. Afterward, the same pulse procedure is applied with 2/3 C and 1 C.

In this CM, the capacity is determined by performing two consecutive full cycles in order to minimize the influence of the possible recovery effect due to the anode overhang. Furthermore, both full cycles are performed with CV-phases in the charge and also in the discharge direction aiming to obtain all the available capacity. Thereby, the discharge CV-phases last on average 285 s for the first cycle and 272 s for the second cycle resulting in about 2.4% and 2.2% of the total capacity at BOL in the respective cycle. After the CM a 12 h relaxation pause is applied to await that the cell internal relaxation processes have declined sufficiently [103]. The following EIS measurement records the cell impedance within a logarithmically spaced frequency range $f \in [10000, 0.01] \text{ Hz}$ using an excitation current amplitude of $\hat{I} = 100 \text{ mA}$. The number of frequencies per decade (FPD) and number of measures per frequency (MPF) changes according to the consecutive sub-intervals: $f \in [10000, 1] \text{ Hz}$ (13 FPD, 10 MPF), $f \in]1, 0.1] \text{ Hz}$ (10 FPD, 5 MPF), $f \in]0.1, 0.01] \text{ Hz}$ (3 FPD, 2 MPF). The EIS measurement is performed at $SOC = 50\%$ and $T = 25 \text{ °C}$.

Within the extended CU an additional low rate charge and discharge measurement is performed at 25 °C with the following test plan:

1. Full charge: CCCV protocol to 3.6 V using a CC $I_{\text{ch,CC}} = 1 \text{ C} = 3 \text{ A}$ followed by a CV until $I_{\text{ch,CV}} < C/200 = 15 \text{ mA}$. No relaxation pause.
2. Slow discharge: CC to 2.0 V using a CC $I_{\text{disch,CC}} = 0.02 \text{ C} = 60 \text{ mA}$. No relaxation pause.
3. Slow charge: CC to 3.6 V using a CC $I_{\text{ch,CC}} = 0.02 \text{ C} = 60 \text{ mA}$. 25 min relaxation pause.
4. Full discharge: CCCV protocol to 2.0 V using a CC $I_{\text{disch,CC}} = 1 \text{ C} = 3 \text{ A}$ followed by a CV until $I_{\text{disch,CV}} < C/20 = 150 \text{ mA}$. 25 min relaxation pause.
5. SOC adjust: CC using a CC $I_{\text{ch,CC}} = 1 \text{ C} = 3 \text{ A}$ until reaching 50% SOC by Ah-counting related to the actual capacity measured in the full discharge step.

The low rate charge and discharge measurements are used later for the DVA.

4.4 Testing procedure

Figure 4.2 gives an overview of the testing procedure applied in the calendar and cycle aging study. For this aging study, 1100 fresh cells of two batches (batch 1: 600 cells, batch 2: 500 cells) were available and were delivered with a SOC of about 30%. All cells had been examined [81] with an initial reduced CU measurement. Then a selection procedure was applied for choosing the count of cells needed for both, the calendar and the cycle aging study (see **Section 4.1.3**). All cells were stored with a storage SOC of 50% at about 8°C in order to minimize the inevitable calendar aging. About 139 days after the CU of the 1100 fresh cells, an initial extended CU was performed with all selected cells at the beginning of the aging studies. Thereby, the capacity of the selected 125 cells decreased slightly by about 0.5-1.2% and 0.8% on average. After this and the following CUs, each cell was charged to the respective storage SOC as defined by the test matrix (see **Table 4.4**) by Ah-counting related to the actual capacity measured in the full discharge step of the prior CM. Thereafter all cells were stored at the temperature defined in the design of the experiments, which are later described in the calendar and cycle aging study. The cells of the cycle aging study are connected individually to CTS channels in order to perform the cycle test plans defined in **Table 4.6**. In order to measure the aging behavior as a function of time, the storage and cyclization of cells had been interrupted after certain time periods to derive periodic CU measurements. Every CU measurement influences the calendar aging behavior of the investigated cells: The different storage SOC and temperature during the CU measurement results in a different calendar aging. For the TPs with temperatures $> 25^\circ\text{C}$, the average aging speed is reduced and consequently increased for the TPs with temperatures $< 25^\circ\text{C}$ during the CU with a storage temperature of about 25°C . However, the CU measurements last in sum only about 0.9% of the total duration of this aging study. Hence, the different calendar aging during the CU measurements can be neglected for the TPs with a storage temperature of $\geq 25^\circ\text{C}$. For the TPs with the storage temperatures of 0°C and 10°C almost no aging is observable in comparison to the higher temperatures. However, by performing the CU measurements at 25°C , higher calendar aging can be expected due to the influence of the elevated test temperature. In order to determine the true calendar aging at the storage temperature of 0°C and 10°C , the later developed calendar

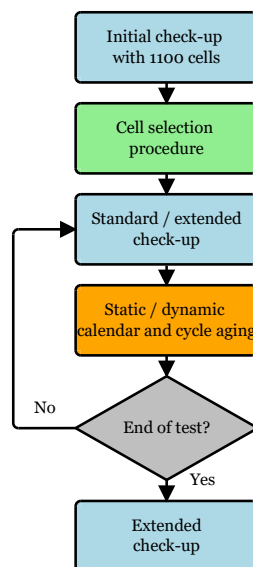


Figure 4.2: Testing procedure of the aging studies.

aging model could give an estimate for the influence of the CU measurements. Another strategy would have been the realization of these TPs with the storage temperature of 0 °C and 10 °C with longer time intervals between the CU measurement in order to minimize the influence of the elevated test temperature. As a result, these TPs are not considered in the parametrization of the calendar aging model in **Section 5.1**.

Additionally, about 3 FEC of each CM might lead to a small portion of cycle aging, however, in sum over the 35 CU measurements only 105 FEC are performed. By assuming a cycle stability of 10 000 cycles until the capacity underruns 80 % of the nominal capacity [7; 8], the pure cycle aging would contribute to only about 0.21 % capacity loss. Hence, the cycle aging influence of the CU on the calendar aging is neglected.

At the beginning of the study, the CU measurements were repeated every week for three periods, every 2 weeks for the next three periods and afterward every 4 weeks. In the last quarter of the aging study, the CU measurements were carried out 2 times at 8-week intervals and continued with 6-week intervals until the end of the study. In total 35 CU of which 4 are extended CU measurements were performed during the aging study. The aging study was stopped (end of test (EOT)) after 970 days duration (885 days under storage conditions) and completed with a final extended CU measurement.

4.5 Concept of the aging studies

4.5.1 Basic assumptions

The following enumeration summarizes the basic assumptions that are applied in the following calendar and cycle study:

1. Superposition principle: Since the cycle aging effects are not able to be measured separately from the calendar aging effects, it must be assumed that the aging effects of the calendar and cyclical aging can be superimposed without affecting each other. At least the trend of the calendar aging effects can be subtracted from the results of the cycle aging tests in order to estimate the sole impact of the cycle aging.
2. Independence of the stress order: It is assumed that the aging effects are independent of each other and that the same aging effect also occurs when the stress order is changed. The assumption of the independence of the order of aging will only be valid for certain time intervals of switching the stress conditions. Thus, the main TPs are designed with a constant load without examining this assumption more closely.
3. Arrhenius law: In order to accelerate the aging studies, the temperature is increased for the majority of the TPs in comparison to the temperatures which are expected in real BESS applications. By considering the Arrhenius law, the aging can then be estimated at lower temperatures as well. For the verification of the assumption, at least a few measuring points are set at lower temperatures.
4. Assumptions about the interpolation of the aging effects: The aging influence of the calendar and cyclic aging, as well as the influences of the temperature and the average SOC, should be determined as independently as possible from each other. However, the number of the measurable TPs is limited and not all theoretically possible combinations of the aging influence factors can

be tested. Thus, the possible TPs should be chosen in a manner, that the results of these TPs can be applied to estimate the effects on the combinations of the aging influence factors which are not measured.

4.5.2 Limitations and principal concept

Due to the fact that both, this calendar aging study and the supplementary cycle aging study, rely on the same measurement equipment, the CU measurement of the calendar aging study had to be integrated into the test procedure of the cycle aging study. In order to minimize the break times of the cyclization realized with the CTS, the CU measurement of the calendar aging study was integrated into the obligatory relaxation time between the CM and EIS measurements of the cycle aging study. Hence, the maximum count of cells under investigation was limited by the available 64 CTS channels.

3 cells are used for every TP in order to reduce the influence of cell-to-cell parameter variation and therefore dependent possible deviations in the aging behavior and to reduce the danger of premature cell failures. Furthermore, neither published aging data nor experience derived from own measurements were available for the investigated cell in order to estimate the development of cell-to-cell variation during the aging study. Thus, originating from 64 available CTS channels, the number of TPs was limited to 17 because 9 channels had to be reserved for the CU measurements of some of the cycle aging TPs. Nonetheless, with 17 TPs it is possible to cover the whole SOC-range at different temperatures with adequate step sizes of both influence parameters. Furthermore, the calendar aging studies shown in **Table 2.2** used less than 17 TPs. Only [50] performed a calendar aging study with more than 48 TPs, however, with only one cell each.

4.5.3 Static calendar aging

Although stationary BESS are designed to operate over more than 20 years, the experiment was naturally limited by time in addition to the limitations of the available measurement equipment. In order to reach the often used EOL limit of SOH < 80 % (given by different standards for PbA batteries [104]) during the limited time of this aging study, the aging is accelerated by increasing the storage temperature. Assuming that the cell aging rate follows the exponential temperature influence given by the Arrhenius-law, the aging of TPs at higher temperatures can be used as a forecast for the TPs at lower temperatures. 60 °C was chosen as maximum TP temperature because the datasheet provides

Table 4.4: Test matrix of the static calendar aging study with the number of cells for each storage condition.

| Temperature SOC | 0 °C | 10 °C | 25 °C | 40 °C | 60 °C |
|--------------------|------|-------|-------|-------|-------|
| 0 % | | | 3 | 3 | 3 |
| 12.5 % | | | | 3 | |
| 25 % | | | | 3 | |
| 37.5 % | | | | 3 | |
| 50 % | 3 | 3 | 3 | 3 | 3 |
| 62.5 % | | | | 3 | |
| 75 % | | | | 3 | |
| 87.5 % | | | | 3 | |
| 100 % | | | 3 | 3 | 3 |

this as the maximum temperature for cell operation (see **Table 4.1**). Furthermore, it is not expected that battery cells are exposed to ambient conditions $> 60\text{ }^{\circ}\text{C}$ in BESS applications. To prove the Arrhenius-law on the cell aging and to also test realistic storage conditions, TPs were also chosen at lower temperatures. Because almost no calendar aging effects are expected at temperatures lower than $0\text{ }^{\circ}\text{C}$, this temperature was set here as the lower limit. In accordance with the temperature range specified in the cell's datasheet, TP temperatures at $0\text{ }^{\circ}\text{C}$, $10\text{ }^{\circ}\text{C}$, $25\text{ }^{\circ}\text{C}$, $40\text{ }^{\circ}\text{C}$ and $60\text{ }^{\circ}\text{C}$ were chosen. In stationary BESS applications, in most cases, a climatization system is able to maintain the battery cells at optimal temperatures with respect to aging. A commonly used reference temperature is $25\text{ }^{\circ}\text{C}$ since additional cooling leads to higher overall system efficiency losses.

In order to achieve accelerated aging, all relevant SOC are tested at $40\text{ }^{\circ}\text{C}$, which is also the operation temperature of most of the TPs in the cycle aging study. To verify the Arrhenius-law here, one TP with 50% SOC is chosen at all temperatures. Furthermore, 50% is expected to be the average SOC in stationary BESS operation. In order to be able to assess the aging effects over the entire SOC-range, for the reference temperature of $25\text{ }^{\circ}\text{C}$ and also for $60\text{ }^{\circ}\text{C}$, the SOC values 0% and 100% are added. At the main temperature of $40\text{ }^{\circ}\text{C}$, more SOC steps are necessary since nonlinear sensitivity could be expected. Hence, an evenly spaced graduation in 12.5% steps to reach exactly the middle SOC between the previous SOC of the TPs is applied.

On the basis of this design of experiment, it should be possible to estimate the aging even for SOC not to be tested at other temperatures on the basis of the detailed SOC partition of the main temperature. From the previously described considerations, 17 TPs have been defined for the static calendar aging study and are shown in the TP matrix in **Table 4.4**. Each of the 17 TPs is covered with 3 cells.

4.5.4 Dynamic calendar aging

The additional dynamic calendar aging study with alternating test conditions was motivated by the three following issues:

1. To validate the calendar aging model derived from the static calendar aging study.
2. To investigate the independence of the order of storage conditions.
3. To examine how the aging rate is influenced when changing storage SOC and/or temperature.

The main focus of this additional study was to validate the calendar aging models to be derived with measurements relying on different aging conditions. However, these measurements helped to develop the aging model by understanding the dependance of the order of storage conditions and the effect

Table 4.5: Test matrix of the dynamic calendar aging study with one cell for each test point.

| Test point | Temperature | SOC |
|------------|---------------------------------|------------|
| TP1/TP2 | $25/40\text{ }^{\circ}\text{C}$ | 100% |
| TP3/TP4 | $25/60\text{ }^{\circ}\text{C}$ | 100% |
| TP5/TP6 | $40/60\text{ }^{\circ}\text{C}$ | 100% |
| TP7/TP8 | $0/60\text{ }^{\circ}\text{C}$ | 100% |
| TP9/TP10 | $60\text{ }^{\circ}\text{C}$ | $0/50\%$ |
| TP11/TP12 | $60\text{ }^{\circ}\text{C}$ | $0/100\%$ |
| TP13/TP14 | $60\text{ }^{\circ}\text{C}$ | $50/100\%$ |
| TP15 | Dynamic | 100% |

of switching between different conditions. Due to the fact that this dynamic aging study was started about 2 years after the start of the static aging study some of the results have been applied to design this experiment: First, only 1 cell instead of 3 cells have been selected for each TP, because the cell-to-cell parameter variation did not increase significantly during the static study of 3 cells stored at each TP. The respective static parameter of each TP was chosen as maximum possible value, i.e. 100 % SOC or 60 °C, to accelerate the aging effects.

The experimental setup with 15 TPs with a total of 15 cells was then designed as shown in **Table 4.5**. Each TP is realized with one cell having one static and one dynamic condition (temperature or SOC). In order to investigate the independence of the order of storage conditions, one cell of each pair (e.g. TP1/TP2) is stored under the first given condition, the other cell of each pair on the secondly given conditions. Thereby, the dynamic condition of each cell is changed after a period of 4 weeks, when a CU measurement is performed. For instance, the cell of TP1 is stored at 100 % SOC in the first interval at 25 °C and at 40 °C afterward. The cell of TP2 is stored at 100 % SOC but with the antithetic temperature order. In contrast, in the TP9-TP14 the temperatures are kept constant but the SOC is changed after every storing period. The last TP15 is carried out with one cell stored constantly at 100 % SOC and the temperature is changed dynamically after every storing period in this order: 60, 25, 40, 60, etc. °C.

4.5.5 Static cycle aging

In order to accelerate the cyclic aging tests, higher temperatures are also applied here. The datasheet (see **Table 4.1**) limits the maximum ambient temperature to 45 °C for the charge direction together with a maximum cell surface temperatures of 60 °C when the cell is charged. A maximum ambient temperature of 60 °C is permitted for the discharge, whereby the cell surface temperature should be below 80 °C. In order to remain within the specifications of the cell, 45 °C would be the maximum ambient temperature for the cycle aging tests because the ambient temperature should be kept constant. For comparability with other aging studies, the slightly lower ambient temperature of 40 °C was chosen as the main temperature for the cycle aging TPs. For the verification of the measurements, some TPs are also defined at the reference temperature of 25 °C.

The cyclic aging should be investigated with by defining TPs with constant C-rates and SOC-ranges. Based on the aging effects of the individual TPs, the aging model can then be parametrized by the effects of the individual influence parameters. The cyclic TPs could ideally be matched to the possible stress values in realistic stationary BESS applications. The evaluation of the later presented dynamic load profiles (see **Section 4.5.6**), revealed, that cycles with DOCs <5% dominate and the average C-rate is about 0.2 C. Only in some cases, deeper cycles with higher C-rates occur. However, the investigated cell can be charged up to 1 C and discharged up to 6 C.

The minimum C-rate in the charge and discharge direction is set to be 0.2 C because this is the average C-rate of the dynamic load profiles. Furthermore, it is to be expected that at low C-rates it is likely that cycle aging effects will not be noticeable because the calendar aging effects could dominate. As a reference test point, the load of 1 C/1 C (charge/discharge) is defined for different temperatures in order to evaluate the influence of the temperature on cycle aging independently of the calendar aging. Due to the fact, that the C-rates vary in the course real load profiles as well as dynamic load profiles, different combinations of charge and discharge rates are also tested with respect to this reference test point. Because only C-rates up to 1 C can be expected in stationary BESS applications, the maximum

Table 4.6: Test matrix of the static cycle aging study with three cells for each test point. The test points marked with * were started later during the course of the static cycle aging study.

| Test point | Temperature | DOC | Avg. SOC | Charge C-rate | Discharge C-rate | CV-phase |
|------------|-------------|-------|----------|---------------|------------------|----------|
| TP1* | 25 °C | 100 % | 50 % | 1.0 C | 1.0 C | Charge |
| TP2 | 25 °C | 80 % | 50 % | 1.0 C | 1.0 C | None |
| TP3* | 25 °C | 20 % | 50 % | 1.0 C | 1.0 C | None |
| TP4 | 40 °C | 100 % | 50 % | 1.0 C | 1.0 C | Charge |
| TP5 | 40 °C | 100 % | 50 % | 1.0 C | 1.0 C | None |
| TP6 | 40 °C | 80 % | 50 % | 1.0 C | 1.0 C | None |
| TP7 | 40 °C | 40 % | 50 % | 1.0 C | 1.0 C | None |
| TP8 | 40 °C | 20 % | 50 % | 1.0 C | 1.0 C | None |
| TP9 | 40 °C | 10 % | 50 % | 1.0 C | 1.0 C | None |
| TP10 | 40 °C | 5 % | 50 % | 1.0 C | 1.0 C | None |
| TP11* | 40 °C | 1 % | 50 % | 1.0 C | 1.0 C | None |
| TP12 | 40 °C | 20 % | 75 % | 1.0 C | 1.0 C | None |
| TP13 | 40 °C | 20 % | 25 % | 1.0 C | 1.0 C | None |
| TP14 | 40 °C | 80 % | 50 % | 0.5 C | 0.5 C | None |
| TP15 | 40 °C | 80 % | 50 % | 0.2 C | 0.2 C | None |
| TP16 | 40 °C | 80 % | 50 % | 1.0 C | 0.5 C | None |
| TP17 | 40 °C | 80 % | 50 % | 0.5 C | 1.0 C | None |
| TP18 | 40 °C | 80 % | 50 % | 1.0 C | 2.0 C | None |
| TP19* | 40 °C | 40 % | 50 % | 1.0 C | 2.0 C | None |

discharge current is limited to 2 C in order to accelerate the cycle aging.

In contrast to EV, there are no common test profiles for stationary applications. Depending on the application, the battery is charged and discharged with variable currents. Furthermore, the resulting cycle depths depend strongly on the application, on the dimensioning of the battery and its inverter. Hence, the TPs must be cover different large DOCs. In the later applied dynamic load profiles, the average SOC is about 50 %, which is typical for stationary applications. Thus, the TPs with DOCs smaller than 100 % are defined with the cyclization around 50 % SOC. Despite this assumption, at least two TPs with cyclization in a higher and a lower SOC range are applied to check the dependence of the aging effects on the average SOC.

In consequence of the described considerations, the definition of the static cycle aging TPs are given in the following and summarized in **Table 4.6**. The avg. SOC column indicates the average SOC of the respective cycles with individual DOCs.

TP1-2: These TPs with a temperature of 25 °C allows to verify whether the elevated temperature of 40 °C in the reference TP 6 has only an influence on the calendar aging or also affects the cycle aging.

TP3: This TP with a temperature of 25 °C was added to analyze the influence of the DOC of 20 % at a lower temperature than for the TP8.

TP4: This TP enables to analyze the influence of the CV phase in charge direction in comparison with the reference TP 6. The CV phase is defined with a charge termination current of 100 mA given by the datasheet after reaching the charging end voltage of 3.6 V.

TP5: Compared to the TP4, in this TP the cycles are performed without applying a CV phase in order to be able to distinguish the aging effects of the CV phase. Compared to the reference test point 6, however, the full SOC range is cycled here. However, a DOC of 100 % with respect to the nominal

capacity is only possible at the beginning of the aging study. Similar to the TP4, the Ah-throughput per cycle will decrease continuously due to the expected cycle aging leading to less usable capacity.

TP6: This TP is the reference, to which the other TPs are related to.

TP7-11: In comparison with the reference TP6, the influence of the DOC can be investigated with these TPs. The DOCs of 80 %, 40 %, 20 % and 5 % are examined. The smaller step size in the range of smaller DOC is necessary because a stronger sensitivity of the cycle lifetime is expected here. The TP with 20 % DOC is required as a reference to TP12 and TP13.

TP12-13: These TPs are cycled with the same DOC of 20 % but around different average SOC values in comparison to TP8. 25 % and 75 % are chosen as average SOC values because these SOC values are also investigated in the static calendar aging study. Furthermore, this definition would ensure that a constant Ah-throughput can still be achieved up to a capacity loss of about 10 %.

TP14-15: In comparison to the reference TP6, this TP is cycled with low C-rates in order to investigate the influence of lower currents on the cycle lifetime. It can be expected that the sensitivity of the C-rate is relatively high. Hence, in addition to the minimum C-rate of 0.2 C, 0.5 C is chosen additionally to enable the evaluation of the influence of the C-rate.

TP16-17: These TPs are used to examine the influence of unsymmetrical charge and discharge C-rates compared to the reference TP6. The charge and discharge rate is reduced to 0.5 C in each case to meet with the reference of TP14 and sufficient high the cycle throughput.

TP18-19: These TPs enable the evaluation of the effects of larger discharge rates compared to reference TP6. With these TPs, the fastest Ah-throughput of all TPs would be achieved, whereby the development of the aging effects of the further TPs can be predicted.

For the TPs with the DOCs smaller than 100 %, the DOC is related to the nominal capacity and the Ah-throughput per cycle is kept constant as long as possible. As soon as the voltage limits are reached as a result of the capacity loss, the Ah-throughput per cycle will also drop continuously.

The cyclization of all TPs is defined by starting at the defined minimum SOC_{\min} , which is obtained by subtracting the half of the respective DOC from the average \overline{SOC} :

$$SOC_{\min} = \overline{SOC} - \frac{DOC}{2} \quad (4.1)$$

After every CU, the average SOC is adapted with respect to the remaining capacity (CC and CV phase) determined in the preceding CM.

Figure 4.3 shows a so-called 'Wöhler curve', representing the cycle stability over the DOC until a capacity loss of 20 % is reached. The curve represents the values when a constant cycle stability of 6000 FEC is assumed over the whole DOC range. The above defined TPs of the static cycle aging study with charge and discharge rates of 1 C/1 C are marked with the respective DOC for both test temperatures in order to illustrate that there TPs with the same DOC values for both test temperatures.

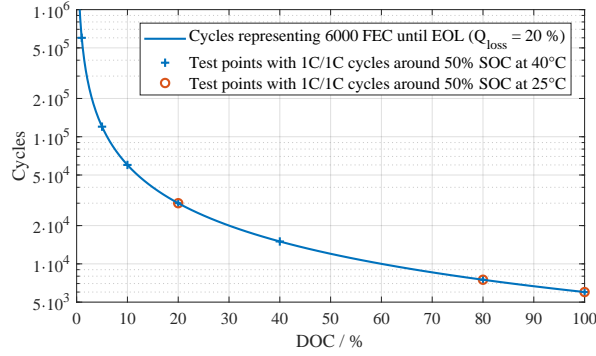


Figure 4.3: Wöhler curve representing the possible number of cycles over the DOC until $Q_{\text{loss}} = 20\%$ is reached. The DOCs of the TPs at 25 °C and 40 °C are marked individually.

4.5.6 Dynamic cycle aging

In addition to static TPs with constant C-rates and DOC, a dynamic cycle aging study is performed with dynamic stress profiles. The results of these dynamic stress profiles are later utilized to validate the developed combined aging model (see **Section 5.3.2**).

Within the framework of the work in the *ESPEN* project [105], the two applications PV-HESS and the combined use of the PV-HESS with the simultaneous provision of PCR-power (PV-PCR-BESS) have been investigated. For these two applications, measurements of the resulting currents for the battery were carried out within field tests by the *Fraunhofer Institute for Solar Energy Systems* (Fraunhofer ISE). Based on this measurement data, synthetic current profiles with a duration of less than 24 h were created, which represent the condensed profile characteristics of the course over one year. These so-called load collectives of the two applications have been used by Fraunhofer ISE et al. in the aging studies within the *ESPEN* project and are also applied here for comparability reasons.

These two load collectives/dynamic stress profiles are tested in the dynamic cycle aging study each on 3 cells at an ambient temperature of 40 °C with the same testing procedure as applied in the static calendar and cycle aging study (see **Section 4.4**). Due to capacity degradation in the course of the aging study, these profiles have to be adapted by updating the start SOCs with respect to the residual capacity determined in the previous CM by counting the Ah-throughput.

In the following, these two load collectives/dynamic stress profiles are briefly described.

PV-HESS profile

This profile was created with measurements of the consumption and PV feed-in data of a real model house in Freiburg with a PV-system but without a battery storage for a period longer than one year. These profiles were separated into a summer and a winter part and processed individually to load collectives. Currents in and out of the battery have been defined as follows: If the PV power is greater than the household consumption and SOC less than 100 %, the battery should be charged. If the PV power is less than the power requirement and the SOC is greater than 0 %, the battery should be discharged in order to reduce the power consumption from the electricity grid. An efficiency of 100 % was assumed. Current values < 30 mA (minimum value of the measuring device) and time periods with no load were removed, resulting in a profile of less than 24 h duration. In order to generate a condensed test profile, frequencies of the measured profile were analyzed and synthetic data was generated in the

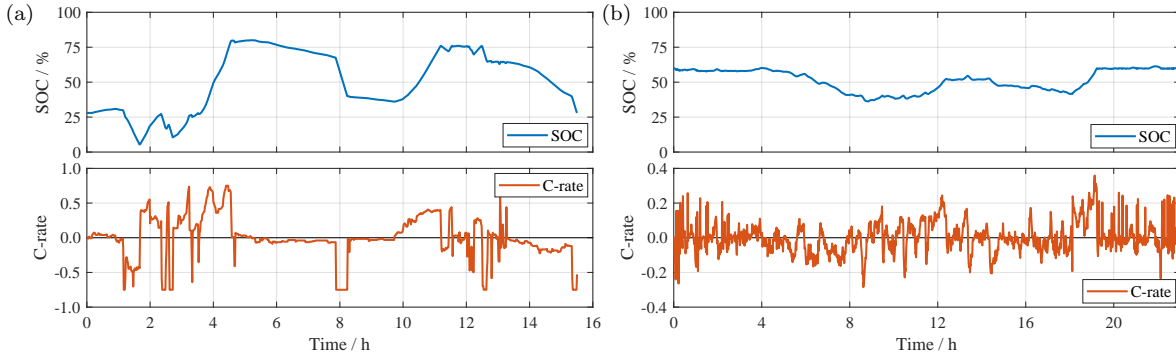


Figure 4.4: Course of the PV-HESS profile in Figure 4.4a and PV-PCR-BESS profile in Figure 4.4b: The upper plot shows the SOC course, the lower plot the C-rate course.

form of a summer and winter day load collective. These two-day profiles were combined to one profile, normalized on the nominal capacity of the here investigated cell with 3 Ah capacity, shifted to a SOC range between 9 to 80%, and the few load peaks over 0.75 C were curtailed [105].

The following **Figure 4.4a** shows the PV-HESS load collective with the C-rate and the resulting SOC-curve and the main characteristics are summarized in **Table 4.7**.

PV-PCR-BESS profile

The PV-PCR-BESS profile represents a synthetically constructed load collective of a PV-HESS profile with a superimposed PCR-supply profile. The assumed BESS has an energy capacity of 10 kWh, the PV-system has a peak power of 10 kW and a 7.5 kW of the power is offered for the PCR-supply. The efficiency of the BESS is set to 100%. The power line frequency of the year 2012 was used to generate the PCR profile. The energy capacity of the BESS can only be used freely in the SOC range of 50 to 60%. Outside of these limits, only corrections are allowed to reach the setpoint SOC of 50%. Current values < 30 mA (minimum value of the measuring device) and time periods with no load were removed, resulting in a profile of less than 24 h duration. This PV-PCR-BESS profile is shown in **Figure 4.4b** with the C-rate and the resulting SOC-curve in comparison to the PV-HESS.

The main characteristics are summarized in **Table 4.7**. The characteristics of both profiles deviate in

Table 4.7: Characteristics of the PV-HESS and PV-PCR-BESS profiles.

| Characteristic / Profile | PV-HESS | PV-PCR-BESS |
|--------------------------|-------------|-------------|
| Duration | 15.50 h | 22.85 h |
| Resolution | 1 min | 1 min |
| Charge Ah-throughput | 1.562 C_N | 0.732 C_N |
| Discharge Ah-throughput | 1.562 C_N | 0.732 C_N |
| Average charge C-rate | 0.243 C | 0.073 C |
| Average discharge C-rate | 0.172 C | 0.057 C |
| Maximum charge C-rate | 0.750 C | 0.359 C |
| Maximum discharge C-rate | 0.750 C | 0.285 C |
| Average SOC | 51.4 % | 51.2 % |
| Minimum SOC | 5.4 % | 36.3 % |
| Maximum SOC | 80.0 % | 61.4 % |

part from the expected results of both applications and also from results of the later applied baseline scenarios (see **Table 6.14**) because they represent synthetic profiles designed to accelerate the aging effects in battery aging studies. Both profiles are applied in this dynamic cycle aging study each on three cells in unlimited repetition without brake periods and are only paused by the CU measurements.

4.6 Aging results

In this section, first of all, the results of the calendar aging study are presented and primarily discussed. Then, the results of the cycle aging study are shown. Afterward, in **Chapter 5** the aging model for the calendar and cycle aging is developed and validated with the results of the dynamic calendar and cycle aging studies.

Although a variety of parameters are available from the CU measurements, here only the relative discharge capacity C_{disch} and relative resistance $R_{\text{DC},10\text{s}}$ is evaluated, because they are the most representative parameters and commonly used in aging models for lifetime simulations. Later on, also the low rate charge and discharge-curves measured in the extended CU and the impedance-spectra of the EIS measurement as part of every CU are evaluated. C_{disch} is determined as the mean of the entire discharge capacity (CC + CV-phase) in the two full cycles of the periodic CU (see **Equation 4.2**). $R_{\text{DC},10\text{s}}$ is defined as the voltage difference measured between the beginning of relaxation after a constant current pulse $V(t = 0\text{s})$ and after 10s of relaxation $V(t = 10\text{s})$ divided by the current of each pulse. Here, $R_{\text{DC},10\text{s}}$ is calculated as the mean value of $R_{\text{DC},10\text{s}}$ determined after a 1 C discharge pulse (disch) and 1 C charge pulse (ch) in the 4th phase of the CM (see **Section 4.3**) during the periodic CU (see **Equation 4.3**).

$$C_{\text{disch}} = \frac{1}{2} (C_{\text{CC1,disch}} + C_{\text{CV1,disch}} + C_{\text{CC2,disch}} + C_{\text{CV2,disch}}) \quad (4.2)$$

$$R_{\text{DC},10\text{s}} = \frac{1}{2} \left(\frac{V_{0\text{s}} - V_{10\text{s}}}{|I_{\text{disch}}|} + \frac{V_{0\text{s}} - V_{10\text{s}}}{|I_{\text{ch}}|} \right) \quad (4.3)$$

4.6.1 Static calendar aging

4.6.1.1 Capacity and resistance measurements

In **Figure 4.5** the development of the relative discharge capacity C_{disch} and the relative resistance $R_{\text{DC},10\text{s}}$ are shown for selected TPs at different temperatures and storage SOC over the whole aging study with 35 CU measurements. All values are related to the measurements of the first CM. Since the cell-to-cell variation with identical storage conditions is minimal at BOL and even at EOL with $\Delta C_{\text{disch}} < 0.6\%$ and $\Delta R_{\text{DC},10\text{s}} < 2.1\%$, only the mean value of the three cells each with same storage condition, is shown in the following aging figures.

Figure 4.5a and **4.5b** show the aging trend for different storage temperatures 0 °C, 10 °C, 25 °C, 40 °C and 60 °C at the storage $\text{SOC} = 0\%$, 50% and 100%. The capacity is decreasing for all temperatures over time, however, the rate of capacity decrease is slowing down over time as well. This capacity fade behavior was also shown in different publications [61; 71] and modeled with a square root dependance over time. Ploehn et al. explained this square root dependance over time of the capacity fade with

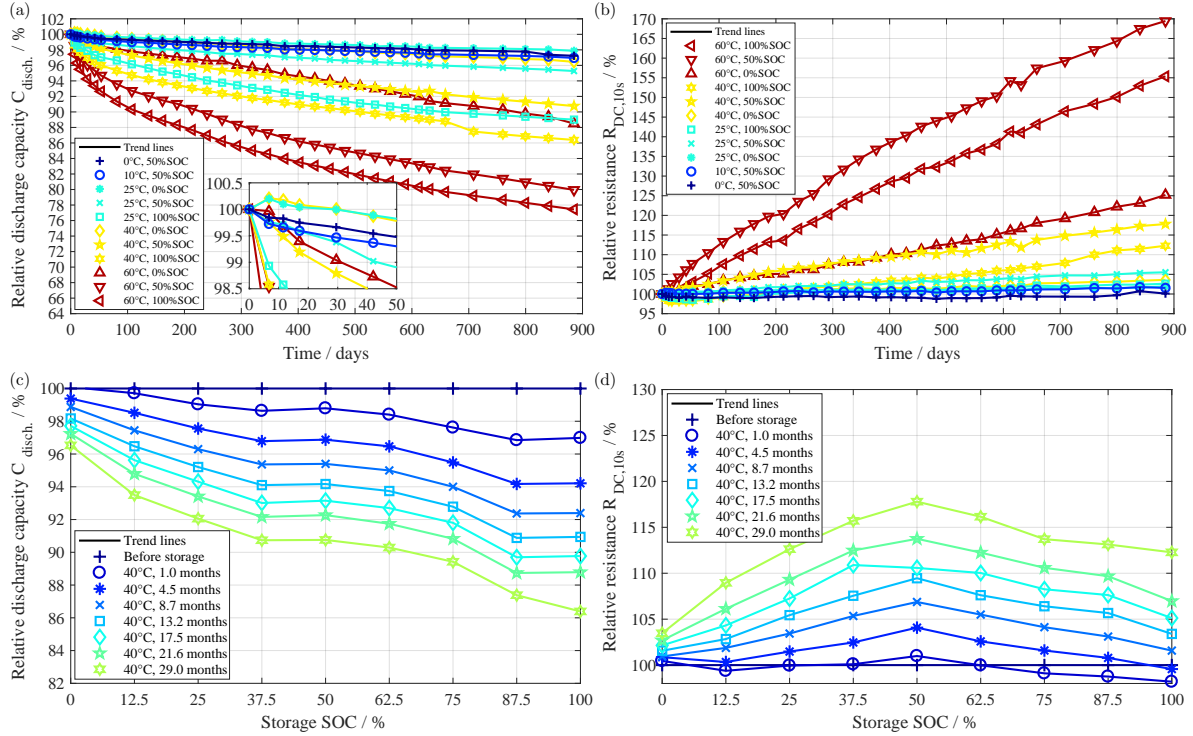


Figure 4.5: Degradation over 885 days of selected TPs under different storage SOC and temperatures: (a) Relative discharge capacity C_{disch} at $\text{SOC} = 0\%$, 50% and 100% at 0°C , 10°C , 25°C , 40°C and 60°C . (b) Relative resistance $R_{\text{DC},10\text{s}}$ at $\text{SOC} = 0\%$, 50% and 100% at 0°C , 10°C , 25°C , 40°C and 60°C . (c) Relative discharge capacity C_{disch} at 40°C at $\text{SOC} = 0 - 100\%$. (d) Relative resistance $R_{\text{DC},10\text{s}}$ at 40°C at $\text{SOC} = 0 - 100\%$. All values are related to the measurements of the first CM. Each subplot shows the mean values of the three cells of each TP. In subplot (a) the first 50 days are displayed enlarged in an extra view in order to see more details.

the growth rate of the SEI and their thickness [106]. They state, that the SEI thickness increase leads to a decrease of the solvent diffusion rate and consequently to a slowing down of SEI growth rate and capacity loss. Further publications [73; 107; 108] stated similar concepts and approved their observations and models with measurements of the calendar aging of lithium-ion cells with graphite anodes.

For the aging trend of the capacity and the resistance, higher temperatures lead to higher rates of decrease or increase of both parameters respectively, however, the relative resistance increase is almost double the relative capacity decrease for the respective TPs.

For the TP with 0% SOC at 25°C and 40°C the capacity increases slightly by maximum 0.22% in the first storage period probably due to the influence of the overhang areas but decreases afterward. This capacity trend could be interpreted as a superposition of the capacity fade due to the aging by the SEI growth together with the limited capacity recovery from the anode overhang areas. It is assumed that the same trend cannot be observed for the TP with 0% SOC at 60°C because the capacity fade is probably stronger than the capacity recovery from the anode overhang areas. The resistance decreases for most of the TPs without a clear correlation to temperature or SOC at the beginning of the aging study by maximum 1.90% but increases thereafter for all temperatures, but in contrast to the capacity fade, the rate of resistance increase remains constant. The resistance decrease at the beginning could be explained by the possible influence of measurement uncertainties when measuring the resistance

during the CM. Due to the fact, that the resistance changes are partly quite small at the beginning of the aging study for some TPs, small measurement errors at the first CM could lead to different trends in the subsequent CM. This inverse aging trend of the resistance at the beginning of aging study could be related as well to the effects of the anode overhang areas. However, the influence of the anode overhang areas on the resistance change remains unclear, because also the TPs in the middle SOC-range showed the same behavior as the TPs with very low and very high SOC, where the anode overhang effect could influence the capacity trends the strongest.

Between the CM of day 659 and 708, the capacity of the TP with 100 % at 40 °C decreases faster in comparison to the aging before and after this interval. Though, the interval between this CM and the preceding CM is with 50 days the first time during the aging study longer than the before performed interval of 27 days. However, the longer storage time is probably not the reason for this unique kink in the capacity loss of this TP, because the further TPs with 100 % SOC at 25 °C and 60 °C show no similar trends.

The influence of storage SOC is shown in **Figure 4.5.c** and **4.5d** at 40 °C for the storage SOC from 0 % to 100 % for selected points in time from the beginning until the end of the aging study. The capacity decrease is stronger with higher SOC. However, for the $SOC = 37.5 - 62.5\%$ there is almost no difference in the capacity fade observable for all shown points in time. Similar SOC behavior was shown by Keil et al. [50] for different lithium-ion cells with graphite anodes and explained with the stages in the graphite anode potential. In contrast, the resistance increase shows a non-monotonic dependance over the storage SOC with the highest increase in the middle SOC-range. The evaluation of the EIS measurements in **Table 4.8** shows a similar behavior for the TPs with the storage temperature of 60 °C, since for all EIS-parameters the highest increase was observed for the TPs with 50 % SOC. However, for the further TPs with 25 °C and 40 °C, no clear trend of the impedance increase due to the storage SOC was seen. This influence of storage SOC on the resistance increase seems to be a special artifact of the investigated cell because no publication has been found where this behavior was observed. A possible explanation of this behavior could be the assumption, that the SEI grows homogeneously across the whole anode only when the cells are stored in the middle SOC-range where little capacity fade differences were observed over the storage SOC (see **Figure 4.5.c**). Then, a homogeneous SEI would lead to relatively higher resistance increase than an inhomogeneous SEI, because the areas with less SEI thickness would dominate the measurable resistance. However, the resistance measurements are possibly influenced by the effects of the anode overhang areas, whereby different relaxation time constants might occur at different SOC. These assumptions remain to be proven by further experiments and post-mortem analysis of the investigated cell.

4.6.1.2 Differential voltage analysis

For a deeper understanding of the capacity fade, **Figure 4.6** shows the DVA curves for selected TPs at different SOC and temperatures. Thereby every subplot shows the dV/dQ -curve of only one of the three cells under the same storage conditions of each TP because the averaged values of three cells of one TP would erase possible differences between the curves. The DVA was applied on the discharge phase with 0.02 C in the low rate charge and discharge measurements in the 4 extended CU during the aging study (see **Section 4.3**) and is related to the work of Keil et al. [60].

In all dV/dQ -curves, the main peak in the DVA is between 2.3 to 2.5 Ah of the capacity. It results from a potential step, which indicates a different staging configuration of the intercalated lithium in the

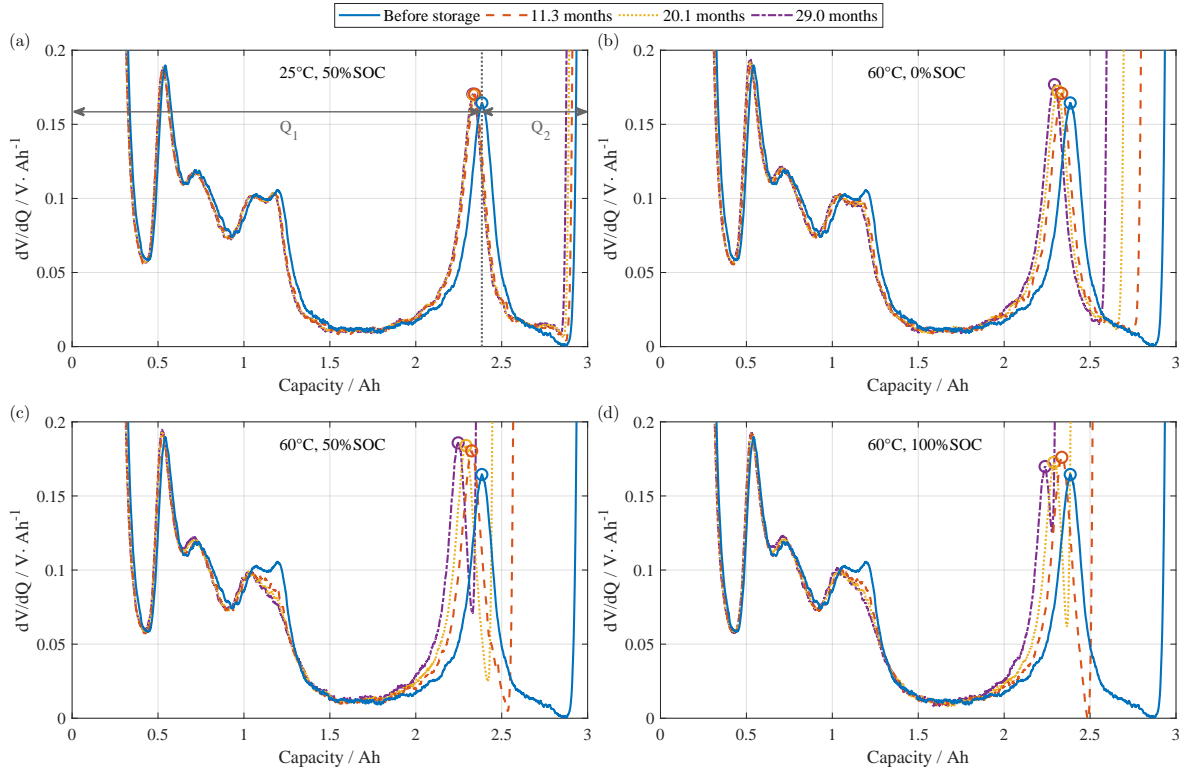


Figure 4.6: DVA of selected TPs with different storage SOC and temperatures at different points in time during the aging study:

- (a) At $SOC = 50\%$ at 25°C . (b) At $SOC = 0\%$ at 60°C . (c) At $SOC = 50\%$ at 60°C . (d) At $SOC = 100\%$ at 60°C . The circles show in each dV/dQ -curve the peak which is related to the single phase of LiC_{12} in the graphite-anode. The DVA is applied on the low rate discharge measurement described in Subsection 4.3.

graphite-anode. Thereby, this main peak represents the single phase of LiC_{12} and is marked with circles in the respective color of each point in time. The area left and towards to this peak, corresponds to the transformation from LiC_{18} to LiC_{12} and the area right and away from the peak to the transformation of LiC_{12} to LiC_6 . This peak divides the cell capacity C_{actual} into two characteristic capacities Q_1 and Q_2 . Q_1 is the interval between 0% SOC and the main graphite peak, providing information about the capacity of the graphite anode. Q_2 , is the interval between the main graphite peak and 100% SOC, providing information about the balancing of both electrodes. The sum of Q_1 and Q_2 is the respective remaining discharge capacity C_{actual} at each point in time of the shown TPs, which correlates with the capacity decrease shown in **Figure 4.5**. Q_1 and Q_2 are defined graphically in **Figure 4.6a** and are evaluated for all subplots in **Figure 4.7** as absolute values for better comparability.

The TP with a storage $SOC = 50\%$ at 25°C shows almost no variation of the dV/dQ -curves because the capacity decreased only about 4.7% during the 885 days of the aging study. Only a slight shift to the left is observable for the LiC_{12} peak, resulting in a decrease of Q_2 and nearly no change of Q_1 .

The TPs at the higher temperature of 60°C show a stronger variation of the dV/dQ -curves, however only the LiC_{12} peak is shifting to the left and the other parts almost remain in the same position and shape. Consequently, in **Figure 4.7** a decrease of both Q_1 and Q_2 of the TPs at the higher temperature of 60°C can be observed. With higher storage SOC, Q_2 is decreasing stronger, but Q_1 is decreasing nearly constant for all SOC. Since almost no decrease of Q_1 at 25°C is observed, it can

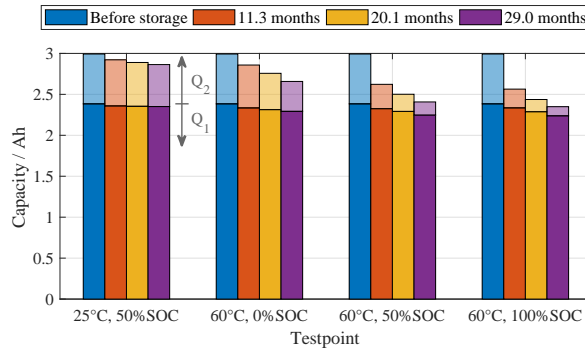


Figure 4.7: Development of the Q_1 and Q_2 parameters of the dV/dQ -curves shown in Figure 4.6.

be assumed, that no LAM occurs and the capacity fade results solely from LLI for this test point. In contrast, a slight decrease of Q_1 is observable in the dV/dQ -curves at 60 °C. Hence, there might be some LAM of the negative electrode as already shown by Li et al. and Lewerenz et al. for LFP/C cells [49; 109] at elevated temperatures caused by the deposition of Fe on the anode. However, LLI remains the dominating factor for capacity fade, which can be identified by the marked reductions in Q_2 for all shown dV/dQ -curves. Due to the fact that the capacity fade correlates with the decrease of Q_2 , the observed aging effects result mostly from the SEI growth on the graphite anode.

4.6.1.3 Electrochemical impedance spectroscopy

The EIS-curves in **Figure 4.8** give an insight into the development of the impedances for selected TPs at different SOC and temperatures at selected points in time during the aging study. Thereby every subplot shows the EIS-curve of only one of the three cells under the same storage conditions of each TP because the averaged values of three cells of one TP would impede the comparability of the curves.

The EIS measurement conditions are described in detail in **Section 4.3**. In all EIS subplots the following parameters are labeled respectively with markers:

- $R_{AC,1000\text{ Hz}}$ indicates the real part of the impedance measured with 1000 Hz, which is commonly applied for a quick characterization of the cell impedance.
- $R_{AC,5\text{ Hz}}$ represents the real part of the impedance measured with 5 Hz and is used here to show the deviation of the impedance-curve due to the frequency.
- Z_{\max} marks the local extremum of the impedance measured between 1000 Hz and 5 Hz.
- Z_{\min} marks the local extremum of the impedance measured between Z_{\max} and the impedances at the lowest frequencies on the right side.

The development of $R_{AC,1000\text{ Hz}}$, $R_{AC,5\text{ Hz}}$, Z_{\max} , and Z_{\min} together with the real and imaginary part of Z_{\min} and Z_{\max} are summarized in **Table 4.8**, where the relative change of each parameter from the beginning until the end of the aging study is shown for the selected TPs of **Figure 4.8**. The test point with a storage $SOC = 50\%$ at 25 °C shows only a slight shift of the EIS-curves to the right with higher resistances. However, the selected EIS-parameters that are shown in **Table 4.8** increase very little for this test point. The decrease of Z_{\min} and Z_{\max} originate from the difficult exact determination of these parameters due to the flat curve shape and the limited FPD in the respective areas. Little absolute measurement uncertainties lead to a big relative deviation of the extracted parameters' values.

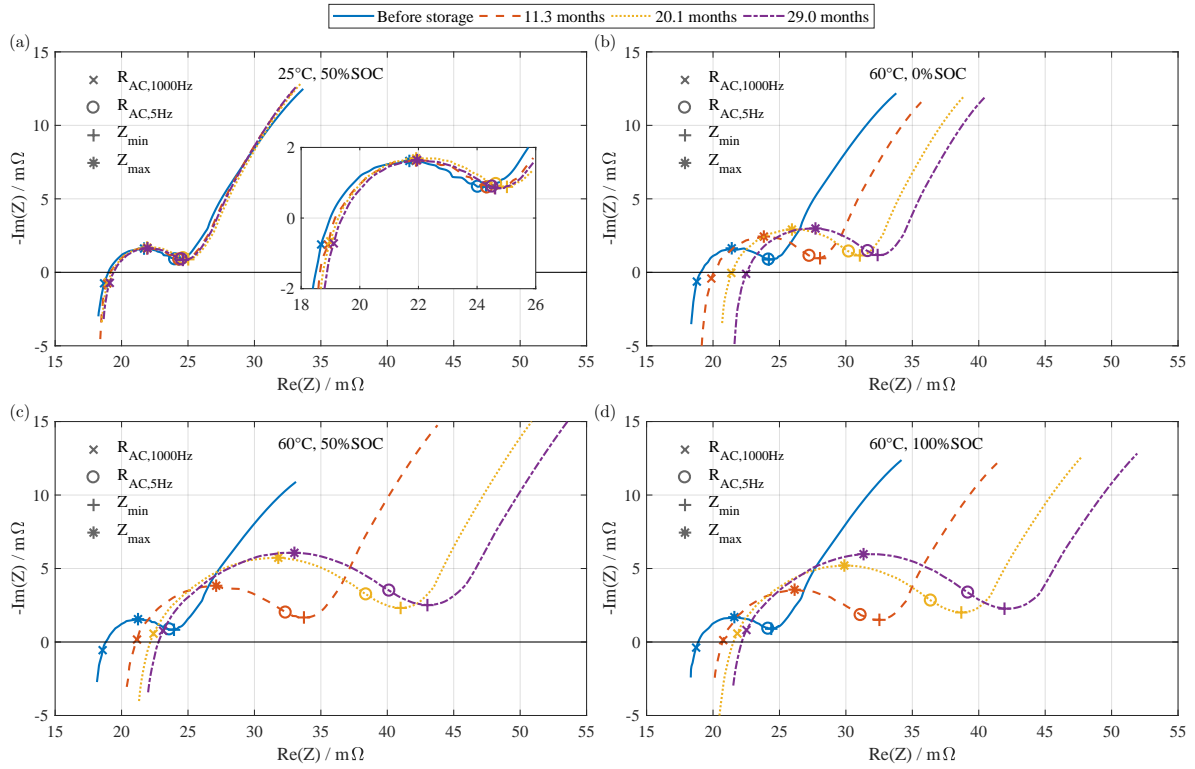


Figure 4.8: EIS of selected TPs with different storage SOC and temperatures at selected points in time during the aging study:
 (a) $SOC = 50\%$ at 25°C . (b) $SOC = 0\%$ at 60°C . (c) $SOC = 50\%$ at 60°C . (d) $SOC = 100\%$ at 60°C . The Nyquist-plots are drawn with an inverse y-axis due to the common form of presentation. In subplot (a) the area between $18\text{ m}\Omega$ and $26\text{ m}\Omega$ is displayed enlarged in an extra view in order to see more details. The parameters $R_{AC,1000\text{ Hz}}$, $R_{AC,5\text{ Hz}}$, Z_{\min} and Z_{\max} are displayed each with markers. The EIS measurement procedure is described in Subsection 4.3.

Table 4.8: Relative change of EIS-parameters from the beginning until the end of the aging study for selected TPs.

| TP-Temp. | 25°C | 60°C | 60°C | 60°C |
|-------------------------|--------------------|--------------------|--------------------|--------------------|
| -SOC | 50% | 0% | 50% | 100% |
| Parameters | | | | |
| $R_{AC,1000\text{ Hz}}$ | 2.3 % | 19.7 % | 24.5 % | 20.2 % |
| $R_{AC,5\text{ Hz}}$ | 2.0 % | 30.9 % | 70.1 % | 62.3 % |
| Z_{\min} | -1.9 % | 91.2 % | 292.2 % | 257.6 % |
| $Re(Z_{\min})$ | -1.8 % | 92.5 % | 294.3 % | 259.9 % |
| $Im(Z_{\min})$ | -4.3 % | 35.6 % | 201.7 % | 152.6 % |
| Z_{\max} | -3.5 % | 110.1 % | 313.0 % | 241.8 % |
| $Re(Z_{\max})$ | -5.4 % | 122.5 % | 322.0 % | 237.4 % |
| $Im(Z_{\max})$ | 1.5 % | 85.5 % | 290.2 % | 253.2 % |

The further TPs at 60 °C with $SOC = 0\%$, 50 % and 100 % show a stronger shift of the EIS-curves to the upper right during the aging study in **Figure 4.8b-4.8d**. Again a higher SOC leads to a stronger increase of all impedances, however, at $SOC = 50\%$ the biggest increase of all impedances is observable. This behavior was also observed with the highest increase of $R_{DC,10s}$ at $SOC = 50\%$ obtained in the CM shown in **Figure 4.5d**. **Table 4.8** shows these observations in more detail: For all SOC at 60 °C $R_{AC,1000 Hz}$ increases by about 20 %. However, the further EIS-parameters increase a lot more at $SOC = 50\%$ and 100 % with the highest values at 50 %.

4.6.2 Static cycle aging

4.6.2.1 Capacity and resistance measurements

Here the results of the cycle aging TPs are shown grouped into the single influence parameters on cycle aging, C-rate, DOC around a fixed SOC, and fixed DOC around different SOC. The data to be shown in the following figures represents the total aging and includes, therefore, the superposition of calendar aging. For the creation of the aging models in **Chapter 5**, the calendar aging results are subtracted from the total aging results shown here. For the same reason, the temperature influence is investigated in **Section 5.2.2.4**, because the calendar aging influence has to be taken into account. Similar to the calendar aging TPs, the cell-to-cell variation with identical cycle conditions is minimal. Therefore, only the mean value of the three cells each with same cycle condition is shown in the following aging figures. All values are related to the measurements of the first CM.

Influence of C-rate

Figure 4.9 shows the development of the relative discharge capacity C_{disch} and the relative resistance $R_{DC,10s}$ for selected cycle aging TPs with different C-rates but all with $DOC = 80\%$ cycles around $SOC = 50\%$ at 40 °C. The degradation over the whole aging study with 35 CU measurements is illustrated in the upper panel over time and in the lower panel over the Ah-throughput related to the nominal cell capacity represented by the FEC. Due to the different C-rates of the shown TPs, different trends are observable between the illustration over time and over FEC.

However, the relative discharge capacity is decreasing for all C-rates over time, see **Figure 4.9a**, and over FEC, see **Figure 4.9c**, and follows a square root dependance of time as well as of FEC as also shown in different publications [10; 72].

The resistance is increasing for all C-rates over time, see **Figure 4.9a**, and over FEC, see **Figure 4.9c**, but in contrast to the capacity fade the rate of increase remains constant over time as well as over FEC.

Considering only the degradation over time of C_{disch} in **Figure 4.9a** and $R_{DC,10s}$ in **Figure 4.9b**, it is observable that higher charge and discharge C-rates lead to higher rates of decrease or increase of both parameters respectively, however, the relative capacity decrease is almost double the relative resistance increase for the respective TPs. The comparison of the TPs with asymmetric charge and discharge currents (0.5 C/1 C and 1 C/0.5 C) reveals, that almost no differences are observable in the course of the capacity loss and resistance increase. When assuming that SEI growth is the dominating aging effect for calendar and cycle aging, the Ah-throughput is the main measure of the additional cycle aging effect. Then, by plotting the degradation over FEC instead of the time of C_{disch} in **Figure 4.9c** and $R_{DC,10s}$ in **Figure 4.9d**, it is observable that higher charge and discharge C-rates leads to smaller

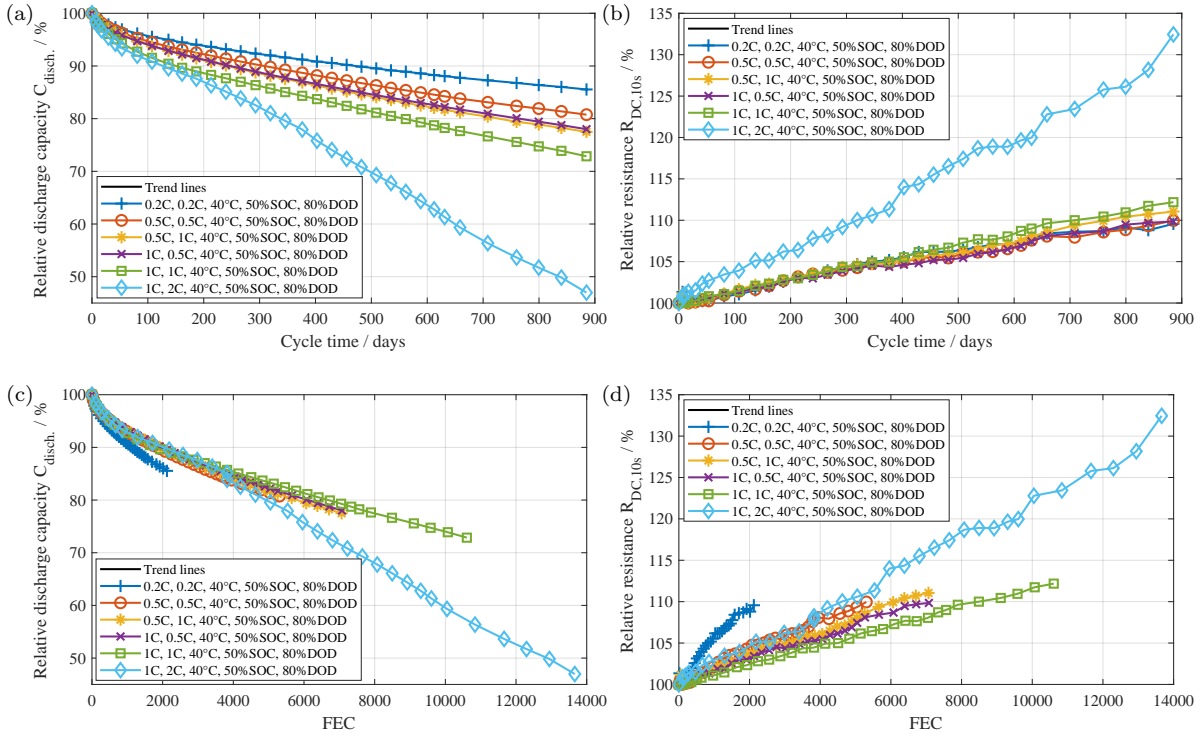


Figure 4.9: Degradation over 885 days of selected cycle aging TPs with different C-rates (xC charge direction, xC discharge direction) with $DOC = 80\%$ around $SOC = 50\%$ at 40°C : (a) Relative discharge capacity C_{disch} over time. (b) Relative resistance $R_{\text{DC},10\text{s}}$ over time. (c) Relative discharge capacity C_{disch} over FEC. (d) Relative resistance $R_{\text{DC},10\text{s}}$ over FEC. All values are related to the measurements of the first CM. Each subplot shows the mean values of the three cells of each TP.

rates of decrease or increase of both parameters respectively in contrast to the plotting over time. However, by subtracting respective calendar aging of each TP, the pure cycle aging shows a different influence due to the C-rate (see **Section 5.2.2.2**). Only for the TP with 2C in the discharge direction, a change of the degradation rate occurs after about 4000 FEC, which might be induced by a further aging mechanism like lithium plating.

Influence of DOC

Figure 4.10 shows the development of the relative discharge capacity C_{disch} and the relative resistance $R_{\text{DC},10\text{s}}$ for selected cycle aging TPs with different DOC around $\text{SOC} = 50\%$ all with 1C in charge and discharge direction at 40°C over FEC. For both parameters very different degradation trends are observable due to the DOC. Only for the higher $\text{DOCs} = 80\%$ and 100% the degradation follows a square root dependance of time/FEC for C_{disch} and a linear trend for $R_{\text{DC},10\text{s}}$. However, an almost linear degradation is observable for the C_{disch} in **Figure 4.10a** and for $R_{\text{DC},10\text{s}}$ in **Figure 4.10b** with the highest degradation rates for the $\text{DOCs} = 10\%$ and 20% . Since the $\text{DOCs} = 5\%$ and 40% show lower degradation rates, no clear influence of the cycles DOC on degradation can be stated. In comparison, Sarasketa-Zabala et al. [87] observed stronger capacity loss performing cycles with a DOC between 10% and 50% than performing cycles with larger DOCs for a different LFP/C cell. After about 1000 FEC the rate of capacity fade slows down for the TPs with $\text{DOCs} < 80\%$ and is continued by a period with almost no capacity fade for at least 2000 FEC for the TP with $\text{DOC} = 40\%$. For the $\text{DOCs} = 10\%$ and 20% , which showed the strongest capacity decrease in the beginning, the capacity is increasing again and shows almost no capacity fade until 7000 passed FEC. Finally, at the EOT at about 10600 FEC the capacity degradation rates are higher with bigger DOC showing the expected influence of DOC on the capacity loss. For the resistance increase after the first 1000 FEC a similar picture is observable due to the influence of DOC, however, in contrast to the capacity degradation trends, the resistances are increasing for all TPs with an almost linear trend. Additionally, at EOT no clear influence of DOC on the absolute resistance increase is observable [.]

Influence of SOC

The influence of the SOC-range on cycle aging is shown in **Figure 4.11** with three TPs with $\text{DOC} = 20\%$ around $\text{SOC} = 25\%$, 50% and 75% . The aging trend of TP with cycles around $\text{SOC} = 50\%$ was already shown **Figure 4.10** in comparison to further DOC. For all TPs, the rate of capacity decreases showing a square root behavior of FEC in **Figure 4.11a**. Similar to the other cycle aging influence factors, the rate of resistance increase remains constant over the whole test duration, see **Figure 4.11b**. For both the capacity and resistance degradation it can be observed, that cycles around $\text{SOC} = 25\%$ lead to less aging than higher SOC-ranges. Due to special aging trends around $\text{soc} = 50\%$, no clear relation between SOC-range and degradation can be stated for the first 5000 FEC. However, in the following cycles until EOT the degradation rates of capacity and resistance are

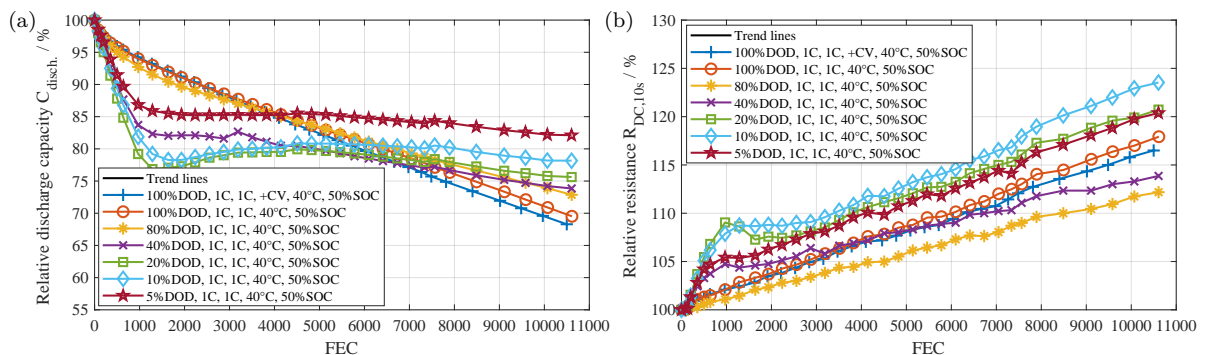


Figure 4.10: Degradation over 885 days of selected cycle aging TPs with different DOC around $\text{SOC} = 50\%$ all with 1C in charge and discharge direction at 40°C over FEC: (a) Relative discharge capacity C_{disch} . (b) Relative resistance $R_{\text{DC},10\text{s}}$.

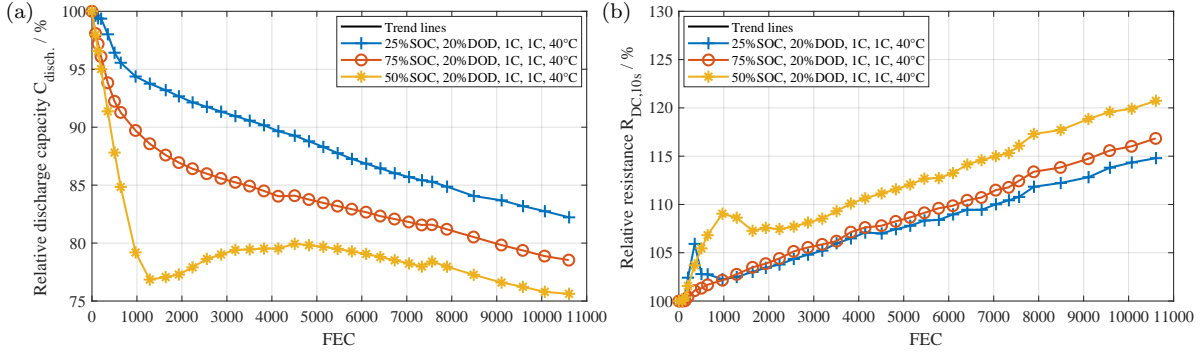


Figure 4.11: Degradation over 885 days of selected cycle aging TPs with different DOC around $SOC = 50\%$ all with $1C$ in charge and discharge direction at $40^\circ C$ over FEC: (a) Relative discharge capacity C_{disch} . (b) Relative resistance $R_{DC,10s}$.

almost the same for all tested SOC-ranges.

4.6.2.2 Differential voltage analysis

In order to understand the cycle aging mechanism **Figure 4.13** shows the DVA curves for selected cycle aging TPs at $40^\circ C$ with different C-rates and DOC at different points in time during the aging study. This analysis was derived similarly to the DVA in **Section 4.6.1**. Again, the distance/capacity from the beginning and the end of the discharge phase are labeled with Q_1 and Q_2 , respectively, individually in **Figure 4.13a** and evaluated for all subplots in **Figure 4.12**. The sum of Q_1 and Q_2 is the respective discharge capacity at each point in time of the shown TPs, which correlates with the capacity decrease shown in **Figure 4.5**.

The TP with $DOC = 80\%$ around $SOC = 50\%$ with $0.2C/0.2C$ in **Figure 4.13c** shows only small changes of the dV/dQ -curves although the capacity decreased about 14.5% during the 885 days of the aging study. Furthermore, only a slight shift to the left is observable for the peak which is related to the single phase of LiC_{12} in the graphite-anode, resulting in a decrease of Q_2 and nearly no change of Q_1 . Comparing this curve and the Q_1 and Q_2 values with the DVA results of the calendar aging TPs in **Figure 4.13**, it can be stated that the aging of this TP is dominated by calendar aging due to small additional cycle aging with low C-rates of $0.2C/0.2C$.

The TPs with higher C-rates of $1C/1C$ show a stronger variation of the dV/dQ -curves: The peak

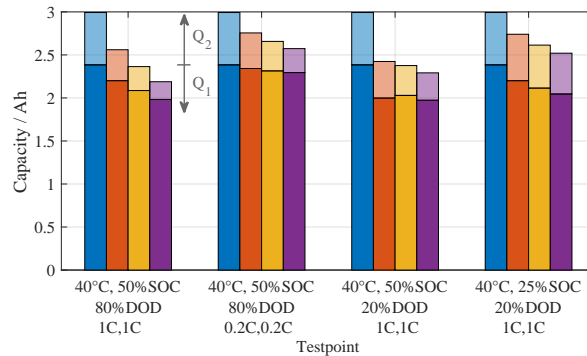


Figure 4.12: Development of the Q_1 and Q_2 parameters of the dV/dQ -curves shown in Figure 4.13.

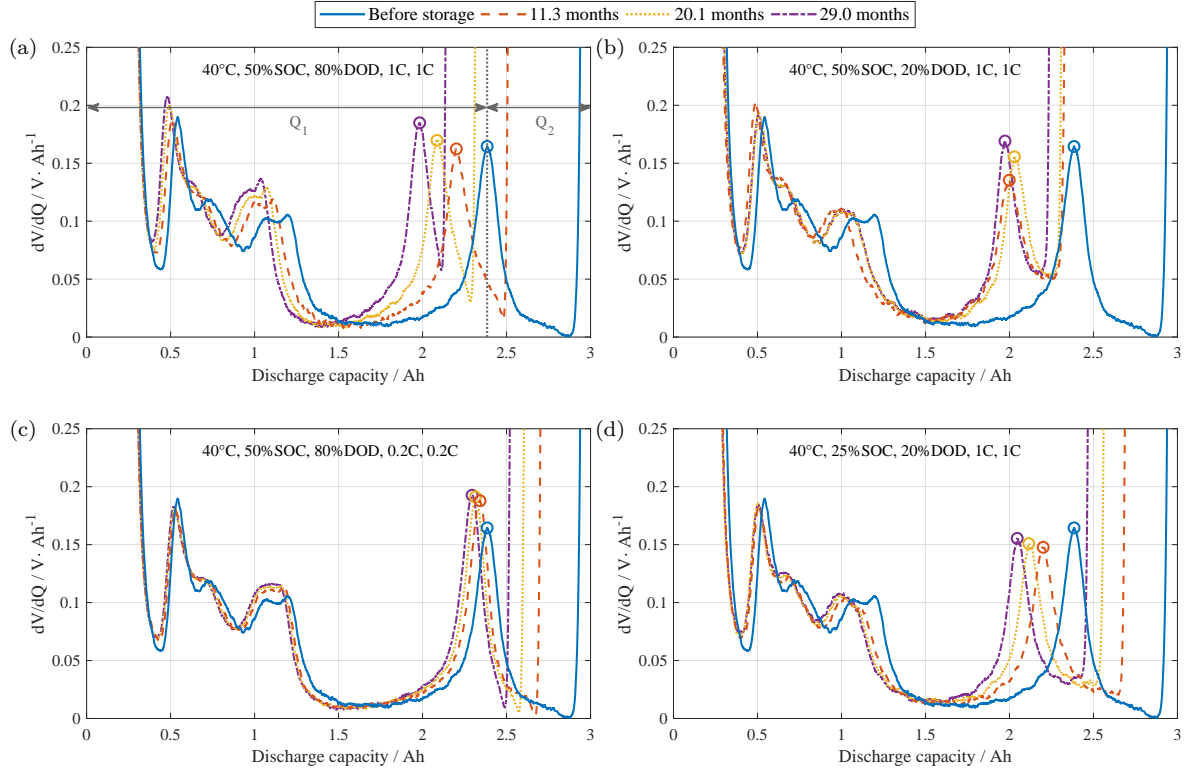


Figure 4.13: DVA of selected TPs cycled at 40 °C with different C-rates and DOC at different points in time during the aging study: (a) $DOC = 80\%$ around $SOC = 50\%$ with 1C/1C. (b) $DOC = 20\%$ around $SOC = 50\%$ with 1C/1C. (c) $DOC = 80\%$ around $SOC = 50\%$ with 0.2C/0.2C. (d) $DOC = 20\%$ around $SOC = 25\%$ with 1C/1C. The circles show in each dV/dQ -curve the peak which is related to the single phase of LiC_{12} in the graphite-anode. The DVA is applied on the discharge phase of the OCV measurements described in Subsection 4.3.

which is related to the single phase of LiC_{12} in the graphite-anode and the other visible peaks are shifting to the left, however, all peaks remain in the same shape. Consequently, in **Figure 4.12** a decrease of both Q_1 and Q_2 of the TPs at the higher C-rates of 1C/1C is observable. Hence, it can be assumed that in addition to the LLI due to SEI growth the LAM on the anode causes a supplementary capacity decrease. **Figure 4.13a** and **Figure 4.13b** show the influence of DOC on the DVA-curves. For the TP with $DOC = 80\%$ around $SOC = 50\%$ a strong and steady decrease of Q_1 and Q_2 is observable. The same applies for the TP with $DOC = 20\%$ around $SOC = 25\%$ (see **Figure 4.13d**), however, the decrease is weaker than observed for the TP with $DOC = 80\%$ around $SOC = 25\%$. In contrast, the TP with $DOC = 20\%$ around $SOC = 50\%$ shows from the first to the second DVA-curve a strong decrease of both Q_1 and Q_2 . Hence, at the beginning Q_1 decreases by the LAM of the graphite anode and Q_2 decreases with the LLI. Then, only Q_2 continues decreasing and Q_1 remains almost constant, what means that no further LAM occurs and the capacity decreases only by LLI. Although the development of Q_2 is connected with LLI due to SEI growth, further aging experiments revealed that the capacity is not irreversible lost for this and similar TP with cycles around $SOC = 50\%$. However, LLI remains the dominating factor for capacity fade due to the superposed calendar and cycle aging, which can be identified by the marked reductions in Q_2 for all shown dV/dQ -curves. Due to the fact that the capacity fade correlates with the decrease of Q_2 , the observed aging effects result mostly from the SEI growth on the graphite anode. Since the

capacity fade and Q_2 decrease is significantly stronger for the cycle aging TPs than for the calendar aging TPs at the same temperatures and SOC-ranges, it can be stated that the constant cyclization leads to an accelerated SEI growth.

4.6.2.3 Electrochemical impedance spectroscopy

The EIS-curves in **Figure 4.14** show the development of the impedances for selected TPs cycled at 40 °C with different C-rates and DOC at selected points in time during the aging study. This analysis was derived similarly to the EIS in **Section 4.6.1**. The development of $R_{AC,1000\text{ Hz}}$, $R_{AC,5\text{ Hz}}$, Z_{\max} , and Z_{\min} together with the real and imaginary part of Z_{\min} and Z_{\max} are summarized in **Table 4.9**, where the relative change of each parameter from the beginning until the end of the aging study is shown for the selected TPs of **Figure 4.14**. For all shown TPs the impedance increase due to the calendar and cycle aging leads to a shift of the EIS-curves to higher real and imaginary parts of the impedances, however, the increase of the inner ohmic resistance represented with $R_{AC,1000\text{ Hz}}$ dominates the right shift of all EIS-curves.

The TP with $DOC = 80\%$ around $SOC = 50\%$ with 0.2 C/0.2 C in **Figure 4.14c** shows the smallest changes of the EIS-curves as also observed in the capacity decrease and DVA-curves. The TPs with

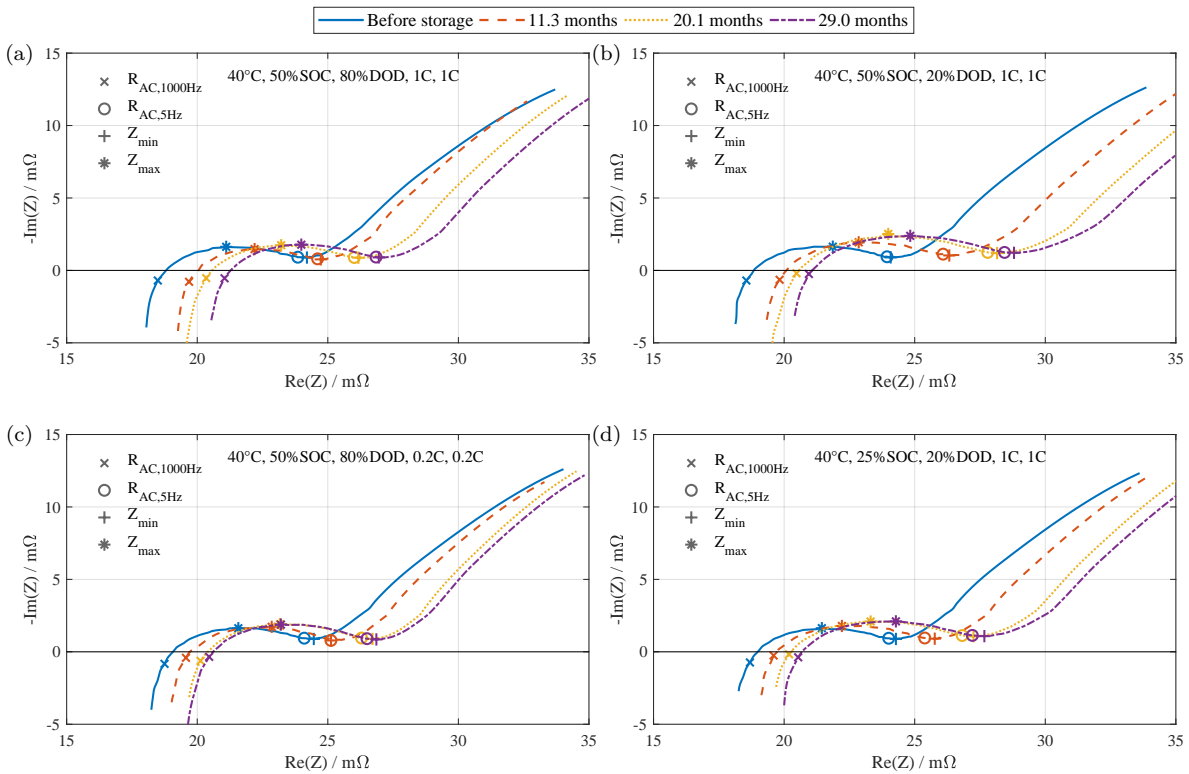


Figure 4.14: EIS of selected TPs cycled at 40 °C with different C-rates and DOC at selected points in time during the aging study: (a) $DOC = 80\%$ around $SOC = 50\%$ with 1 C/1 C. (b) $DOC = 20\%$ around $SOC = 50\%$ with 1 C/1 C. (c) $DOC = 80\%$ around $SOC = 50\%$ with 0.2 C/0.2 C. (d) $DOC = 20\%$ around $SOC = 25\%$ with 1 C/1 C. The Nyquist-plots are drawn with an inverse y-axis due to the common form of presentation. The parameters $R_{AC,1000\text{ Hz}}$, $R_{AC,5\text{ Hz}}$, Z_{\min} and Z_{\max} are displayed each with markers. The EIS measurement procedure is described in Subsection 4.3.

Table 4.9: Relative change of EIS-parameters from the beginning until the end of the aging study for selected TPs.

| | 50 % | 50 % | 50 % | 25 % |
|-------------------------|-------------|-------------|-------------|-------------|
| TP-SOC | 50 % | 50 % | 50 % | 25 % |
| -DOC | 80 % | 80 % | 20 % | 20 % |
| -C-rate | 1.0 C/1.0 C | 0.2 C/0.2 C | 1.0 C/1.0 C | 1.0 C/1.0 C |
| Parameters | | | | |
| $R_{AC,1000\text{ Hz}}$ | 13.8 % | 9.1 % | 12.9 % | 9.9 % |
| $R_{AC,5\text{ Hz}}$ | 12.6 % | 10.0 % | 18.8 % | 13.3 % |
| Z_{\min} | 5.0 % | 15.5 % | 47.2 % | 31.9 % |
| $Re(Z_{\min})$ | 5.1 % | 16.0 % | 47.5 % | 32.1 % |
| $Im(Z_{\min})$ | 0.9 % | -3.6 % | 35.3 % | 22.1 % |
| Z_{\max} | 14.7 % | 7.4 % | 29.5 % | 41.5 % |
| $Re(Z_{\max})$ | 17.4 % | 3.8 % | 24.3 % | 46.8 % |
| $Im(Z_{\max})$ | 9.0 % | 15.4 % | 45.6 % | 28.8 % |

higher C-rates of 1 C/1 C show a stronger increase of the real and imaginary part of the impedances in the EIS-curves in **Figure 4.14a**.

The inner resistance represented with $R_{AC,1000\text{ Hz}}$ increases slightly less for the TP with $DOC = 20\%$ around $SOC = 50\%$ (see **Figure 4.13b**) and the TP with $DOC = 20\%$ around $SOC = 25\%$. However, in this TP with smaller DOC the impedances increase stronger for all lower frequencies than for the TP with $DOC = 80\%$ although the capacity decrease was stronger for this TP.

The development of the EIS-curves of both TPs with $DOC = 20\%$ can be compared better with the EIS parameters in **Table 4.9** because the curves show almost no difference to each other. Even though the increase of $R_{AC,1000\text{ Hz}}$ is almost in the same magnitude of both TPs, the impedance values of Z_{\min} increase stronger for the TP with cycles around $SOC = 50\%$. However, the impedance values of Z_{\max} increase stronger for the TP with cycles around $SOC = 25\%$. Hence, no clear influence of the cycles SOC-range on the impedance increase can be stated.

A possible reason for the described EIS parameter development could be the difficult determination of Z_{\min} and Z_{\max} due to the flat curve shape in the respective areas. Little absolute measurement uncertainties lead to a big relative deviation of the extracted parameters' values. However, comparing the capacity decrease of the selected TPs of **Figure 4.12** with the impedance increase in **Table 4.9** no clear correlation can be stated between these two parameters for all the different cycle aging influence factors.

5 Aging model development of the investigated LiFePO₄-graphite cell

In this chapter, the aging models are developed for both the relative discharge capacity C_{disch} and the relative resistance $R_{\text{DC},10\text{s}}$ on the base of the measurement data from the static calendar and cycle aging study presented in **Chapter 4**. For better comparability, in the following Q_{loss} represents the decrease/loss of the relative discharge capacity C_{disch} and R_{inc} the increase of the relative resistance $R_{\text{DC},10\text{s}}$. First, the calendar aging model is presented in **Section 5.1** and followed by the development of the cycle aging model in **Section 5.2**. Finally, the superposition of the calendar and cycle aging model within a combined aging model is shown in **Section 5.3**.

5.1 Calendar aging model

5.1.1 Model limitations

The measurement data shown in **Section 4.6** revealed, that the capacity of the TPs with 0% SOC at 25 °C and 40 °C increased at the beginning of the aging study and decreased thereafter steadily. Furthermore, the resistance of most of the TPs decreased at the beginning of the aging study slightly and increased afterward continuously. These inverse aging trends at the beginning of the test duration, which could be related to the effects of the anode overhang area, are not covered by the aging model. Due to the fact, that the aging model is developed for the application in BESS lifetime simulations, the fade of the usable capacity and the decrease of the performance in limited temperature and SOC ranges are required. Hence, the influence of the anode overhang effect is neglected, because BESS are normally not operated at very low or high SOC where this effects mainly occurs. Although the measured capacity values can deviate from the theoretical usable capacity maximal by about $\pm 2.2\%$ for the TPs with 0% and 100% SOC due to the effect of the anode overhang areas, all measured capacity values are used for the parametrization of the aging model without any adaption. Similarly, the measured resistance values are used without any adaption for the parametrization of the aging model.

5.1.2 Development

The calendar aging model to be developed here should be able to represent the individual influence on the aging of the temperature T , SOC , and passed time t since BOL. Furthermore, the model should be described with formulas that only depend on the influencing parameters (T , SOC , and t) and a small set of constants that are determined separately for each influence parameter. Therefore, the development of Q_{loss} dependent on T , SOC , and t is expressed by **Equation 5.1** and of R_{inc} with **Equation 5.2** in the form of a product that consists of three factors that represent the influence of

T with $k_{\text{temp},Q_{\text{loss}}/R_{\text{inc}}}(T)$, of SOC with $k_{\text{SOC},Q_{\text{loss}}/R_{\text{inc}}}(T)$ and of t individually. The formulas' factors are derived separately in the following and their parameters are shown in **Table 5.1**.

$$Q_{\text{loss,cal}}(T, SOC, t) = k_{\text{temp},Q_{\text{loss}}}(T) \cdot k_{\text{SOC},Q_{\text{loss}}}(SOC) \cdot \sqrt{t} \quad (5.1)$$

$$R_{\text{inc,cal}}(T, SOC, t) = k_{\text{temp},R_{\text{inc}}}(T) \cdot k_{\text{SOC},R_{\text{inc}}}(SOC) \cdot t \quad (5.2)$$

There are different methods to determine the model parameters with the measurement data of this calendar aging study because the test matrix was designed redundantly. In the following, the different possibilities to obtain the model parameters are explained, however, only the methods giving the best and most feasible results are applied in the aging model validation in **Section 5.1.3**.

5.1.2.1 Influence of time

Due to the fact that the rough trend of the capacity loss follows a square root dependance over time for most of TPs (see **Figure 4.5a** and **4.5c**), the time influence is therefore represented by the factor \sqrt{t} for Q_{loss} in accordance with the models shown in different publications [61; 71]. In contrast, the resistance increases rather linearly over time for most of TPs (see **Figure 4.5b** and **4.5d**). Consequently, the time influence is represented by the linear factor t for R_{inc} . However, the slight resistance increase for most of TPs at the beginning of the aging study cannot be represented with this aging model.

5.1.2.2 Influence of temperature

The temperature influence factor $k_{\text{temp},Q_{\text{loss,cal}}}(T)$ for $Q_{\text{loss,cal}}$ and $k_{\text{temp},R_{\text{inc,cal}}}(T)$ for $R_{\text{inc,cal}}$ can be modeled according to the Arrhenius-law, showing an exponential influence of the inverse of temperature on the resulting aging effect. Therefore the formula shown in **Equation 5.3** and **Equation 5.4**, which is commonly used to model the temperature influence on aging in different publications [66; 75], is applied to determine $k_{\text{temp},Q_{\text{loss}}}(T)$ for Q_{loss} and $k_{\text{temp},R_{\text{inc}}}(T)$ for R_{inc} each with individual parameters but with the same formula structure. Due to the fact that the SOC influences the temperature non-linearly, all values have to be related to a reference temperature and SOC. Here the reference conditions are set with $T_{\text{ref}} = 25^\circ\text{C} = 298.15\text{K}$ and $SOC_{\text{ref}} = 100\%$. In addition to the only influence parameter T , the formula consists of $R = 8.314\text{J mol}^{-1}\text{K}^{-1}$ representing the universal gas constant and two parameters representing the individual aging of the investigated cell: the reference aging rates $k_{\text{ref},Q_{\text{loss}}}$ and $k_{\text{ref},R_{\text{inc}}}$ and the activation energies $E_{\text{a},Q_{\text{loss}}}$ and $E_{\text{a},R_{\text{inc}}}$, which are determined in the following for Q_{loss} and R_{inc} separately.

$$k_{\text{temp},Q_{\text{loss}}}(T) = k_{\text{ref},Q_{\text{loss}}} \cdot \exp\left(-\frac{E_{\text{a},Q_{\text{loss}}}}{R} \left(\frac{1}{T} - \frac{1}{T_{\text{ref}}}\right)\right) \quad (5.3)$$

$$k_{\text{temp},R_{\text{inc}}}(T) = k_{\text{ref},R_{\text{inc}}} \cdot \exp\left(-\frac{E_{\text{a},R_{\text{inc}}}}{R} \left(\frac{1}{T} - \frac{1}{T_{\text{ref}}}\right)\right) \quad (5.4)$$

The reference aging rates $k_{\text{ref},Q_{\text{loss}}}$ and $k_{\text{ref},R_{\text{inc}}}$ can be obtained by transposing **Equation 5.1** and **Equation 5.2** respectively, which lead to **Equation 5.5** and **Equation 5.6**. The factors representing

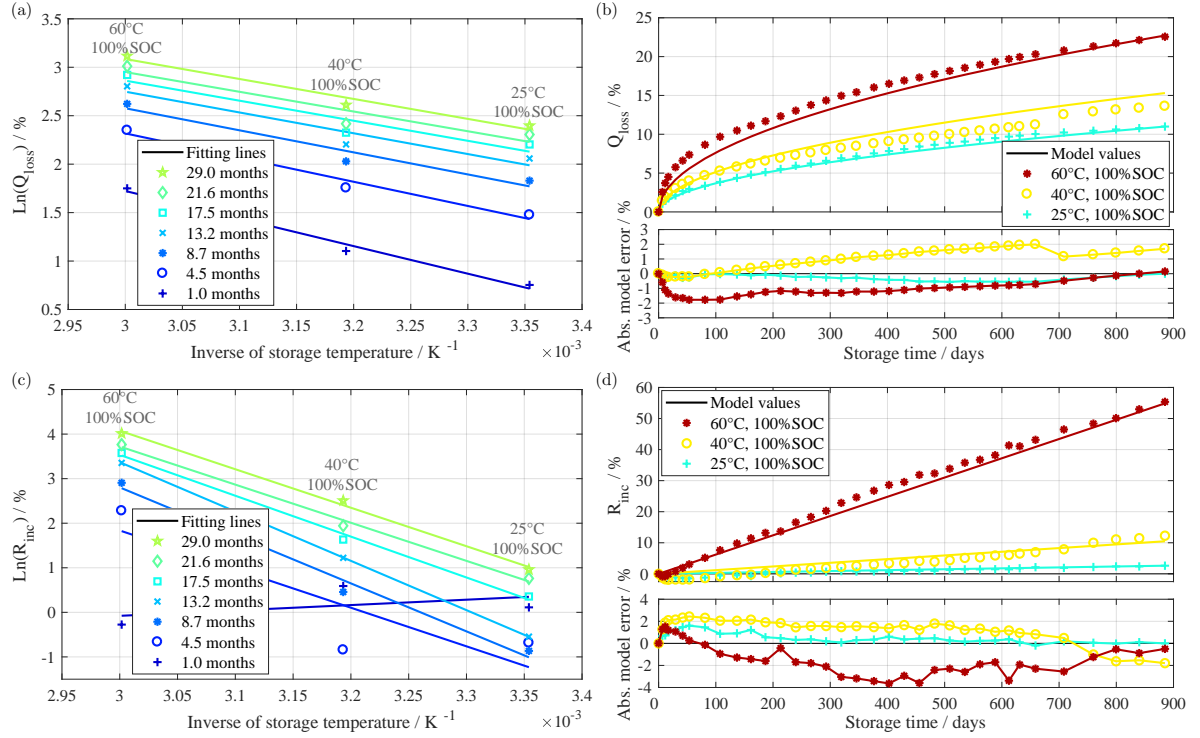


Figure 5.1: Influence of temperature on the aging of Q_{loss} and R_{inc} at $SOC = 100\%$ evaluated for the temperatures $25\text{ }^{\circ}\text{C}$, $40\text{ }^{\circ}\text{C}$ and $60\text{ }^{\circ}\text{C}$:

(a) Results of evaluating Q_{loss} with Equation 5.7 and applying a linear fitting for each shown point in time. (c) Results of evaluating R_{inc} with Equation 5.8 and applying a linear fitting for each shown point in time. (b)/(d) Comparison of measured values of $Q_{\text{loss}}/R_{\text{inc}}$ with model values determined by Equation 5.1/Equation 5.2. The lower panels show the absolute model error in %.

the SOC influence $k_{SOC, Q_{\text{loss}}}(SOC)$ and $k_{SOC, R_{\text{inc}}}(SOC)$ can be set to a value of 1 because k_{ref} is defined with $SOC_{\text{ref}} = 100\%$. By using the reference temperature T_{ref} and therefore applying $T = 25\text{ }^{\circ}\text{C}$ in **Equation 5.9**, the exponential term of **Equation 5.3** also obtains a value of 1. Thus $k_{\text{ref}, Q_{\text{loss}}}$ can be determined by dividing the measured value of Q_{loss} at the end of the aging study ($t = t_{\text{end}}$) from the TP with $T = 25\text{ }^{\circ}\text{C}$ and $SOC = 100\%$ with the time factor $\sqrt{t_{\text{end}}}$. The parameter $k_{\text{ref}, R_{\text{inc}}}$ can be calculated similarly by dividing the measured value of R_{inc} at the end of the aging study ($t = t_{\text{end}}$) from the TP with $T = 25\text{ }^{\circ}\text{C}$ and $SOC = 100\%$ with the time factor t_{end} .

$$k_{\text{ref}, Q_{\text{loss}}} = \frac{Q_{\text{loss, cal}}(T_{\text{ref}} = 25\text{ }^{\circ}\text{C}, SOC_{\text{ref}} = 100\%, t_{\text{end}})}{k_{SOC, Q_{\text{loss}}}(SOC_{\text{ref}} = 100\%) \cdot \sqrt{t_{\text{end}}}} \quad (5.5)$$

$$k_{\text{ref}, R_{\text{inc}}} = \frac{R_{\text{inc, cal}}(T_{\text{ref}} = 25\text{ }^{\circ}\text{C}, SOC_{\text{ref}} = 100\%, t_{\text{end}})}{k_{SOC, R_{\text{inc}}}(SOC_{\text{ref}} = 100\%) \cdot t_{\text{end}}} \quad (5.6)$$

Although all parameters are thereby available to determine respectively $E_{a, Q_{\text{loss}}}$ in **Equation 5.3** and $E_{a, R_{\text{inc}}}$ in **Equation 5.4** by evaluating the aging of two TPs with the same SOC but different temperatures, $E_{a, Q_{\text{loss}}}$ and $E_{a, R_{\text{inc}}}$ are determined here with a fitting procedure to obtain better model results. Therefore, first **Equation 5.3** for $k_{\text{temp}, Q_{\text{loss}}}(T)$ and **Equation 5.4** for $k_{\text{temp}, R_{\text{inc}}}(T)$ are each inserted in **Equation 5.1** and **Equation 5.2** respectively. Then the equations for Q_{loss} and R_{inc} can be expressed in a linear form by applying the natural logarithm on both sides, getting **Equation 5.7**

and **Equation 5.8** respectively.

$$\ln(Q_{\text{loss}}(T, SOC_{\text{ref}} = 100\%, t)) = \underbrace{-\frac{E_{a,Q_{\text{loss}}}}{R}}_a \frac{1}{T} + \underbrace{\left(\frac{E_{a,Q_{\text{loss}}}}{R T_{\text{ref}}} + \ln(k_{\text{ref},Q_{\text{loss}}} \cdot \sqrt{t})\right)}_b \quad (5.7)$$

$$\ln(R_{\text{inc}}(T, SOC_{\text{ref}} = 100\%, t)) = \underbrace{-\frac{E_{a,R_{\text{inc}}}}{R}}_a \frac{1}{T} + \underbrace{\left(\frac{E_{a,R_{\text{inc}}}}{R T_{\text{ref}}} + \ln(k_{\text{ref},R_{\text{inc}}} \cdot t)\right)}_b \quad (5.8)$$

Again $k_{\text{SOC},Q_{\text{loss}}}(SOC)$ and $k_{\text{SOC},R_{\text{inc}}}(SOC)$ can be set to a value of 1, because the equations are evaluated for $SOC_{\text{ref}} = 100\%$. Thus, derive linear formulas can be derived in the form $a \cdot \frac{1}{T} + b$. This linear relationship is shown in **Figure 5.1a** and **5.1c** respectively for Q_{loss} and R_{inc} , where **Equation 5.7** and **Equation 5.8** are evaluated for selected points in time.

Here, only the temperatures 25 °C, 40 °C and 60 °C are shown and used for the fitting procedure. The aging of the TPs with 0 °C and 10 °C show ambiguous results and might, in comparison to the little calendar aging at the low temperatures, be strongly influenced by temperature deviations due to the periodic CM at 25 °C. For each point in time shown in **Figure 5.1**, a linear fitting is applied resulting in lines with almost the same slope (factor a) at every point in time but shifted with an offset (factor b) dependent on the point in time. With this linear fitting in form of $a \cdot \frac{1}{T} + b$, $E_{a,Q_{\text{loss}}}$ and $E_{a,R_{\text{inc}}}$ can be obtained using the slope a at any time of the aging study (thus independent of b) with **Equation 5.9** for Q_{loss} and for R_{inc} with **Equation 5.10**.

$$E_{a,Q_{\text{loss}}}(t_{\text{end}}) = -a_{Q_{\text{loss}}}(t_{\text{end}}) \cdot R \quad (5.9)$$

$$E_{a,R_{\text{inc}}}(t_{\text{end}}) = -a_{R_{\text{inc}}}(t_{\text{end}}) \cdot R \quad (5.10)$$

However, the model is parametrized by evaluating the slope at the end of the aging study ($t_{\text{end}} = 29$ months) leading to better model results. Having determined $E_{a,Q_{\text{loss}}/R_{\text{inc}}}$, the same fitting could be used to determine $k_{\text{ref},Q_{\text{loss}}}$ and $k_{\text{ref},R_{\text{inc}}}$ by transposing **Equation 5.7** and **Equation 5.8** respectively. Nevertheless, better model results are obtained by determining $k_{\text{ref},Q_{\text{loss}}}$ and $k_{\text{ref},R_{\text{inc}}}$ by applying $T_{\text{ref}} = 25\text{ °C} = 298.15\text{ K}$ in **Equation 5.5** and **Equation 5.6** respectively. The results of the aging model with a static $SOC = 100\%$ for the temperatures 25 °C, 40 °C and 60 °C are compared with measured values in **Figure 5.1b** for Q_{loss} and in **Figure 5.1d** for R_{inc} . In **Figure 5.1b** and **5.1d**, the lower panels show the absolute model errors in % for each TP for Q_{loss} and R_{inc} respectively. Q_{loss} can be estimated with this model for the TP at 25 °C and with $SOC = 100\%$ with almost no error. The model values deviate for the TPs with 40 °C and 60 °C up to 2 % but follow the trend of the measured values well. The same observations apply for R_{inc} . However, the model values deviate for 60 °C up to 4 % in the middle time segment of the aging study.

5.1.2.3 Influence of SOC

As shown in **Figure 4.5c** and **4.5d**, no linear trend is observable for the influence of SOC on calendar aging of Q_{loss} and R_{inc} . Furthermore, the aging trend neither follows the trend of the OCV-values of

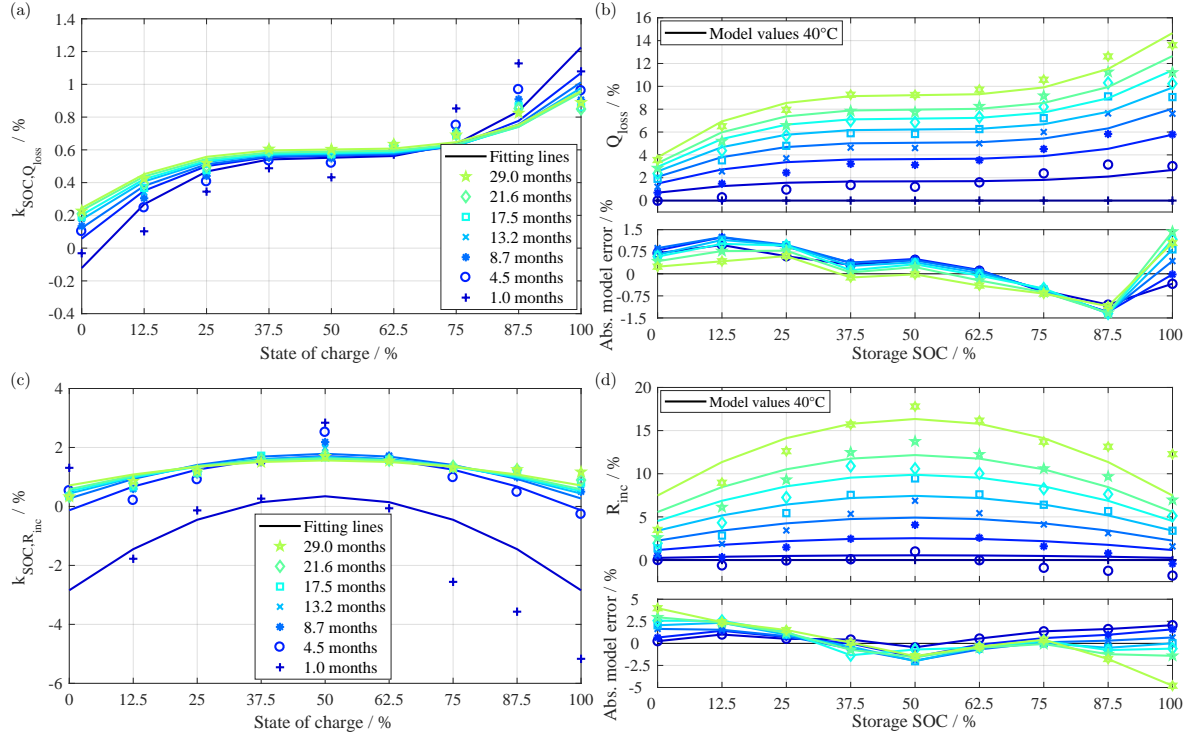


Figure 5.2: Influence of SOC on the aging of Q_{loss} and R_{inc} evaluated at 40 °C: (a) Results of evaluating Q_{loss} with Equation 5.11 and applying a fitting with a cubic function for each shown point in time. (c) Results of evaluating R_{inc} with Equation 5.13 and applying a fitting with a quadratic function for each shown point in time. (b)/(d) Comparison of measured values of $Q_{\text{loss}}/R_{\text{inc}}$ with model values determined by Equation 5.1/Equation 5.2. The lower panels show the absolute model error in %.

each SOC nor the open-circuit voltages of each TP at the beginning of the CM. However, empirical models for Q_{loss} and R_{inc} are applied respectively, which should be able to follow the aging trend of a long timescale only influenced by the particular storage SOC-values.

Although a slight capacity increase is possible due to the effect of the anode overhang areas as mentioned above, this aging model is parametrized by the measured trend over time with static storage conditions. In order to model the step-like shape of Q_{loss} over SOC shown in **Figure 4.5c**, a cubic function is applied to determine $k_{\text{SOC},Q_{\text{loss}}}$ dependent on SOC with **Equation 5.12**. Due to the rotational symmetry of Q_{loss} over SOC due to 50% SOC, the SOC parameter is subtracted by 0.5 in **Equation 5.12**. The fitting is performed with the TPs at 40 °C leading to more pronounced differentiation with the 9 storage SOC at this temperature. Then $k_{\text{SOC},Q_{\text{loss}}}$ can be determined by transposing **Equation 5.1** resulting in **Equation 5.11**. To obtain $k_{\text{SOC},Q_{\text{loss}}}$ correctly, $k_{\text{temp},Q_{\text{loss}}}(T)$ has to be adapted with $T = 40$ °C.

$$k_{\text{SOC},Q_{\text{loss}}}(SOC) = \frac{Q_{\text{loss,cal}}(T = 40 \text{ °C}, SOC, t)}{k_{\text{temp},Q_{\text{loss}}}(T = 40 \text{ °C}) \cdot \sqrt{t}} \quad (5.11)$$

$$k_{\text{SOC},Q_{\text{loss}}}(SOC) = c_{Q_{\text{loss}}}(SOC - 0.5)^3 + d_{Q_{\text{loss}}} \quad (5.12)$$

In **Figure 5.2a** the results of **Equation 5.11** are drawn for selected points in time over the SOC

of the TPs at 40 °C. The fitting lines are obtained by deriving a curve fit with **Equation 5.12** for each point in time including the whole SOC range. Even though the fitting lines of the first points in time deviate from the measured values, the fitting lines at the end of the aging study correspond well with the measurements. Therefore, the parameters $c_{Q_{\text{loss}}}$ and $d_{Q_{\text{loss}}}$ are obtained with a curve fit of $k_{\text{SOC},Q_{\text{loss}}}$ at the end of aging study ($t_{\text{end}} = 29$ months), resulting in the parameter values shown in **Table 5.1** for Q_{loss} . **Figure 5.2b** shows the model values calculated by **Equation 5.1** by applying the here determined $k_{\text{SOC},Q_{\text{loss}}}$ factor in comparison with the measured values of the TPs at 40 °C. The lower panel again shows the absolute model error in %, which stays below 1.5 % over the whole SOC range during the entire aging study. However, the resulting capacity losses at the TPs with $\text{SOC} = 87.5\%$ and 100% show larger errors compared to the lower SOC.

In order to model the shape of R_{inc} over SOC shown in **Figure 4.5d**, a quadratic function is applied to determine $k_{\text{SOC},R_{\text{inc}}}$ dependent on SOC with **Equation 5.14**. Due to the axial symmetry of Q_{loss} over SOC due to 50 % SOC, the SOC parameter is subtracted by 0.5 in **Equation 5.14**. Similar to the procedure to determine $k_{\text{SOC},Q_{\text{loss}}}$, the fitting for $k_{\text{SOC},R_{\text{inc}}}$ is executed with the TPs at 40 °C. Again $k_{\text{SOC},R_{\text{inc}}}$ can be determined by transposing **Equation 5.2** resulting in **Equation 5.13** and using $k_{\text{temp},R_{\text{inc}}}(T)$ with $T = 40$ °C.

$$k_{\text{SOC},R_{\text{inc}}}(SOC) = \frac{R_{\text{inc,cal}}(T = 40 \text{ °C}, SOC, t)}{k_{\text{temp},R_{\text{inc}}}(T = 40 \text{ °C}) \cdot t} \quad (5.13)$$

$$k_{\text{SOC},R_{\text{inc}}}(SOC) = c_{R_{\text{inc}}}(SOC - 0.5)^2 + d_{R_{\text{inc}}} \quad (5.14)$$

In **Figure 5.2c** the results of **Equation 5.13** are drawn for selected points in time over the SOC of the TPs at 40 °C. The fitting lines are obtained by deriving a curve fit with **Equation 5.14** for each point in time including the whole SOC-range. Again the fitting lines of the first points in time deviate from the measured values, however, the fitting lines at the end of the aging study match well the measured values. Thus, the parameters $c_{R_{\text{inc}}}$ and $d_{R_{\text{inc}}}$ are obtained with a curve fit of $k_{\text{SOC},R_{\text{inc}}}$ at the end of aging study ($t_{\text{end}} = 29$ months), resulting in the parameter values shown in **Table 5.1** for R_{inc} . **Figure 5.2d** shows the model values calculated by **Equation 5.2** by applying the here determined $k_{\text{SOC},R_{\text{inc}}}$ factor in comparison with the measured values of the TPs at 40 °C. The lower panel again shows the absolute model error in %, which stays below 2.5 % for most of the SOC values during the entire aging study. However, larger model errors result at $\text{SOC} = 0\%$ and 100% .

Table 5.1: Q_{loss} and R_{inc} aging model reference values and parameters.

| Parameter | Q_{loss} | R_{inc} |
|---------------------------|------------------------------------|--|
| T_{ref} | 298.15 K | 298.15 K |
| SOC_{ref} | 100 % | 100 % |
| k_{ref} | $0.001\,257\,1 \text{ \%s}^{-0.5}$ | $3.4194 \times 10^{-8} \text{ \%s}^{-1}$ |
| a | -2059.8 K | -8638.8 K |
| b | 9.2644 | 29.992 |
| E_a | $17.126 \text{ kJ mol}^{-1}$ | $71.827 \text{ kJ mol}^{-1}$ |
| c | 2.8575 | -3.3903 |
| d | 0.60225 | 1.5604 |

5.1.3 Validation

Subsequent to the aging model development which proved a good consistency for static conditions, here the performance of the aging model for dynamic storage conditions is evaluated with the measurements from the dynamic calendar aging study (see **Section 4.5.4**). To apply the model equations with variable temperatures or SOC over time, a differential form of the aging models is derived by differentiating **Equation 5.1** with respect to time for Q_{loss} getting **Equation 5.15** and differentiating **Equation 5.2** for R_{inc} resulting in **Equation 5.16**.

$$\frac{dQ_{\text{loss}}}{dt}(T, SOC, t) = q_{\text{loss}}(T, SOC, t) = k_{\text{temp}, Q_{\text{loss}}}(T) \cdot k_{\text{SOC}, Q_{\text{loss}}}(SOC) \cdot (2\sqrt{t})^{-1} \quad (5.15)$$

$$\frac{dR_{\text{inc}}}{dt}(T, SOC) = r_{\text{inc}}(T, SOC) = k_{\text{temp}, R_{\text{inc}}}(T) \cdot k_{\text{SOC}, R_{\text{inc}}}(SOC) \quad (5.16)$$

Furthermore, it has to be identified how to apply the aging models correctly when the storage conditions are varied. The results of the dynamic calendar aging study show (see **Figure 5.3**) the independence of the order of storage conditions. Additionally, it can be concluded that the calendar aging rate is dependent on the current SOH. Thus, the particular SEI growth depends on former aging history (SEI thickness). Hence, to determine the differential capacity loss q_{loss} when varying the storage conditions, the virtual time t^* is defined, representing the time until the same Q_{loss} is reached under the new storage conditions. As the resistance increase is constant over time, no additional measures for time compensation of R_{inc} have to be taken. The virtual time t^* can be derived by solving **Equation 5.1** for time resulting in **Equation 5.17** for Q_{loss} .

$$t_{Q_{\text{loss}}}^{\text{cal}}(T, SOC, Q_{\text{loss}}) = \left(\frac{Q_{\text{loss}}}{k_{\text{temp}, Q_{\text{loss}}}(T) \cdot k_{\text{SOC}, Q_{\text{loss}}}(SOC)} \right)^2 \quad (5.17)$$

Thus, when applying the aging model with changing storage conditions, the virtual time t^* has to be determined for each time step. Then t^* is applied to calculate the differential capacity loss q_{loss} in the next time interval with new storage conditions.

Based on these equations for the application of the aging models of Q_{loss} and R_{inc} , the results of the dynamic calendar aging study can be compared with the developed aging model. For selected TPs (see **Table 4.5**) **Figure 5.3** shows the measured aging results in comparison with the model values for Q_{loss} on the left side with **Figure 5.3a**, **5.3c**, and **5.3e** and for R_{inc} on the right side with **Figure 5.3b**, **5.3d** and **5.3f**. In every plot, the lower panel shows the absolute model error in % compared to the measured values. The storage conditions of each TP are switched 7 times each at time intervals of about 4 weeks. The results of all TPs of this dynamic calendar aging study are summarized in **Table 5.2** alongside with the absolute model error of Q_{loss} and R_{inc} at the end of the test.

Figure 5.3a/5.3b represent the TP7/TP8 with switching between the storage temperatures 0 °C and 60 °C at storage $SOC = 100\%$ with two cells. TP7 (blue) starts with 0 °C and TP8 (red) with 60 °C. Here, always after two-time intervals, the two cells reach almost the same Q_{loss} value, proving the theory of independence of the order of storage conditions. The model values for each cell very closely follow the measured values even when the storage temperature changes. The error increases slightly over time but underestimates Q_{loss} by less than 1%. For R_{inc} the observations are different since the

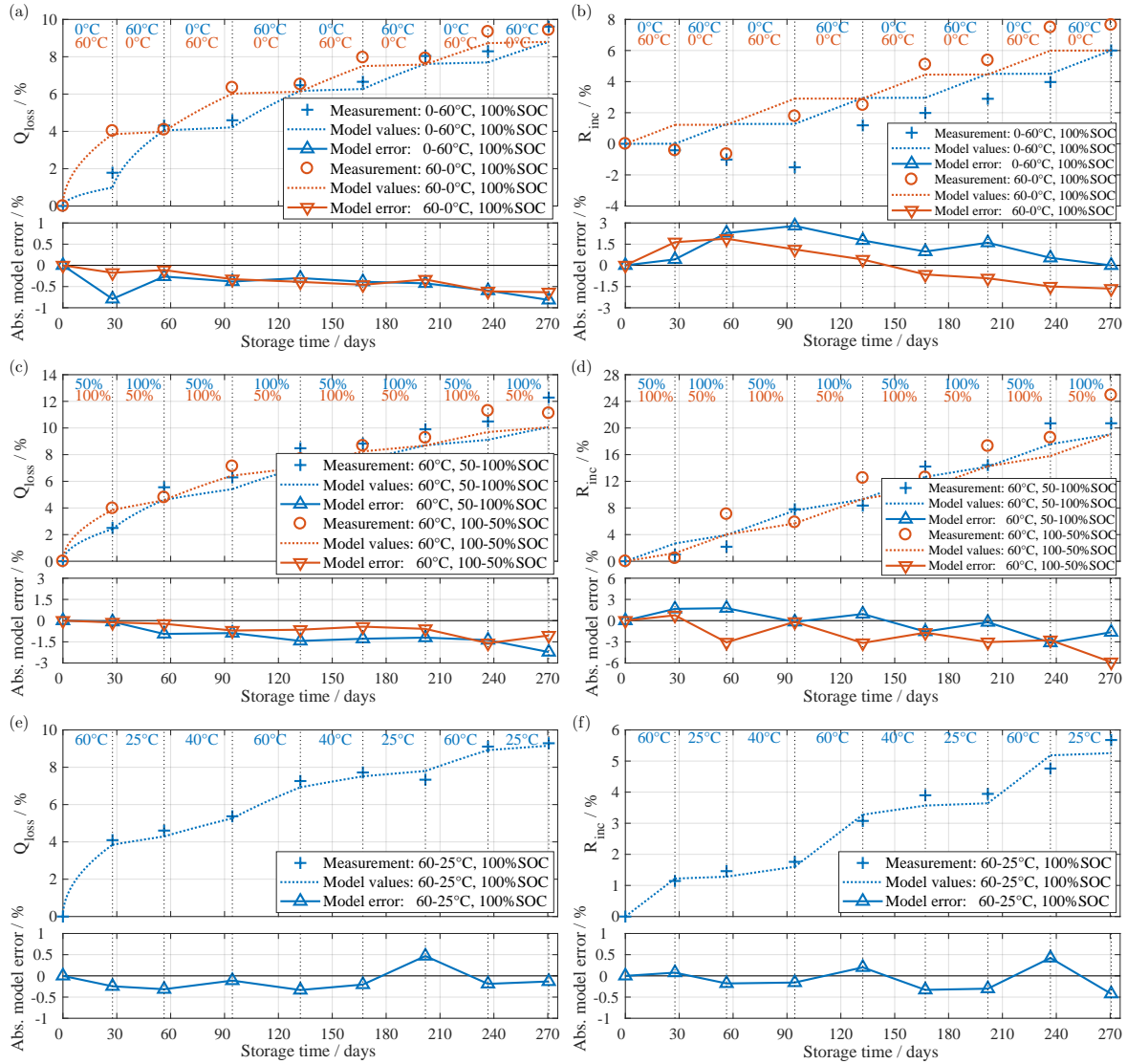


Figure 5.3: Aging model validation with dynamic calendar aging study over 270 days with 8 intervals each with constant storage conditions. Each measurement represents one cell whose storage condition, temperature or SOC, is changed after one interval according to the test matrix Table 4.5. In every plot, the lower panel shows the absolute model error in % compared to the measured values. The plots on the left side represent the capacity loss and the plots on the right side resistance increase of each TP. (a/b) TP7/TP8 with switching between storage temperature 0 °C and 60 °C at storage SOC = 100 %. TP7 (blue) starts with 0 °C and TP8 (red) with 60 °C. (c/d) TP13/TP14 with switching between storage SOC = 50 % and 100 % at storage temperature 60 °C. TP13 (blue) starts with SOC = 50 % and TP14 (red) with SOC = 100 %. (e/f) TP15 with changing storage temperature dynamically between 60 °C, 25 °C and 40 °C at storage SOC = 100 %.

Table 5.2: Absolute model errors of Q_{loss} and R_{inc} of all TPs of the dynamic calendar aging study.

| Test point | Temperature | SOC | Absolute model error at EOT | |
|------------|-------------|----------|-----------------------------|------------------|
| | | | Q_{loss} | R_{inc} |
| TP1/TP2 | 25/40 °C | 100 % | +1.1 % / +1.2 % | +1.6 % / +1.6 % |
| TP3/TP4 | 25/60 °C | 100 % | +0.0 % / -0.3 % | -1.5 % / -0.8 % |
| TP5/TP6 | 40/60 °C | 100 % | -0.1 % / -0.1 % | -0.7 % / -2.4 % |
| TP7/TP8 | 0/60 °C | 100 % | -0.8 % / -0.6 % | +0.0 % / -1.6 % |
| TP9/TP10 | 60 °C | 0/50 % | -1.9 % / +0.5 % | -4.7 % / +6.9 % |
| TP11/TP12 | 60 °C | 0/100 % | -2.2 % / -1.9 % | -2.9 % / +0.0 % |
| TP13/TP14 | 60 °C | 50/100 % | -2.2 % / -1.1 % | -1.6 % / -5.9 % |
| TP15 | Dynamic | 100 % | -0.1 % | -0.4 % |

resistances decreased in this TP at the beginning. Afterward, the R_{inc} values of the two cells get closer again but do not match each other as well as the Q_{loss} values. Even though the model cannot represent the R_{inc} in the beginning, the subsequent increase is estimated with errors below 1.5 %.

Figure 5.3c/5.3d show the TP13/TP14 with alternating between the storage $SOC = 50\%$ and 100% at 60 °C with two cells. TP13 (blue) starts with $SOC = 50\%$ and TP14 (red) with $SOC = 100\%$. Again the two cells' Q_{loss} values each meet after two passed time intervals, but not as close as observed with TP7/TP8. The model values follow the measured values but underestimate the measured values by around 1.5 % at the end of the aging study. In contrast to the TP7/TP8, here the R_{inc} values remain close together over all intervals. Although the model values show an error of about 6 % for cell 2 at the end of the aging study, the model follows the trend of the measured values.

Figure 5.3e/5.3f illustrate the TP15 with changing storage temperature dynamically between 60 °C , 25 °C and 40 °C at storage $SOC = 100\%$ with one cell. Here, the model follows the measured Q_{loss} values very well and the model error is not increasing over time by remaining below 0.5 %. The same applies to R_{inc} , although the increase rates are changing stronger than seen for Q_{loss} .

5.2 Cycle aging model

5.2.1 Model limitations

The aging model to be developed in the following section is only able to cover the range of influence parameters which have been subject to the measurements. For example, the measurements showed almost no temperature influence on the cycle aging, however with temperatures lower than 25 °C or higher than 40 °C additional aging effects can be expected as mentioned in **Section 2.4.2**. In contrast to the static calendar aging study, the measurement data of the static cycle aging showed no capacity increase or resistance decrease at the beginning of the aging study. However, similar effects related to the effects of the anode overhang area can be expected for the cycle aging TPs as well, but are not covered by the aging model. Furthermore, the TPs with $DOCs < 80\%$ revealed unsteady aging trends with periods in which the capacity increases again, which is not described by the aging model.

5.2.2 Development

In order to create a combined aging model by superimposing the calendar aging with the cycle aging model, the cycle aging model has to represent the pure cycle aging. Therefore, the respective calendar

aging of each TP is subtracted from the cycle aging measurement values to obtain the pure cycle aging to be modeled. It is assumed, that the average SOC of the cyclization is the respective influence parameter of the underlying calendar aging. Hence, the calendar aging results of the respective TPs with the appropriate SOC and temperature due to the respective cycle aging TP are subtracted to obtain the pure cycle aging results of each CM. For example, the pure cycle aging of the reference TP6 with 80 % cycles around the average SOC of 50 % at 40 °C is obtained by subtracting the results of the calendar aging TP with a storage SOC of 50 % at 40 °C.

Furthermore, the cycle aging model should be able to represent the individual influence on the aging of the C-rate, the DOC, and the Ah-throughput in FEC since BOL. Similar to the calendar aging model, the cycle aging model should be described with formulas that only depend on the relevant influencing parameters (C-rate, DOC , and FEC) and a small set of constants that are determined separately for each influence parameter. Hence, the degradation of Q_{loss} dependent on C-rate, DOC , and FEC is expressed by **Equation 5.18** and of R_{inc} with **Equation 5.19** in the form of a product that consists of three factors that represent the influence of C-rate with $k_{\text{C-rate}, Q_{\text{loss}}/R_{\text{inc}}}(\text{C-rate})$, of DOC with $k_{\text{DOC}, Q_{\text{loss}}/R_{\text{inc}}}(DOC)$ and of FEC individually. The formulas' factors are derived separately in the following and their parameters are shown in **Table 5.3**.

$$Q_{\text{loss}, \text{cyc}}(\text{C-rate}, \text{DOC}, \text{FEC}) = k_{\text{C-rate}, Q_{\text{loss}}}(\text{C-rate}) \cdot k_{\text{DOC}, Q_{\text{loss}}}(DOC) \cdot \sqrt{\text{FEC}} \quad (5.18)$$

$$R_{\text{inc}, \text{cyc}}(\text{C-rate}, \text{DOC}, \text{FEC}) = k_{\text{C-rate}, R_{\text{inc}}}(\text{C-rate}) \cdot k_{\text{DOC}, R_{\text{inc}}}(DOC) \cdot \text{FEC} \quad (5.19)$$

5.2.2.1 Influence of Ah-throughput

For all the cycle aging TPs the capacity loss follows a square root dependance of the Ah-throughput for different C-rates and DOC (see **Figure 4.9c** and **4.10a**), the Ah-throughput is therefore represented with the factor $\sqrt{\text{FEC}}$ for Q_{loss} . In contrast, the resistance increases rather linearly over the Ah-throughput for all C-rates and DOC (see **Figure 4.9c** and **4.10b**). Consequently, the Ah-throughput influence is represented by the linear factor FEC for R_{inc} .

5.2.2.2 Influence of C-rate

For the parametrization of the C-rate influence factor $k_{\text{C-rate}, Q_{\text{loss}}/R_{\text{inc}}}(\text{C-rate})$, only the cycle aging TPs are evaluated which differ to each other only in the C-rate and thus the TPs with $DOC = 80\%$ cycles around $SOC = 50\%$ at 40 °C are selected. To obtain the pure cycle aging values $Q_{\text{loss}, \text{cyc}}$ and $R_{\text{inc}, \text{cyc}}$ of these TPs, the measured calendar aging $Q_{\text{loss}, \text{cal}}$ and $R_{\text{inc}, \text{cal}}$ of the TP with $SOC = 50\%$ at 40 °C is subtracted respectively. The pure cycle aging results are shown in **Figure 5.4b** for $Q_{\text{loss}, \text{cyc}}$ and in **Figure 5.4d** for $R_{\text{inc}, \text{cyc}}$.

In order to model the sole influence of the C-rate with the factor $k_{\text{C-rate}, Q_{\text{loss}}/R_{\text{inc}}}(\text{C-rate})$, the DOC influence factor $k_{\text{DOC}, Q_{\text{loss}}}(DOC)$ is set to the value of 1 for evaluation of the C-rate influence with the selected TPs. The C-rate influence factor $k_{\text{C-rate}, Q_{\text{loss}}/R_{\text{inc}}}(\text{C-rate})$ for Q_{loss} and $k_{\text{C-rate}, R_{\text{inc}}}(\text{C-rate})$ for R_{inc} can be modeled for Q_{loss} and R_{inc} with the same formula structure with **Equation 5.20** and

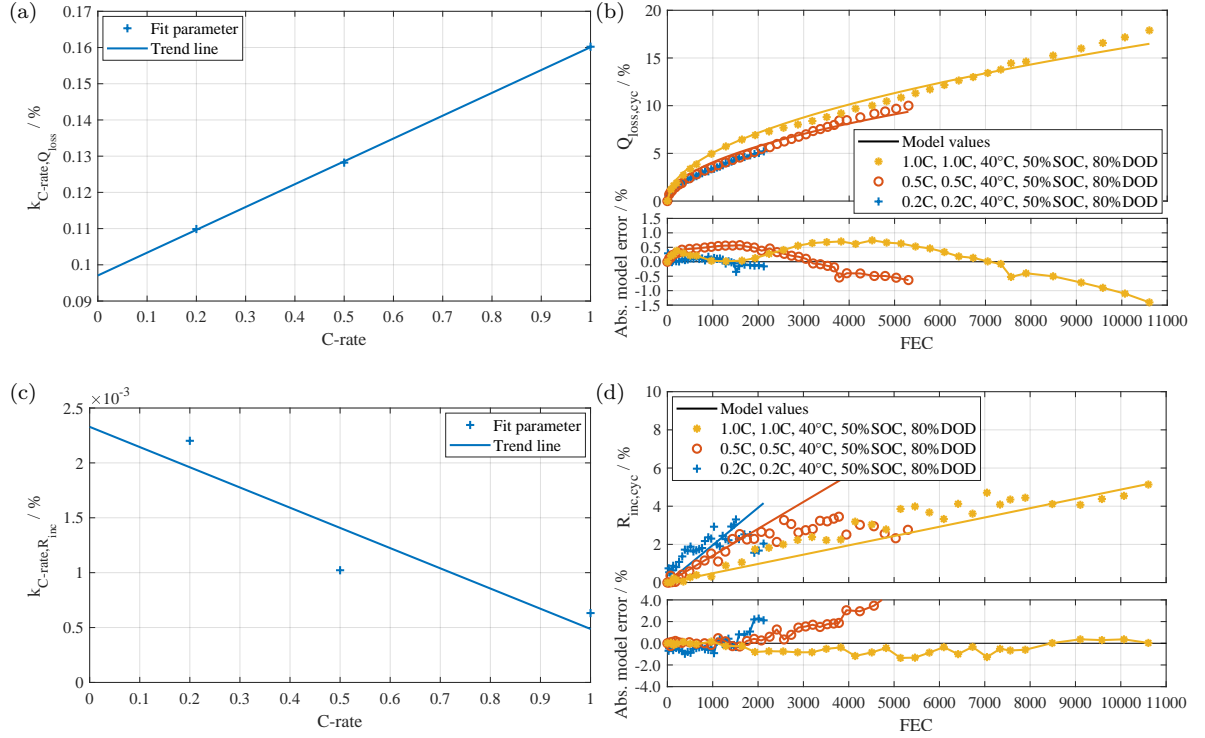


Figure 5.4: Influence of the C-rate on the pure cycle aging of Q_{loss} and R_{inc} for the TPs with $DOC = 80\%$ cycles around $SOC = 50\%$ at 40°C for the C-rates 0.2C , 0.5C and 1.0C : (a) $k_{\text{C-rate},Q_{\text{loss}}}(\text{C-rate})$ determined by fitting separately the aging curves of $Q_{\text{loss,cyc}}$ of the single C-rates with Equation 5.18. (b)/(d) Comparison of measured values of $Q_{\text{loss}}/R_{\text{inc}}$ with model values determined by Equation 5.18/Equation 5.19 and using the $k_{\text{C-rate},Q_{\text{loss}}}(\text{C-rate})$ values determined by Equation 5.20 and $k_{\text{C-rate},R_{\text{inc}}}(\text{C-rate})$ by Equation 5.21. The lower panels show the absolute model error in %.

Equation 5.21 respectively, however with different parameter values a and b :

$$k_{\text{C-rate},Q_{\text{loss}}}(\text{C-rate}) = a_{Q_{\text{loss}}} \cdot \text{C-rate} + b_{Q_{\text{loss}}} \quad (5.20)$$

$$k_{\text{C-rate},R_{\text{inc}}}(\text{C-rate}) = a_{R_{\text{inc}}} \cdot \text{C-rate} + b_{R_{\text{inc}}} \quad (5.21)$$

To obtain the parameters a and b , the C-rate influence factor $k_{\text{C-rate},Q_{\text{loss}}/R_{\text{inc}}}(\text{C-rate})$ is firstly determined by fitting separately the aging curves of $Q_{\text{loss,cyc}}$ and $R_{\text{inc,cyc}}$ of the single C-rates with **Equation 5.18** and **Equation 5.19** respectively. The resulting $k_{\text{C-rate},Q_{\text{loss}}/R_{\text{inc}}}(\text{C-rate})$ of the single C-rates are shown in **Figure 5.4a** for $Q_{\text{loss,cyc}}$ and **Figure 5.4c** for $R_{\text{inc,cyc}}$. Then, the parameters a and b can be obtained by applying **Equation 5.20** for $Q_{\text{loss,cyc}}$ and **Equation 5.21** for $R_{\text{inc,cyc}}$ individually in a curve fitting approach.

For $Q_{\text{loss,cyc}}$ the $k_{\text{C-rate},Q_{\text{loss}}}(\text{C-rate})$ values match a linear trend line over the evaluated C-rates. The resulting aging model curves are compared in the upper panel of **Figure 5.4b** with the measured values. The absolute model errors between the capacity loss values and the model values for $Q_{\text{loss,cyc}}$ is illustrated in the lower panel of **Figure 5.4b**. For the TP with the C-rates 0.2C and 0.5C , the model values follow very closely the pure cycle aging capacity loss values and the model error stays

below $\pm 0.5\%$. For the TP with 1.0 C, the model errors are with maximum $\pm 1.5\%$ at the EOT higher, however, the model follows the trend of the pure cycle aging capacity loss values. Smaller model errors at EOT could be obtained by choosing another exponent than 0.5 for the influence of the Ah-throughput. However, the overall course of all measured values for different TPs can be reproduced best by the exponent of 0.5. In contrast to the very clear trends of $Q_{\text{loss,cyc}}$, the pure cycle aging resistance increase values $R_{\text{inc,cyc}}$ are fluctuating around a linear trend shown in **Figure 5.4d**. For this reason, for $R_{\text{inc,cyc}}$ the $k_{\text{C-rate},R_{\text{inc}}}$ (C-rate) values do not match exactly a linear trend over the evaluated C-rates due to the uncertain determination of the rate of resistance increase for the respective C-rates. However, the same formula structure is chosen to determine the parameters of $k_{\text{C-rate},R_{\text{inc}}}$ (C-rate) with **Equation 5.21**. The absolute model errors for $R_{\text{inc,cyc}}$ are shown in the lower panel of **Figure 5.4d**: Only for the TP with 1 C, the model values follow quite well the determined pure cycle aging values of $R_{\text{inc,cyc}}$ with errors below 2%. For the lower C-rates 0.2 C and 0.5 C, the model values match only in the first 3000 FEC the determined values. Afterward, strong deviations in the determined pure cycle aging values of $R_{\text{inc,cyc}}$ are observed which cannot be estimated with the model.

5.2.2.3 Influence of DOC

As shown in **Figure 4.10a** and **4.10b**, no linear trend is observable for the influence of DOC on the aging of $Q_{\text{loss,cyc}}$ and $R_{\text{inc,cyc}}$. Again the capacity loss and resistance increase due to the pure cycle aging are evaluated by subtracting the measured calendar aging $Q_{\text{loss,cal}}/R_{\text{inc,cal}}$ of the TP with $\text{SOC} = 50\%$ at 40°C and are shown in **Figure 5.5b** for $Q_{\text{loss,cyc}}$ and in **Figure 5.5d** for $R_{\text{inc,cyc}}$ respectively.

Since the capacity loss trend of the TPs with $\text{DOC} < 80\%$ shows several trend changes the aging trend of the TPs with $\text{DOC} = 80\%$ and 100% are applied to the further TPs. Then, the formula for $k_{\text{DOC},Q_{\text{loss}}}$ (DOC) can be derived by evaluating **Equation 5.22** with $Q_{\text{loss,cyc}}$ at the EOT:

$$k_{\text{DOC},Q_{\text{loss}}}(DOC) = \frac{Q_{\text{loss,cyc}}(\text{C-rate} = 1 \text{ C}, \text{DOC}, \text{FEC})}{k_{\text{C-rate},Q_{\text{loss}}}(\text{C-rate} = 1 \text{ C}) \cdot \sqrt{\text{FEC}_{\text{end}}}} \quad (5.22)$$

$$k_{\text{DOC},Q_{\text{loss}}}(DOC) = c_{Q_{\text{loss}}}(DOC - 0.6)^3 + d_{Q_{\text{loss}}} \quad (5.23)$$

These values of $k_{\text{DOC},Q_{\text{loss}}(\text{EOT})}(DOC)$ at the EOT are shown in **Figure 5.5a** over the respective DOC. The trend line matches the course of the DOC influence on $k_{\text{DOC},Q_{\text{loss}}}(DOC)$ very close and can be obtained by using the formula of **Equation 5.23** and deriving the parameters c and d (see **Table 5.3**) with a curve fitting procedure. The results of evaluating **Equation 5.18** with the model values of $k_{\text{DOC},Q_{\text{loss}}}(DOC)$ are compared in **Figure 5.5b** in the upper panel with the determined capacity loss due to pure cycle aging. The absolute model errors in the lower panel show the big differences between the model and the determined pure cycle aging capacity loss, however, to the EOT the errors decrease again since the model was fitted to the values at EOT.

The DOC influence on the resistance increase due to pure cycle aging is modeled similarly to the capacity loss. The formula for $k_{\text{DOC},R_{\text{inc}}}(DOC)$ is derived by evaluating **Equation 5.24** with the

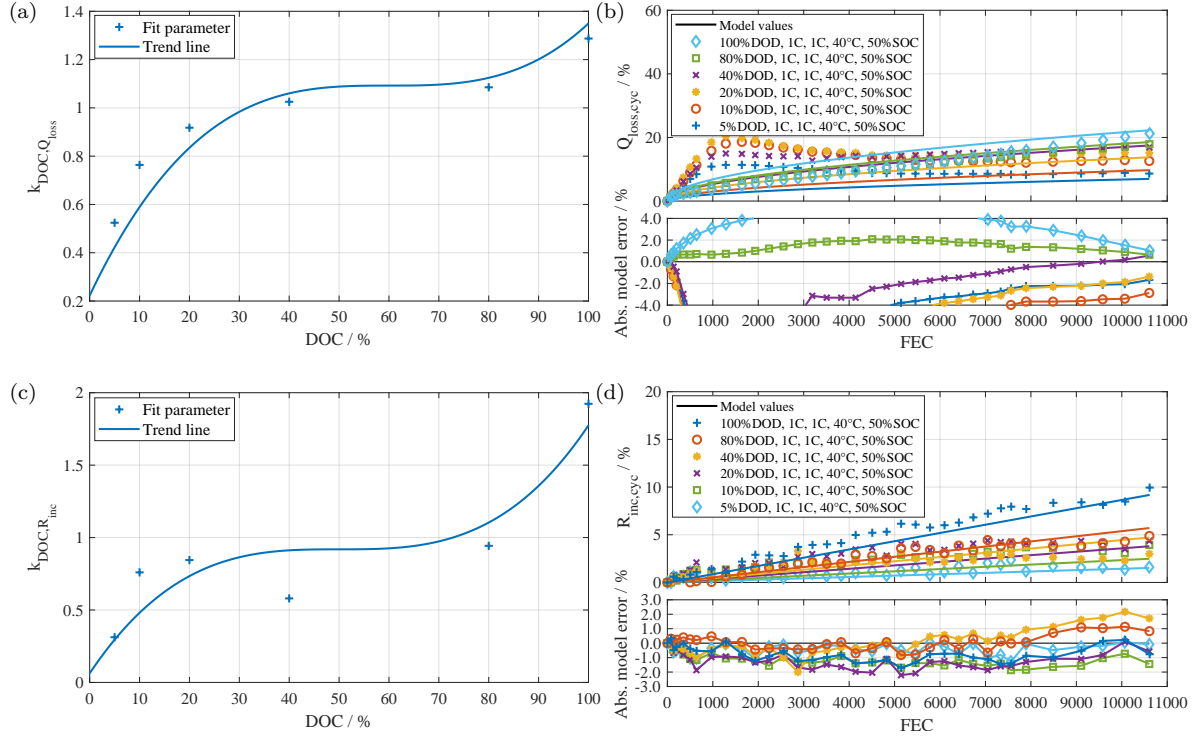


Figure 5.5: Influence of the DOC on the pure cycle aging of $Q_{\text{loss,cyc}}$ and $R_{\text{inc,cyc}}$ for the TPs with 1.0 C cycles around $SOC = 50\%$ at 40°C with $DOC = 5\%$, 10% , 20% , 40% , 80% and 100% : (a) $k_{\text{DOC},Q_{\text{loss}}}(DOC)$ determined by fitting separately the aging values at EOT of $Q_{\text{loss,cyc}}$ of the single DOC with Equation 5.22. (b) Comparison of measured values of $Q_{\text{loss,cyc}}$ with model values determined by Equation 5.18 and using the $k_{\text{DOC},Q_{\text{loss}}}(DOC)$ values determined by Equation 5.23. The lower panels show the absolute model error in %. (c) $k_{\text{DOC},R_{\text{inc}}}(DOC)$ determined by fitting separately the aging values at EOT of $R_{\text{inc,cyc}}$ of the single DOC with Equation 5.24. (d) Comparison of measured values of $R_{\text{inc,cyc}}$ with model values determined by Equation 5.19 and using the $k_{\text{DOC},R_{\text{inc}}}(DOC)$ values determined by Equation 5.25. The lower panels show the absolute model error in %.

$R_{\text{inc,cyc}}$ at the EOT:

$$k_{\text{DOC},R_{\text{inc}}}(DOC) = \frac{R_{\text{inc,cyc}}(\text{C-rate} = 1\text{ C}, DOC, FEC)}{k_{\text{C-rate},R_{\text{inc}}}(\text{C-rate} = 1\text{ C}) \cdot FEC_{\text{end}}} \quad (5.24)$$

$$k_{\text{DOC},R_{\text{inc}}}(DOC) = c_{R_{\text{inc}}}(DOC - 0.5)^3 + d_{R_{\text{inc}}} \quad (5.25)$$

These values of $k_{\text{DOC},R_{\text{inc}}(EOT)}(DOC)$ at the EOT are shown by the marks in **Figure 5.5b** over the respective DOC. The trend line matches the course of the DOC influence on $k_{\text{DOC},R_{\text{inc}}}(DOC)$ for most of the DOC, however, the deviations are bigger than for $k_{\text{DOC},Q_{\text{loss}}}(DOC)$ show in **Figure 5.5a**. Still, the same formula structure with **Equation 5.25** is applied and the parameters c and d (see **Table 5.3**) are derived with a curve fitting procedure. The results of evaluating **Equation 5.19** with the model values of $k_{\text{DOC},R_{\text{inc}}}(DOC)$ are compared in **Figure 5.5d** in the upper panel with the determined resistance increase due to pure cycle aging. The model trend lines follow the determined pure cycle

aging resistance increase for all DOC, however, due to the fluctuating values of the resistance increase the model errors alternates between $\pm 2.0\%$ for all DOC.

5.2.2.4 Influence of temperature

With the cycle aging TPs at 25°C and 40°C with $DOC = 80\%$ and 100% around $SOC = 50\%$ for the C-rate 1.0C the temperature influence on the pure cycle aging can be evaluated. Again the capacity loss and resistance increase due to the pure cycle aging are evaluated by subtracting the measured calendar aging $Q_{\text{loss,cal}}/R_{\text{inc,cal}}$ of the TP with $SOC = 50\%$ at 25°C and 40°C respectively and are shown in **Figure 5.6a** for $Q_{\text{loss,cyc}}$ and in **Figure 5.6b** for $R_{\text{inc,cyc}}$. For the TPs with $DOC = 80\%$ at 25°C and 40°C ambient temperature, the trend lines of both $Q_{\text{loss,cyc}}$ and $R_{\text{inc,cyc}}$, despite the temperature difference, are in a good accordance to each other from the beginning until about 8000 FEC are reached. For the TPs with $DOC = 100\%$ at 25°C and 40°C ambient temperature, the trend lines of both $Q_{\text{loss,cyc}}$ and $R_{\text{inc,cyc}}$, follow almost the same course but start to differ after the first 4000 FEC.

Although the temperatures 25°C and 40°C do not cover the whole possible operation temperature of battery cells, this temperature can be assumed as the target temperature for the BESS operation since lower and higher temperatures lead to accelerated degradation of both capacity and resistance. However, due to the small temperature influence on the pure cycle aging between 25°C and 40°C , the temperature influence is neglected in this cycle aging model and only represented in the calendar aging model.

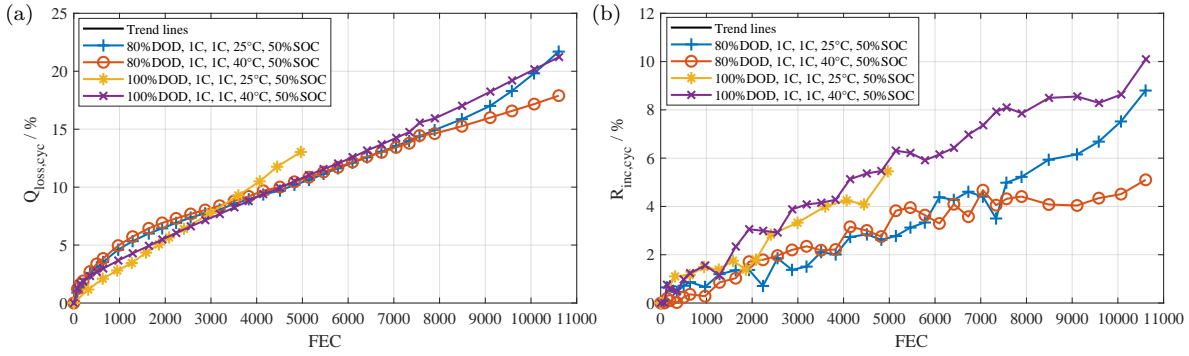


Figure 5.6: Influence of the temperature on the pure cycle aging of $Q_{\text{loss,cyc}}$ and $R_{\text{inc,cyc}}$ for the TPs with $DOC = 80\%$ and 100% cycles around $SOC = 50\%$ for the C-rate 1.0C . (a) $Q_{\text{loss,cyc}}$. (b) $R_{\text{inc,cyc}}$.

Table 5.3: Q_{loss} and R_{inc} aging model reference values and parameters.

| Parameter | Q_{loss} | R_{inc} |
|-----------|-------------------|------------------|
| a | 0.0630 | -0.0020 |
| b | 0.0971 | 0.0021 |
| c | 4.0253 | 6.8477 |
| d | 1.0923 | 0.91882 |

5.2.3 Validation

To apply the cycle aging model equations with varying C-rates or DOCs over FEC during a lifetime simulation, a differential form of the cycle aging models is derived by differentiating **Equation 5.18** with respect to FEC for $Q_{\text{loss,cyc}}$ getting **Equation 5.26** and differentiating **Equation 5.19** for $R_{\text{inc,cyc}}$ resulting in **Equation 5.27**.

$$\begin{aligned} \frac{dQ_{\text{loss,cyc}}}{dFEC}(\text{C-rate}, \text{DOC}, \text{FEC}) &= q_{\text{loss,cyc}}(\text{C-rate}, \text{DOC}, \text{FEC}) \\ &= k_{\text{C-rate}, Q_{\text{loss}}}(\text{C-rate}) \cdot k_{\text{DOC}, Q_{\text{loss}}}(\text{DOC}) \cdot (2\sqrt{\text{FEC}})^{-1} \end{aligned} \quad (5.26)$$

$$\frac{dR_{\text{inc,cyc}}}{dFEC}(\text{C-rate}, \text{DOC}) = r_{\text{inc,cyc}}(\text{C-rate}, \text{DOC}) = k_{\text{C-rate}, R_{\text{inc}}}(\text{C-rate}) \cdot k_{\text{DOC}, R_{\text{inc}}}(\text{DOC}) \quad (5.27)$$

Similar to the approach for the calendar aging model in **Section 5.1.3**, it has to be identified how to apply the cycle aging models correctly when the cycle influence factors are varied. The results of the dynamic calendar aging study proved (see **Figure 5.3**) the independence of the order of storage conditions and that the calendar aging rate is dependent on the current SOH. The same approach is applied for the pure cycle aging model, however, to determine the differential capacity loss $q_{\text{loss,cyc}}$ when varying the cycle influence factors, the virtual Ah-throughput with FEC^* is defined, representing the FEC until the same $Q_{\text{loss,cyc}}$ is reached under the new cycle conditions. As the resistance increase due to pure cycle aging is constant over FEC, no additional measures for Ah-throughput compensation of R_{inc} have to be taken. The virtual FEC^* can be derived by solving **Equation 5.18** for FEC resulting in **Equation 5.28** for $Q_{\text{loss,cyc}}$.

$$FEC_{Q_{\text{loss}}}^{\text{cyc}}(\text{C-rate}, \text{DOC}, Q_{\text{loss,comb.}}) = \left(\frac{Q_{\text{loss,comb.}}}{k_{\text{C-rate}, Q_{\text{loss}}}(\text{C-rate}) \cdot k_{\text{DOC}, Q_{\text{loss}}}(\text{DOC})} \right)^2 \quad (5.28)$$

When applying the cycle aging model with changing cycle influence factors, the virtual FEC^* has to be determined for each step. Then FEC^* is applied to calculate the differential capacity loss $q_{\text{loss,cyc}}$ in the next interval with new cycle conditions.

The pure cycle aging models cannot be validated directly as done before for the calendar aging model because the aging of the dynamic stress profiles represents always the superposition of calendar and cycle aging. One possible option would be the operation of the dynamic validation profile with low temperature, where only little influence of calendar aging can be expected. However, at low temperatures, additional cycle aging effects due to lithium plating could occur which are not represented by this cycle aging model. Still, the pure cycle aging model is validated with the dynamic stress profiles in the next section with the combination of the calendar and cycle aging model.

Another way to validate the cycle aging model is the comparison with the manufacturer values for the investigated cell [7]. However, only for full cycles with a $DOC = 100\%$ and a C-rate of 1.0 C at 23 °C different datasheet versions state from 6000 up to 10.000 FEC until 20 % of the nominal capacity is lost. By using the cycle aging model the FEC until the EOL criteria with 20 % capacity loss due to pure cycle aging can be calculated with **Equation 5.28** and are shown in **Figure 5.7**. The FEC until the EOL with $Q_{\text{loss,cyc}} = 20\%$ are marked for the DOC investigated in this aging study and connected by a trend line. A logarithmic scale is chosen for the y-axis representing the FEC until EOL because for $DOC < 10\%$ the count of FEC is increasing exponentially. The TP at a $DOC = 100\%$

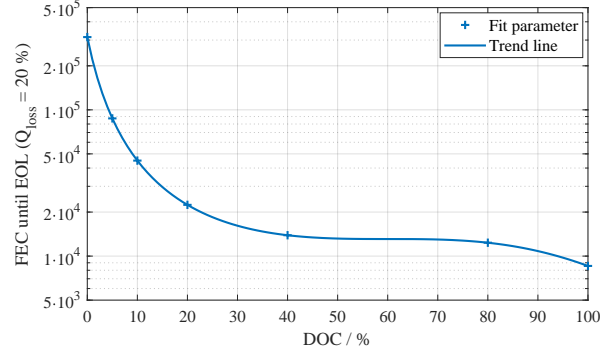


Figure 5.7: Estimation of the FEC until the EOL with $Q_{\text{loss,cyc}} = 20\%$ with Equation 5.28. The y-axis is drawn on a logarithmic scale.

would reach the EOL after about 8500 FEC, which fits the range given by the different datasheet numbers between 6000 and 10.000 FEC, however, the datasheet values include normally the overlain by calendar aging.

5.3 Combined aging model

5.3.1 Development

In order to estimate the calendar and cycle aging in lifetime simulations of BESS, a combined aging model is developed and presented here. Since the cycle aging model represents only the pure cycle aging without the overlying calendar aging, a combined aging equation for the capacity loss can be established as a simple superposition of the calendar aging model **Equation 5.1** with the cycle aging model **Equation 5.18** resulting in the combined aging model **Equation 5.29**. For the resistance increase, the calendar aging model **Equation 5.2** can be superposed with the cycle aging model **Equation 5.19** getting the combined aging model with **Equation 5.30**.

$$\begin{aligned}
Q_{\text{loss,comb.}}(T, SOC, t, \text{C-rate}, DOC, FEC) &= Q_{\text{loss,cal}}(T, SOC, t) + Q_{\text{loss,cyc}}(\text{C-rate}, DOC, FEC) \\
&= k_{\text{temp}, Q_{\text{loss}}}(T) \cdot k_{\text{SOC}, Q_{\text{loss}}}(SOC) \cdot \sqrt{t} \\
&\quad + k_{\text{C-rate}, Q_{\text{loss}}}(\text{C-rate}) \cdot k_{\text{DOC}, Q_{\text{loss}}}(DOC) \cdot \sqrt{FEC}
\end{aligned} \tag{5.29}$$

$$\begin{aligned}
R_{\text{inc,comb.}}(T, SOC, t, \text{C-rate}, DOC, FEC) &= R_{\text{inc,cal}}(T, SOC, t) + R_{\text{inc,cyc}}(\text{C-rate}, DOC, FEC) \\
&= k_{\text{temp}, R_{\text{inc}}}(T) \cdot k_{\text{SOC}, R_{\text{inc}}}(SOC) \cdot t \\
&\quad + k_{\text{C-rate}, R_{\text{inc}}}(\text{C-rate}) \cdot k_{\text{DOC}, R_{\text{inc}}}(DOC) \cdot FEC
\end{aligned} \tag{5.30}$$

When applying this combined aging models in BESS lifetime simulations, no particular step size of time or Ah-throughput has to be considered, because the influence factor for time t and for Ah-throughput FEC are included in the equations. However, whenever an influence factor of the calendar or of the cycle aging model changes, the combined capacity loss $Q_{\text{loss,comb.}}$ has to be calculated. For this

purpose, the virtual time t^* with **Equation 5.17** and the virtual FEC^* with **Equation 5.28** has to be determined and to be used respectively to calculate the capacity loss due to the calendar and cycle aging. Since the resistance increase follows for the calendar aging model the time t and for the cycle aging model the FEC linearly, no adaptation of the time or the FEC factor is necessary whenever the influence factors are changing. Although the resistance increase shows no path dependency, $R_{inc,comb.}$ should be calculated whenever an influence factor changes and so in the same frequency as $Q_{loss,comb.}$ since they depend on the same influence factors.

5.3.2 Validation

Similar to the validation of the calendar aging model with the results of the dynamic calendar aging study in **Section 5.1.3**, the combined aging model is validated here with the results of the dynamic cycle aging study. The two load profiles presented in **Section 4.5.6** have been applied each to three of the investigated cells at an ambient temperature of 40 °C. Due to the cyclization of the cells, the cells' temperature elevated from 40 °C to a mean value of 40.8 °C for the PV-HESS profile and 40.6 °C for the PV-PCR-BESS profile. These temperatures are applied in the estimation of the combined aging since the temperature has a big impact on the calendar aging. Within the 885 days of the aging study, the PV-HESS profile was carried out 1368 times and the PV-PCR-BESS profile 928 times. In order to calculate the combined aging, the load profile stress is characterized by the half-cycle detection algorithm (see **Section 3**) applied on the original SOC-course of both profiles. Thereby the DOC, the mean C-rate and the mean SOC of every half-cycle is determined. Hence, after every half-cycle, the calendar and cycle aging is calculated and summed up to get the combined aging.

Figure 5.8 shows the development of the capacity loss $Q_{loss,meas}$ and resistance increase $R_{inc,meas}$ out of the regulars performed CU measurements for the PV-HESS profile on the left side and the PV-PCR-BESS profile on the right side. In addition to the calculated combined aging values for $Q_{loss,comb.}$ and $R_{inc,comb.}$, the particular fractions of the calendar and pure cycle aging are shown for both profiles.

PV-HESS profile

For the PV-HESS profile, the aging model results follow very closely the trend of the capacity loss and deviate at the EOT only about 0.5%. The estimated capacity loss due to calendar aging at the EOT $Q_{loss,cal} = 9.21\%$ matches well the capacity loss measured within the static calendar static aging with the TP at 40 °C with a $SOC = 50\%$ $Q_{loss,cal} = 9.24\%$. The capacity loss due to pure cycle aging results in $Q_{loss,cyc} = 3.64\%$ and is representing thereby a fraction of 28.35% of the combined estimated aging.

For the resistance, the combined aging model results follow very closely the measured trend in the first 500 days, however, the measured values deviate from the original linear trend line resulting in a model error up to 2% afterward. This deviation derives mainly from the model error of cycle aging, since the resistance increase due to calendar aging at the EOT with $R_{inc,cal} = 8.07\%$ only exceeds slightly the resistance increase measured within the static calendar static aging study with $Q_{loss,cal} = 7.31\%$ (TP at 40 °C with a $SOC = 50\%$). The resistance increase due to pure cycle aging results in $R_{inc,cyc} = 2.80\%$ and representing thereby a fraction of 25.74% of the combined estimated aging.

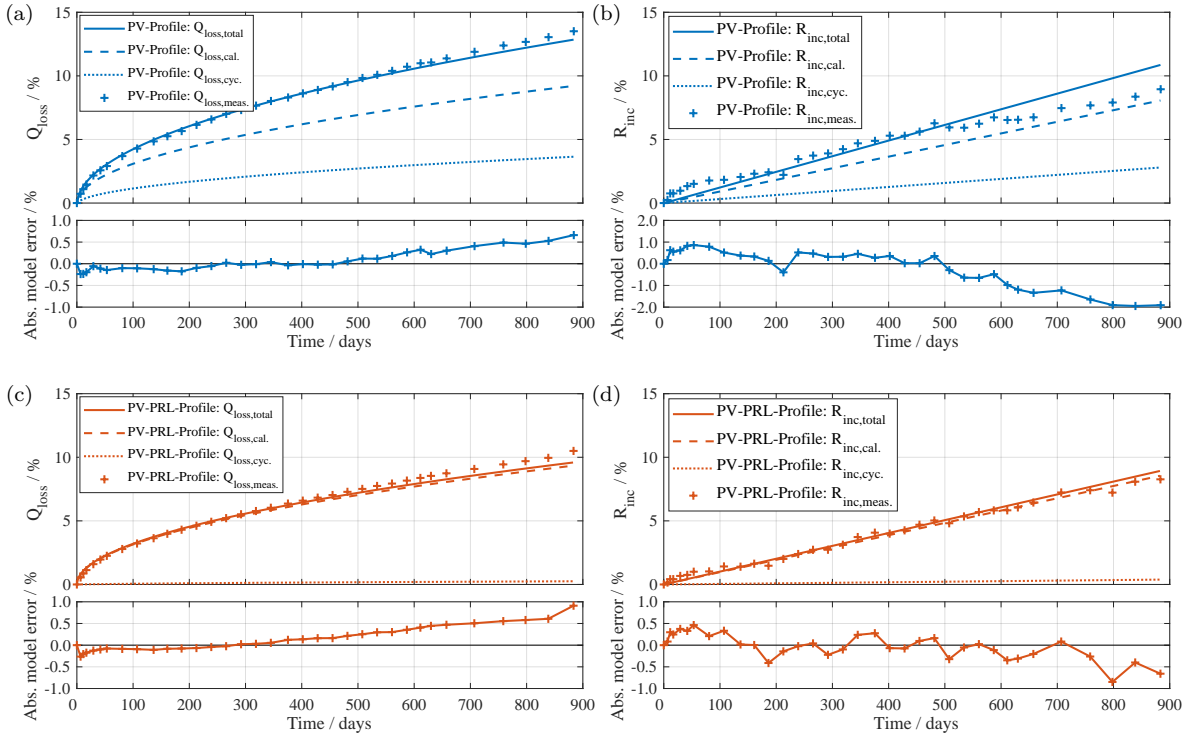


Figure 5.8: Combined aging model validation with the aging results of the dynamic cycle aging study with the two load profiles operated over 885 days at 40 °C. Each plot shows the mean values of the measured $Q_{\text{loss,comb.}}/R_{\text{inc,comb.}}$ of the three cells of each load profile. The plots on the left side represent the capacity loss and the plots on the right side resistance increase of the respective load profile. Additional to the estimated combined aging, the particular fractions of the calendar and pure cycle aging are drawn in every plot. The lower panel in every plot shows the absolute model error in % compared to the measured values. (a/b) PV-HESS load profile (c/d) PV-PCR-BESS load profile.

PV-PCR-BESS profile

For the PV-PCR-BESS profile, the aging model results follow again closely the trend of the capacity loss and deviate at the EOT about 1%. The estimated capacity loss due to calendar aging at the EOT $Q_{\text{loss,cal}} = 9.34\%$ matches well the capacity loss measured within the static calendar static aging with the TP at 40 °C with a $SOC = 50\%$ $Q_{\text{loss,cal}} = 9.24\%$.

The capacity loss due to pure cycle aging results in $Q_{\text{loss,cyc}} = 0.25\%$ and representing thereby a fraction of 2.61% of the combined estimated aging. This small fraction of cycle aging can be explained by the characteristics of the PV-PCR-BESS profile, showing mainly very small half-cycles with $DOC < 1\%$ which lead to almost no capacity loss due to cycle aging.

For the resistance, the combined aging model results follow also very closely the trend of the measured resistance increase, showing only small model errors $< 1\%$. Similar to the capacity loss, the resistance increase due to pure cycle aging represents only a small fraction of 4.28% of the combined estimated aging resulting in $R_{\text{inc,cyc}} = 0.38\%$.

In conclusion, the results of the combined aging model validation with these two dynamic load profiles demonstrate, that the pure cycle aging model is able to estimate the capacity loss and the resistance increase with sufficient precision even on a long time scale with dynamic profiles.

6 Techno-economic evaluation of battery energy storage system applications

In this chapter the SimSES framework (see **Chapter 3.1**) is applied to evaluate and compare the techno-economic results of two stationary BESS applications in Germany PV-Home energy storage system (PV-HESS) and the primary control reserve (PCR)-supply, which are introduced in **Chapter 2**.

Both applications consist of a plenty of parameters that can technically and economically optimized in various scenarios. In this chapter, a parameter study on the key technical and economic parameters is conducted for both applications considering a realistic technical framework and a baseline scenario for the variation of selected technical and economic parameters.

First of all, the BESS system model and the most important parameters are described **Section 6.1**, because the simulations of both applications are performed with the same BESS model. Afterward, both applications are presented separately by showing the simulation input, the design of the system parameters and the results of the simulated operation. Then, the technical and economic key results of both applications are compared. Finally, different economic scenarios are applied on both applications to show the potential economic benefit when realizing these systems.

6.1 General simulation configuration

6.1.1 Technical parameters

The BESS is modeled as described in **Section 3.1.4** and parametrized completely with the measured data from the investigated LFP/C cell Sony US26650 (see **Section 4.1**). **Table 6.1** summarizes the system model configurations, which are explained in the following.

The battery ECM is parametrized with the single-cell measurement data from the Sony US26650 cell and applying a '0D lumped mass thermal cell model' to estimate the thermal operation. The self-discharge is applied with 0.1 % per month as an average value that was measured at an ambient temperature between 25 to 40 °C during the calendar aging study **Section 4.6.1**. The degradation of the batteries' capacity and resistance is estimated with the calendar and cycle aging model described

Table 6.1: Battery energy storage system models and parameters.

| Input variable | Model / Value |
|-----------------------------|--|
| Battery cell model | Sony US26650 equivalent circuit (OCV-R) cell model |
| Battery aging model | Sony US26650 experimental calendar and cycle aging model |
| Battery thermal model | 0D lumped mass thermal cell model |
| Power electronics model | Power dependent efficiency curve |
| Start SOC | 50 % |
| Battery self-discharge rate | 0.1 % per month |

in **Chapter 5**. The battery cell parameters and model results are scaled up linearly to achieve the battery sizes used in the system design in **Section 6.2.2**.

6.1.2 Economic parameters

6.1.2.1 General economic parameters

The economic assessment is based on the parameters given in **Table 6.2** and is explained in the following. All simulations are performed with the regulatory framework of the year 2015 in Germany with simulation periods of 20 years. In order to calculate the economic metrics presented in **Section 3.2.2**, all monetary values are compared by applying the net present value method considering a constant interest rate and a constant inflation rate. Many different assumptions for the interest rate and inflation rate can be found in the literature for the economic assessment of BESS [110–113]. For the baseline scenario, the assumptions of Dufo-López [113] of the year 2015 are applied with an interest rate of 4% and an inflation rate 2%. Both rates result in a net interest rate/discount factor of 1.96%.

Table 6.2: General economic parameters.

| Input variable | Value |
|---------------------|--|
| Interest rate | 4% |
| Inflation rate | 2% |
| Discount factor | 1.96% |
| Depreciation period | 20 years |
| Simulation period | 1 st Jan. 2015 - 31 st Dec. 2034 |

6.1.2.2 BESS economic parameters

In the baseline scenario, the BESS investment costs for the battery and the power electronics shown in **Table 6.3** are used. The numbers are based on a literature review for PV-HESS costs by Hesse et al. [5] in 2017 with the data from 2016. Although the baseline scenario starts with the parameters of 2015, the costs of 2016 are used to estimate the investment costs. However, the BESS investment costs are varied later on by applying the specific battery system costs as the sum of system and variable costs with values between 500 to 2500 Euro/kWh related to the battery nominal energy. 2500 Euro/kWh can be assumed as the maximum investment price when considering a system with a battery size of 1 kWh and a small inverter with less than 1 kW rated power. The minimum price of the specific battery system costs is set to 500 Euro/kWh due to the fact that the cheapest available PV-HESS system with LFP/C [114] (11/2017) is priced with about 576 Euro/kWh for a BESS size of 10.24 kWh. The additional installation and maintenance costs are neglected because they depend strongly on the specific BESS and the installation environment.

6.2 PV-Home energy storage system

The PV-HESS application represents a residential customer with a PV-system and BESS installed with the aim to time-shift local surplus PV-electricity generation and thus reduce electricity purchase at a

Table 6.3: BESS economic parameters (Data from [5]).

| Input variable | Value |
|--|--------------|
| Battery investment fixed cost | 1723 Euro |
| Battery investment variable cost | 752 Euro/kWh |
| Power electronics investment system cost | 0 Euro |
| Power electronics variable cost | 155 Euro/kW |
| Installation costs | 0 Euro |
| Maintenance costs | 0 Euro |

given retail-tariff. The PV-HESS application fundamentals are presented in **Section 2.2**. The individual input data is given in this section and followed by the determination of the system configuration of the baseline scenario, which is afterward evaluated in its operation.

6.2.1 Input data

Table 6.4 gives an overview of the general technical parameters which are explained in the following.

Table 6.4: PV-HESS: General technical parameters.

| Input variable | Value |
|---|--|
| Annual household electricity consumption | 4400 kWh |
| Household electricity consumption profile | HTW household profiles 1-8 from 2010 [115] |
| PV electricity generation profile | TUM-EEN PV-system profiles from 2011-2014 |
| Maximum grid feed-in | 60 % |
| PV power degradation per year | 0.1 % |
| Operation strategy | Immediate battery usage |

6.2.1.1 Household electricity consumption

The PV-HESS evaluation is exemplified for a single-family house with four persons in Germany with an anticipated electricity consumption of 4400 kWh per year. Households with higher electricity consumption might gain major economic profits by using BESS in combination with a PV-system [32], however, 4400 kWh per year has been the average electricity consumption in 2014 in Germany for a four-person single-family house [116] and is therefore applied here in the baseline scenario.

In order to model the course of the residential power-consumption, representative electrical load profiles for residential buildings in Germany on a 1 s database created by Tjaden et al. [115] are used. The load profile is linearly interpolated to match the sampling-time of the simulation with SimSES and the magnitude is scaled to achieve an electricity consumption of 4400 kWh per year.

6.2.1.2 PV electricity generation

Due to the reason, that the size of PV rooftop systems is limited to the usable roof surface, the PV-system size is considered as an optimization parameter in the following design evaluation. However, the upper peak power limit with 10 kW is given through the [28], because above this limit less than 100 % of the feed-in energy are reimbursed. Furthermore, the average peak power for PV-systems installed in Bavaria is with 6.2 kW (2015) [117] lower than economic optimum with 10 kW based probably by the usable limited roof surface on most houses.

The course of the PV electricity generation is modeled with the AC-power data acquired in the years 2011-2014 recorded in one-minute resolution from a photovoltaic system with 11 kWp installed on the rooftop of building N2 of the Technical University of Munich. The degradation of the PV-panels and the small constant decrease of the resulting power is modeled with a degradation factor of 0.1 % per year [118], which is applied with a linear interpolation over the simulation time on the generation profile. The measured PV-generation profile is scaled to achieve the peak power magnitudes used in the system design in **Section 6.2.2**. The maximum grid feed-in of the PV electricity surplus is limited to 60 % of the PV peak power (instead of 70 % as limit for PV power feed-in by the EEG [28]), according to the German regulation conditions for 'grid-relieving' battery investment incentives granted [119], which are included in the economic evaluations.

6.2.1.3 Operation strategy

In order to maximize the economic benefit of a BESS in a PV-HESS application, the technical goal is to maximize the coverage of the residual power profile with the BESS. The residual power profile is given by the difference of the electricity consumption profile and the PV electricity generation profile.

An example course of both profiles together with the residual power profile (green) is given in **Figure 6.7**, however, the residual power profile is already reduced by the utilization of the BESS. Due to the fact, that the electricity consumption and generation prices are constant in time and no additional costs/remunerations are given to reduce the peaks of the consumption profile, the BESS can be operated directly with the available residual power. However, the PV electricity grid feed-in power is limited in this setting to 60 % of the nominal peak power of the PV-system. All power of the residual profile exceeding this limit has to be curtailed (red area in **Figure 6.7**). In this case, the BESS operation could be optimized to reduce the curtailment losses.

Different operation strategies are supposed [33] to control the BESS power and/or the times where the system is charged and discharged to minimize the curtailment losses in this PV-HESS setting. However, with these operation strategies, it cannot be guaranteed that the curtailment losses are reduced together with the optimal coverage of the residual power profile with the BESS without having a perfect foresight. Due to the fact that this study focus on aging, only the 'conventional' strategy is used which implies an immediate BESS charging or discharge whenever the residual power is available. In consequence, the BESS utilization is maximized with the disadvantage that curtailment losses cannot be avoided completely.

6.2.1.4 Economic parameters

The economic assessment of the PV-HESS application is based on the comparison with the case of the same technical and economic setting but without a BESS reducing the residual power profile. Hence, only the investment and the operational cash flow due to the BESS installation are considered. Besides the general economic parameters shown in **Section 6.1.2**, the specific parameters for the PV-HESS application are presented in the following and summarized in **Table 6.5**.

Different potential developments of the private household electricity price in Germany are evaluated and are illustrated in **Figure 6.1**: The low price scenario consists of a yearly increase of the historical electricity prices by the inflation rate of 2 % starting with 0.2870 Euro/kWh (1st Jan. 2015). The high price scenario represents an extrapolation of the historical electricity prices by using the average values

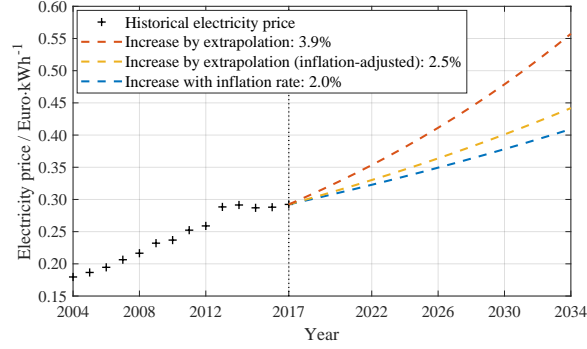


Figure 6.1: Historical electricity prices and different scenarios for electricity price over the years.

of the annual growth rates between 2004 and 2015 of 3.9%. The medium price scenario represents again an extrapolation of the historical electricity prices by using the average values of the annual growth rates between 2004 and 2015, however, the individual historical inflation rates are considered in order to present the net growth rate of the electricity prices of 2.5%.

The feed-in remuneration for the feed-in of the PV generated electricity into the power grid is given through the German EEG with 0.1256 Euro/kWh [28]. These wages are guaranteed for 20 years and valid for PV-household plants installed and used since 1st Jan. 2015. The depreciation period of 20 years of PV-systems [120] is also chosen to be the operating life of the whole BESS. The BESS investment costs are reduced by the investment subsidy of 25% given by the 'KfW-Programm Erneuerbare Energien - Speicher (275)' (1st Jan. 2015) [119].

Table 6.5: PV-HESS economic parameters.

| Input variable | Value |
|----------------------------|---|
| Investment subsidy | 25% |
| Electricity price | 0.2870 Euro/kWh (1 st Jan. 2015) |
| Electricity price scenario | Yearly increase by 3.9% |
| PV feed-in remuneration | 0.1256 Euro/kWh (1 st Jan. 2015) |

6.2.1.5 Simulation parameters

Table 6.6 summarizes the applied parameters of the simulation with SimSES. The BESS load is characterized by the half-cycle counting method, allowing a precise calculation of the storage degradation. The sample time is chosen with 5 min according to the performance and aging evaluations described in **Section 3.3**.

Based on the same analysis, the aging model is called with the average values from the battery load characterization with a step size of 10.

The BESS ambient temperature is set to 25 °C due to the assumption that the system is installed inside a residential building without any active climatization system. Considering that all efficiency losses are dissipated inside the BESS, the system would have an average temperature above a supposed room temperature of 20 °C.

Table 6.6: PV-HESS: Simulation parameters.

| Input variable | Value |
|--|---------------------|
| Sample time | 5 min |
| Load characterization method | Half-cycle counting |
| Method for calling of battery aging model | Average values |
| Step size for calling of battery aging model | 10 steps |
| Ambient temperature | 25 °C |

6.2.2 System configuration

In the following the technical and economic results of the system configuration for the PV-HESS application are obtained by the simulations with SimSES with the before described input parameters of the baseline scenario. Although there are a lot of different technical parameters of the system configuration that could be varied, only the most important parameters are evaluated here: The battery nominal energy, the battery inverter AC rated power (by using the PER) and the PV peak power.

Furthermore, there are numerous assessment parameters that can be optimized (**Section 3.2**), however, the PI is chosen to compare different technical configurations and find the best economic sizing of the system configuration parameters. The evaluation of the system configuration parameters is exemplified for a single-family house with four persons in Germany with an anticipated electricity consumption of 4400 kWh per year as explained in **Section 6.2.1.1**.

Although Waffenschmidt [30] and similar Weniger et al. [31] proposes the sizing of 1:1 (kWh:kWp) of the battery nominal energy to the PV peak power, all combinations of the battery sizes from 1 to 10 kWh with a step size 1 kWh of together with the PV peak power from 1 to 10 kW with a step size 1 kW are simulated. Additionally, the battery's inverter rated power is varied in relation to the respective battery nominal energy with the PER = 0.2, 0.5, 0.75 and 1.0. For instance, a PER = 1.0 for a battery nominal energy of 5 kWh is defined by the battery inverter AC rated power of 5 kW.

The defined combinations of the battery nominal energy, the PER and the PV peak power account for 400 single simulations that are performed for the HTW household profiles 1-8.

Due to the fact, that the results from all combinations of the system configurations cannot be illustrated, the best PER is initially determined by evaluating its influence together with the battery nominal energy and the PV peak power on the PI shown in **Figure 6.2a** for the PER = 0.2 and in **Figure 6.2b** for the PER = 1.0. Both figures show the PI at the end of the depreciation period dependent on the chosen battery nominal energy and the PV peak power. The maximum PI = 0.56 is obtained with a battery nominal energy of 5 kWh together with a PV peak power of 10 kW with the PER = 0.2. With the higher PER = 1.0, the maximum PI = 0.40 is significant lower than for PER = 0.2. In addition to system configuration with the maximum PI (purple cross), the purple dashed lines mark the best economic battery nominal energy for every PV peak power configuration or vice versa. Although the best-suited battery sizes are bigger for the PER = 0.2 than for the PER = 1.0, higher PI values are obtained with the smaller sizing of the battery inverter. The thick black solid lines mark the system configurations which are at the break-even point.

For both PERs positive PI values are gained with PV-system sizes above 2 kW. Below this PV peak power size, the battery size does nearly not influence the PI due to the fact, that the few PV generated energy is used almost completely for the energy consumption of the household. However, the residual

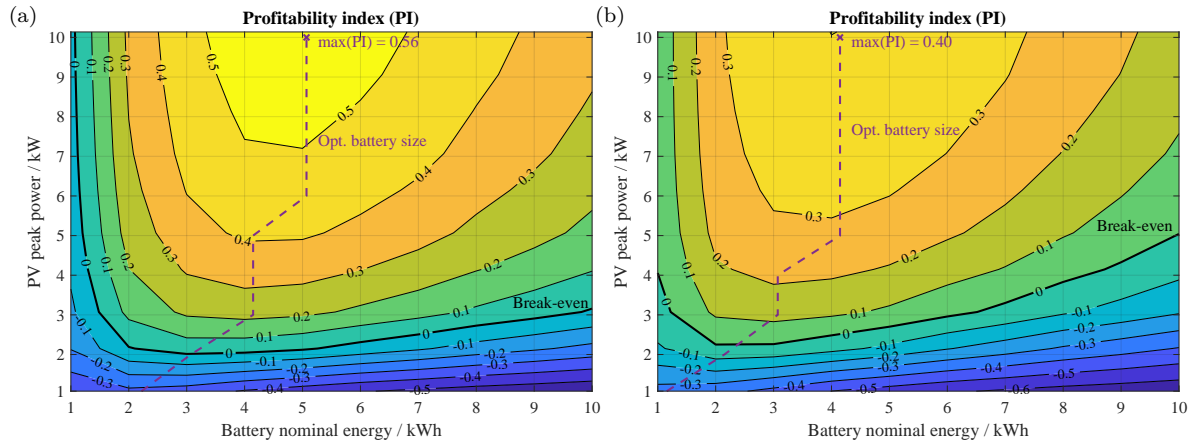


Figure 6.2: PV-HESS: Influence of the system configuration with different battery and PV-system sizes on the PI. The PER is scaled to the individual battery size: Figure 6.2a with $PER = 0.2$. Figure 6.2b: $PER = 1.0$. The purple lines mark the best economic battery size for each PV-system size or vice versa. The system sizing with the maximum PI is marked with a purple cross in both figures.

power profile can be reduced with bigger BESS and consequently the self-consumption ratio (see **Figure 6.3a**) improves significantly when increasing the BESS at this low PV peak power size. When looking at the system configurations with a positive PI, the profitability can be maximized by increasing the PV peak power together with increasing the battery nominal energy up to 5 kWh for the $PER = 0.2$. Though bigger battery sizes can increase the self-consumption ratio (see **Figure 6.3a**), the PI decreases with too big batteries because the additional investment costs cannot be completely recovered by additional savings due to a higher ratio of the self-consumed PV energy.

In the following, only the system configuration with $PER = 0.2$ is discussed and shown in the succeeding figures due to better economic results in comparison to configurations with bigger battery inverters.

Figure 6.3a shows the increase of the self-consumption ratio with respect to the system configuration in comparison to the case of the same household without a BESS. Again the system configuration with the maximum PI is marked with a red cross representing an increase of the self-consumption rate of about 13.8%. However, the self-consumption ratio does not correlate with the dependency of the PI regarding the system configuration. With bigger PV peak powers, smaller portions of the PV energy can be self-consumed by the household or stored temporarily. Though the self-consumption rate can be increased by installing bigger batteries, the self-consumption rate converges with respect to the battery size.

The self-sufficiency rate is shown in **Figure 6.3b** with respect to the system configuration in comparison to the case of the same household without a BESS. Here, the trend is inverse in comparison to the self-consumption rate because by increasing both, the battery nominal energy and the PV peak power, the self-sufficiency rate rises. However, maximizing the self-sufficiency rate with the biggest PV-system and battery size does not lead to the best economic result, because the best PI is already achieved with an increase of the self-sufficiency rate of about 25.5%. Hence, both evaluation parameters, the self-consumption rate, and the self-sufficiency rate cannot be used to define the best economic suited system configuration due to the fact that both parameters are not correlating with the PI.

Due to given limit of the maximum grid feed-in of the PV electricity with 60% of the PV peak power,

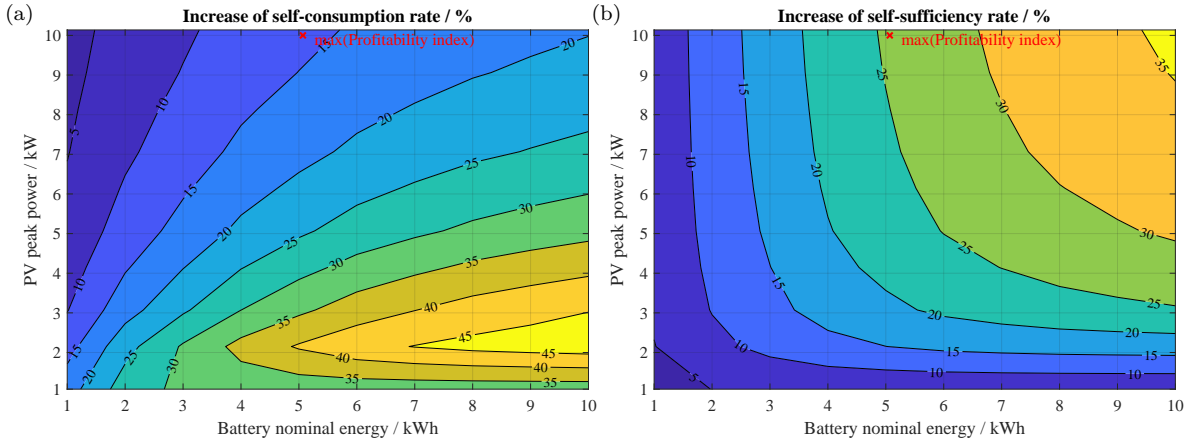


Figure 6.3: PV-HESS: Influence of the system configuration with different battery and PV-system sizes (PER = 0.2) on the self-consumption rate (Figure 6.3a) and self-sufficiency rate (Figure 6.3b) in comparison to the case without a BESS. The system sizing with the maximum PI is marked with a purple cross in both figures.

PV curtailment losses can occur which can be reduced by using a BESS. The ratio of the curtailed PV energy with respect to the system configuration (see **Figure 6.4a**) increases when using bigger PV-systems due to same reason as stated for the self-consumption rate: Especially the peak power at noon in summer time cannot be self-consumed in the household or stored in the BESS due to limited power capabilities or energetic capacities leading to a curtailed PV energy ratio between 0 to 3.1 % in this setting with a BESS. In the case without a BESS, PV energy curtailment losses up to 3.2 % can occur when using a PV-system with 10 kW peak power.

The curtailed PV energy increases slightly with BESS sizes larger than 4 kWh when keeping constant the respective PV peak power. Larger battery sizes should lead to smaller ratios of the curtailed PV energy, however, the here applied operation strategy with the immediate BESS utilization charges the battery already before the PV power peak at noon. Due to the fixed PER, larger battery sizes are operated with larger inverters and in consequence, the battery is charged faster than a smaller battery at the same PV peak power configuration. Then, the larger BESS reaches earlier the upper SOC limit and cannot cover the PV power peaks around noon time leading to higher ratios of the curtailed PV energy. By applying other operation strategies like the 'Feed-in damping' [33], the curtailment losses could be reduced by shifting the battery charging temporarily to noon and controlling the power considering a PV generation forecast. However, by using a relatively small battery inverter with the here applied PER = 0.2, the battery can be charged only slowly within about 5 h from 0 to 100 % SOC leading to energy capabilities at noon when most of the PV energy is generated and possibly curtailed. Hence, with the PER = 0.2 the BESS is operated similarly to the 'Feed-in damping' by automatically reducing the PV curtailment losses without any further controllers or the consideration of PV power generation forecasts.

Although the BESS utilization can increase the direct consumption of the energy generated by the PV-system, additional energetic losses occur due to energy conversion and storage with the utilization of the battery. **Figure 6.4b** shows the dependency of the average system efficiency with respect to the system configuration. The average system efficiency range between 88.7 % and 92.0 % and is basically undifferentiated regarding the system configuration. Furthermore, the average system efficiency reveals no clear relation with respect to the battery nominal energy or the PV peak power. However, when

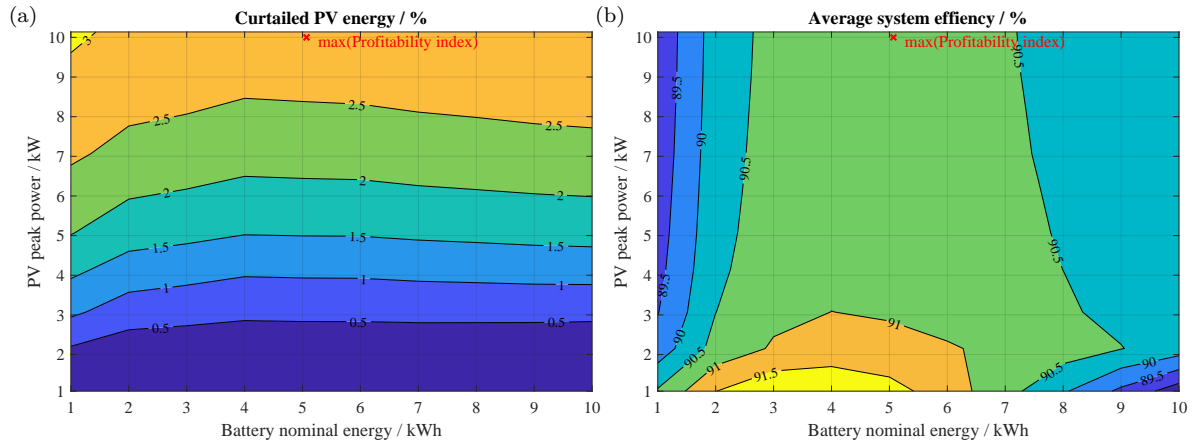


Figure 6.4: PV-HESS: Influence of the system configuration with different battery and PV-system sizes (PER = 0.2) on the curtailed PV energy (Figure 6.4a) and the average system efficiency (Figure 6.4b). The system sizing with the maximum PI is marked with a red cross in both figures.

choosing bigger battery inverters with a PER = 1.0 the average system efficiency can be significantly smaller with a range between 62.8% and 89.4% due to the partial-load operation of the inverter with worse efficiencies than the full-load operation. By choosing a small inverter with a PER = 0.2, the inverter is less often operated in the partial-load operation leading to fewer efficiency losses (see **Equation 3.4**).

The influence of the system configuration on the battery aging is illustrated in **Figure 6.5**. **Figure 6.5a** shows the count of FEC at the end of the depreciation period. The count of FEC reveals also the utilization ratio of the BESS system and one of the indicators for the resulting cycle aging. The FEC range between 530 and 5579 representing about 26.5 up to 279 FEC per year. In contrast to the before shown trends with respect to the system configuration, the FEC decrease with larger battery sizes but increases concurrently with larger PV-systems.

The resulting aging after 20 years of operation is expressed with the SOH of the battery capacity in

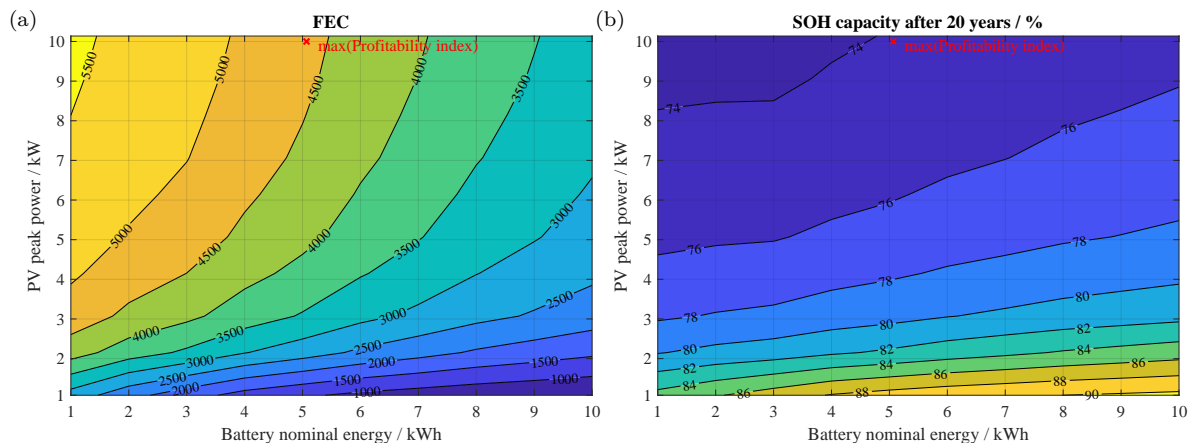


Figure 6.5: PV-HESS: Influence of the system configuration with different battery and PV-system sizes (PER = 0.2) on the FEC (Figure 6.5a) and the SOH capacity after 20 years (Figure 6.5b). The system sizing with the maximum PI is marked with a red cross in both figures.

Figure 6.5b with respect to the system configuration. The SOH range between 73.5 to 90.5%. Due to the fact, that the SOH expresses the sum of calendar and cycle aging, all system configurations should result in almost the same calendar aging. However, as shown in **Figure 6.5a** the absolute cycle aging decreases with larger batteries leading to higher SOH values.

To conclude, the economic best system configuration with a $PER = 0.2$ is defined by the maximum value of the PI leading to a battery nominal energy of 5 kWh and PV peak power of 10 kW. This system configuration, summarized in **Table 6.7**, is defined as baseline scenario together with the utilization of the household profile number 1. Although the particular technical evaluation parameters showed individually better results with different system configurations, the PI summarizes all single technical trends with respect to the economic outcome of the system.

Table 6.7: PV-HESS: Baseline scenario.

| Input variable | Value |
|---|-------------------------|
| Annual Household electricity consumption | 4400 kWh |
| Household electricity consumption profile | HTW household profile 1 |
| Battery nominal energy | 5 kWh |
| PV peak power | 10 kW |
| Power-to-energy ratio (PER) | 0.2 |
| Inverter rated power | 1 kW |

6.2.3 Performance

This section will give deeper insights of the BESS performance in the PV-HESS baseline scenario. First, the battery operation is shown and followed by the evaluation of the battery aging. Finally, the main economic results are presented.

6.2.3.1 Power and SOC course

Figure 6.6 shows the course of the different power paths (upper plot) and the SOC together with the SOH (lower plot) over the first simulation year out of the 20 years of simulated operation for the baseline scenario. By defining the power exchange with the electricity grid with the load convention, the power generation has a negative sign, however, the y-axis of the upper plot is drawn inverse to highlight the course of the PV generation over the year. The influence of the seasons is clearly observable, showing almost a sine-wave shape over the year. The electricity consumption fluctuates even stronger than the PV power, however, no seasonal shape trend is observable. The SOC course follows the trend of the PV power by showing a higher cyclization frequency in the middle of the year than at the beginning and at end of the year. Furthermore, the average SOC remains in the middle of the year significantly higher due to the fact, that in many cases the daily residual power surplus stored in the BESS cannot be discharged completely until the next day, which consequently begins with an energy surplus.

In order to evaluate the daily power flows and the BESS utilization more in detail, **Figure 6.7** shows exemplary the time interval between day 135 and 138 of the first year. Here, the different power flows and energy exchanges are clearly visible in the upper plot: The yellow areas mark the energy generated by the PV-system, which is partly consumed directly by feeding the household loads or charging the

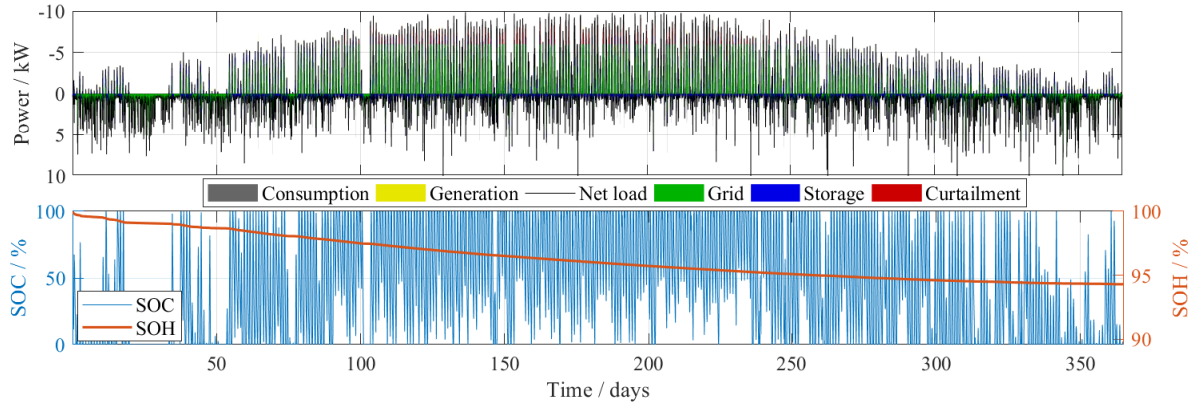


Figure 6.6: PV-HESS: Course of the different power paths (upper plot) and the SOC together with the SOH (lower plot) over the first simulation year.

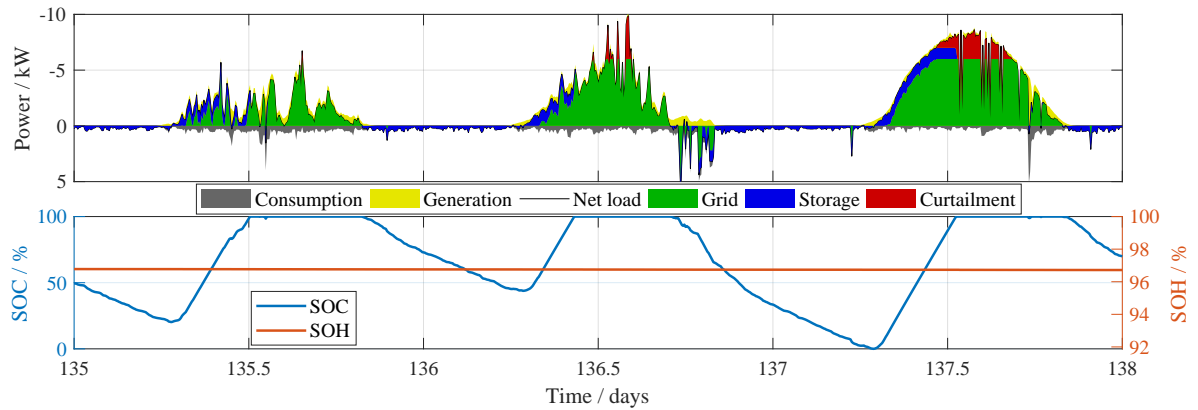


Figure 6.7: PV-HESS: Course of the different power paths (upper plot) and the SOC together with the SOH (lower plot) over the days 135-138 of the first simulation year.

BESS, however, in case of a fully charged BESS, the surplus power is feed into the power grid and partially curtailed when the power feed-in exceeds the maximum grid feed-in limit of 60 %, represented by the red areas. The households power consumption is illustrated with the areas on the positive side of the power axis but covered with different colors: Grey, when the household power consumption is covered by the PV power generation. Blue, when the BESS supplies the household load and green if the household power demand has to be supplied by the power grid because neither sufficient PV power nor BESS power is available. The BESS utilization is illustrated with the blue areas, with negative power when charging the battery with power generated by the PV-system, and with positive powers when discharging the battery to supply the household loads. The same utilization trend of the BESS can be seen in SOC course in the lower plot of **Figure 6.7**. Although the BESS seems to be too small due to the fact that the upper SOC limit is reached for the second and third day before noon, the energy stored suffices to supply the nightly household energy demand.

Due to the fact, that the shown residual power profiles and energy exchanges together with BESS utilization diverge strongly over the course of the year (due to the seasonal dependency of the PV power generation), the simulation has to cover at least one year in order to evaluate the technical and economic benefit of a BESS in the PV-HESS application properly. Therefore, the **Figure 6.8** can illustrate BESS utilization in detail by showing the 'heat map' of the battery C-rate and SOC

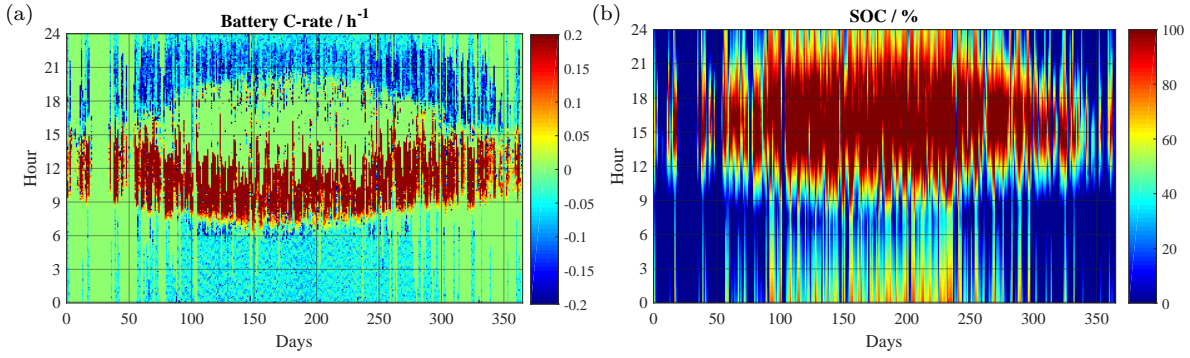


Figure 6.8: PV-HESS: Temporal distribution of the battery C-rate (Figure 6.8a) and the SOC (Figure 6.8b) over the first simulation year.

with respect to the date in the course of one year on the x-axis and the daily course on the y-axis simultaneously.

The battery C-rate in **Figure 6.8a** shows charging periods (positive sign) with reddish colors and discharging periods with bluish colors. The greenish colors mark the time periods with almost or even no battery utilization with < 0.01 C. Due to the daily sinus-wave shape of the PV power generation with its maximum at noon, the battery is charged relatively fast in the morning and discharged in the evening, often with the maximum possible C-rate in both directions. However, overnight the battery is discharged relatively slow due to the little power consumption in the household. The green gaps between the charging period and the discharging periods are caused by the missing energy capacities of the BESS in this periods by having reached the upper SOC limit. These gaps between noon and the evening correlate with the high SOC shown in reddish colors in the heat map of the SOC in **Figure 6.8b**. This utilization gap changes in the course of the year due to seasonal dependency of the PV generated energy. The bluish colors in the SOC heatmap show the time periods with low SOC, which occur in the middle of the year in the early morning and more significant at the beginning and at the end of the year when the daily PV generated energy does not suffice to supply the energy consumption of the household. In these time periods of the year the battery utilization is relatively weak, which can be seen with green areas of the C-rate in **Figure 6.8a** at the beginning and at the end of the year.

6.2.3.2 Battery load characterization

In order to understand the calendar and cycle aging as result of the applied aging model of the here investigated LFP/C cell (see **Chapter 5**), the battery load characteristics have to be evaluated first in the following.

The calendar aging rate is influenced by the SOC and temperature and changes over time. The BESS system temperature is influenced by the system operation but almost no deviate from the assumed ambient temperature of 25°C due to the limitations of the applied thermal model. However, the course of the SOC over time influences the calendar aging. In contrast to the SOC heatmap shown before, **Figure 6.9b** and the following histogram figures give a statistical insight into the BESS load characteristics over the whole simulation time of 20 years. The y-axes are drawn on a logarithmic scale due to the unequal distribution of the relative frequency of each evaluation parameter and to enable

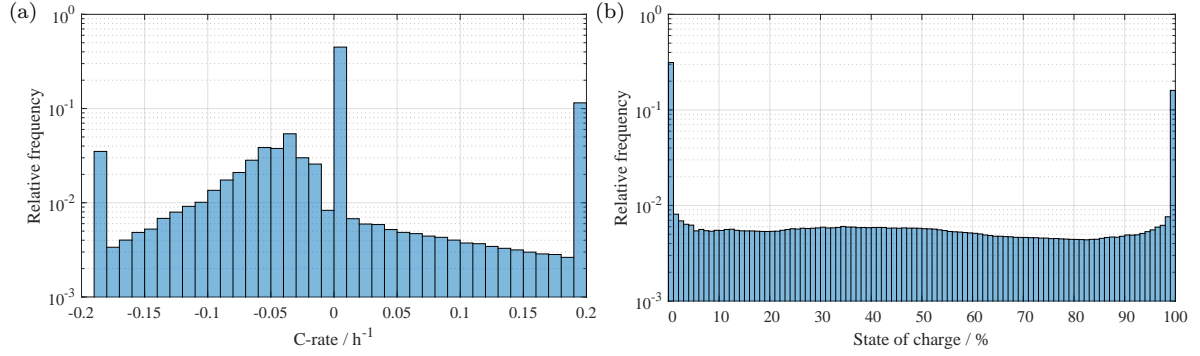


Figure 6.9: PV-HESS: Distribution of the relative frequency of the battery C-rate (Figure 6.9a) and the SOC (Figure 6.9b) over 20 years of simulation.

a proper overview over the whole value range on the x-axes. It can be seen, that the BESS in this PV-HESS baseline scenario is either empty or fully charged by having a low SOC of 0% for about 30% of the simulation time and a high SOC of 100% almost 10% of the simulation time. Between these two extremes, the frequency of the further single SOC is almost equally distributed.

The cycle aging rate of the here applied aging model is influenced by the C-Rate and the DOC and changes over the FEC-throughput.

Figure 6.9a shows the histogram of the BESS C-rate, with positive values for the charge and the negative values for the discharge direction. Here, the distribution of the single C-rates is relatively inhomogeneous: The BESS is charged relative often in about 10% of the time with the maximum C-rate of 0.2C in comparison with the lower charging C-rates. In contrast, the maximum discharge C-rate of $-0.19C$ occurs in about 3% of the time. Furthermore, the lower discharging C-rates occur significantly more often than the lower charging C-rates.

Figure 6.10a shows the histogram of the half-cycle depth separated into the charge (positive) and discharge (negative) direction. All half-cycle depths from 0 to 100% occur in charge and discharge direction, however, half-cycles with 100% DOC have a relatively high proportion of about 5% of all detected cycles in the charge direction and about 4% in the discharge direction. Only half-cycles with very small $DOC < 10\%$ have a higher proportion of more than 20% of all detected cycles.

In order to evaluate the correlation of the two cycle aging influence factors, **Figure 6.10b** shows the histogram of the half-cycle depth together with the respective C-rate of every half-cycle depth in charge and discharge direction. The central bars in green and yellow colors represent the small half-cycle depths, which have a high proportion, however, the C-rate of these half-cycles is with values $< 0.02C$ relatively low. In charge direction, the frequency distribution of the further bars is almost equal and covers the whole value range of the half-cycle depth and C-rate. In contrast, in discharge direction not the whole value range of the half-cycle depth and C-rate is covered because most of the half-cycles $> 20\%$ show absolute C-rates $> 0.1C$. However, almost all bars in discharge direction have roughly the same proportion.

In order to summarize and to compare the single distribution of the shown aging influence parameters, the average values of SOC, C-rates and DOC are shown in **Table 6.14** in comparison with the results from the PCR-supply application.

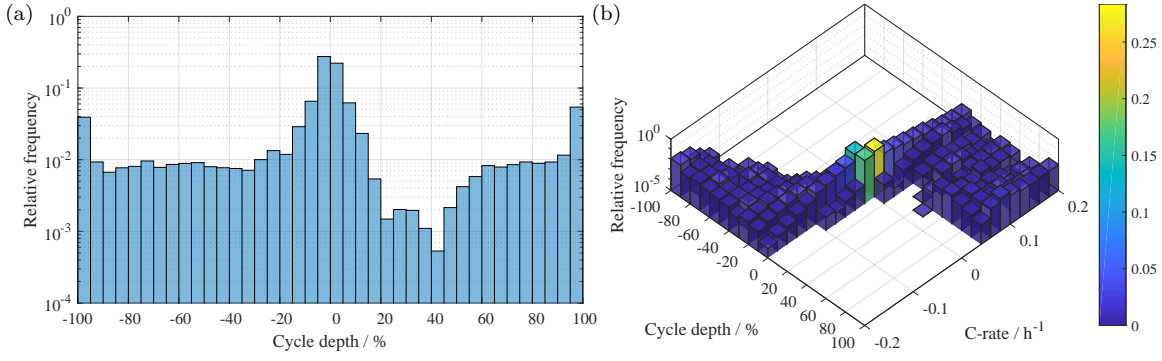


Figure 6.10: PV-HESS: Distribution of the relative frequency of the cycle depth (Figure 6.10a) and the cycle depth over C-rate (Figure 6.10b) over 20 years of simulation. The color bar of Figure 6.10b represents the relative frequency values of the histogram.

6.2.3.3 Battery aging

The battery aging course of the capacity and the resistance is shown in **Figure 6.11** over the whole simulation time of 20 years. Both figures show the proportion of the calendar and cycle aging in comparison to the sum of both as the total aging.

The battery capacity loss illustrated in **Figure 6.11a** follow a logarithmic shape due to decreasing aging rates with the decreasing capacity. Both, the calendar and cycle aging curves, show the same curve shape. The seasonal impact of the PV generation and the thereof dependent BESS utilization can be seen in the slight overlaid wavelike shape of the total and calendar aging curve. From the end until the beginning of every year, the PV generation is less and consequently, the calendar aging is smaller due to the low average SOC levels in comparison to the summer period. At the end of the simulation, the capacity decreased by about 25.7% dominated by the calendar aging with a proportion of about 73.9% in comparison to the cycle aging. Although the BESS average SOC was relatively low with about 41.4% together with the fact that the temperature has been constant at 25 °C, the calendar aging rate is higher than the cycle aging rate over the whole simulation time. The count of 4786 FEC over the 20 years operation represents more than the half of the anticipated cycle lifetime until EOL with $Q_{\text{loss,cyc}} = 20\%$ with a DOC of 100% shown in **Figure 5.7**, however, most of the cycles lead to low cycle aging due to the small individual DOC and low C-rates of the most of the half-cycles.

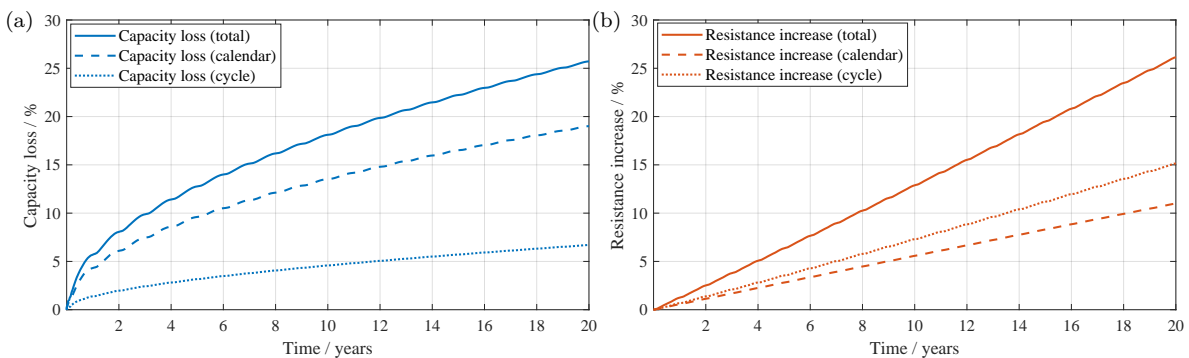


Figure 6.11: PV-HESS: Course of the capacity loss (Figure 6.11a) and the resistance increase (Figure 6.11b) over 20 years of simulation.

The battery resistance, shown in **Figure 6.11b**, increases quite linear, however, a small wavelike shape can be observed due to the same reasons as explained for the capacity loss. The total resistance increases with about 26.1% almost the in the same absolute value as observed for the capacity loss, however, the proportion of the total resistance increase due to calendar aging is with 42.1% obviously smaller than the same ratio observed for the capacity loss. Hence, the resistance increase is dominated slightly by the cycle aging. The smaller influence of the calendar aging on the resistance increase can be explained by the SOC distribution, where relative often very low and very high values occur. These two SOC extremes lead to less resistance increase than the SOC range around 50% as shown in **Figure 4.5d**. Furthermore, the proportion of the cycle aging on the total resistance could be higher due to the fact, that influence of the C-rate is inverse in comparison to the behavior due to capacity loss. Smaller C-rates lead to higher cycle aging rates of the resistance as shown in **Figure 5.4d**.

Although the absolute aging values of the capacity loss and resistance increase influence significantly the BESS operation over the whole simulation time, there is no need to replace the battery before the end of the depreciation period of 20 years. However, it remains to investigate how the decrease of the available capacity together with efficiency decrease impact the economic profitability in detail in the course of the 20 years.

6.2.3.4 Economic results

The overall economic results of the baseline scenario of the PV-HESS application are compared with the results from PCR application in **Section 6.4.1.2**. However, the particular results of the PV-HESS application are presented here as net present values by applying the discount factor of 1.96% (see **Table 6.2**). **Table 6.8** summarizes and compares the particular results for the simulations of a PV-household without a BESS installed (PV-system only) and with a PV-household with BESS installed as described in the baseline scenario (PV-HESS). In order to understand the influence of the battery aging on the economic results, an additional case of the baseline scenario is simulated in which the battery aging is completely neglected (PV-HESS no aging).

In the PV-HESS baseline scenario, the BESS investment for the battery size of 5 kWh costs 5689.70 Euro. This investments costs are reduced by the investment subsidy of 1422.40 Euro due to the investment subsidy of 25% given by the 'KfW-Programm Erneuerbare Energien - Speicher (275)' [119].

Without a BESS, the households electricity bill (total electricity costs), as the sum of costs for the electricity consumption together with the remuneration of PV electricity feed-in, would result in a total cash flow $C_{\text{cash flow, total}}^{\text{NPV}}$ of -4892.60 Euro over the 20 years of operation. With the BESS, the same household electricity bill results with earnings of 2968.20 Euro due to less electricity consumption of about 41.6% in comparison to the case without a BESS even though the PV electricity feed-in decreased by about 16.3%. Hence, the BESS household would have total cash flow $C_{\text{cash flow, total}}^{\text{NPV}}$ of 7860.80 Euro in comparison to the household without a BESS.

Table 6.8: PV-HESS economic results.

| Parameter | PV-system only | PV-HESS | PV-HESS (no aging) |
|----------------------------------|----------------|--------------|--------------------|
| Total electricity costs | -4892.60 Euro | 7860.80 Euro | 8624.30 Euro |
| Investment costs (subsidy incl.) | 0 Euro | 4267.30 Euro | 4267.30 Euro |
| Total return | | 3593.50 Euro | 4357.00 Euro |
| Profitability index (PI) | | 0.6316 | 0.76576 |

By subtracting the BESS investment costs and considering the investment subsidy, the BESS household receives a total return $R_{\text{total}}^{\text{NPV}}$ of 3593.50 Euro reflecting a PI of 0.6316.

When comparing the results of this baseline scenario with the case without aging, the total return $R_{\text{total}}^{\text{NPV}}$ of the case without aging is estimated with 763.50 Euro about 21.3% higher than the baseline scenario with realistic battery aging. This relatively low impact of the battery aging on the total economic result of the PV-HESS application would be stronger in case of less calendar and cycle lifetime of other lithium-ion batteries than the here applied LFP/C cell.

6.3 Primary control reserve supply

The PCR application of BESS is introduced in **Section 2.3**. Here, the simulation of this application with SimSES is presented by describing first the input data, then the BESS system configuration and finally giving insight into the operation by showing the technical and economic results.

6.3.1 Input data

The PCR simulation is generally based on the same technical and economic input parameters like for the PV-HESS application presented in **Section 6.1**, however, there are some specific parameters which are presented in the following.

Table 6.9 summarizes the additional parameters that are used for the PCR simulation which are explained in the following.

The maximum PCR power supply is set to ± 1 MW in accordance with the minimum lot size defined by the prequalification for the PCR [36]. The PCR-supply is simulated with SimSES by applying a power grid frequency profile of the UCTE electricity grid, which was measured in 1 s resolution in the year 2015.

In order to assure the supply of PCR power with regard to the course of the frequency deviation in any moment, the BESS SOC has to be adjusted sometimes by exchanging power with the electricity grid. These power exchanges are regulated by performing transactions on the IDM of the EPEX SPOT. Therefore, the weighted average IDM prices from the year 2015 of the EPEX SPOT are applied [37] in the baseline scenario.

Table 6.9: PCR-supply: General technical parameters.

| Input variable | Value |
|------------------------------|--|
| Maximum PCR power supply | $P_{\text{max}}^{\text{PCR}} = 1 \text{ MW}$ |
| Power grid frequency profile | Data from the year 2015 in 1 s resolution in the UCTE electricity grid (data measured and provided by the <i>Smart Power GmbH & Co. KG</i>) |
| PCR-supply prices | Average tender prices from the year 2015 from [36] |
| IDM-electricity prices | Weighted average price of the EPEX SPOT IDM from the year 2015 [121] |
| PCR operation strategy | Apply all degrees of freedom to control SOC |
| SOC setpoint | 50 % |

6.3.1.1 Operation strategy

Degrees of freedom

In every simulation step, first, the required PCR is determined with the P - $f_{\text{power line}}$ characteristic by evaluating the current frequency deviation from the nominal frequency (see **Section 2.3**). Subsequently, it is checked whether the SOC is above or below the SOC_{setpoint} . Depending on this, the degrees of freedom are utilized in order to adjust the current SOC closer to the SOC_{setpoint} . For example, in case that the SOC is above the SOC_{setpoint} , it will be attempted to discharge as much energy as possible by using the overfulfillment or the '30 s slope' degree of freedom. Consequently, the overfulfillment is only used to provide negative PCR power at frequencies less than 50 Hz. In case of small frequency deviations below the nominal frequency, the deadband is not utilized. However, the deadband will be held as long as allowed to consume as little energy as possible if the frequency rises above the nominal frequency.

Setpoint SOC

The setpoint SOC is defined as the value from which in both charge and discharge direction the widest operation range is possible. It is assumed, that the BESS can be operated in the entire SOC range between 0 to 100 %. Considering the overall BESS efficiency losses η^{Sys} , the SOC_{setpoint} has to be above 50 %, due to the fact, that energy is lost in charge and discharge direction. Thereby, η^{Sys} is defined as the system efficiency for a single charge or discharge operation. In contrast, the average roundtrip efficiency η^{BESS} is defined for a complete charge and discharge cycle of the BESS (see **Equation 3.5**). Hence, the SOC_{setpoint} is defined by the following equation to a value, from which in both directions the same amount of energy can be charged or discharged:

$$SOC_{\text{setpoint}} = \left(\frac{E_{\text{nom.}}}{2} + (1 - \eta^{\text{Sys}}) \cdot \frac{E_{\text{nom.}}}{2} \right) \cdot \frac{1}{E_{\text{nom.}}} = 1 - \frac{\eta^{\text{Sys}}}{2} \quad (6.1)$$

Due to the fact, that the BESS system efficiency η^{Sys} depends strongly on the individual operation, the theoretical average system efficiencies of the battery and the inverter are applied:

$$\eta_{\text{theor.}}^{\text{Sys}} = \eta_{\text{avg.}}^{\text{Batt}} \cdot \eta_{\text{avg.}}^{\text{Inverter}} \quad (6.2)$$

In the baseline scenario the $\eta_{\text{avg.}}^{\text{Inverter}} = 92\%$ and the $\eta_{\text{avg.}}^{\text{Batt}} = 95\%$ resulting in a theoretical average system efficiency $\eta_{\text{theor.}}^{\text{Sys}} = 0.92 \cdot \sqrt{0.95} = 90\%$ and hence in a $SOC_{\text{setpoint}} = 55.0\%$. In consequence, the maximum amount of energy that can be converted in both directions is given with:

$$E_{\text{charge/discharge}} = SOC_{\text{setpoint}} \cdot \eta_{\text{theor.}}^{\text{Sys}} \cdot E_{\text{nom.}} = 49.46\% \cdot E_{\text{nom.}} \quad (6.3)$$

IDM transactions

Subsequently, it is checked if the SOC is at a level which ensures that the provision of the current required PCR power can be continued in the next steps. If the SOC reaches a certain value, IDM transactions have to be applied to balance the SOC again. As described in **Section 2.3.1.3**, the shortest lead time for trading transactions at the EPEX SPOT is 30 min. Hence, in every time step the time interval is determined, how long the BESS can be operated providing the current PCR power demand constantly in the worst case until the BESS is fully charged or discharged. These time intervals

can be expressed by the following equations in charge t_{charge} and discharge $t_{\text{discharge}}$ direction:

$$t_{\text{charge}} = \frac{E_{\text{nom.}}}{P_{\text{max}}^{\text{PCR}} \cdot \eta_{\text{theor.}}^{\text{Sys}}} \cdot (1 - \text{SOC}) \quad (6.4)$$

$$t_{\text{discharge}} = \frac{E_{\text{nom.}}}{P_{\text{max}}^{\text{PCR}} \cdot \frac{1}{\eta_{\text{theor.}}^{\text{Sys}}}} \cdot (\text{SOC}) \quad (6.5)$$

As soon as one of these values passed the 30 min lead time of the IDM trading, the appropriate trading decisions are taken. Due to the fact, that the IDM enables only 15 min trading blocks, this decision will only be taken every 15 min. Once an IDM transaction has been made, the offered power will be considered in addition to the required PCR power after the lead time of 30 min has passed.

6.3.1.2 Economic parameters

In addition to the general economic parameters shown in **Section 6.1.2**, the specific parameters for the PCR application are summarized in **Table 6.10**.

Table 6.10: PCR-supply: General economic parameters.

| Input variable | Value |
|------------------------------|-------------------------------|
| PCR tender prices | 2015: Different scenarios |
| IDM transaction prices | 2015: Weighted average values |
| EPEX SPOT participation fees | 1 st Jan. 2015 |

Figure 6.12a shows the course of the weekly PCR tender prices during 2015 public available at 'Regelleistung.net' [36]. The yellow curve represents the average price of all tenders and reveals a price high deviations during the course of one year. In addition, two further scenarios are defined with the minimum and maximum tender prices of every week. Thereby, large price spreads for the same week are observable during the entire year with its maximum in the last week of the year with 3968 Euro between the highest and lowest tender price. Due to the high impact of the PCR tender prices on the economic result, these three price scenarios are examined in the sensitivity analysis in **Section 6.4.2**. However, the baseline scenario of the PCR application uses the average price scenario.

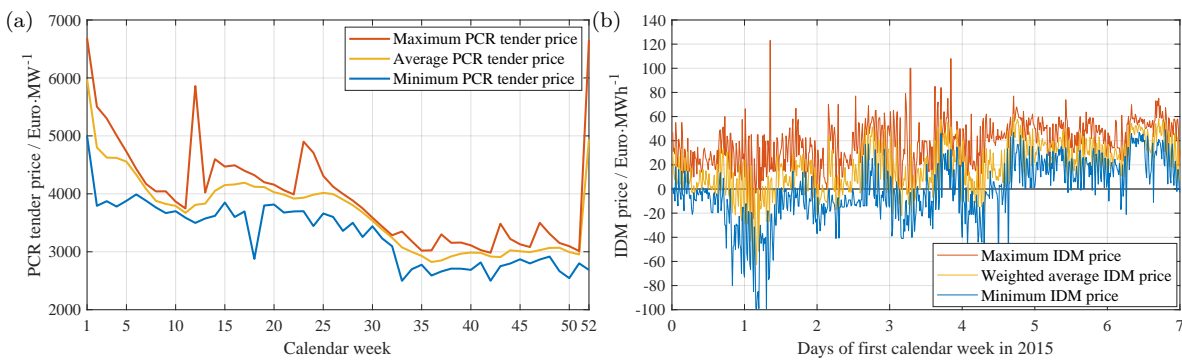


Figure 6.12: Figure 6.12a: Weekly course of the PCR tender prices in Germany in 2015.

Figure 6.12b: Course of the IDM prices profiles in the first week of 2015.

Table 6.11: Fees and costs for the participation on the IDM.

| Fix costs | | Variable costs | |
|--------------------------|-------------|-------------------------------|---------------|
| Entrance fees (one-time) | 25 000 Euro | Trading costs | 0.10 Euro/MWh |
| Annual fees | 5000 Euro | Trading costs per transaction | 0 Euro |

The fees and costs for the participation on the IDM of the EPEX SPOT are given in **Table 6.11** for 2015. The fix costs consist of the entrance fees of 25 000 Euro, which are considered only once in the depreciation period, and the annual fees of 5000 Euro, in sum 30 000 Euro. The trading costs for the IDM transactions are given with 0.10 Euro/MWh and no additional fee is charged per transaction.

The IDM transaction prices profiles of 2015 are used to calculate the costs or revenues of every IDM buying or selling transaction during the simulation. The original IDM price data obtained from the EPEX SPOT shows different prices profiles for the same market. **Figure 6.12b** shows the low, high and weighted average price profiles of the first week of 2015. Again, different price scenarios could be applied in the sensitivity analysis. However, the price spread of the available profiles is relatively small and the impact is small due to the fact, that only a few IDM transactions have to be performed during the whole depreciation period. Hence, the PCR baseline scenario uses the weighted average values of the IDM prices profiles.

6.3.1.3 Simulation parameters

Table 6.12 summarizes the applied parameters of the PCR simulation with SimSES. The BESS load is characterized by the half-cycle counting method, allowing a precise calculation of the battery degradation. The sample time has to be chosen with 1 s according to the sample time of the frequency profile which the BESS has to follow instantaneously. Similar to the PV-HESS application, the aging model is called with the average values from the battery load characterization with the same sample time of 600 s. The BESS ambient temperature is set to 25 °C due to the assumption that the system is installed inside an industrial building providing a constant temperature with a climatization system. However, the additional losses in order to control the BESS temperature are not considered, due to wide possible range in dependency of the installation environment.

Table 6.12: PCR-supply: Simulation parameters.

| Input variable | Value |
|--|---------------------|
| Sample time | 1 s |
| Load characterization method | Half-cycle counting |
| Method for calling of battery aging model | Average values |
| Step size for calling of battery aging model | 600 steps / 10 min |

6.3.2 System configuration

The BESS in the PCR application has to be operated with respect to the rules explained in **Section 2.3.2**. At any time under the conditions of the 'normal progression', the BESS has to be able to provide the positive or negative tendered PCR power P_{\max}^{PCR} at least 30 min. Furthermore, it takes 45 min until an ordered IDM transaction is realized to balance the SOC again. Hence, the maximum total derivative time results in $t^{\text{derivative}} = 75$ min, which has to be considered in both, charge and discharge direction. Based on the theoretical average system efficiency $\eta_{\text{theor.}}^{\text{Sys}} = 90.0\%$ and the

efficiency-dependent $SOC_{\text{setpoint}} = 55\%$ the following derivative time $t_{\text{discharge}}^{\text{derivative}}$ results for the discharge case:

$$t_{\text{discharge}}^{\text{derivative}} = \frac{SOC_{\text{setpoint}} \cdot E_{\text{nom.}}}{P_{\text{max}}^{\text{PCR}} \cdot \frac{1}{\eta_{\text{theor.}}^{\text{Sys}}}} = \frac{SOC_{\text{setpoint}}}{PER_{\text{PCR}} \cdot \frac{1}{\eta_{\text{theor.}}^{\text{Sys}}}} \quad (6.6)$$

The derivate time $t_{\text{charge}}^{\text{derivative}}$ in charge direction can be expressed similarly by applying the inverse of the theoretical average system efficiency $\eta_{\text{theor.}}^{\text{Sys}}$ and the SOC buffer of $1 - SOC_{\text{setpoint}}$:

$$t_{\text{charge}}^{\text{derivative}} = \frac{(100\% - SOC_{\text{setpoint}}) \cdot E_{\text{nom.}}}{P_{\text{max}}^{\text{PCR}} \cdot \eta_{\text{theor.}}^{\text{Sys}}} = \frac{100\% - SOC_{\text{setpoint}}}{PER_{\text{PCR}} \cdot \eta_{\text{theor.}}^{\text{Sys}}} \quad (6.7)$$

In both equations, the ratio of the maximum tendered PCR power $P_{\text{max}}^{\text{PCR}}$ to the nominal energy capacity $E_{\text{nom.}}$ can be expressed as the maximum PER_{PCR} , which is a target value for the PCR system configuration. In order to solve the equations for this target value PER_{PCR} , both equations can be equated by inserting and eliminating the setpoint SOC_{setpoint} in both equations:

$$PER_{\text{PCR}} \cdot \eta_{\text{theor.}}^{\text{Sys}} \cdot t_{\text{forward}} = 1 - t_{\text{forward}} \cdot PER_{\text{PCR}} \cdot \frac{1}{\eta_{\text{theor.}}^{\text{Sys}}} \quad (6.8)$$

This equation can be solved for PER_{PCR} :

$$PER_{\text{PCR}} = \frac{1}{\eta_{\text{theor.}}^{\text{Sys}} \cdot t_{\text{forward}} + t_{\text{forward}} \cdot \frac{1}{\eta_{\text{theor.}}^{\text{Sys}}}} = \frac{1}{t_{\text{forward}} \cdot (\eta_{\text{theor.}}^{\text{Sys}} + \frac{1}{\eta_{\text{theor.}}^{\text{Sys}}})} \quad (6.9)$$

By using the $\eta_{\text{theor.}}^{\text{Sys}} = 90.0\%$ and the derivative time $t^{\text{derivative}} = 75 \text{ min}$, the PER_{PCR} results in about 0.4 C. Hence, to provide the $P_{\text{max}}^{\text{PCR}} = 1 \text{ MW}$ the BESS energetic capacity has to be at least 2.5 MWh:

$$E_{\text{nom.}} = \frac{P_{\text{max}}^{\text{PCR}}}{PER_{\text{PCR}}} = \frac{1 \text{ MW}}{0.4 \text{ C}} = 2.5 \text{ MWh} \quad (6.10)$$

6.3.3 Performance

This section will give deeper insights of the BESS performance in the PCR-supply baseline scenario. First, the BESS operation is shown and followed by the evaluation of the battery aging. Finally, the main economic results are presented.

6.3.3.1 Power and SOC course

Figure 6.13 shows the BESS power course in the upper plot and the respective SOC course together with the SOH in the lower plot of the first year of the 20 years of simulation. The C-rates are fluctuating strongly between the charge and discharge direction due to dynamic power grid frequency profile and exceed rarely 0.1 C. The C-rates peaks represents mostly the IDM transaction in order to shift the SOC to the SOC_{setpoint} , which can be seen in the lower plot in **Figure 6.13** more clearly: The SOC fluctuates due to power grid frequency profile and is overlain by the IDM charge and discharge intervals controlling the SOC to be an average of about 51.0%. Thereby, the SOC range between 17.9 to 84.8%.

Figure 6.14 illustrates the BESS utilization in detail by showing the heatmap of the battery C-rate and SOC with respect to the date in the course of the first year on the x-axis and the daily course

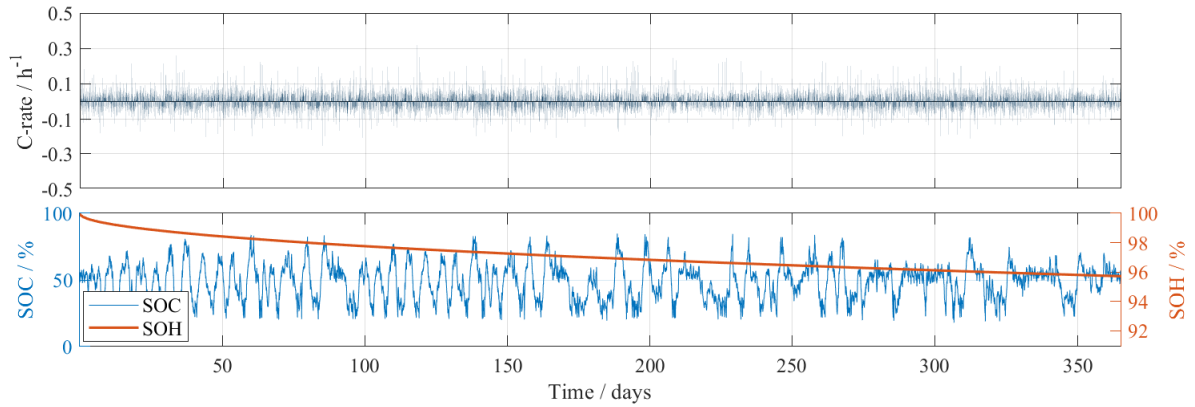


Figure 6.13: PCR-supply: Course of the battery C-rate (upper plot) and the SOC and SOH (lower plot) over the first simulation year.

on the y-axis simultaneously. The battery C-rate in **Figure 6.14a** shows charging periods (positive sign) with reddish colors and discharging periods with bluish colors. The greenish colors mark the time periods with almost or even no battery utilization with < 0.01 C. In contrast to the PV-HESS application shown in **Figure 6.9a**, the BESS is almost not utilized in the PCR application since most of the time the C-rate is < 0.01 C. However, the small and red lines scattered over the whole year represent charging and discharging events with C-rates up to 0.4 C due to the IDM transaction.

The resulting SOC distribution over time is shown in **Figure 6.14b**. In contrast to the stochastic distribution of the C-rate over time, the SOC seems to remain constant during the days and changes in between a couple of days.

6.3.3.2 Battery load characterization

Again, the battery load characteristics of the PCR application are evaluated here before the resulting calendar and cycle aging is shown afterward.

The BESS system temperature is influenced by the system operation but almost no deviate from the assumed ambient temperature of 25 °C due to the limitations of the applied thermal model. However, the course of the SOC over time influences the calendar aging. In contrast to the SOC heatmap shown

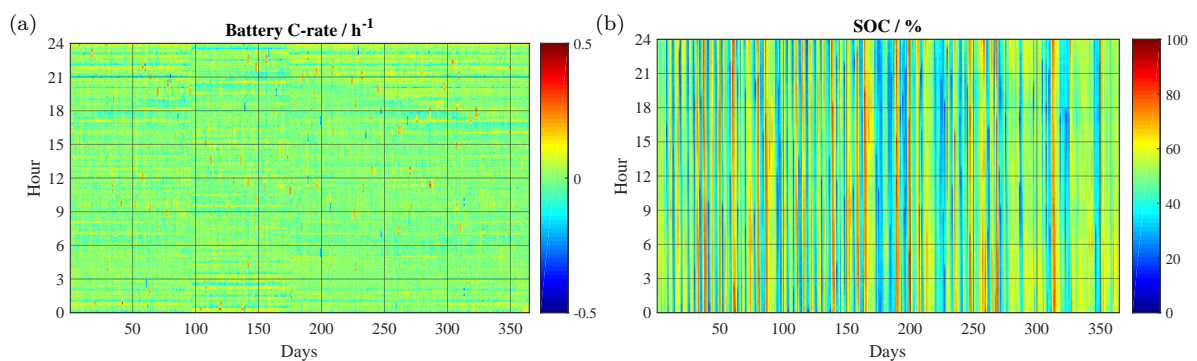


Figure 6.14: PCR-supply: Temporal distribution of the battery C-rate (Figure 6.14a) and the SOC (Figure 6.14b) over the first simulation year.

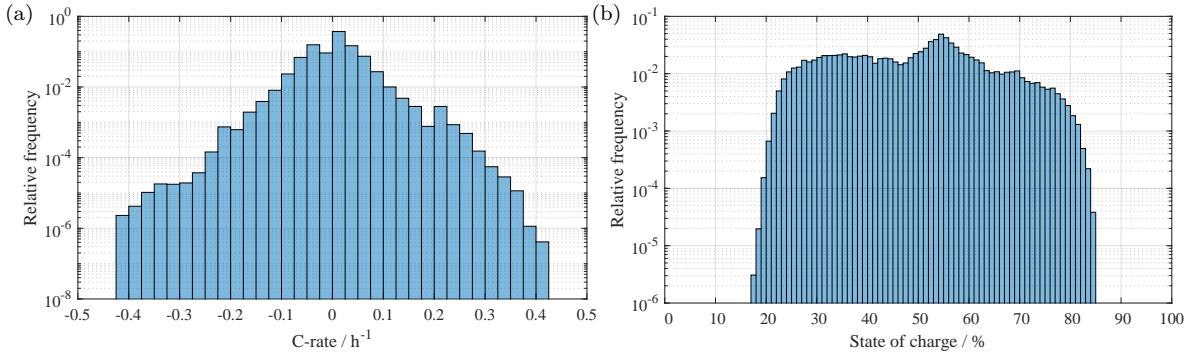


Figure 6.15: PCR-supply: Distribution of the relative frequency of the battery C-rate (Figure 6.15a) and the SOC (Figure 6.15b) over the first simulation year.

before, **Figure 6.15b** and the following histogram figures give a statistical insight into the BESS load characteristics over the first year of the 20 years of simulation. The y-axes are drawn on a logarithmic scale due to the unequal distribution of the relative frequency of each evaluation parameter and to enable a proper overview over the whole value range on the x-axes. The BESS SOC in this PCR baseline scenario is almost distributed equally over the SOC in the range between 17.9 to 84.8% due to the requirements of the PCR power supply. Towards to these limits, the frequency decreases. The SOC_{setpoint} appears significantly with a peak at about 55% SOC occurring at about 5% of the total time.

Figure 6.15a shows the histogram of the BESS C-rate, with positive values for the charge and the negative values for the discharge direction. The C-rate distribution is almost symmetrical between the charge and discharge direction due to the stochastic characteristic of the power grid frequency. The frequency of the single C-rates is decreasing with higher absolute C-rates linearly in this logarithmic scale, however, with a linear scaled y-axis the decrease would appear even stronger. The small peaks at about 0.21 C in this frequency distribution represent the IDM transactions in the charge and discharge direction, which are applied always with same absolute power.

Figure 6.16a shows the histogram of the half-cycle depth separated into the charge (positive) and discharge (negative) direction. Again, the frequency distribution of the half-cycle depths appears almost symmetrical between the charge and discharging direction in a range between 0 to 20%. The very small half-cycles with < 1% DOC have a relatively high proportion of about 5% of all detected cycles in charge and about 4% in discharge direction representing the small but very often required PCR power supply due to the power grid frequency deviations. The occurrences of the single DOC values decrease strongly with deeper absolute DOC, however, half-cycles with about DOC 15% in charge and discharge direction show significant frequencies in the range of bigger DOC. These DOC frequency peaks represent the IDM transactions which have to be applied with a constant time interval of at least 15 min due to regulations of the EPEX SPOT.

In order to evaluate the correlation of the two cycle aging influence factors, **Figure 6.16b** shows the histogram of the half-cycle depth together with the respective C-rate of every half-cycle depth in charge and discharge direction. The central bars in green and yellow colors represent the small half-cycle depths < 1%, which have a high proportion, however, the C-rate of these half-cycles is with values < 0.01 C relative low. The frequency distribution of the half-cycle over the C-rate occurrences appear almost symmetrical between the charge and discharging direction and almost all bars in discharge

direction have roughly the same proportion.

In order to summarize and to compare the single distribution of the shown aging influence parameters, the average values of SOC, C-rates and DOC are shown in **Table 6.14** in comparison with the results from the PV-HESS application.

6.3.3.3 Battery aging

The battery aging course of the capacity and the resistance of the PCR application with the baseline scenario is shown in **Figure 6.17** over the first year of the 20 years simulation time. Both figures show the portion of the calendar and cycle aging in comparison to the sum of both as the total aging. The battery capacity loss illustrated in **Figure 6.17a** follows a square root trend due to decreasing aging rates with the decreasing capacity. The total aging with 4.3% after the first year is dominated strongly by the calendar aging, due to the fact, that almost no cycle aging occurs. Although about 140.3 FEC occur during one year, the capacity loss of the cycle aging is very small because most of the half-cycles occur with very small C-rates and DOCs as shown in **Figure 6.16**. At the end of the 20 years of simulation, the capacity decreased by about 19.3% dominated by the calendar aging with a proportion of about 98.6% in comparison to the cycle aging. About 2896 FEC occur over the 20 years operation, however, the majority with half-cycle depths < 1%. By considering the 'Woehler-curve' of the applied cycle aging model shown in **Figure 5.7**, it is obvious that the cycle aging of this PCR baseline scenario is very weak due to high cycle stability with half-cycle depths < 1%.

The battery resistance, shown in **Figure 6.17b**, increases linearly and again the calendar aging dominates strongly the total aging. The total resistance increases of about 0.8% in the first year with a portion of about 96.6% due to calendar aging. In 20 years of operation, the total resistance increases with about 17.0%, representing thereby almost the same absolute value as observed for the capacity loss. The small influence of the cycle aging on the resistance increase is related to the low utilization of the BESS in this PCR application due to dominating half-cycles with small C-rates and depths < 1%.

Although the absolute aging values of the capacity loss and resistance increase influence significantly the BESS operation over the whole simulation time, there is no need to replace the battery before the end of the depreciation period of 20 years. However, the tendered PCR power P_{\max}^{PCR} should be adapted steadily during the 20 years of operation to fulfill the PCR supply requirements [36] even with less

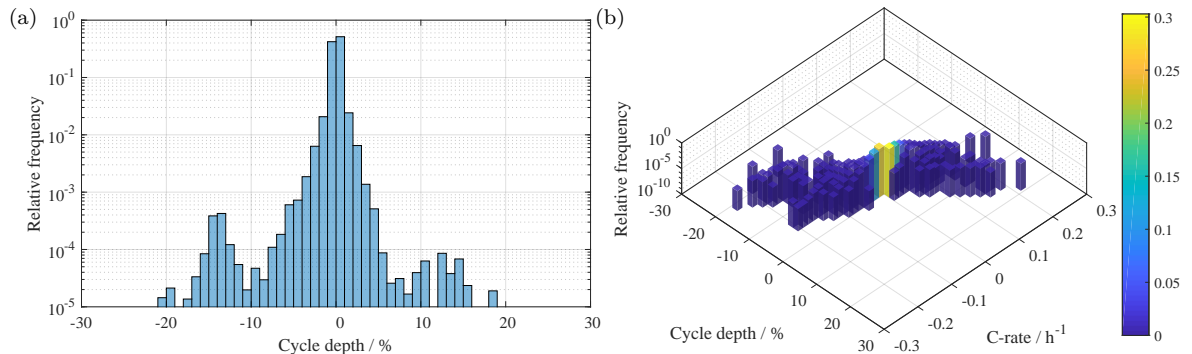


Figure 6.16: PCR-supply: Distribution of the relative frequency of the cycle depth (Figure 6.16a) and the cycle depth over C-rate (Figure 6.16b) over the first simulation year. The color bar of Figure 6.16b represents the relative frequency values of the histogram.

available capacity due to aging. The resistance increase can be neglected due to fact that the average system efficiency is limited by the inverter efficiency.

6.3.3.4 Economics

The overall economic results of the baseline scenario of the PCR application are compared with the results from the PV-HESS application in **Section 6.4.1.2**. Here, the particular results of the PCR application are presented as net present values by applying the discount factor of 1.96 % (see **Table 6.2**).

In the PCR baseline scenario, the BESS investment for the battery size of 2500 kWh costs 2043 kEuro. The supply of 1 MW PCR power over the 20 years of operation results in earnings of 4767 kEuro.

The fixed costs to participate on the IDM at the EPEX SPOT are in sum 125 kEuro. Over the 20 years of operation, 2107 selling transaction with 202.7 MWh discharged energy and 6097 buying transactions with 762.1 MWh charged energy are realized resulting in a sum of 8204 IDM transactions with 263.4 MWh energy throughput. Each transaction has fix trading costs of 0.10 Euro/MWh resulting in total costs of 102.50 Euro. The variable costs are calculated with the IDM price profile leading to earnings of 7832.60 Euro for the selling and costs of 28 639 Euro for the buying transactions summing up to variable costs of 20 806 Euro. The IDM participation costs together with the operational costs (fixed and variable costs) result in a sum of 180 kEuro costs for the IDM transactions.

Hence, the net earnings of the PCR supply are reduced by the total costs of the IDM transaction resulting in a total cash flow $C_{\text{cash flow, total}}^{\text{NPV}}$ of 4587 kEuro. By subtracting the BESS investment costs, the BESS earnings in the baseline scenario of the PCR application result in a total return $R_{\text{total}}^{\text{NPV}}$ of 2544 kEuro.

Table 6.13: PCR-supply economic results.

| Parameter | Values |
|--------------------------|------------|
| Total cash flow | 4587 kEuro |
| Investment costs | 2043 kEuro |
| Total return | 2544 kEuro |
| Profitability index (PI) | 1.2452 |

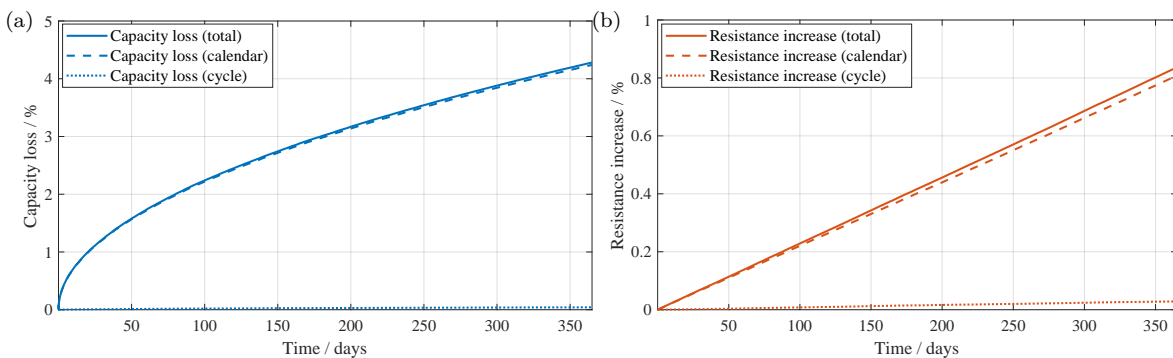


Figure 6.17: PCR-supply: Course of the capacity loss (Figure 6.17a) and the resistance increase (Figure 6.17b) over the first simulation year.

6.4 Comparison of the battery energy storage system applications

The before presented two stationary BESS applications PV-HESS and PCR-supply differ from each other in many aspects, however, there are technical and economic key characteristics that allow for a technical and economic comparison of both applications each with the defined baseline scenario in this section. In addition, examination of the baseline scenarios of both applications is extended afterward by a sensitivity analysis of the economic outcome with respect to the BESS investment costs and different price scenarios.

6.4.1 Analysis of the key characteristics

In the following, the technical and economic key characteristics of the PV-HESS and PCR-supply application are compared. Therefore, the evaluation parameters presented in **Section 3.2** are applied.

6.4.1.1 Technical key characteristics

Table 6.14 shows all technical key characteristics of both, the PV-HESS and the PCR application, as a result of 20 years simulated operation with the respective baseline scenarios. Both applications depend strongly on the specific system configuration due to technical and economic requirements, however, the applied baseline scenarios for both applications represent a realistic setting. Most of the parameters have been compared already in the preceding section, however, the most relevant characteristics are summarized here.

Although both applications show a similar average SOC, they are operated very differently: The PV-HESS uses the whole capacity between 0 to 100 % by being fully charged and discharged in a daily frequency most of the time having an average SOC of about 41.4%. In contrast, the SOC of the PCR BESS remains most of the time near to the average SOC of about 51.0 % and shows only rarely fluctuations between a SOC range of 17.9 to 84.8 %.

The same observation can be made when comparing the DOC key characteristics: In the PV-HESS application, DOCs up to 100 % in charge and discharge direction occur and in average the half-cycles

Table 6.14: Technical results of baseline scenarios of PV-HESS and PCR simulations.

| Parameter | PV-HESS | PCR |
|---|---------|--------|
| Average SOC | 41.4 % | 51.0 % |
| Average DOC | 25.1 % | 0.39 % |
| Average charge DOC | 27.7 % | 0.38 % |
| Average discharge DOC | 23.0 % | 0.41 % |
| Average charge C-rate | 0.11 C | 0.04 C |
| Average discharge C-rate | 0.07 C | 0.04 C |
| Maximum charge C-rate | 0.20 C | 0.42 C |
| Maximum discharge C-rate | 0.19 C | 0.42 C |
| Average system efficiency | 90.9 % | 86.7 % |
| Temporal utilization τ_{time} | 37.1 % | 22.1 % |
| Energy-based utilization τ_{energy} | 30.0 % | 8.6 % |
| FEC_E | 4786.2 | 2895.8 |
| Capacity loss after 20 years | 25.7 % | 19.3 % |
| Resistance increase after 20 years | 26.1 % | 17.0 % |

depth is about 25.1%. The PCR BESS is operated very rarely with cycles up to 20% in charge and discharge direction and more often with very small cycles < 1% leading to an average half-cycle depth of about 0.39%.

Both applications operate the BESS with relatively low average C-rates in charge and discharge directions < 0.1 C. Even though the maximum charge and discharge C-rates of the PCR application with about 0.4 C seems to be high, these C-rate extremes are rarely applied in comparison to the PV-HESS, where the C-rate extremes with about 0.2 C are achieved almost every day.

These characteristics of the C-rate result in different average system efficiencies: The PV-HESS achieves an average system efficiency of about 90.9% and the PCR application less with 86.7% due to higher losses in the partial-load operation of the inverter when operating the BESS with relative low C-rates.

The temporal utilization rate τ_{time} shows that both applications use the BESS with 37.1% for the PV-HESS and 22.1% for the PCR application quite often during the whole simulation time. However, the energy-based utilization rate τ_{energy} reveals that the PCR application uses the BESS with 8.6% significantly less than the PV-HESS application with 30.0% of theoretically possible maximum energy throughput.

Although the energetic throughput expressed as FEC_E is for both applications in the same range with 4786.2 FEC_E for the PV-HESS and 2895.8 FEC_E for the PCR application, the PV-HESS application utilizes the BESS significantly stronger with higher C-rates and DOC in comparison to the PCR application.

Both applications result in similar values of the capacity loss and resistance increase after 20 years of operation due to the predominant influence of the calendar aging.

6.4.1.2 Economic key characteristics

For both baseline scenarios in the PV-HESS and the PCR application, the BESS investments costs are calculated with the same prices given in **Table 6.3**. A lower value for the variable investment costs could be expected for the PCR-supply application with a storage size by a factor of about 500 bigger than the PV-HESS in the baseline scenario due to the economies of scale. However, the same variable investment costs are applied to both applications and the dimensional difference is considered with the battery investment cost, which has a high proportion of the total investments costs of the PV-HESS BESS in comparison to the investment costs of the PCR BESS. Hence, the BESS specific total investment costs are 1122.5 Euro/kWh for the PV-HESS and 817.27 Euro/kWh for the PCR-supply application.

The further specific costs and revenues in the baseline scenarios of both applications are given in

Table 6.15: Economic results of baseline scenarios of PV-HESS and PCR simulations.

| Parameter | PV-HESS | PCR |
|---|---------------------|---------------------|
| Levelized cost of energy stored (LCOES) | 0.1814 Euro/kWh | 0.3027 Euro/kWh |
| Levelized earnings of energy stored (LEOES) | 0.3341 Euro/kWh | 0.6796 Euro/kWh |
| Levelized profit of energy stored (LPOES) | 0.1527 Euro/kWh | 0.3769 Euro/kWh |
| Profit per energy installed (PPEI) | 35.45 Euro/kWh/Year | 50.88 Euro/kWh/Year |
| Internal rate of return (IRR) | 3.26 % | 6.53 % |
| Profitability index | 0.6316 | 1.2452 |

the evaluation for the PV-HESS in **Section 6.2.3.4** and for the PCR-supply application in **Section 6.3.3.4**

Here the economic key results are compared: **Table 6.15** shows the economic results of both application with diverse economic result parameters, which are defined in **Section 3.2.2**.

Although the specific investments costs are higher in the PV-HESS application, the LCOES are with a value of 0.1814 Euro/kWh significantly lower than the LCOES in the PCR application with 0.3027 Euro/kWh related to the total discharged energy. The reason for this difference is the utilization rate or given in detail with the FEC with about 65.3% more FEC in the PV-HESS application than in the PCR application over the same operation time. However, the LEOES of the PCR-supply application are with 0.6796 Euro/kWh about 103.4% higher in comparison to the LEOES with 0.3341 Euro/kWh of the PV-HESS application. In consequence, the LPOES, as the difference between LCOES and LEOES, results with 0.3769 Euro/kWh for the PCR-supply application about 146.8% higher than the LPOES of the PV-HESS with 0.1527 Euro/kWh.

Another perspective on the economics is given with the PPEI, which relates the economic result to the installed BESS energetic capacity. Thereby, the PCR-supply application shows again a better absolute value with 50.88 Euro/kWh/Year in comparison with the PPEI of the PV-HESS with 35.45 Euro/kWh/Year related to the respective installed energy, however, the difference is with a factor of about 43.5% smaller in comparison to the LPOES.

Besides the storage-specific evaluation parameters discussed before, the IRR and the PI allow for an economic comparison independent from the specific application. The IRR of the PV-HESS application is with 3.26% below the assumed investment interest rate of 4%. Hence, the BESS investment in the PV-HESS baseline scenario would be less profitable than realizing a capital investment with a fixed term of 20 years with the interest rate of 4% instead. However, the IRR of the PCR-supply application with 6.53% shows again the higher profitability in comparison to the PV-HESS application. Although the IRR of the PCR-supply application in the baseline scenario is above the assumed interest rate of 4%, this BESS investment can comprise different risks: The better profitability depends strongly on the assumed PCR tender result price, which vary in a wide range during the course of a year and shows, in addition, no clear trend in the past years. Furthermore, it remains vague if the market volume with the tendered PCR power will be reduced in the future to the growing PCR-supply with BESS which are able to supply the required power more effective than the existing power plants. The investment in a PV-HESS BESS can comprise different risks as well, however, the PV feed-in remuneration is legally stipulated for the simulated operation time of 20 years. Only the electricity price can change in future and is consequently object to the sensitivity analysis in the next section.

Similar to the IRR, the PI shows also a better profitability for the PCR application with a value of 1.2452 in comparison to 0.6316 of the PV-HESS application.

6.4.2 Economic sensitivity analysis

The economic results shown in the preceding section rely on one setting of economic input parameters. Due to the fact that the costs and revenues in the PV-HESS and PCR-supply application can comprise uncertainties, the relevant input parameters are varied in the following sensitivity analysis.

Therefore, all BESS investment costs are summarized in one single parameter, the specific battery system costs, representing the total BESS investments related to the battery nominal energy without

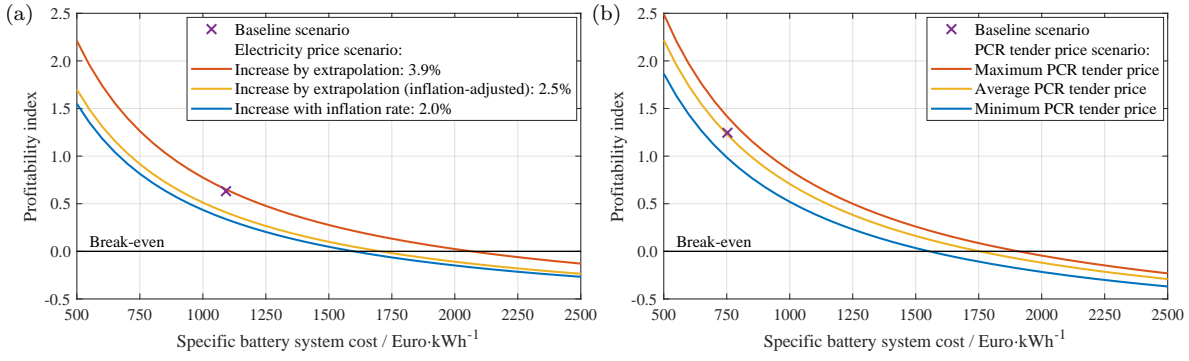


Figure 6.18: PI over the specific battery system costs for the baseline scenarios of the PV-HESS application (Figure 6.18a) and PCR supply (Figure 6.18b) subject to different economic scenarios.

any fixed price parts. As stated above in **Section 6.1.2.2**, a price range between 500 to 2500 Euro/kWh related to the battery nominal energy is applied.

In order to consider the different risks discussed in preceding section, the relevant revenue parameters are additionally examined in this sensitivity analysis: For the PV-HESS application, the electricity price is varied with the three scenarios presented in **Figure 6.1**. For the PCR-supply application, the tender results of 2015 are varied with the minimum, average and maximum prices.

Figure 6.18 shows the PI of the baseline scenarios of both applications over the variation of the specific battery system costs. The PI is drawn for both applications in an individual subplot in order to better distinguish the differences between the respective scenarios. The black line at the PI value of 0 marks the break-even in both applications and the purple crosses label the result of the baseline scenarios of both applications with the standard economic parameters described in **Section 6.1.2.2**.

In the baseline scenario of the PV-HESS application, all electricity prices scenarios lead to a positive PI > 0.33 when considering the current specific battery systems costs of BESS with LFP/C batteries (see **Section 6.1.2.2**) of about 1091.90 Euro/kWh. Even in the worst case with the lowest increase of the electricity prices by 2.0 % per year, the PI would be positive with prices below specific battery systems costs of about 1600 Euro/kWh.

Almost similar absolute values for the PI result in the baseline scenario of the PCR-supply application with the three different PCR tender price scenarios (see **Section 6.3.1.2**). With the assumed specific battery systems costs (see **Section 6.1.2.2**) of about 752.70 Euro/kWh for this BESS, in all scenarios, the PI is higher than in the PV-HESS application with values > 1.0 . However, the break-even of the PI is in the worst case with the 'Minimum PCR tender price' scenario again at specific battery systems costs of about 1600 Euro/kWh.

In conclusion, both, the PV-HESS and the PCR-supply application are economically viable in all particular price scenarios when considering the current specific battery systems costs.

7 Conclusion

This work presented a techno-economic evaluation of stationary BESS in the two applications PV-HESS and PCR-supply with special consideration of aging. In order to perform this evaluation, the model framework SimSES was introduced together with the methods to assess the technical and economic results of stationary BESS. The influence of battery aging was simulated with a detailed calendar and cycle aging model, developed for a widely used LFP/C cell. These aging models are based on comprehensive experimental studies on this battery cell, which have been performed and presented in this work.

In this conclusion, first, the results of the LFP/C aging studies and the consecutive aging model development are summarized. Afterward, the main results of the techno-economic evaluation of the PV-HESS and PCR-supply application are presented.

7.1 Aging and modeling of LiFePO₄/graphite cells

Calendar aging

The static calendar aging study on the LFP/C cells with 17 TPs with 3 cells each over almost 900 days revealed a strong influence of storage temperature and SOC on both capacity loss and resistance increase. In line with the literature, the observed calendar aging of LFP/C cells leads predominantly to LLI due to the SEI growth on the graphite anode and only minor contributions from LAM. Hence, Q_{loss} and R_{inc} are increasing over time, however, the rate of Q_{loss} is slowing down in a square root dependance over time. In contrast, the rate of R_{inc} stays constant over time. The temperature influence appeared as observed in other aging studies, showing an exponential dependancy of the increase rate of Q_{loss} and R_{inc} with respect to the storage temperature. The influence of storage SOC on Q_{loss} over time showed similar results as observed in [50]. With higher storage SOC the rates of Q_{loss} are increasing, but in the middle SOC-range, the rate stays almost constant. In contrast, R_{inc} showed the highest values in the middle SOC-range. Based on the static calendar aging study, a semi-empirical model was developed to estimate Q_{loss} and R_{inc} for the influence of temperature, SOC and time. The resulting aging equations are products that consist of three factors, each representing one of the influence parameters. The temperature influence can be modeled with the widely used Arrhenius-term for both Q_{loss} and R_{inc} . However, due to the long test duration, this study proves that the temperature influence can be modeled with the Arrhenius-term over long timescales. The temperature factor parameters have been determined with the TPs at $SOC = 100\%$ of 25 °C, 40 °C and 60 °C. The SOC influence factor was modeled with a cubic function for Q_{loss} and a quadratic function for R_{inc} . The functions' parameters have been determined with the TPs at 40 °C with 9 SOC values between 0-100 %.

The necessary equations for the rate of Q_{loss} and R_{inc} have been derived for the application of the aging model in lifetime simulations. Furthermore, an equation for the virtual time t^* was introduced which enables the correct simulation of varying storage conditions when applying the aging model.

Finally, the aging model was validated with the measurement values of a dynamic calendar aging study. This study proved the hypothesis of independence of the order of storage conditions on the resulting Q_{loss} and R_{inc} and the fact that the calendar aging rate is dependent on the current SOH. The aging model is able to estimate the aging of the dynamic calendar aging TPs fairly accurately with a maximum absolute error of 2.2% for Q_{loss} and 6.9% for R_{inc} . This work shows that the aging of the investigated LFP/C cells can be estimated relatively precisely with a semi-empirical aging model based on few fitting parameters that do not have to be adapted for each storage condition. Due to the good correspondence of the temperature influence on Q_{loss} and R_{inc} with the Arrhenius-law, an extrapolation passing the measurement time of almost 900 days is allowed leading to calendar lifetime of more than 22 years (assuming a EOL at $Q_{loss} = 20\%$) for the storage conditions with 25 °C at $SOC = 50\%$. Assuming an operating life of 20 years for stationary BESS [2; 6], the calendar aging of the investigated LFP/C cell would account for about 19.0% decrease of the initial capacity and about 33.7% increase of the initial resistance in case that the SOC remains at 50% and the temperature at 25 °C. By considering the additional cycle aging of a stationary battery application, the capacity would underrun the EOL criteria at typically $Q_{loss} = 20\%$ before having passed 20 years of operating life with the described operation conditions.

Cycle aging

The static cycle aging study on the LFP/C cells was performed with more than 19 TPs with 3 cells each over almost 900 days. The values of the capacity loss and resistance increase have been corrected with the results of the calendar aging study to obtain the pure cycle aging values as necessary input for the aging model development.

The results reveal a strong influence of the cycles DOC and SOC on both capacity loss and resistance increase. For both parameters very different degradation trends are observable: The capacity degradation of the TPs with the $DOCs = 80\%$ and 100% follows a square root dependance of time/FEC for C_{disch} and a linear trend for $R_{DC,10s}$. For the TPs with lower DOC, the capacity degradation rates are higher with linear trends, however, after about 1000 FEC the rate of capacity fade slows down and is continued by a period with almost no capacity fade for almost 7000 FEC. Finally, at the EOT at about 10600 FEC the capacity degradation rates are higher with bigger DOC showing the expected influence of DOC on the capacity loss. For the resistance increase after the first 1000 FEC a similar picture is observable due to the influence of DOC, however, in contrast to the capacity degradation trends, the resistances are increasing for all TPs with an almost linear trend. For both, the capacity and resistance degradation, it was observed, that the cyclization with $DOCs = 20\%$ around $SOC = 50\%$ lead to the highest aging than lower and higher SOC-ranges. Due to special aging trends around $soc = 50\%$ no clear relation between SOC-range and degradation can be stated for the first 5000 FEC.

The C-rate showed only small influence on the capacity loss, however, higher degradation was observed for the relatively high discharge C-rate of 2 C at 40 °C. For the resistance increase, the influence of the C-rate revealed, that the resistance increased stronger with smaller C-rates. Only for the relatively high discharge C-rate of 2 C at 40 °C the strongest resistance increased was measured.

Due to the correction of the measured aging values with the calendar aging values, the temperature influence on the degradation was already considered and the pure cycle aging results showed almost no additional influence of the temperature on the degradation due to the cyclization.

Based on the static cycle aging study, a semi-empirical model was developed to estimate Q_{loss} and R_{inc} for the influence of C-rate, DOC, and Ah-throughput. The resulting aging equations are products

that consist of three factors, each representing one of the influence parameters. The Ah-throughput is considered with a square root of the FEC for the capacity loss and with a linear influence on the resistance increase. The influence of the C-rate on the degradation was modeled with a linear factor with higher values at higher C-rates for the capacity loss. For the resistance increase, the C-rate influence factor was modeled with an inverse trend over the C-rate with respect to the measured results. Due to the special aging trends for the different tested DOC, only the values at EOT and the trends of the TPs with $DOCs = 80\%$ and 100% have been used for the model development. Finally, a cubic trend over the DOC was applied to model the influence of the DOC with good accordance for the values at EOT.

In order to validate the cycle aging model, a combined aging model was developed and applied in the BESS simulations. This combined aging model is able to reflect the influence of temperature, SOC, time, C-rate, DOC, and FEC on both, the capacity loss and resistance increase, of load profiles with dynamically changing parameters.

When applying this combined aging models in BESS lifetime simulations with changing parameters, the virtual time t^* and the virtual FEC^* have to be determined and to be used respectively to calculate the capacity loss due to the calendar and cycle aging. Since the resistance increase follows for the calendar aging model the time t and for the cycle aging model the FEC linearly, no adaption of the time or the FEC factor is necessary whenever the influence factors are changing.

This combined aging model has been validated with the two dynamic load profiles PV-HESS and PV-PCR-BESS, tested over almost 900 days simultaneously to the further static TPs. For both profiles, the simulated aging trends followed very close the measured values of the capacity loss and resistance increase. Due to the fact, that the absolute model errors remained less than 1% for the capacity loss and less than 2% for the resistance increase over the whole course of the measurement. Consequently, the developed aging model was considered to be sufficiently accurate for the lifetime estimations for BESS applications within the mentioned limits and ranges of the influence parameters.

7.2 Techno-economic simulation results of the investigated applications

The presented model framework SimSES was parametrized and applied to perform a techno-economic evaluation of the two stationary BESS applications PV-HESS and PCR-supply. The evaluation of the PV-HESS application revealed, that the sizing of the BESS capacity and the inverter's rated power with regard to the rated power of the PV-system has a strong influence on the technical and economic evaluation parameters. However, the particular influence of the sizing on the overall economic results cannot be reproduced by a single technical evaluation parameter, which showed individual and also inverse trends. Hence, the economic optimal sizing of the BESS components has to be determined individually with regard to the electricity consumption and the PV-system size of a household. In contrast, the sizing of the BESS components in the PCR-supply application allow almost no optimization potential due to the regulatory framework. However, the degrees of freedom in the PCR operation allows for the implementation of advanced operation strategies to control the SOC together with the aim to increase the profit with revenue potentials with IDM-transactions at the EPEX SPOT market.

The individual battery load was evaluated for both applications, revealing very different characteristics

of the SOC, C-rate and cycle depth. In both applications, the total capacity loss and resistance increase were dominated by the influence of the calendar aging, due to high cycle lifetime of the investigated and modeled LFP/C cell. However, at the end of the simulated depreciation period of 20 years, the capacity loss and resistance increase resulted in a similar value range with about 26 % for the PV-HESS and about 18 % for the PCR-supply application. Hence, the investigated LFP/C cell is able to be operated over this long time period at least in the baseline scenarios of both applications. Furthermore, the economic impact of the battery aging was revealed for the PV-HESS application: If the battery aging is neglected, the total return would be about 21.3% higher than the baseline scenario applying the developed aging model of the investigated LFP/C cell.

The economic sensitivity analysis with regard to different price scenarios and the specific battery system costs revealed that the economic result depends strongly on the assumed investment costs for the BESS and less on the chosen price scenarios. However, with the current specific battery system costs, both applications showed positive economic results in all particular price scenarios.

8 Outlook

Modeling of battery aging

In order to reduce the measurement efforts in future aging studies on LFP/C cells, the test matrix could cover only two temperatures: one with the standard conditions of application (e.g. 25 °C) and the second at the highest possible operation temperature (e.g. 60 °C).

Because the SOC-influence on the calendar aging of Q_{loss} and R_{inc} does not follow the SOC in a simple functional dependence, the TPs should cover various SOC values (e.g. with multiple points of support, evenly spaced or aggregated at the SOC-values where phase changes of the graphite anode are expected).

Although the developed and applied aging model of the investigated LFP/C cell showed acceptable results in the validation with the measured dynamic profiles, the results confirmed the limits of the applied semi-empirical aging model approach: Both, the influence of the anode overhang areas and the capacity recovery effects in the cycle aging are not reflected by this aging model.

Furthermore, the influence of the temperature on cycle aging was only evaluated in a limited temperature range with similar results and should be investigated for lower and higher temperature. Hence, further aging studies should try to cover also the individual limits in addition to the expected standard operation range of each aging influence parameter in order to understand the influence properly.

Nevertheless, due to the limits of the applied semi-empirical aging model, the individual dependence of the aging influence parameters should be analyzed and explained with physico-chemical models more thorough in future studies. Furthermore, in order to model the influence of the anode overhang effect on the usable cell capacity as well as on the resistance properly and, in addition, the influence of the observed capacity recovery effect, further measurements and possibly post-mortem analysis of the investigated cell are necessary in future investigations.

Techno-economic evaluation of stationary battery energy storage systems

The stationary BESS model framework SimSES allows for comprehensive techno-economic evaluations of the two stationary applications PV-HESS and PCR-supply. However, further possible reasonable BESS applications, such as the peak shaving of electricity load profiles or the BESS supplied integration of renewable energy sources in micro grids, can be modeled and evaluated with this tool as well.

The impact of the battery aging on the technical and economic result was investigated with a comprehensive aging model of the investigated LFP/C cell. However, it remains to be investigated if less complex aging model would lead to comparable results in order to enhance the simulation performance and to reduce the model parametrization efforts.

Furthermore, the BESS system model should be enhanced by including a proper thermal system model together with a more detailed model of the power electronics in order to simulate the BESS efficiency losses and the thermal impact on battery aging more precisely.

It is assumed, that the combined operation of different stationary BESS applications within one system could lead to better economic results than performing the single applications. Hence, the SimSES BESS model framework could be improved by developing control algorithms which enable operation strategies being able to cover the requirements of different applications simultaneously with the improvement of the economic result in comparison to operation of the single applications.

In this work, solely one type LFP/C of cells have been assessed in the two stationary applications PV-HESS and PCR-supply. In addition, the techno-economic suitability of further battery and energy storage technologies can be assessed with SimSES as well and could be evaluated for the different BESS applications and compared critically with the mainly implemented lithium-ion batteries.

List of References

- [1] Dena. *Netzflexstudie - Optimierter Einsatz von Speichern für Netz- und Marktanwendungen in der Stromversorgung*. Berlin, 2017.
- [2] A. Zeh, M. Müller, M. Naumann, H. Hesse, A. Jossen, and R. Witzmann. “Fundamentals of Using Battery Energy Storage Systems to Provide Primary Control Reserves in Germany”. In: *Batteries* 2.3 (2016), p. 29. ISSN: 2313-0105. DOI: 10.3390/batteries2030029.
- [3] VDE - Energietechnische Gesellschaft. *Batteriespeicher in der Nieder- und Mittelspannungsebene: Anwendungen und Wirtschaftlichkeit sowie Auswirkungen auf die elektrischen Netze*. Ed. by VDE - ETG. Frankfurt a.M., 2015.
- [4] A. Bräutigam. “Batteries for stationary energy storage in Germany: Market status & outlook”. In: *Intersolar*. Munich, 2016.
- [5] H. C. Hesse, R. Martins, P. Musilek, M. Naumann, C. N. Truong, and A. Jossen. “Economic Optimization of Component Sizing for Residential Battery Storage Systems”. In: *Energies* 10.7 (2017), p. 835. ISSN: 1996-1073. DOI: 10.3390/en10070835.
- [6] M. Naumann, R. C. Karl, C. N. Truong, A. Jossen, and H. C. Hesse. “Lithium-ion Battery Cost Analysis in PV-household Application”. In: *Energy Procedia* 73 (2015), pp. 37–47. ISSN: 18766102. DOI: 10.1016/j.egypro.2015.07.555.
- [7] Masayuki Yasuda. “Sony energy storage system using olivine type battery”. In: *International Conference on Olivines for Rechargeable Batteries*. Montreal, 2014.
- [8] Kokam Battery Cells. *Lithium Ion Polymer Cells - High Energy High Power*. URL: <http://kokam.com/cell/> (visited on 06/20/2017).
- [9] F. Gatta, A. Geri, R. Lamedica, S. Lauria, M. Maccioni, F. Palone, M. Rebolini, and A. Ruvio. “Application of a LiFePO₄ Battery Energy Storage System to Primary Frequency Control: Simulations and Experimental Results”. In: *Energies* 9.12 (2016), p. 887. ISSN: 1996-1073. DOI: 10.3390/en9110887.
- [10] J. Schmalstieg, S. Käbitz, M. Ecker, and D. U. Sauer. “A holistic aging model for Li(NiMnCo)O₂ based 18650 lithium-ion batteries”. In: *Journal of Power Sources* 257 (2014), pp. 325–334. ISSN: 0378-7753. DOI: 10.1016/j.jpowsour.2014.02.012.
- [11] M. Naumann, M. Schimpe, P. Keil, H. C. Hesse, and A. Jossen. “Analysis and modeling of calendar aging of a commercial LiFePO₄/graphite cell”. In: *Journal of Energy Storage* 17 (2018), pp. 153–169. URL: <https://doi.org/10.1016/j.est.2018.01.019>.
- [12] Institut für Stromrichtertechnik und Elektrische Antriebe der RWTH Aachen. *Wissenschaftliches Mess- und Evaluierungsprogramm Solarstromspeicher 2.0: Jahresbericht 2017*. Aachen. URL: http://www.speichermonitoring.de/fileadmin/user_upload/Speichermonitoring_Jahresbericht_2017_ISEA_RWTH_Aachen.pdf (visited on 2017).
- [13] M. Schlossarczyk. *Wie viel Batteriegroßspeicher verträgt der Primärregelleistungsmarkt?* Ed. by enervis energy advisors GmbH. URL: https://enervis.de/wp-content/uploads/2017/12/enerviews_2016_Maerz_Batteriespeicher_und_PRL.pdf (visited on 03/01/2016).

- [14] H. Staubitz. *The German energy transition - Status quo and what lies ahead*. Ed. by GTAI - Germany Trade & Invest. URL: <https://www.powerhouse-eastern-germany.de/PEG/Content/EN/Events/Event-reviews/review-2016-06-20-investorconference-montreal/colnatec.pdf?v=2> (visited on 06/01/2016).
- [15] Technical University of Munich. *EEBatt – Interdisciplinary Energy Storage Research Project*. URL: <https://www.mse.tum.de/en/eebatt/> (visited on 06/14/2017).
- [16] H. Hesse, M. Schimpe, D. Kucevic, and A. Jossen. “Lithium-Ion Battery Storage for the Grid—A Review of Stationary Battery Storage System Design Tailored for Applications in Modern Power Grids”. In: *Energies* 10.12 (2017), p. 2107. ISSN: 1996-1073. DOI: 10.3390/en10122107.
- [17] H. C. Hesse, M. Naumann, M. Müller, N. C. Truong, M. Schimpe, and A. Jossen. “A Holistic Battery Simulation Tool for Use Case Specific Cost Analysis”. In: *IREES*. Düsseldorf, 2016.
- [18] B. Battke, T. S. Schmidt, D. Grosspietsch, and V. H. Hoffmann. “A review and probabilistic model of lifecycle costs of stationary batteries in multiple applications”. In: *Renewable and Sustainable Energy Reviews* 25 (2013), pp. 240–250. ISSN: 13640321. DOI: 10.1016/j.rser.2013.04.023.
- [19] I. Pawel. “The Cost of Storage – How to Calculate the Levelized Cost of Stored Energy (LCOE) and Applications to Renewable Energy Generation”. In: *Energy Procedia* 46 (2014), pp. 68–77. ISSN: 18766102. DOI: 10.1016/j.egypro.2014.01.159.
- [20] S. You and C. N. Rasmussen. “Generic modelling framework for economic analysis of battery systems”. In: *IET Conference on Renewable Power Generation (RPG 2011)*. 6-8 Sept. 2011, p. 122. DOI: 10.1049/cp.2011.0147.
- [21] J. Weniger, T. Tjaden, and V. Quaschnig. “Vergleich verschiedener Kennzahlen zur Bewertung der energetischen Performance von PV-Batteriesystemen”. In: *32. Symposium Photovoltaische Solarenergie*. Kloster Banz, Bad Staffelstein, 2017, pp. 1–23.
- [22] J. Neubauer. *Battery Lifetime Analysis and Simulation Tool (BLAST): Documentation*. National Renewable Energy Laboratory (NREL), 2014. DOI: 10.2172/1167066.
- [23] N. Blair, A. P. Dobos, J. Freeman, T. Neises, M. Wagner, T. Ferguson, P. Gilman, and S. Janzou. *System Advisor Model (SAM): General Description*. Ed. by NREL. Denver, 2014.
- [24] J. Dersch. *greenius - GREEN ENERGY SYSTEM ANALYSIS: greenius User Manual*. Ed. by Deutsches Zentrum für Luft- und Raumfahrt e.V. Köln. URL: http://www.dlr.de/sf/desktopdefault.aspx/tabid-11688/20442_read-44865/ (visited on 02/13/2018).
- [25] T. Lambert, P. Gilman, and P. Lilienthal. “Micropower System Modeling with Homer”. In: *Integration of Alternative Sources of Energy*. Ed. by F. A. Farret and M. G. Simões. Hoboken, NJ, USA: John Wiley & Sons, Inc, 2005, pp. 379–418. ISBN: 9780471755623. DOI: 10.1002/0471755621.ch15.
- [26] J. Hoppmann, J. Volland, T. S. Schmidt, and V. H. Hoffmann. “The economic viability of battery storage for residential solar photovoltaic systems – A review and a simulation model”. In: *Renewable and Sustainable Energy Reviews* 39 (2014), pp. 1101–1118. ISSN: 13640321. DOI: 10.1016/j.rser.2014.07.068.
- [27] J. Moshövel, K.-P. Kairies, D. Magnor, M. Leuthold, M. Bost, S. Gähns, E. Szczechowicz, M. Cramer, and D. U. Sauer. “Analysis of the maximal possible grid relief from PV-peak-power impacts by using storage systems for increased self-consumption”. In: *Applied Energy* 137 (2015), pp. 567–575. ISSN: 03062619. DOI: 10.1016/j.apenergy.2014.07.021.

-
- [28] Bundesministerium für Wirtschaft und Energie. *Erneuerbare-Energien-Gesetz: EEG 2014*. Berlin. URL: <http://www.bmwi.de/Redaktion/DE/Downloads/G/gesetz-fuer-den-ausbau-erneuerbarer-energien.html> (visited on 08/01/2014).
- [29] M. Braun, K. Büdenbender, D. Magnor, and A. Jossen. “Photovoltaic self-consumption in Germany - using lithium-ion storage to increase self-consumed photovoltaic energy”. In: *24th EU PVSEC*. 21.-25.09.2009.
- [30] E. Waffenschmidt. “Dimensioning of Decentralized Photovoltaic Storages with Limited Feed-in Power and their Impact on the Distribution Grid”. In: *Energy Procedia* 46 (2014), pp. 88–97. ISSN: 18766102. DOI: 10.1016/j.egypro.2014.01.161.
- [31] J. Weniger, T. Tjaden, and V. Quaschnig. “Sizing of Residential PV Battery Systems”. In: *Energy Procedia* 46 (2014), pp. 78–87. ISSN: 18766102. DOI: 10.1016/j.egypro.2014.01.160.
- [32] C. Truong, M. Naumann, R. Karl, M. Müller, A. Jossen, and H. Hesse. “Economics of Residential Photovoltaic Battery Systems in Germany: The Case of Tesla’s Powerwall”. In: *Batteries* 2.2 (2016), pp. 14–30. ISSN: 2313-0105. DOI: 10.3390/batteries2020014.
- [33] A. Zeh and R. Witzmann. “Operational Strategies for Battery Storage Systems in Low-voltage Distribution Grids to Limit the Feed-in Power of Roof-mounted Solar Power Systems”. In: *Energy Procedia* 46 (2014), pp. 114–123. ISSN: 18766102. DOI: 10.1016/j.egypro.2014.01.164.
- [34] ENTSO-E. *ENTSO-E: Mission and Vision*. URL: <https://www.entsoe.eu/about-entso-e/inside-entso-e/mission-and-vision/Pages/default.aspx> (visited on 02/13/2018).
- [35] Consentec GmbH. *Description of load-frequency control concept and market for control reserves: Study commissioned by the German TSOs*. Aachen. URL: http://www.consentec.de/wp-content/uploads/2014/08/Consentec_50Hertz_Regelleistungsmarkt_en__20140227.pdf (visited on 02/27/2014).
- [36] 50Hertz Transmission GmbH, Amprion GmbH, TenneT TSO GmbH, and TransnetBW GmbH. *Regelleistung.net: Internetplattform zur Vergabe von Regelleistung*. URL: <https://www.regelleistung.net/> (visited on 02/26/2018).
- [37] EPEX Spot. *EPEX SPOT SE: Kontinuierlicher Intraday-Handel*. URL: <https://www.epexspot.com/de/marktdaten/intradaycontinuous> (visited on 2016).
- [38] 50Hertz Transmission GmbH, Amprion GmbH, TenneT TSO GmbH, and TransnetBW GmbH. *Anforderungen an die Speicherkapazität bei Batterien für die Primärregelleistung*. URL: <https://www.regelleistung.net/ext/download/anforderungBatterien> (visited on 02/26/2018).
- [39] 50hertz, Amprion, Tennet, and Transnet BW. *Eckpunkte und Freiheitsgrade bei Erbringung von Primärregelleistung*. URL: <https://www.regelleistung.net/ext/download/eckpunktePRL> (visited on 02/26/2018).
- [40] M. Koller. “Optimierte Betriebsführung eines 1MW Batteriespeichers im Verteilnetz”. Masterarbeit. ETH Zürich, November 2012.
- [41] R. Hollinger, L. M. Diazgranados, C. Wittwer, and B. Engel. “Optimal Provision of Primary Frequency Control with Battery Systems by Exploiting All Degrees of Freedom within Regulation”. In: *Energy Procedia* 99 (2016), pp. 204–214. ISSN: 18766102. DOI: 10.1016/j.egypro.2016.10.111.
- [42] F. Braam, L. M. Diazgranados, R. Hollinger, B. Engel, G. Bopp, and T. Erge. “Distributed solar battery systems providing primary control reserve”. In: *IET Renewable Power Generation* 10.1 (2016), pp. 63–70. ISSN: 1752-1416. DOI: 10.1049/iet-rpg.2015.0147.

- [43] J. Fleer, S. Zurmühlen, J. Badeda, P. Stenzel, J.-F. Hake, and D. U. Sauer. “Model-based Economic Assessment of Stationary Battery Systems Providing Primary Control Reserve”. In: *Energy Procedia* 99 (2016), pp. 11–24. ISSN: 18766102. DOI: 10.1016/j.egypro.2016.10.093.
- [44] C. R. Birkl, M. R. Roberts, E. McTurk, P. G. Bruce, and D. A. Howey. “Degradation diagnostics for lithium ion cells”. In: *Journal of Power Sources* 341 (2017), pp. 373–386. ISSN: 0378-7753. DOI: 10.1016/j.jpowsour.2016.12.011.
- [45] Technical University of Munich. *Web portal of the Energy Neighbor*. URL: <https://www.energyneighbor.de/en/home.html> (visited on 06/14/2017).
- [46] C. N. Truong, M. Schimpe, M. Naumann, A. Jossen, and H. C. Hesse. “Impact of Sub-Components on the Overall Performance of Stationary Battery Systems: Insights on the Prototype Energy Neighbor”. In: *International ETG Congress 2017*. ETG-Fachbericht. Berlin and Offenbach: VDE Verlag, 2017. ISBN: 9783800745050.
- [47] M. Lepiorz. *Betriebsbedingte Alterung von Lithium-Ionen Batterien in stationären und mobilen Anwendungen: Dissertation*. 1. Auflage. Ingenieurwissenschaften. München: Verlag Dr. Hut, 2016. ISBN: 3843926557.
- [48] A. Barré, B. Deguilhem, S. Grolleau, M. Gérard, F. Suard, and D. Riu. “A review on lithium-ion battery ageing mechanisms and estimations for automotive applications”. In: *Journal of Power Sources* 241 (2013), pp. 680–689. ISSN: 0378-7753. DOI: 10.1016/j.jpowsour.2013.05.040.
- [49] D. Li, D. L. Danilov, J. Xie, L. Raijmakers, L. Gao, Y. Yang, and P. H. Notten. “Degradation Mechanisms of C6/LiFePO4 Batteries: Experimental Analyses of Calendar Aging”. In: *Electrochimica Acta* 190 (2016), pp. 1124–1133. ISSN: 00134686. DOI: 10.1016/j.electacta.2015.12.161.
- [50] P. Keil, S. F. Schuster, J. Wilhelm, J. Travi, A. Hauser, R. C. Karl, and A. Jossen. “Calendar Aging of Lithium-Ion Batteries: I. Impact of the Graphite Anode on Capacity Fade”. In: *Journal of The Electrochemical Society* 163.9 (2016), A1872–A1880. ISSN: 00134651. DOI: 10.1149/2.0411609jes.
- [51] B. Gyenes, D. A. Stevens, V. L. Chevrier, and J. R. Dahn. “Understanding Anomalous Behavior in Coulombic Efficiency Measurements on Li-Ion Batteries”. In: *Journal of The Electrochemical Society* 162.3 (2014), A278–A283. DOI: 10.1149/2.0191503jes.
- [52] M. Lewerenz, J. Münnix, J. Schmalstieg, S. Käbitz, M. Knips, and D. U. Sauer. “Systematic aging of commercial LiFePO4|Graphite cylindrical cells including a theory explaining rise of capacity during aging”. In: *Journal of Power Sources* 345 (2017), pp. 254–263. ISSN: 0378-7753. DOI: 10.1016/j.jpowsour.2017.01.133.
- [53] M. Lewerenz, A. Warnecke, and D. U. Sauer. “Post-mortem analysis on LiFePO 4 |Graphite cells describing the evolution & composition of covering layer on anode and their impact on cell performance”. In: *Journal of Power Sources* 369 (2017), pp. 122–132. ISSN: 0378-7753. DOI: 10.1016/j.jpowsour.2017.10.003.
- [54] J. Wilhelm, S. Seidlmayer, P. Keil, J. Schuster, A. Kriele, R. Gilles, and A. Jossen. “Cycling capacity recovery effect: A coulombic efficiency and post-mortem study”. In: *Journal of Power Sources* 365 (2017), pp. 327–338. ISSN: 0378-7753. DOI: 10.1016/j.jpowsour.2017.08.090.
- [55] A. Eddahech, O. Briat, and J.-M. Vinassa. “Performance comparison of four lithium-ion battery technologies under calendar aging”. In: *Energy* 84 (2015), pp. 542–550. ISSN: 0360-5442. DOI: 10.1016/j.energy.2015.03.019.

-
- [56] M. Kassem, J. Bernard, R. Revel, S. Pélissier, F. Duclaud, and C. Delacourt. “Calendar aging of a graphite/LiFePO₄ cell”. In: *Journal of Power Sources* 208 (2012), pp. 296–305. ISSN: 0378-7753. DOI: 10.1016/j.jpowsour.2012.02.068.
- [57] Y. Zheng, Y.-B. He, K. Qian, B. Li, X. Wang, J. Li, C. Miao, and F. Kang. “Effects of state of charge on the degradation of LiFePO₄/graphite batteries during accelerated storage test”. In: *Journal of Alloys and Compounds* 639 (2015), pp. 406–414. ISSN: 09258388. DOI: 10.1016/j.jallcom.2015.03.169.
- [58] I. Bloom et al. “An accelerated calendar and cycle life study of Li-ion cells”. In: *Journal of Power Sources* 101.2 (2001), pp. 238–247. ISSN: 0378-7753. DOI: 10.1016/S0378-7753(01)00783-2.
- [59] M. Ecker, N. Nieto, S. Käbitz, J. Schmalstieg, H. Blanke, A. Warnecke, and D. U. Sauer. “Calendar and cycle life study of Li(NiMnCo)O₂-based 18650 lithium-ion batteries”. In: *Journal of Power Sources* 248 (2014), pp. 839–851. ISSN: 0378-7753. DOI: 10.1016/j.jpowsour.2013.09.143.
- [60] P. Keil and A. Jossen. “Calendar Aging of NCA Lithium-Ion Batteries Investigated by Differential Voltage Analysis and Coulomb Tracking”. In: *Journal of The Electrochemical Society* 164.1 (2016), A6066–A6074. ISSN: 00134651. DOI: 10.1149/2.0091701jes.
- [61] E. Sarasketa-Zabala, I. Gandiaga, L. M. Rodriguez-Martinez, and I. Villarreal. “Calendar ageing analysis of a LiFePO₄/graphite cell with dynamic model validations: Towards realistic lifetime predictions”. In: *Journal of Power Sources* 272 (2014), pp. 45–57. ISSN: 0378-7753. DOI: 10.1016/j.jpowsour.2014.08.051.
- [62] M. Swierczynski, D.-I. Stroe, A.-I. Stan, R. Teodorescu, and S. K. Kaer. “Lifetime Estimation of the Nanophosphate LiFePO₄/C Battery Chemistry Used in Fully Electric Vehicles”. In: *IEEE Transactions on Industry Applications* 51.4 (2015), pp. 3453–3461. ISSN: 0093-9994. DOI: 10.1109/TIA.2015.2405500.
- [63] E. V. Thomas, I. Bloom, J. P. Christophersen, and V. S. Battaglia. “Rate-based degradation modeling of lithium-ion cells”. In: *Journal of Power Sources* 206 (2012), pp. 378–382. ISSN: 0378-7753. DOI: 10.1016/j.jpowsour.2012.01.106.
- [64] S. Käbitz, J. B. Gerschler, M. Ecker, Y. Yurdagel, B. Emmermacher, D. Andr, T. Mitsch, and D. U. Sauer. “Cycle and calendar life study of a graphite|LiNi_{1/3}Mn_{1/3}Co_{1/3}O₂ Li-ion high energy system. Part A: Full cell characterization”. In: *Journal of Power Sources* 239 (2013), pp. 572–583. ISSN: 0378-7753. DOI: 10.1016/j.jpowsour.2013.03.045.
- [65] L. Su, J. Zhang, J. Huang, H. Ge, Z. Li, F. Xie, and B. Y. Liaw. “Path dependence of lithium ion cells aging under storage conditions”. In: *Journal of Power Sources* 315 (2016), pp. 35–46. ISSN: 0378-7753. DOI: 10.1016/j.jpowsour.2016.03.043.
- [66] S. Grolleau, A. Delaille, H. Gualous, P. Gyan, R. Revel, J. Bernard, E. Redondo-Iglesias, and J. Peter. “Calendar aging of commercial graphite/LiFePO₄ cell – Predicting capacity fade under time dependent storage conditions”. In: *Journal of Power Sources* 255 (2014), pp. 450–458. ISSN: 0378-7753. DOI: 10.1016/j.jpowsour.2013.11.098.
- [67] M. Petit, E. Prada, and V. Sauvant-Moynot. “Development of an empirical aging model for Li-ion batteries and application to assess the impact of Vehicle-to-Grid strategies on battery lifetime”. In: *Applied Energy* 172 (2016), pp. 398–407. ISSN: 03062619. DOI: 10.1016/j.apenergy.2016.03.119.

- [68] M. Broussely, S. Herreyre, P. Biensan, P. Kasztejna, K. Nechev, and R. Staniewicz. “Aging mechanism in Li ion cells and calendar life predictions”. In: *Journal of Power Sources* 97-98 (2001), pp. 13–21. ISSN: 0378-7753. DOI: 10.1016/S0378-7753(01)00722-4.
- [69] M. Ecker, J. B. Gerschler, J. Vogel, S. Käbitz, F. Hust, P. Dechent, and D. U. Sauer. “Development of a lifetime prediction model for lithium-ion batteries based on extended accelerated aging test data”. In: *Journal of Power Sources* 215 (2012), pp. 248–257. ISSN: 0378-7753. DOI: 10.1016/j.jpowsour.2012.05.012.
- [70] K. Smith, E. Wood, Santhanagopalan, S.: Kim, G.-H., J. Neubauer, and A. Pesaran. “Models for Battery Reliability and Lifetime”. In: *Battery Congress 2013*. Ann Arbor, Michigan, 2013, pp. 1–8.
- [71] J. Wang et al. “Degradation of lithium ion batteries employing graphite negatives and nickel-cobalt-manganese oxide + spinel manganese oxide positives: Part 1, aging mechanisms and life estimation”. In: *Journal of Power Sources* 269 (2014), pp. 937–948. ISSN: 0378-7753. DOI: 10.1016/j.jpowsour.2014.07.030.
- [72] C. Delacourt and M. Safari. “Life Simulation of a Graphite/LiFePO₄ Cell under Cycling and Storage”. In: *Journal of The Electrochemical Society* 159.8 (2012), A1283–A1291. DOI: 10.1149/2.049208jes.
- [73] H. Ekström and G. Lindbergh. “A Model for Predicting Capacity Fade due to SEI Formation in a Commercial Graphite/LiFePO₄ Cell”. In: *Journal of The Electrochemical Society* 162.6 (2015), A1003–A1007. DOI: 10.1149/2.0641506jes.
- [74] M. Safari and C. Delacourt. “Simulation-Based Analysis of Aging Phenomena in a Commercial Graphite/LiFePO₄ Cell”. In: *Journal of The Electrochemical Society* 158.12 (2011), A1436. ISSN: 00134651. DOI: 10.1149/2.103112jes.
- [75] E. Prada, D. Di Domenico, Y. Creff, J. Bernard, V. Sauvant-Moynot, and F. Huet. “A Simplified Electrochemical and Thermal Aging Model of LiFePO₄-Graphite Li-ion Batteries: Power and Capacity Fade Simulations”. In: *Journal of The Electrochemical Society* 160.4 (2013), A616–A628. DOI: 10.1149/2.053304jes.
- [76] K. L. Gering. “Novel Method for Evaluation and Prediction of Capacity Loss Metrics in Li-Ion Electrochemical Cells”. In: *Electrochimica Acta* 228 (2017), pp. 636–651. ISSN: 00134686. DOI: 10.1016/j.electacta.2017.01.052.
- [77] M. Lewerenz, S. Käbitz, M. Knips, J. Münnix, J. Schmalstieg, A. Warnecke, and D. U. Sauer. “New method evaluating currents keeping the voltage constant for fast and highly resolved measurement of Arrhenius relation and capacity fade”. In: *Journal of Power Sources* 353 (2017), pp. 144–151. ISSN: 0378-7753. DOI: 10.1016/j.jpowsour.2017.03.136.
- [78] K. L. Gering, S. V. Sazhin, D. K. Jamison, C. J. Michelbacher, B. Y. Liaw, M. Dubarry, and M. Cugnet. “Investigation of path dependence in commercial lithium-ion cells chosen for plug-in hybrid vehicle duty cycle protocols”. In: *Journal of Power Sources* 196.7 (2011), pp. 3395–3403. ISSN: 0378-7753. DOI: 10.1016/j.jpowsour.2010.05.058.
- [79] Z. Ma, J. Jiang, W. Shi, W. Zhang, and C. C. Mi. “Investigation of path dependence in commercial lithium-ion cells for pure electric bus applications: Aging mechanism identification”. In: *Journal of Power Sources* 274 (2015), pp. 29–40. ISSN: 0378-7753. DOI: 10.1016/j.jpowsour.2014.10.006.

-
- [80] M. Lepiorz, W. Weydanz, and A. Jossen. “Ah-Throughput versus residual capacity method for prediction of capacity loss of Li-Ion batteries at alternating temperatures”. In: *Kraftwerk Batterie*. Aachen: Haus der Technik e.V., 2013.
- [81] K. Rumpf, M. Naumann, and A. Jossen. “Experimental investigation of parametric cell-to-cell variation and correlation based on 1100 commercial lithium-ion cells”. In: *Journal of Energy Storage* 14 (2017), pp. 224–243. ISSN: 2352152X. DOI: 10.1016/j.est.2017.09.010.
- [82] M. Schimpe, M. Naumann, N. Truong, H. C. Hesse, S. Santhanagopalan, A. Saxon, and A. Jossen. “Energy efficiency evaluation of a stationary lithium-ion battery container storage system via electro-thermal modeling and detailed component analysis”. In: *Applied Energy* 210 (2018), pp. 211–229. ISSN: 03062619. DOI: 10.1016/j.apenergy.2017.10.129.
- [83] Y. Zheng, M. Ouyang, L. Lu, and J. Li. “Understanding aging mechanisms in lithium-ion battery packs: From cell capacity loss to pack capacity evolution”. In: *Journal of Power Sources* 278 (2015), pp. 287–295. ISSN: 0378-7753. DOI: 10.1016/j.jpowsour.2014.12.105.
- [84] D. Li, D. L. Danilov, L. Gao, Y. Yang, and P. H. L. Notten. “Degradation Mechanisms of the Graphite Electrode in C6/LiFePO₄ Batteries Unraveled by a Non-Destructive Approach”. In: *Journal of The Electrochemical Society* 163.14 (2016), A3016–A3021. DOI: 10.1149/2.0821614jes.
- [85] S. F. Schuster, T. Bach, E. Fleder, J. Müller, M. Brand, G. Sextl, and A. Jossen. “Nonlinear aging characteristics of lithium-ion cells under different operational conditions”. In: *Journal of Energy Storage* 1 (2015), pp. 44–53. ISSN: 2352152X. DOI: 10.1016/j.est.2015.05.003.
- [86] D. Li, D. L. Danilov, L. Gao, Y. Yang, and P. H. Notten. “Degradation Mechanisms of C6/LiFePO₄ Batteries: Experimental Analyses of Cycling-induced Aging”. In: *Electrochimica Acta* 210 (2016), pp. 445–455. ISSN: 00134686. DOI: 10.1016/j.electacta.2016.05.091.
- [87] E. Sarasketa-Zabala, I. Gandiaga, E. Martinez-Laserna, L. M. Rodriguez-Martinez, and I. Villarreal. “Cycle ageing analysis of a LiFePO₄/graphite cell with dynamic model validations: Towards realistic lifetime predictions”. In: *Journal of Power Sources* 275 (2015), pp. 573–587. ISSN: 0378-7753. DOI: 10.1016/j.jpowsour.2014.10.153.
- [88] J. Wang, P. Liu, J. Hicks-Garner, E. Sherman, S. Soukiazian, M. Verbrugge, H. Tataria, J. Musser, and P. Finamore. “Cycle-life model for graphite-LiFePO₄ cells”. In: *Journal of Power Sources* 196.8 (2011), pp. 3942–3948. ISSN: 0378-7753. DOI: 10.1016/j.jpowsour.2010.11.134.
- [89] J. de Hoog, J.-M. Timmermans, D. Ioan-Stroe, M. Swierczynski, J. Jaguemont, S. Goutam, N. Omar, J. van Mierlo, and P. van den Bossche. “Combined cycling and calendar capacity fade modeling of a Nickel-Manganese-Cobalt Oxide Cell with real-life profile validation”. In: *Applied Energy* 200 (2017), pp. 47–61. ISSN: 03062619. DOI: 10.1016/j.apenergy.2017.05.018.
- [90] E. Sarasketa-Zabala, E. Martinez-Laserna, M. Bercibar, I. Gandiaga, L. M. Rodriguez-Martinez, and I. Villarreal. “Realistic lifetime prediction approach for Li-ion batteries”. In: *Applied Energy* 162 (2016), pp. 839–852. ISSN: 03062619. DOI: 10.1016/j.apenergy.2015.10.115.
- [91] M. Naumann and C. N. Truong. *SimSES - Software for techno-economic simulation of stationary energy storage systems*. 2017. DOI: 10.14459/2017MP1401541. URL: <https://mediatum.ub.tum.de/1401541>.
- [92] A. Nottrott, J. Kleissl, and B. Washom. “Energy dispatch schedule optimization and cost benefit analysis for grid-connected, photovoltaic-battery storage systems”. In: *Renewable Energy* 55 (2013), pp. 230–240. ISSN: 09601481. DOI: 10.1016/j.renene.2012.12.036.

- [93] A. Oudalov, D. Chartouni, and C. Ohler. “Optimizing a Battery Energy Storage System for Primary Frequency Control”. In: *IEEE Transactions on Power Systems* 22.3 (2007), pp. 1259–1266. ISSN: 0885-8950. DOI: 10.1109/TPWRS.2007.901459.
- [94] M. Müller, L. Viernstein, C. N. Truong, A. Eiting, H. C. Hesse, R. Witzmann, and A. Jossen. “Evaluation of grid-level adaptability for stationary battery energy storage system applications in Europe”. In: *Journal of Energy Storage* 9 (2017), pp. 1–11. ISSN: 2352152X. DOI: 10.1016/j.est.2016.11.005.
- [95] T. Borsche, A. Ulbig, M. Koller, and G. Andersson. “Power and energy capacity requirements of storages providing frequency control reserves”. In: *IEEE Power and Energy Society general meeting (PES), 2013*. Piscataway, NJ: IEEE, 2013, pp. 1–5. ISBN: 978-1-4799-1303-9. DOI: 10.1109/PESMG.2013.6672843.
- [96] B. Kroposki, R. Lasseter, T. Ise, S. Morozumi, S. Papathanassiou, and N. Hatziargyriou. “Making microgrids work”. In: *IEEE Power and Energy Magazine* 6.3 (2008), pp. 40–53. ISSN: 1540-7977. DOI: 10.1109/MPE.2008.918718.
- [97] M. Naumann, V. Kumtepli, H. C. Hesse, A. Tripathi, and A. Jossen. “Design and control of battery energy storage systems in island grids”. In: *Singapore Battery Meeting*. Singapore: TUM Create, 2 2017.
- [98] G. Notton, V. Lazarov, and L. Stoyanov. “Optimal sizing of a grid-connected PV system for various PV module technologies and inclinations, inverter efficiency characteristics and locations”. In: *Renewable Energy* 35.2 (2010), pp. 541–554. ISSN: 09601481. DOI: 10.1016/j.renene.2009.07.013.
- [99] A. Stephan, B. Battke, M. D. Beuse, J. H. Clausdeinken, and T. S. Schmidt. “Limiting the public cost of stationary battery deployment by combining applications”. In: *Nature Energy* 1.7 (2016), p. 16079. ISSN: 2058-7546. DOI: 10.1038/nenergy.2016.79.
- [100] M. Lewerenz, A. Warnecke, and D. U. Sauer. “Introduction of capacity difference analysis (CDA) for analyzing lateral lithium-ion flow to determine the state of covering layer evolution”. In: *Journal of Power Sources* 354 (2017), pp. 157–166. ISSN: 0378-7753. DOI: 10.1016/j.jpowsour.2017.04.043.
- [101] F. R. Connor. *Rauschen: Zufallssignale, Rauschmessung, Systemvergleich*. Wiesbaden: Vieweg+Teubner Verlag, 1987. ISBN: 9783528043766. DOI: 10.1007/978-3-322-83035-7. URL: <http://dx.doi.org/10.1007/978-3-322-83035-7>.
- [102] HAMEG Instruments. *Was ist Rauschen?* URL: https://cdn-reichelt.de/documents/datenblatt/TIPP/HAMEG_WasistRauschen.pdf (visited on 03/18/2018).
- [103] F. M. Kindermann, A. Noel, S. V. Erhard, and A. Jossen. “Long-term equalization effects in Li-ion batteries due to local state of charge inhomogeneities and their impact on impedance measurements”. In: *Electrochimica Acta* 185 (2015), pp. 107–116. ISSN: 00134686. DOI: 10.1016/j.electacta.2015.10.108.
- [104] IEEE Computer Society/SESC. *IEEE recommended practice for maintenance, testing, and replacement of vented lead-acid batteries for stationary applications*. New York, N.Y: Institute of Electrical and Electronics Engineers, 2003. ISBN: 9780738134918. URL: <http://ieeexplore.ieee.org/servlet/opac?punumber=8507>.

-
- [105] Energie-Forschungszentrum Niedersachsen, H.-P. Beck, H. Bart, B. Bayer, J. Klee Barillas, M. Danzer, M. Dennenmoser, and M. Naumann. *Potentiale elektrochemischer Speicher in elektrischen Netzen in Konkurrenz zu anderen Technologien und Systemlösungen (ESPEN): Abschlussbericht*. Göttingen, 2016. ISBN: 9783736994232. DOI: 10.2314/GBV:869930222.
- [106] H. J. Ploehn, P. Ramadass, and R. E. White. “Solvent Diffusion Model for Aging of Lithium-Ion Battery Cells”. In: *Journal of The Electrochemical Society* 151.3 (2004), A456. DOI: 10.1149/1.1644601.
- [107] A. J. Smith, J. C. Burns, D. Xiong, and J. R. Dahn. “Interpreting High Precision Coulometry Results on Li-ion Cells”. In: *Journal of The Electrochemical Society* 158.10 (2011), A1136. DOI: 10.1149/1.3625232.
- [108] F. Single, B. Horstmann, and A. Latz. “Dynamics and morphology of solid electrolyte interphase (SEI)”. In: *Physical chemistry chemical physics : PCCP* 18.27 (2016), pp. 17810–17814. ISSN: 1463-9084. DOI: 10.1039/c6cp02816k.
- [109] M. Lewerenz, A. Marongiu, A. Warnecke, and D. U. Sauer. “Differential voltage analysis as a tool for analyzing inhomogeneous aging: A case study for LiFePO₄ | Graphite cylindrical cells”. In: *Journal of Power Sources* 368 (2017), pp. 57–67. ISSN: 0378-7753. DOI: 10.1016/j.jpowsour.2017.09.059.
- [110] S. Diaf, M. Belhamel, M. Haddadi, and A. Louche. “Technical and economic assessment of hybrid photovoltaic/wind system with battery storage in Corsica island”. In: *Energy Policy* 36.2 (2008), pp. 743–754. ISSN: 03014215. DOI: 10.1016/j.enpol.2007.10.028.
- [111] H. Yang, Z. Wei, and L. Chengzhi. “Optimal design and techno-economic analysis of a hybrid solar–wind power generation system”. In: *Applied Energy* 86.2 (2009), pp. 163–169. ISSN: 03062619. DOI: 10.1016/j.apenergy.2008.03.008.
- [112] A. Zucker and T. Hinchliffe. “Optimum sizing of PV-attached electricity storage according to power market signals – A case study for Germany and Italy”. In: *Applied Energy* 127 (2014), pp. 141–155. ISSN: 03062619. DOI: 10.1016/j.apenergy.2014.04.038.
- [113] R. Dufo-López. “Optimisation of size and control of grid-connected storage under real time electricity pricing conditions”. In: *Applied Energy* 140 (2015), pp. 395–408. ISSN: 03062619. DOI: 10.1016/j.apenergy.2014.12.012.
- [114] C.A.R.M.E.N. e.V. *Marktübersicht für Batteriespeichersysteme*. Ed. by C.A.R.M.E.N. e.V. URL: <https://www.carmen-ev.de/sonne-wind-co/stromspeicher/batterien/813-marktuebersicht-fuer-batteriespeichersysteme> (visited on 01/01/2017).
- [115] T. Tjaden, J. Bergner, J. Weniger, and V. Quaschnig. *Repräsentative elektrische Lastprofile für Wohngebäude in Deutschland auf 1-sekündiger Datenbasis*. Ed. by Hochschule für Technik und Wirtschaft Berlin. Berlin, 2015.
- [116] co2online gGmbH. *Stromverbrauch im Haushalt: Durchschnitt & Einspartipps*. Ed. by Bundesministerium für Umwelt, Naturschutz, Bau und Reaktorsicherheit. URL: <https://www.die-stromsparinitiative.de/stromkosten/stromverbrauch-pro-haushalt/4-personen-haushalt/index.html> (visited on 11/01/2014).
- [117] Bayerisches Staatsministerium für Wirtschaft und Medien, Energie und Technologie. *Daten und Fakten - Photovoltaik - Sonne - Energie-Atlas Bayern*. URL: https://www.energieatlas.bayern.de/thema_sonne/photovoltaik/daten.html (visited on 02/26/2018).

- [118] Kiefer K., Dirnberger D., Müller B., Heydenreich W., and Kröger-Vodde A. “A Degradation Analysis of PV Power Plants”. In: *25th European Photovoltaic Solar Energy Conference and Exhibition*. 2010.
- [119] Kreditanstalt für Wiederaufbau - KfW. *KfW-Programm Erneuerbare Energien – Speicher (275)*. Frankfurt am Main. URL: <https://www.kfw.de/inlandsfoerderung/Unternehmen/Energie-Umwelt/F%C3%B6rderprodukte/Erneuerbare-Energien-%E2%80%93-Speicher-%28275%29/> (visited on 01/01/2015).
- [120] Bundesfinanzministerium. *AfA-Tabelle für die allgemein verwendbaren Anlagegüter*. Berlin. URL: http://www.bundesfinanzministerium.de/Web/DE/Themen/Steuern/Weitere_Steuerthemen/Betriebspruefung/AfA_Tabellen/afa_tabellen.html (visited on 12/15/2000).
- [121] EPEX Spot. *Price List January 2015*. URL: <https://www.epexspot.com/> (visited on 01/01/2015).

List of Figures

| | | |
|-----|---|----|
| 1.1 | Overview regarding stationary energy storage applications, possible design scopes and a selection of energy storage technologies. The orange marked parts are in the main focus of this work. | 2 |
| 1.2 | Structure of this thesis 'Techno-economic evaluation of stationary battery energy storage systems with special consideration of aging' with assigned numbers of chapters. | 4 |
| 2.1 | Schematic of BESS and its main components together with the system coupling to the power grid or further technical units (Derivative of Figure from [16]). | 7 |
| 2.2 | Comparison of different battery technologies with respect to the price, lifetime, efficiency / self-discharge and scalability (Derivative of Figure from [17]). | 9 |
| 2.3 | Schematic of power and SOC course of a PV-HESS during one day (Derivative of Figure from [29]). | 11 |
| 2.4 | Historical PCR power demand and average tender prices between 2011 and 2017 (Data from [36]). | 14 |
| 2.5 | Degradation mechanisms in Lithium-ion battery cells (Figure from [44]). | 17 |
| 2.6 | Schematic of the calendar aging mechanism at low (a) and at elevated temperatures (b) (Figures from [49]). | 18 |
| 2.7 | Schematic of the cycle aging mechanism at low (a) and at elevated temperatures (b) (Figures from [86]). | 21 |
| 3.1 | SimSES structure and functional blocks. | 24 |
| 3.2 | SimSES battery degradation model. | 27 |
| 3.3 | Influence of the sample time between 60 to 7200 s on the calculation time: Calculation time in relation to the simulation with a sample time of 60 s (red curve). Number of the relative simulation steps for each sample time in relation to the sample time of 60 s (blue curve). Resulting calculation time per step (yellow curve). | 36 |
| 3.4 | Influence of sample time and step size of aging calculation with single and average values on calculation time. Figure 3.4a: 60 s sample time. Figure 3.4b: 300 s sample time. . . . | 36 |
| 3.5 | Influence of the sample time between 60 to 7200 s on the capacity loss: Deviation of the capacity loss due to calendar aging (blue curve), cycle aging (red curve) and the total aging (yellow curve) in relation to the simulation with a sample time of 60 s. | 37 |
| 3.6 | Influence of sample time and step size of aging calculation with single and average values on calculation time. Figure 3.6a: 60 s sample time. Figure 3.6b: 300 s sample time. . . . | 37 |
| 3.7 | Influence of aging calculation step size with single values on the deviation of the capacity loss with different sample times. Figure 3.7a: 60 s sample time. Figure 3.7b: 300 s sample time. | 38 |
| 3.8 | Influence of aging calculation step size with average values on the capacity loss with different sample times. Figure 3.8a: 60 s sample time. Figure 3.8b: 300 s sample time. . . | 38 |

| | | |
|------|--|----|
| 4.1 | Variation of the cell parameters of the 1100 investigated cells. The individual plots on the left side show the parameter histograms by indicating the mean value and the values for the $\pm\sigma \cdot \alpha \in [1, 2]$ as well as the curve representing an assumed normal distribution. The individual plots on the right side show the same parameter over the respective cell number again with the markings for the mean value and the further σ factors. Figure 4.1a shows the discharge capacity $C_{\text{DCH,CCCV}}$ of the cells 1-600 (batch 1) and Figure 4.1b of the cells 601-1100 (batch 2). Figure 4.1c shows the $R_{\text{DC},10\text{s}}$ of the cells 1-600 and Figure 4.1d of the cells 601-1100. | 44 |
| 4.2 | Testing procedure of the aging studies. | 48 |
| 4.3 | Wöhler curve representing the possible number of cycles over the DOC until $Q_{\text{loss}} = 20\%$ is reached. The DOCs of the TPs at 25 °C and 40 °C are marked individually. | 55 |
| 4.4 | Course of the PV-HESS profile in Figure 4.4a and PV-PCR-BESS profile in Figure 4.4b: The upper plot shows the SOC course, the lower plot the C-rate course. | 56 |
| 4.5 | Degradation over 885 days of selected TPs under different storage SOC and temperatures: (a) Relative discharge capacity C_{disch} at $\text{SOC} = 0\%$, 50% and 100% at 0 °C, 10 °C, 25 °C, 40 °C and 60 °C. (b) Relative resistance $R_{\text{DC},10\text{s}}$ at $\text{SOC} = 0\%$, 50% and 100% at 0 °C, 10 °C, 25 °C, 40 °C and 60 °C. (c) Relative discharge capacity C_{disch} at 40 °C at $\text{SOC} = 0 - 100\%$. (d) Relative resistance $R_{\text{DC},10\text{s}}$ at 40 °C at $\text{SOC} = 0 - 100\%$. All values are related to the measurements of the first CM. Each subplot shows the mean values of the three cells of each TP. In subplot (a) the first 50 days are displayed enlarged in an extra view in order to see more details. | 58 |
| 4.6 | DVA of selected TPs with different storage SOC and temperatures at different points in time during the aging study: (a) At $\text{SOC} = 50\%$ at 25 °C. (b) At $\text{SOC} = 0\%$ at 60 °C. (c) At $\text{SOC} = 50\%$ at 60 °C. (d) At $\text{SOC} = 100\%$ at 60 °C. The circles show in each dV/dQ -curve the peak which is related to the single phase of LiC_{12} in the graphite-anode. The DVA is applied on the low rate discharge measurement described in Subsection 4.3. | 60 |
| 4.7 | Development of the Q_1 and Q_2 parameters of the dV/dQ -curves shown in Figure 4.6. | 61 |
| 4.8 | EIS of selected TPs with different storage SOC and temperatures at selected points in time during the aging study: (a) $\text{SOC} = 50\%$ at 25 °C. (b) $\text{SOC} = 0\%$ at 60 °C. (c) $\text{SOC} = 50\%$ at 60 °C. (d) $\text{SOC} = 100\%$ at 60 °C. The Nyquist-plots are drawn with an inverse y-axis due to the common form of presentation. In subplot (a) the area between 18 m Ω and 26 m Ω is displayed enlarged in an extra view in order to see more details. The parameters $R_{\text{AC},1000\text{ Hz}}$, $R_{\text{AC},5\text{ Hz}}$, Z_{min} and Z_{max} are displayed each with markers. The EIS measurement procedure is described in Subsection 4.3. | 62 |
| 4.9 | Degradation over 885 days of selected cycle aging TPs with different C-rates (xC charge direction, xC discharge direction) with $\text{DOC} = 80\%$ around $\text{SOC} = 50\%$ at 40 °C: (a) Relative discharge capacity C_{disch} over time. (b) Relative resistance $R_{\text{DC},10\text{s}}$ over time. (c) Relative discharge capacity C_{disch} over FEC. (d) Relative resistance $R_{\text{DC},10\text{s}}$ over FEC. All values are related to the measurements of the first CM. Each subplot shows the mean values of the three cells of each TP. | 64 |
| 4.10 | Degradation over 885 days of selected cycle aging TPs with different DOC around $\text{SOC} = 50\%$ all with 1 C in charge and discharge direction at 40 °C over FEC: (a) Relative discharge capacity C_{disch} . (b) Relative resistance $R_{\text{DC},10\text{s}}$ | 65 |

-
- 4.11 Degradation over 885 days of selected cycle aging TPs with different DOC around $SOC = 50\%$ all with 1C in charge and discharge direction at 40°C over FEC: (a) Relative discharge capacity C_{disch} . (b) Relative resistance $R_{\text{DC},10\text{s}}$ 66
- 4.12 Development of the Q_1 and Q_2 parameters of the dV/dQ -curves shown in Figure 4.13. 66
- 4.13 DVA of selected TPs cycled at 40°C with different C-rates and DOC at different points in time during the aging study: (a) $DOC = 80\%$ around $SOC = 50\%$ with 1C/1C. (b) $DOC = 20\%$ around $SOC = 50\%$ with 1C/1C. (c) $DOC = 80\%$ around $SOC = 50\%$ with 0.2C/0.2C. (d) $DOC = 20\%$ around $SOC = 25\%$ with 1C/1C. The circles show in each dV/dQ -curve the peak which is related to the single phase of LiC_{12} in the graphite-anode. The DVA is applied on the discharge phase of the OCV measurements described in Subsection 4.3. 67
- 4.14 EIS of selected TPs cycled at 40°C with different C-rates and DOC at selected points in time during the aging study: (a) $DOC = 80\%$ around $SOC = 50\%$ with 1C/1C. (b) $DOC = 20\%$ around $SOC = 50\%$ with 1C/1C. (c) $DOC = 80\%$ around $SOC = 50\%$ with 0.2C/0.2C. (d) $DOC = 20\%$ around $SOC = 25\%$ with 1C/1C. The Nyquist-plots are drawn with an inverse y-axis due to the common form of presentation. The parameters $R_{\text{AC},1000\text{Hz}}$, $R_{\text{AC},5\text{Hz}}$, Z_{min} and Z_{max} are displayed each with markers. The EIS measurement procedure is described in Subsection 4.3. 68
- 5.1 Influence of temperature on the aging of Q_{loss} and R_{inc} at $SOC = 100\%$ evaluated for the temperatures 25°C , 40°C and 60°C : (a) Results of evaluating Q_{loss} with Equation 5.7 and applying a linear fitting for each shown point in time. (c) Results of evaluating R_{inc} with Equation 5.8 and applying a linear fitting for each shown point in time. (b)/(d) Comparison of measured values of $Q_{\text{loss}}/R_{\text{inc}}$ with model values determined by Equation 5.1/Equation 5.2. The lower panels show the absolute model error in %. 73
- 5.2 Influence of SOC on the aging of Q_{loss} and R_{inc} evaluated at 40°C : (a) Results of evaluating Q_{loss} with Equation 5.11 and applying a fitting with a cubic function for each shown point in time. (c) Results of evaluating R_{inc} with Equation 5.13 and applying a fitting with a quadratic function for each shown point in time. (b)/(d) Comparison of measured values of $Q_{\text{loss}}/R_{\text{inc}}$ with model values determined by Equation 5.1/Equation 5.2. The lower panels show the absolute model error in %. 75
- 5.3 Aging model validation with dynamic calendar aging study over 270 days with 8 intervals each with constant storage conditions. Each measurement represents one cell whose storage condition, temperature or SOC, is changed after one interval according to the test matrix Table 4.5. In every plot, the lower panel shows the absolute model error in % compared to the measured values. The plots on the left side represent the capacity loss and the plots on the right side resistance increase of each TP. (a/b) TP7/TP8 with switching between storage temperature 0°C and 60°C at storage $SOC = 100\%$. TP7 (blue) starts with 0°C and TP8 (red) with 60°C . (c/d) TP13/TP14 with switching between storage $SOC = 50\%$ and 100% at storage temperature 60°C . TP1 (blue) starts with $SOC = 50\%$ and TP14 (red) with $SOC = 100\%$. (e/f) TP15 with changing storage temperature dynamically between 60°C , 25°C and 40°C at storage $SOC = 100\%$ 78

5.4 Influence of the C-rate on the pure cycle aging of Q_{loss} and R_{inc} for the TPs with $DOC = 80\%$ cycles around $SOC = 50\%$ at 40°C for the C-rates 0.2 C, 0.5 C and 1.0 C: (a) $k_{C\text{-rate}, Q_{\text{loss}}}$ (C-rate) determined by fitting separately the aging curves of $Q_{\text{loss, cyc}}$ of the single C-rates with Equation 5.18. (b)/(d) Comparison of measured values of $Q_{\text{loss}}/R_{\text{inc}}$ with model values determined by Equation 5.18/Equation 5.19 and using the $k_{C\text{-rate}, Q_{\text{loss}}}$ (C-rate) values determined by Equation 5.20 and $k_{C\text{-rate}, R_{\text{inc}}}$ (C-rate) by Equation 5.21. The lower panels show the absolute model error in % 81

5.5 Influence of the DOC on the pure cycle aging of $Q_{\text{loss, cyc}}$ and $R_{\text{inc, cyc}}$ for the TPs with 1.0 C cycles around $SOC = 50\%$ at 40°C with $DOC = 5\%, 10\%, 20\%, 40\%, 80\%$ and 100% : (a) $k_{DOC, Q_{\text{loss}}}$ (DOC) determined by fitting separately the aging values at EOT of $Q_{\text{loss, cyc}}$ of the single DOC with Equation 5.22. (b) Comparison of measured values of $Q_{\text{loss, cyc}}$ with model values determined by Equation 5.18 and using the $k_{DOC, Q_{\text{loss}}}$ (DOC) values determined by Equation 5.23. The lower panels show the absolute model error in %. (c) $k_{DOC, R_{\text{inc}}}$ (DOC) determined by fitting separately the aging values at EOT of $R_{\text{inc, cyc}}$ of the single DOC with Equation 5.24. (d) Comparison of measured values of $R_{\text{inc, cyc}}$ with model values determined by Equation 5.19 and using the $k_{DOC, R_{\text{inc}}}$ (DOC) values determined by Equation 5.25. The lower panels show the absolute model error in % 83

5.6 Influence of the temperature on the pure cycle aging of $Q_{\text{loss, cyc}}$ and $R_{\text{inc, cyc}}$ for the TPs with $DOC = 80\%$ and 100% cycles around $SOC = 50\%$ for the C-rate 1.0 C. (a) $Q_{\text{loss, cyc}}$. (b) $R_{\text{inc, cyc}}$ 84

5.7 Estimation of the FEC until the EOL with $Q_{\text{loss, cyc}} = 20\%$ with Equation 5.28. The y-axis is drawn on a logarithmic scale. 86

5.8 Combined aging model validation with the aging results of the dynamic cycle aging study with the two load profiles operated over 885 days at 40°C . Each plot shows the mean values of the measured $Q_{\text{loss, comb.}}/R_{\text{inc, comb.}}$ of the three cells of each load profile. The plots on the left side represent the capacity loss and the plots on the right side resistance increase of the respective load profile. Additional to the estimated combined aging, the particular fractions of the calendar and pure cycle aging are drawn in every plot. The lower panel in every plot shows the absolute model error in % compared to the measured values. (a/b) PV-HESS load profile (c/d) PV-PCR-BESS load profile. . . 88

6.1 Historical electricity prices and different scenarios for electricity price over the years. . . 93

6.2 PV-HESS: Influence of the system configuration with different battery and PV-system sizes on the PI. The PER is scaled to the individual battery size: Figure 6.2a with $PER = 0.2$. Figure 6.2b: $PER = 1.0$. The purple lines mark the best economic battery size for each PV-system size or vice versa. The system sizing with the maximum PI is marked with a purple cross in both figures. 95

6.3 PV-HESS: Influence of the system configuration with different battery and PV-system sizes ($PER = 0.2$) on the self-consumption rate (Figure 6.3a) and self-sufficiency rate (Figure 6.3b) in comparison to the case without a BESS. The system sizing with the maximum PI is marked with a purple cross in both figures. 96

6.4 PV-HESS: Influence of the system configuration with different battery and PV-system sizes ($PER = 0.2$) on the curtailed PV energy (Figure 6.4a) and the average system efficiency (Figure 6.4b). The system sizing with the maximum PI is marked with a red cross in both figures. 97

| | | |
|------|---|-----|
| 6.5 | PV-HESS: Influence of the system configuration with different battery and PV-system sizes ($PER = 0.2$) on the FEC (Figure 6.5a) and the SOH capacity after 20 years (Figure 6.5b). The system sizing with the maximum PI is marked with a red cross in both figures. | 97 |
| 6.6 | PV-HESS: Course of the different power paths (upper plot) and the SOC together with the SOH (lower plot) over the first simulation year. | 99 |
| 6.7 | PV-HESS: Course of the different power paths (upper plot) and the SOC together with the SOH (lower plot) over the days 135-138 of the first simulation year. | 99 |
| 6.8 | PV-HESS: Temporal distribution of the battery C-rate (Figure 6.8a) and the SOC (Figure 6.8b) over the first simulation year. | 100 |
| 6.9 | PV-HESS: Distribution of the relative frequency of the battery C-rate (Figure 6.9a) and the SOC (Figure 6.9b) over 20 years of simulation. | 101 |
| 6.10 | PV-HESS: Distribution of the relative frequency of the cycle depth (Figure 6.10a) and the cycle depth over C-rate (Figure 6.10b) over 20 years of simulation. The color bar of Figure 6.10b represents the relative frequency values of the histogram. | 102 |
| 6.11 | PV-HESS: Course of the capacity loss (Figure 6.11a) and the resistance increase (Figure 6.11b) over 20 years of simulation. | 102 |
| 6.12 | Figure 6.12a: Weekly course of the PCR tender prices in Germany in 2015. Figure 6.12b: Course of the IDM prices profiles in the first week of 2015. | 106 |
| 6.13 | PCR-supply: Course of the battery C-rate (upper plot) and the SOC and SOH (lower plot) over the first simulation year. | 109 |
| 6.14 | PCR-supply: Temporal distribution of the battery C-rate (Figure 6.14a) and the SOC (Figure 6.14b) over the first simulation year. | 109 |
| 6.15 | PCR-supply: Distribution of the relative frequency of the battery C-rate (Figure 6.15a) and the SOC (Figure 6.15b) over the first simulation year. | 110 |
| 6.16 | PCR-supply: Distribution of the relative frequency of the cycle depth (Figure 6.16a) and the cycle depth over C-rate (Figure 6.16b) over the first simulation year. The color bar of Figure 6.16b represents the relative frequency values of the histogram. | 111 |
| 6.17 | PCR-supply: Course of the capacity loss (Figure 6.17a) and the resistance increase (Figure 6.17b) over the first simulation year. | 112 |
| 6.18 | PI over the specific battery system costs for the baseline scenarios of the PV-HESS application (Figure 6.18a) and PCR supply (Figure 6.18b) subject to different economic scenarios. | 116 |

List of Tables

| | | |
|------|---|-----|
| 2.1 | Comparison of software tools for the simulation of energy storage systems. | 10 |
| 2.2 | Overview of lithium-ion battery calendar aging literature classified into different aging models and cell types. | 19 |
| 2.3 | Overview of lithium-ion battery cycle aging literature classified into different aging models and cell types. | 21 |
| 4.1 | Datasheet values of the investigated LiFePO ₄ /graphite cell Sony US26650FTC1. | 41 |
| 4.2 | Anode overhang areas: Position and areas. (Top side: Inner side of the jelly roll. Bottom side: Outer side of the jelly roll.) | 42 |
| 4.3 | Measured cell-to-cell parameter variation of 1100 units out of two batches of the investigated cell. | 43 |
| 4.4 | Test matrix of the static calendar aging study with the number of cells for each storage condition. | 50 |
| 4.5 | Test matrix of the dynamic calendar aging study with one cell for each test point. | 51 |
| 4.6 | Test matrix of the static cycle aging study with three cells for each test point. The test points marked with * were started later during the course of the static cycle aging study. | 53 |
| 4.7 | Characteristics of the PV-HESS and PV-PCR-BESS profiles. | 56 |
| 4.8 | Relative change of EIS-parameters from the beginning until the end of the aging study for selected TPs. | 62 |
| 4.9 | Relative change of EIS-parameters from the beginning until the end of the aging study for selected TPs. | 69 |
| 5.1 | Q_{loss} and R_{inc} aging model reference values and parameters. | 76 |
| 5.2 | Absolute model errors of Q_{loss} and R_{inc} of all TPs of the dynamic calendar aging study. | 79 |
| 5.3 | Q_{loss} and R_{inc} aging model reference values and parameters. | 84 |
| 6.1 | Battery energy storage system models and parameters. | 89 |
| 6.2 | General economic parameters. | 90 |
| 6.3 | BESS economic parameters (Data from [5]). | 91 |
| 6.4 | PV-HESS: General technical parameters. | 91 |
| 6.5 | PV-HESS economic parameters. | 93 |
| 6.6 | PV-HESS: Simulation parameters. | 94 |
| 6.7 | PV-HESS: Baseline scenario. | 98 |
| 6.8 | PV-HESS economic results. | 103 |
| 6.9 | PCR-supply: General technical parameters. | 104 |
| 6.10 | PCR-supply: General economic parameters. | 106 |
| 6.11 | Fees and costs for the participation on the IDM. | 107 |
| 6.12 | PCR-supply: Simulation parameters. | 107 |
| 6.13 | PCR-supply economic results. | 112 |
| 6.14 | Technical results of baseline scenarios of PV-HESS and PCR simulations. | 113 |

6.15 Economic results of baseline scenarios of PV-HESS and PCR simulations. 114